ISBN 978-82-326-1926-9 (printed version)
ISBN 978-82-326-1927-6 (electronic version)
ISSN 1503-8181

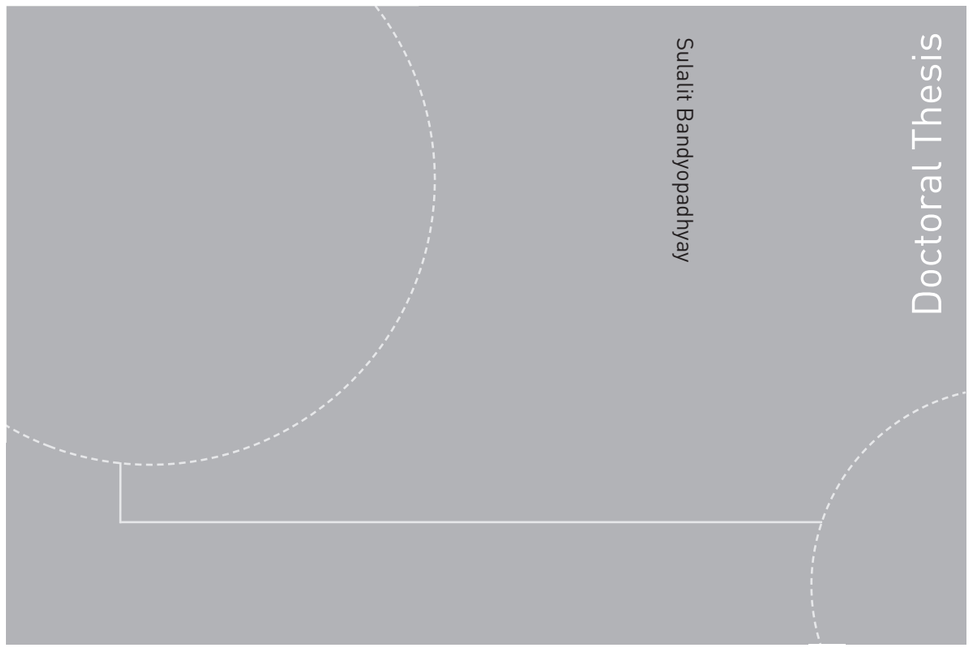

Doctoral theses at NTNU, 2016:294

Sulalit Bandyopadhyay

Smart and Multifunctional Core-Shell Nanoparticles (NPs) for Drug Delivery

NTNU
Norwegian University of
Science and Technology
Faculty of Natural
Sciences and Technology
Department of Chemical Engineering

NTNU
Norwegian University of
Science and Technology

Doctoral theses at NTNU, 2016:294

NTNU

NTNU
Norwegian University of
Science and Technology

Sulalit Bandyopadhyay

Smart and Multifunctional Core-Shell Nanoparticles (NPs) for Drug Delivery

Thesis for the degree of Philosophiae Doctor

Trondheim, October 2016

Norwegian University of Science and Technology
Faculty of Natural
Sciences and Technology
Department of Chemical Engineering

NTNU
Norwegian University of
Science and Technology

NTNU
Norwegian University of Science and Technology

Thesis for the degree of Philosophiae Doctor

Faculty of Natural
Sciences and Technology
Department of Chemical Engineering

ISBN 978-82-326-1926-9 (printed version)
ISBN 978-82-326-1927-6 (electronic version)
ISSN 1503-8181

Doctoral theses at NTNU, 2016:294

Printed by Skipnes Kommunikasjon as

Preface

This thesis is submitted in partial fulfillment of the requirements for the degree of Philosophiae Doctor (PhD) at the Norwegian University of Science and Technology (NTNU) and consists of eight papers. The work presented in this thesis was carried out at the Ugelstad Laboratory, Department of Chemical Engineering; at the Cell Biology laboratories, Department of Neuroscience, Faculty of Medicine and NanoLab, NTNU. The project has been funded by research and development funds from NTNU and support from NorFab. The thesis work has been supervised by Professor II Dr. Wilhelm Robert Glomm and co-supervised by Dr. Gurvinder Singh, Dr. Ioanna Sandvig and MD, PhD Axel Sandvig.

I completed my Bachelors in Chemical Engineering from Jadavpur University in June 2010. Thereafter, being awarded the prestigious Erasmus Mundus Fellowship, I joined NTNU for my Masters in Chemical Engineering. After completion of my master thesis at ETH Zurich and NTNU, I was accepted as a PhD candidate in Ugelstad Laboratory, Department of Chemical Engineering, NTNU in August 2012.

"Dream is not that which you see while sleeping, it is something that does not let you sleep."

Dr. A.P.J. Abdul Kalam, Wings of Fire: An Autobiography

"I slept and dreamt that life was joy. I awoke and saw that life was service. I acted and behold, service was joy."

Rabindranath Tagore

"Logic will get you from A to B. Imagination will take you everywhere."

Albert Einstein

"It doesn't matter how beautiful your theory is, it doesn't matter how smart you are. If it doesn't agree with experiment, it's wrong."

Richard P. Feynman

Acknowledgement

On the verge of plucking yet another wreath in my academic life, I owe this work to two most inspiring characters. After finishing my master thesis at ETH Zurich, the drive I had to come back to Trondheim was because of *bhaijaan*[I], who have always been my greatest motivator. Far from home, in a foreign land, he has been a towering personality shaping my attributes, mostly through constructive criticism and loads of support and encouragement for my cricketing flair and event management qualities. And these event manager roles have very frequently made my supervisor Dr. Wilhelm R. Glomm, the other inspiration, comment that I have been rather a part-time PhD and a full time event manager. Besides getting facebook invites for each and every event I have organized for my entire PhD tenure, he has been a great guide for the scientific merit of this work. What I really like about his scientific persona is to use simple yet novel methods to carry out converging research. And even during his busy workdays, his response time to emails and texts is as fast as a ball travels to fielders in *slip-cordon* area. Sorry, I still haven't explained cricket rules to him! I must admit that he has been very jovial as always and both of us have mutually benefited from the student-supervisor relationship.

I consider myself really lucky to have had three excellent co-supervisors- Dr. Gurvinder Singh, Dr. Ioanna and Dr. Axel Sandvig, who have helped me at important junctures of the thesis. Dr. Singh and me shared the same office for the first 3 years of my PhD. Scientific discussions and what to do next have mostly been the hot topics with him. He loves synthesizing novel materials at the labs, and I complemented him in searching for applications for some of these fascinating shapes. Although located at Øya campus, Dr. Sandvigs have been really helpful in regards to the *in vitro* and *in vivo* studies. In addition, they have always supported the course of the work with valuable research inputs.

Birgitte and me started our PhDs at the same time, although she finished a year back. She has been an awesome colleague and founder member of our facebook group FunNano. Ideas over many experiments resulted over coffee and dinners in our small social group. This group has been frequented by many master students working in the *Nano* niche of the Ugelstad Lab. Marte, Manuel, Alvi, Anuvansh, Haris all contributed immensely towards understanding several aspects of my thesis work through their specialization projects and master theses. Co-supervising them has enriched my professional qualities in designing and executing new sub-

[I] A respectful address for elder brother.

projects within the main scope. Office mates, Lalit and Ahmad have been patient with numerous visits (both official and friendly) during working hours, besides being extra-supportive. Some awesome colleagues at the lab – Andreas, Mehdi, Albert, Sina, Sondre, Bartek, Cathy, May, Bicheng, Serkan, Mona, Sebastien, Marcin, Muh, Sreedhar, Diego, Chris, Aleksandar (just some of them) have been fellas in arranging events together, going on trips, members of lab gossip or just wise advisors for parenting and as such. Of course, some of them have also discussed PhD stuffs as well. You guys will keep rocking wherever you are. Lisbeth, our department secretary, has been superb efficient in administrative matters, always ready to help with a smile. Arne helped with all chemicals and Harry with all gas bottle related issues. Hege always responded to academic matters with promptness.

The number of friends I have made here in T-town exceed overwhelmingly the number of pages this thesis covers. Friends from social networking, MSc studies, cricket, travel, 'by chance' account for most who have helped me in one way or the other. Some of them have supported me throughout the PhD, while some have shared precious moments over dinners, lunches or during social get-togethers whereas some of them have been partners in organizing events, while some have spent nights discussing and debating on topics ranging from religion to history to life. Nico, Fahad, Ashish, Praveen, Daniel, Jeevith, Anirban, Sarmad, Saddam, Hassan are few of them who need special mention. Richa, Urooj *bhabi*,[II] Faheem have actually functioned as family in Trondheim, playing different roles at different times.

I owe limitless thanks to *Ma* and *Baba*[III], both medical doctors, for allowing me to pursue higher studies miles away from home. They have often oversimplified the process in their own minds, only realizing in the end, that rising up the academic ladder is a relatively slow process. However, they have been super helpful as friends and advisors. My entire family back in India and rest of the world (Switzerland, Singapore, Australia, Tanzania) knows that I work with small particles that can be helpful in medicine, and for that, they have always felt proud. It is time for me to feel happy for their constant motivation. My sincerest gratitude to my *amma*[IV] who passed away in 2007. She was my best friend during my childhood and still happens to be a great motivation for each step I take in life. My cousin, Piku, a fresh graduate, has always been a backend support for me and my family back home, filling my place there in Kolkata, my birth town.

[II] Brother's wife.
[III] As I call my mother and father respectively.
[IV] My paternal grandmother.

Trondheim saw me passing from being a bachelor to a married man and to a proud father to Soha. Both Soha and her mother have been immensely helpful in bearing with my workaholic hours trying to finish my PhD within the stipulated time.

And this work wouldn't have seen the light of the day without the blessings from the Almighty, who knows what is in the heart of every human being! All praise to Him.

Abstract

Nanomaterials designed for drug delivery applications require important properties that include monodispersity, biocompatibility, long circulation time which are dependent on size, shape, composition, surface charge among others. Incorporation of targeting and imaging modalities into such nanomaterials allows for both therapeutic and diagnostic functions. Au nanoparticles (NPs), besides being biocompatible, are known to show remarkable optical properties, widely exploited for both bio-sensing and imaging. Setting in of anisotropy causes a wider frequency response range in terms of plasmonic properties, making them promising candidates for hyperthermia. On the other hand, Fe NPs display superparamagnetic properties that can be used for targeting as well as imaging based on magnetic resonance.

Another field of nanomaterials that has garnered interest in recent times is stimuli sensitive hydrogels that swell and collapse in response to temperature and/or pH. These entropically driven volumetric transitions enable release of the cargo as a function of changing stimuli, making them promising candidates for controlled release.

Combination of nanomaterials leads to synergistic enhancement of properties stemming from their respective counterparts. Core-shell NPs is one such combination that has been studied in this work. The main focus of this thesis has been to synthesize, characterize and functionalize core-shell NPs with an aim to use these nanomaterials for theranostic (therapeutic and diagnostic combined) applications. In this pursuit, core-shell Fe@Au NPs, anisotropic Au NPs, poly(N-isopropylacrylamide) (pNIPAM) based hydrogels and hybrid NPs formed by combination of metallic NPs and hydrogels have been studied. The physico-chemical properties of these NPs have been mapped using a wide array of characterization techniques. Size measurements have been done using dynamic light scattering (DLS) and scanning transmission electron microscopy S(T)EM. The plasmonic properties of Au have been characterized primarily using UV-Vis spectroscopy while surface properties of the NPs have been tracked using electrophoretic mobility measurements, X-ray photoelectron spectroscopy (XPS) among other techniques.

Different hybrid NPs have been loaded with model protein drug Cytochrome-*C* or L-Dopa, a drug administered for Parkinson's disease, in order to understand the effects of size, shape, particle number density, drug-carrier interaction, response to stimuli on both loading and release. Release kinetics have been modelled in order to understand the conformational changes in the NPs leading to effective release of the drug.

Fe@Au NPs have been shown to have negligible cytotoxic effects on different cell lines, in addition to their remarkable magnetic and optical properties. In order to further modify the optical properties, anisotropic Au NPs have been synthesized to understand their growth mechanisms. Five differently shaped Au NPs have been thereafter functionalized to assess their cytotoxicity on cancer cells and also to understand the role of shape in the release kinetics of a model protein drug. One of the main findings from the thesis work is that incorporation of metallic NPs inside temperature and/or pH sensitive hydrogels enhances drug loading capacities. In addition, the loaded drug is squeezed out at a faster rate from these systems when the hydrogel units collapse above volume phase transition temperature (VPTT). The swelling-collapse properties of the hydrogels have been captured using a robust methodology developed for the determination of VPTT. A predictive reversibility parameter has been defined for the first time taking all the system state points into consideration. Thus, the NPs studied within the scope of this work provide an incremental contribution to the ever expanding search for smart materials for drug delivery applications.

List of Publications

Paper I

Bandyopadhyay, S.; Singh, G.; Sandvig, I.; Sandvig, A.; Mathieu, R.; Kumar, P.A.; Glomm, W.R.; **Synthesis and *in vitro* cellular interactions of superparamagnetic iron nanoparticles with a crystalline gold shell**; Applied Surface Science; 2014; Volume 316 (1); p. 171-178.

Paper II

Singh, G.; Van Helvoort, A.T.J.; Bandyopadhyay, S.; Volden, S.; Andreassen, J.P.; Glomm, W.R.; **Synthesis of Au nanowires with controlled morphological and structural characteristics**; Applied Surface Science; 2014; Volume 311; p. 780-788.

Paper III

Bandyopadhyay, S.; Andersen, M.K.; Alvi, M.A.A.; Sharma, A.; Raju, R.; McDonagh, B.H.; Glomm, W.R.; **Incorporation of Fe@Au nanoparticles into multiresponsive pNIPAm-AAc colloidal gels modulates drug uptake and release**, Accepted for publication in *Colloid and Polymer Science.*

Paper IV

Bandyopadhyay, S.; Singh, G.; Glomm, W.R.; **Shape Control of gold nanostructures using binary surfactant mixtures**, Under Review in *Journal of American Chemical Society.*

Paper V

Bandyopadhyay, S.; Singh, G.; Sandvig, I.; Sandvig, A.; Glomm, W.R.; ***Makura*-shaped gold nanostructures show high cytotoxicity in cancer cells**, Under Review in *ACS Nano*.

Paper VI

Bandyopadhyay, S.; Sharma, A.; Alvi, M.A.A.; Raju, R.; Glomm, W.R.; **A robust method to calculate VPTT for hydrogels and hybrids**, Manuscript in preparation.

Paper VII

Bandyopadhyay, S.; Alvi, M.A.A.; Sharma, A.; Zhu, K.; Kjøniksen, A.L.; Nyström, B.; Glomm, W.R.; **Influence of polymer coating on release of L-Dopa from Core-shell Fe@Au nanoparticle systems**, Manuscript in preparation.

Paper VIII

Bandyopadhyay, S.; Sharma, A.; Glomm, W.R.; **Influence of different shaped Gold nanoparticles functionalized with NIPAM based hydrogels on the release of Cytochrome *C***, Under Review in *The Journal of Physical Chemistry C.*

Additional Publications

Paper IX

McDonagh, B.H.; Singh, G.; Hak, S.; Bandyopadhyay, S.; Augestad, I.L.; Peddis, D.; Sandvig, I.; Sandvig, A.; Glomm, W.R.; **L-DOPA-Coated Manganese Oxide Nanoparticles as Dual MRI Contrast Agents and Drug-Delivery Vehicles**; Small; 2014; Volume 12 (3); p. 301-306.

Paper X

McDonagh, B.H.; Singh, G.; Bandyopadhyay, S.; Lystvet, S.M.; Ryan, J.A.; Volden, S.; Kim, E.; Sandvig, I.; Sandvig, A.; Glomm, W.R.; **Controlling the self-assembly and optical properties of gold nanoclusters and gold nanoparticles biomineralized with bovine serum albumin**; RSC Advances; 2015; Volume 5; p. 101101-101109.

Paper XI

McDonagh, B.H.; Staudinger, C.; Singh, G.; Normille, P.S.; Toro, J.A.D.; Bandyopadhyay, S.; Leary, R.K.; Myasnichenko, V.S.; Sandvig, A.; Sandvig, I.; Glomm, W.R.; **Pentatwinned iron oxide nanoparticles as glioblastoma-astrocytoma cell actuators**; Manuscript in preparation.

Paper XII

Singh, G.; McDonagh, B.H.; Hak, S.; Bandyopadhyay, S.; Peddis, D.; Sandvig, I.; Sandvig, A.; Glomm, W.R.; **Synthesis of Gd_2O_3 nanodisks and Gd-doped iron oxide nanoparticles**; Manuscript in preparation.

Paper XIII

Rajesh, R.; Bandyopadhyay, S.; Sharma, A.; Glomm, W.R.; **Preparation of multiresponsive p[NIPAm-co-PEGMA](core)/p[NIPAm-co-AAc (shell)] with controlled size and monodispersity**; Manuscript in preparation.

Paper XIV

Singh, G.; Bandyopadhyay, S.; Glomm, W.R.; **Synthesis of different shapes of Au nanostructures using oleic acid**; Manuscript in preparation.

Paper XV

Mohanta, S.C.; Bandyopadhyay, S.; Saha, A.; Devi, P.S.; Glomm, W.R.; **Smart nanogel functionalized iron oxide nanoparticles with temperature tuning characteristics for drug delivery application**; Manuscript in preparation.

Oral Presentations and Invited Talks

1. Oral Presentation at 18th ICNB 2016

Controlling the Release of Cyt C and L- Dopa from pNIPAM-AAc Nanogel Based Systems, 18th International Conference on Nanotechnology and Biotechnology, Melbourne, Australia, 4th – 5th February, 2016.

2. Oral Presentation at Nano@NTNU Symposium 2015

Tailoring the properties of pNIPAM-AAc nanogels with Fe@Au nanoparticles for drug delivery applications, Skistua, Trondheim, 11th November, 2015.

3. Invited Talk at NanoLab-Timini Workshop

Functional Nano, NTNU Nanolab, 5th May, 2015.

4. Oral Presentation at INASCON 2015

Different shaped Au nanostructures for biomedical applications, 9th International Nanoscience Student Conference, University of Basel, Switzerland, 11th – 14th August, 2015.

5. Invited Talk at CGCRI

Synthesis and property control of nanogel coated Fe-oxide nanoparticles for drug delivery, Central Glass and Ceramic Research Institute (CGCRI), Kolkata, India, 24th February, 2015.

6. Oral Presentation at NTNU NanoLab 10 Year Anniversary

Nanogels in targeted drug delivery and hyperthermia treatment, Hotel Britannia, Trondheim, 10th -11th November, 2014.

Posters

1. Sharma, A.; Bandyopadhyay, S.; Alvi, M.A.A.; Rajesh, R.; Glomm, W.R.; *Modelling the Swelling-Collapse Behaviour of Nano Systems Showing Phase Transition*, Nano@NTNU Symposium 2015, Skistua, Trondheim, 11th November, 2015
2. Alvi, M.A.A.; Bandyopadhyay, S.; Zhu, K.; Nyström, B.; Glomm, W.R.; *Controlled Release from Nanoparticles (NPs) for Theranostic Applications*, Nano@NTNU Symposium 2015, Skistua, Trondheim, 11th November, 2015
3. Alvi, M.A.A.; Bandyopadhyay, S.; Zhu, K.; Nyström, B.; Glomm, W.R.; *Controlled Release from Nanoparticles (NPs) for Theranostic Applications*, 9th International Nanoscience Student Conference, University of Basel, Switzerland, 11th – 14th August, 2015.
4. Glomm, W.R.; Bandyopadhyay, S.; McDonagh, B.H.; Singh, G.; *Functional Nanomaterials for Theranostic Applications*, NTNU NanoLab 10 Year Anniversary, Hotel Britannia, Trondheim, 10th -11th November, 2014.
5. Baghirov, H.; Bandyopadhyay, S.; Mørch, Ý.A.; Glomm, W.R.; Davies, C.D.L.; *Nanoparticle uptake and nanoparticle-mediated silencing of efflux transporters in the blood brain barrier*, National PhD Conference in Medical Imaging, Bergen, 17th – 18th June, 2014.
6. Baghirov, H.; Bandyopadhyay, S.; Glomm, W.R.; Davies, C.D.L.; *Ultrasound-assisted transport of nanoparticles across the blood-brain barrier and nanoparticle-mediated silencing of efflux transporters*, National Biophysics Conference, Oslo, 6th – 7th March, 2014.
7. Glomm, W.R.; Bandyopadhyay, S.; McDonagh, B.H.; Singh, G.; *Functional Nanomaterials for Theranostic Applications*, NTNU NanoLab 10 Year Anniversary, Hotel Britannia, Trondheim, 10th -11th November, 2014.
8. Bandyopadhyay, S.; Sandvig, I.; Sandvig, A.; Singh, G.; Glomm, W.R.; *Multifunctional nanoparticles (NPs) for bioimaging*, 5th Norwegian PhD Conference in Medical Imaging, Trmsø, 2nd-3rd October, 2013.
9. Bandyopadhyay, S.; Singh, G.; Glomm, W.R.; *Core Shell Nano-particles (NPs) for Stimuli responsive Targeted Drug delivery*, Myfab and NorFab User Meeting 2013, Ångström Laboratory, Uppsala, Sweden, 17th -18th April, 2013.

10. Bandyopadhyay, S.; Singh, G.; Glomm, W.R.; *Core Shell Nano-particles (NPs) for Stimuli responsive Targeted Drug delivery*, 7th NTNU NanoLab Meeting, Ångström Laboratory, Trondheim, 12th December, 2012.

Popular Science Communications

1. Forsker Grand Prix- Trondheim 2014

Targeting Drugs, Byscenen, Trondheim, 25th September, 2014. The presentation can be found at NRK website. (https://tv.nrk.no/serie/kunnskapskanalen/MDFP15002714/20-12-2014 at 51:45)

2. Invited blog post

Forsker Grand Prix – Targeting Drugs Through the Post, invited by Faculty of Natural Science and Technology (NTNU). (http://blog.nt.ntnu.no/forsker-grand-prix-targeting-drugs-through-the-post/)

Patent

Reversibility parameter- understanding systems that undergo phase change in a new way, Bandyopadhyay, S.; Sharma, A.; Glomm, W.R.; Idea evaluated by NTNU Technology Transfer AS for patenting.

List of Abbreviations

A.R.	Aspect Ratio
BF	Bright Field
CMC	Critical Micelle Concentration
CPP	Critical Packing Parameter
Cyt *C*	Cytochrome *C*
DLS	Dynamic Light Scattering
DSC	Differential Scanning Calorimetry
E.E.	Encapsulation Efficiency
EM	Electromagnetic
EPR	Enhanced Permeability and Retention
L.E.	Loading Efficiency
LCST	Lower Critical Solution Temperature
LSPR	Localized Surface Plasmon Resonance
MRI	Magnetic Resonance Imaging
NGs	Nanogels
NPs	Nanoparticles
RES	Reticuloendothelial system
RP	Reversibility Parameter
S(T)EM	Scanning Transmission Electron Microscopy
SAXS	Small angle X-ray scattering
UPD	Under potential deposition
UV-Vis	Ultraviolet-Visible
VPTT	Volume Phase Transition Temperature
VSM	Vibrating Sample Magnetometry
XPS	X-Ray photoelectron spectroscopy
XRD	X-Ray Diffraction

Table of Contents

1 Motivation 1

2 Inorganic NPs 4

2.1 Classical Nucleation and Growth 4

2.2 Au NPs 8

2.2.1 Optical Properties 8

2.2.2 Anisotropic Au nanostructures 12

2.3 Fe NPs 16

2.3.1 Magnetic properties 16

3 Polymer based NPs 19

3.1 Classification 19

3.1.1 Polymeric NPs 19

3.1.2 Polymeric micelles 19

3.1.3 Dendrimers 20

3.2 Hydrogels – Synthesis, properties and applications 20

4 Hybrid NPs 25

4.1 Synthesis Methods 26

4.2 Drug Delivery Applications 27

4.2.1 Drug Release models 27

4.2.2 Hybrid NPs in drug delivery 29

5 Characterization Techniques 32

5.1 Dynamic Light Scattering (DLS) 32

5.2 Scanning Transmission Electron Microscopy (S(T)EM) 33

5.3 Zeta potential measurements 34

5.4 X-ray photoelectron spectroscopy (XPS) 36

5.5 UV-Vis spectroscopy 37

5.6 Differential Scanning Calorimetry (DSC) 38

6 Results and Discussion 40

6.1 Spherical and Anisotropic metallic NPs 40

6.1.1 Paper-I: Synthesis and *in vitro* cellular interactions of superparamagnetic iron nanoparticles with a crystalline gold shell 41

6.1.2 Paper-II: Synthesis of Au nanowires with controlled morphological and structural characteristics 44

6.1.3 Paper-IV: Shape Control of gold nanostructures using binary surfactant mixtures 49

6.1.4 Paper-V: *Makura*-shaped gold nanostructures show high cytotoxicity in cancer cells 57

6.2 Stimuli-sensitive Hydrogels and their Characterization 61

6.2.1 Paper-III: Incorporation of Fe@Au nanoparticles into multiresponsive pNIPAm-AAc colloidal gels modulates drug uptake and release. 61

6.2.2 Paper-VI: A robust method to calculate VPTT for hydrogels and hybrids 66

6.3 Hybrid NPs 75

6.3.1 Paper-VII: Influence of polymer coating on release of L-Dopa from Core-shell Fe@Au nanoparticle systems 75

6.3.2 Paper-VIII: Influence of different shaped Gold nanoparticles functionalized with NIPAm based hydrogels on the release of Cytochrome C. 82

7 Conclusions and Future Work 90

8 Bibliography 93

List of Figures

Figure 1.1 Major sub-topics covered within this thesis include metallic NPs, nanogels and hybrid NPs formed by combination of the former. 2
Figure 2.1 Lamer diagram showing nucleation and growth of NPs. [12] 6
Figure 2.2 Schematic showing localized surface plasmon reference (LSPR) in a metallic NP. [16] 8
Figure 2.3 UV-Vis spectra of colloidal water suspensions of Au nanostructures. Dotted curve: nanospheres (diameter 15–25 nm). Solid curve: low A.R. NRs. Dashed curve: high A.R. NRs. Extinction is normalized at ca. 520 nm. [20] 11
Figure 2.4 Schematic showing a Ag-assisted seeded growth process for synthesis of anisotropic gold nanostructures. 13
Figure 2.5 Simplistic overview of (a) Ag under potential deposition (b) face specific capping and (c) surfactant templating as mechanism for growth of Au NRs.[36] 14
Figure 2.6 Parameters describing the strength and magnetization of superparamagnetic (SPM), ferrimagnetic and ferromagnetic(FM) materials.[50] 18
Figure 3.1 Schematic showing precipitation polymerization of hydrogels. [65] 22
Figure 4.1 Illustration showing different kinds of Core-Shell Hybrid NPs. 25
Figure 4.2 Schematic showing reverse micelle based synthetic route for metallic NPs 26
Figure 5.1 Schematic showing the main components of a high-resolution S(T)EM.[113] 34
Figure 5.2 Electrical double layer for a charged spherical particle and location of the surface of shear.[115] 35
Figure 5.3 XPS instrument used for surface analysis. 36
Figure 5.4 Transmission of light through a particle solution. 37
Figure 6.1 Flowline of thesis papers showing research work carried out related to metallic NPs, nanogels and hybrid NPs. 40
Figure 6.2 Schematic showing synthesis of Fe@Au NPs followed by functionalization with PEG-SH. Adapted from [119] 41
Figure 6.3 Representative BF S(T)EM images of (a) Fe@FexOy NPs (inset is a magnified image of Fe NPs), (b) Fe@Au NPs (inset is EDX spectrum for Fe@Au NPs), (c) XPS survey spectra of Fe@Au NPs. UV-Vis spectra of (d) Fe, Fe@Au and PEG coated Fe@Au NPs. (e) Fe@Au NPs synthesized using different concentrations of Chloroauric acid 0.9 mM, 1.5 mM and 3.4 mM. (f) Magnetic hysteresis curves at 300K for Fe and Fe@Au NPs. Adapted from [119] 43

Figure 6.4 (a),(b),(d),(e) Live/Dead images of OECs and hNSCs 24h after labelling with Fe@Au NPs (a) Unlabelled OECs, (b) OECs with Fe@Au NPs, (d) Unlabelled hNSCs and (e) hNSCs with Fe@Au NPs. (c), (f) Differential interference contrast (DIC) images of labelled OECs and hNSCs, respectively, showing Fe@Au uptake (arrows). Adapted from [119] 44
Figure 6.5 (a) Schematic illustration showing growth of Au NWs via two different types of seed NPs, (I) spherical NPs yield wavy NWs, and (II) NRs yield straight NWs. (b) BF S(T)EM image of Au NWs growth from seed 1 at pH~6.9. (c) Enlarged BF S(T)EM image of Au NWs (inset in (c) is a diffraction pattern corresponding to square region confirming the polycrystallinity in the NWs. (d) BF S(T)EM image of straight Au NWs grown from seed 2 at pH ~6.9. (e) Enlarged BF S(T)EM view of single NWs synthesized by seed 2 (inset: diffraction pattern corresponding to the region I confirming that growth direction of NWs is [1 1 1]. Adapted from [32].....46
Figure 6.6 Evolution of growth of Au NWs over time, t. (a) BF S(T)EM image, t = 10 min, (b) SEM image, t = 30 min (c) SEM image, t = 60 min (the arrows in the inset show convex/concave regions or neck formation between two adjacent growing nanostructures), and (d) SEM image, t = 120 min. Adapted from [32]. 47
Figure 6.7 SEM images of Au NWs grown via seed 1 at different CTAB concentrations and fixed pH~6.9 (a) 25 mM, (b) 10 mM, (c) 1 mM. Inset in (a) is BF S(T)EM at higher magnification and in (b) is SEM of low A.R. NWs. (d) XPS survey spectrum of CTAB capped wavy Au NWs. XPS high resolution spectra of the (e) Au 4f, (f) N 1s, and (g) C1s (inset: Br 3d). Adapted from [32]. 48
Figure 6.8 Au NPs synthesized at different CTAB/DDAB ratios (x). SEM images of Au bipyramid NPs of (a) l = 1.2 μm and w = 382 nm, x = 2 and (b) l = 666 nm and w = 180 nm, x = 6. (c) TEM image of single Au bipyramid of (b). (d) Electron diffraction pattern taken on bipyramids shown in (c). (e) SEM image of Au THH NPs, l = 198 nm and w = 168 nm, x = 8. BF-STEM images of Au NRs of f) l = 33 nm and w = 11 nm, x = 23, (g) l = 45 nm and w = 24 nm, x = 11 and (h) l = 38 nm and w = 10 nm, x = 46. (i) HRTEM image of Au NR and inset is FFT of NR. l and w are referred to as longitudinal length and transverse width respectively.51
Figure 6.9 The influence of growth solution pH on the sizes of Au NPs synthesized at low and high CTAB/DDAB ratios (6 and 23) . (a-d) SEM images show decrease in the average size of Au bipyramids with decrease in pH from left (1.9) to right (1.0). (e-h) BF S(T)EM images exhibit increase in the average length of Au NRs with decrease in pH from left to right. 53

Figure 6.10 The influence of AA concentration on the morphology of Au NPs. (a) SEM image of Au NPs at low CTAB/DDAB = 6, AA = 270 µL. BFSTEM images of Au nanorods synthesized at high CTAB/DDAB = 23 at different AA concentrations, (b) AA = 270 µL, (c) AA = 500 µL, (d) AA = 1 mL. 55
Figure 6.11 The role of counter ions present in the secondary surfactant on the morphology of Au NPs . (a-c) BF S(T)EM images of Au NRs prepared in the growth solution containing CTAB/DDAC in different ratios. The ratio increases from (a) to (c). (d) SEM images showing Au NRs grown from the solution at high CTAB/TDAI ratio (~ 23). e) Au NRs with facets synthesized in the growth solution of low CTAB/TDAI ratio (~ 11), and (f) is the magnified view of (e). 56
Figure 6.12 Representative BF S(T)EM images of (a) nanorods (inset is a magnified image), (b) tetrahexahedra (inset is a magnified image), (c) nano*makura* (inset is a magnified image), (d) bipyramids and (e) spheres (inset is a magnified image) (f) UV-vis spectra of the Au nanostructures. 57
Figure 6.13 (a) Variation of DLS sizes of the Au nanostructures after each stage of functionalization. (b) Variation of zeta potentials of Au nanostructures with each stage of functionalization. 58
Figure 6.14 a) Percentage cell death of GA cells as a function of concentration of Au nanostructure after incubation for 24 hours. b) TEM image shows an invagination of the cellular membrane (error bar = 1 µm), and c) halogen and d) fluorescence images show association of nano*makura* at the cellular membrane. e) Uptake of nano*makura* was observed after 6 hours (error bar = 500 nm), f) with uptake in intracellular vesicles (error bar = 2 µm). g) Staining of the nucleus suggest that nano*makura* were excluded from the nucleus. h) TEM images taken after 12 hours suggest uptake via micropinocytosis (error bar = 500 nm), with i) intra-vesicular location of nano*makura* (error bar = 500 nm). j) Intracellular compartmentalization was also visible from the microscopy. Uptake of nano*makura* continued at 24 hours as seen in TEM images k) (error bar = 2 µm) and l) (error bar = 5 µm). m) Detachment of GA cells from the surface was observed, which most likely is an indication of cell death. 60
Figure 6.15 (a) Variation of sizes of the NGs synthesized using different parameters. (b) Variation of sizes of the NGs as a function of SDS concentration. 62
Figure 6.16 (a) Swelling ratio (α) of a representative NG as a function of temperature during heating and cooling cycles. (b) Size of a representative NG as a function of pH. (c) Zeta potential of a representative NG as a function of temperature during heating and cooling cycles.

(d) Size of Fe@Au NPs, representative NG, Fe@Au_NG_c and Fe@Au_NG_i as a function of temperature. 63
Figure 6.17 Comparison of release of Cyt *C* (loaded using breathing-in mechanism and traditional method) over time from (a) a representative NG and Fe@Au NPs incorporated into NGs at pH 3, T 40°C. (b) Plot of ln (F) as a function of ln (t) for a representative NG and Fe@Au NPs incorporated into NGs at pH 3, T 40°C. (c) Overall schematic showing release of Cyt-C at pH 3.4 and temperature 40°C from three different NG combinations- NG, Fe@Au_NG_c and Fe@Au_NG_i. 64
Figure 6.18 Schematic showing calculation of VPTT. (a) Normalized spectroscopic parameter as a function of independent variable (temperature, ^{0}C). (b) Fitting of Sigmoid, 5 parameter curve to the experimental dataset. (c) Area equalization algorithm. (d) Determination of VPTT using MATLAB® code. 67
Figure 6.19 Heating and cooling VPTTs for different samples calculated using (a) Method I (b) Method II and (c) Method III respectively. Regression analysis for (d) pNIPAm /PEG200-pNIPAm/AAc, (e) Fe@Au_PEG_nanogel and (f) 80 nm Au IgG nanoclusters using experimental datasets. Yellow, pink and red points refer to volumes obtained at the calculated VPTTs for the respective systems using Methods I, II and III respectively. 70
Figure 6.20 Variation of lnV vs ln T for (a) pNIPAm(PEG200-pNIPAm/Aac, (b) Fe@Au_PEG_nanogel and (c) 80nm Au IgG nanoclusters. 72
Figure 6.21 (a) Reversibility parameters and (b) Percentage irreversibilities for all samples. 74
Figure 6.22 Chemical structures, molecular weights and polydispersities of synthesized and commercial polymers applied in this study. 76
Figure 6.23 (a) Hydrodynamic sizes of both bare and coated Fe@Au NPs. (b) Zeta potentials of both bare and coated Fe@Au NPs. 77
Figure 6.24 (a) Comparison of the UV-Vis spectra for the bare Fe@Au NPs with Fe@Au NPs coated with different polymers. (b) S(T)EM images of Fe@Au_Microgel at 25^{0}C and after heating it to 40^{0}C (top panel). Red circles indicate the location of Fe@Au NPs. Schematic showing the collapse of microgel units above VPTT, which are pulled together by the Fe@Au NPs. Variation of swelling ratios as a function of temperature of (c) Fe@Au_Microgel and (d) Fe@Au_PEG_Microgel. Variation of (g) Hydrodynamic sizes (nm) and (h) Zeta potentials (mV) of different Fe@Au coated systems at 25°C and 40°C. 79
Figure 6.25 Release kinetics of L-Dopa at 40°C and pH 3.5 from (a) Fe@Au_Microgel, Fe@Au_PEG, Fe@Au_PEG_Microgel, (b) Fe@Au_PN(+) and Fe@Au_PNIPAAM-COOH

respectively. Plots of ln F versus ln t for (c) Fe@Au_Microgel, Fe@Au_PEG, Fe@Au_PEG_Microgel, (d) Fe@Au_PN(+) and Fe@Au_PNIPAAM-COOH respectively. 81
Figure 6.26 S(T)EM images of a) AuNR, b) PEG-hydrogel coated AuNR, c) AuHex, d) PEG-hydrogel coated AuHex, e) AuBP, f) PEG-hydrogel coated AuBP, g) AuNM, h) PEG-hydrogel coated AuNM, i) AuNS and j) PEG-hydrogel coated AuNS.....84
Figure 6.27 a) UV-Vis spectra for different shaped AuNPs. Variation of UV-Vis spectra after coating with PEG followed by hydrogel coating for b) AuNR, c) AuHex, d) AuBP, e) AuNM and f) AuNS. Variation of g) hydrodynamic sizes and h) zeta potentials of different shaped AuNPs measured at base and release conditions respectively.....85
Figure 6.28 a) Loading and b) Encapsulation efficiencies for different shaped AuNPs for two different hydrogel concentrations. Release kinetics of Cyt *C* from different shaped AuNPs for c) 1.7 mg/ml and d) 3.3 mg/ml hydrogel concentrations respectively. e) Rate constants and f) release exponents for Cyt *C* release from different shaped AuNPs.....88

1 Motivation

Nanomaterials are promising candidates for diagnosis and treatment of various diseases owing to their tunable physical, chemical, optical, electronic and magnetic properties among others. [1, 2] These unique properties of functionalized nanomaterials make their behaviours different from those of bulk materials with the same compositions.[3] Their physico-chemical properties are dependent on size, shape, composition and surface chemistry and determine their end uses. The journey of such nanomaterials from the lab scale to end uses depends on the identification of a clinical problem and innovative ideas required to solve it through rational design. [4] The success of therapeutics relies on addressing three critical challenges: first, recognition of the target cells and tissues; second, sequential overcoming of the natural defenses to reach the intended site, and third, the ability of delivering multiple therapeutic agents causing a synergistic effect at the diseased site.[5] Targeted drug delivery and controlled release of drugs at the site of action have become important in medical science in order to overcome side-effects caused by accumulation of drugs in healthy tissues and to provide highest therapeutic effect to the diseased site.

Combining nanoparticles (NPs) with pharmaceutically active compounds like drugs, peptides, enzymes, antibodies and so on holds great promise in developing smart drug delivery vectors with unmatched performance and high selectivity. The successful design of these new materials depends on exhibition of emergent properties stemming from either the NP or the pharmaceutical compound alone. In addition to being a vector for the pharmaceutically active compound, the NP core can act as a diagnostic tool, wherein combining therapeutic and diagnostic capabilities in one single entity. This further opens up the possibilities for using a plethora of NP combinations to impart several functionalities on such drug delivery systems. The location of the drug, coupled with interactions between the drug and the carrier become important parameters for controlling drug release.

This thesis has focused on synthesis and characterization of different metallic and hydrogel core-shell NPs, followed by functionalization tailored towards making them suitable candidates in drug delivery. In essence, spherical Fe@Au core-shell NPs and different shapes and sizes of anisotropic Au nanostructures have been synthesized with control of their physico-chemical properties, further tuned through surface functionalization. Another part of the thesis has focused on temperature and pH responsive core-shell nanogels (NGs) that have been synthesized and optimized in terms of loading and release of model drugs. Their swelling-

collapse properties measured using light scattering have been studied to define a novel reversibility parameter, for describing such systems that undergo phase changes. Finally, in an attempt to combine metallic and polymeric NPs, different shapes of nanogel coated Au NPs have been synthesized and shown to have shape dependent effects on drug loading and release kinetics. Figure 1.1 shows a synopsis of the different kinds of NPs studied within the scope of this thesis.

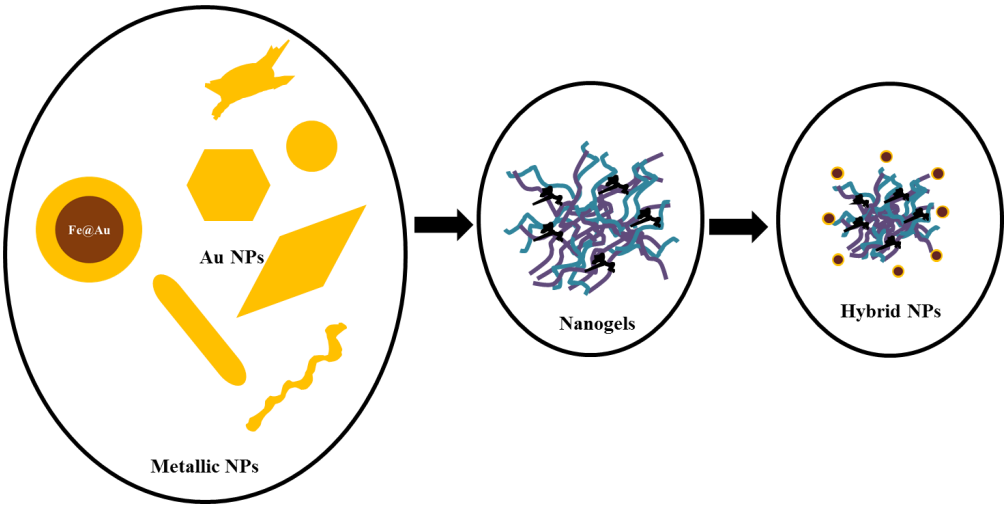

Figure 1.1 Major sub-topics covered within this thesis include metallic NPs, nanogels and hybrid NPs formed by combination of the former.

Within the scope of the introduction to this thesis, a brief overview will be given for different kinds of nanoparticles (NPs) based on their composition- namely inorganic (Chapter 2), polymeric based NPs (Chapter 3) and hybrid NPs (Chapter 4). In these chapters, synthesis of isotropic NPs will be discussed in light of the classical theory of nucleation and growth. This will be followed by an attempt to understand different mechanisms of growth of gold nanostructures via seed mediated synthesis method as an example to understand shape anisotropy in NPs. Different physico-chemical properties of the NPs will be highlighted including magnetic, optical, swelling-collapse properties among others to understand the multifunctionality of such nanoconstructs. Finally, potential therapeutic and diagnostic applications of NPs will be discussed with an aim of understanding the current role of such multifunctional NPs in nanomedicine. In Chapter 5, various characterization techniques for determination of size, composition and other physico-chemical properties of NPs will be discussed within the scope of the research work presented in this thesis. Chapter 6 will highlight

the main findings from the various studies and concluding remarks about the study will be presented in Chapter 7 along with suggestions for future studies in this direction.

2 Inorganic NPs

The fascinating properties of NPs arise from their size (1-100nm in at least one dimension), in which size scale, the quantum effects rule the behaviour of particles. The quantum size effect comes into play when the de Broglie wavelength of the valence electrons is of the same order as the particle size. The particles then behave electronically as zero-dimensional quantum dots which can be described using relevant quantum-mechanical rules. [6] Taking advantage of such properties, it is possible to design multifunctional NPs that can exhibit different emergent properties from the constituting counterparts.

Based on the composition, NPs can be broadly classified into inorganic, polymeric and hybrid NPs, the latter being formed by combining inorganic and polymeric counterparts forming a library of NPs.

Inorganic NPs are primarily constituted of inorganic materials like Au, Ag, Fe, Co, Pt, Ni, Si and so on. A large majority of inorganic NPs are constituted of metals and often referred to as metallic NPs while other different categories include semi-conductor NPs, metal oxide NPs and so on. Metallic NPs can be synthesized using a wide range of methods which vary from solution based bottom-up approach enabling reduction of a metal precursor in the presence of a passivating ligand to top-down approaches like lithography, thermal or mechanical methods. In case of the solution based method, the formation of monodisperse NPs is achieved through reduction of metal complex in solution, leading to initial nucleation and subsequent growth of initial nuclei. In order to prevent aggregation of the synthesized NPs, polymeric stabilizers or other passivating ligands are often used. Thus, this synthesis method requires a precursor, reducing agent and stabilizer.[7] As this thesis has mostly covered solution based bottom up methods, the classical theory of nucleation and growth describing this synthesis will be discussed here.

2.1 Classical Nucleation and Growth

Classical nucleation and growth will be discussed using references [8-11]. Nucleation is the first step to the formation of NPs in solution. Depending on whether the nuclei start forming in bulk solution or on solid substrates (like impurities or already synthesized particles), nucleation could be homogeneous or heterogeneous respectively. In either case, the driving force is supersaturation ($\Delta\mu$) and is defined thermodynamically as follows:

$$\Delta\mu = kT\ln(S) \qquad (1)$$

where k is Boltzmann's constant, T is temperature in K and S is the supersaturation ratio defined as follows:

$$S = \frac{a_1^{n1} a_2^{n2} .... a_j^{nj}}{a_{1e}^{n1} a_{2e}^{n2} .... a_{ne}^{nj}} \qquad (2)$$

where n_i is the number of the ith ions in a molecule of the crystal, a_j and a_{je} are, respectively, the actual and equilibrium activities of these ions in the solution, and the denominator is the solubility product. The activities can be replaced with concentration terms for dilute solutions.

The nucleation rate of N nuclei formed per unit time per unit volume can be expressed as an Arrhenius form of equation

$$\frac{dN}{dt} = A \exp\left(-\frac{\triangle G_{crit}}{k_B T} \right) \qquad (3)$$

where $\triangle G_{crit}$ represents the required lowest energy barrier required to obtain stable nuclei in solution. A is a pre-exponential factor. For homogenous nucleation of spherical particles,

$$\triangle G_{crit} = \frac{16\pi\gamma^3 \nu^2}{3(k_B T \ln S)^2} \qquad (4)$$

where γ is the interfacial tension, ν is the molecular volume. This leads to a final expression for the nucleation rate which shows that temperature, supersaturation and interfacial tension govern the rate.

$$J = A \exp\left(-\frac{16\pi\gamma^3 \nu^2}{3k_B{}^3 T^3 (\ln S)^2} \right) \qquad (5)$$

In case of heterogeneous nucleation, the overall free energy change associated with the formation of critical nucleus ($\triangle G'_{crit}$) is lesser compared to that in homogeneous nucleation, owing to presence of surface (such as container surfaces, primary particles, impurities, grain boundaries, dislocations) where nucleation can begin.

$$\triangle G'_{crit} = \phi \triangle G_{crit} \qquad (6)$$

ϕ is a factor less than unity.

As soon as the stable nuclei are formed, growth of the nuclei sets in and this determines the final shapes of the particles. Lamer diagram, shown in Figure 2.1 shows the nucleation and growth events as a function of time and concentration of the solute.

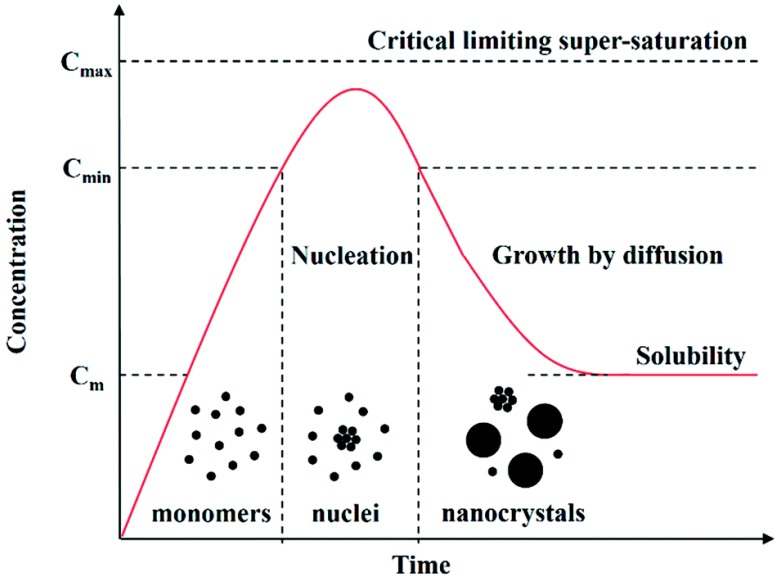

Figure 2.1 Lamer diagram showing nucleation and growth of NPs. [12]

However, there exist several theories which try to explain crystal growth, namely – surface energy theories, adsorption layer theories and diffusion theories. While the surface energy theories are based on the postulation that the shape will be dictated by minimum surface energy, the diffusion theories presume that continuous deposition of matter happens as a result of a concentration gradient between the bulk and the surface. The adsorption layer theories view crystal growth as a discontinuation process, taking place layer by layer. Among all the theories mentioned here, the diffusion-reaction theory will be discussed in detail.

Diffusion-reaction theory considers crystal growth to happen due to two steps: a diffusion process by which solute molecules are transported from the bulk of the solution to the solid surface and a first-order reaction when these transported solute molecules arrange into the crystal lattice. These two processes can be represented by the following equations:

$$\frac{dm}{dt} = k_d A\left(C - C_i\right) \qquad (7)$$

$$\frac{dm}{dt} = k_r A\left(C_i - C^*\right) \qquad (8)$$

Here, m = mass of the solid deposited in time t, k_d = mass transfer coefficient based on diffusion, k_r = rate constant for surface reaction process, A = surface area of the crystal, C_i = solute concentration in the solution at the crystal-solution interface, C^* = equilibrium saturation concentration, C = solute concentration in the supersaturated solution.

A generalized equation for crystallization based on the overall driving force can be written as follows:

$$\frac{dm}{dt} = K_G A\left(C - C^*\right)^g \qquad (9)$$

Where, K_G is the overall crystal growth coefficient and g is referred to as the order of the overall crystal growth.

For growth controlled by surface integration, three mechanisms can be distinguished – namely 2D-nucleation, spiral growth and rough growth. For relatively large values of supersaturations, 2D-nucleation of growth sites can appear. This generates the necessary kinks for further growth. If the rate of lateral growth of the 2D-nuclei is high in comparison to the nucleation rate, the surface is smooth. For even higher supersaturations, the nucleation rate dominates the process and the surface becomes rough. A number of experimental findings have shown that crystals grow fast, at supersaturations much lower than necessary for 2D-nucleation to occur. Most crystals contain dislocations which cause steps to be formed on the faces and promote growth (Spiral growth). For relatively higher supersaturations, growth units attach anywhere on the crystal surface (terraces, steps or kinks) making the crystal surface rough, so called rough growth.

A generalized expression for reaction controlled growth can be represented by the following equation:

$$G = k_g \left(S - 1\right)^g \qquad (10)$$

where, G represents the crystal growth rate, k_g is the growth rate constant that scales with solute concentration and g , known as the order of crystal growth process, takes on different values depending on the type of growth. Most commonly, the following values are observed:

Spiral growth (low S): g =2

Spiral growth (high S): g =1

2D-nucleation: $g > 2$

Rough growth : $g = 1$

Thus, the two principal events, namely nucleation and crystal growth influence both the size as well as the shape of the resultant NPs. In the next subsections, two specific examples of inorganic NPs, viz. Au and Fe will be discussed, with emphasis on their physico-chemical properties.

2.2 Au NPs

Au NPs have proven to be promising candidates for biomedical applications owing to their excellent biocompatibility, ease to be surface-functionalized and low toxicity.[13] Their applications range from bioimaging, immunoanalysis, photothermal therapy, targeted delivery of drugs, DNA and antigens; biosensing and monitoring of cells and tissues using modern registration systems.[14] The wide range of applications of Au NPs stems from the ease with which the gold surface can be functionalized with a large variety of chemical moieties in addition to their remarkable optical properties.

2.2.1 Optical Properties

In a small metal NP (Rayleigh scattering regime; $a/\lambda < 0.1$; where a is the radius of the NP and λ is the wavelength of the incident light)), the incident electromagnetic (EM) wave exerts a force on conductive electrons and displaces them from their equilibrium positions to create uncompensated charges at the NP surface. Polarization of the particle surface produces a restoring force. When the frequency of oscillation matches the frequency of the incoming wave, the excited NP behaves like a resonance oscillator. This effect is termed as localized surface plasmon resonance (LSPR)(Figure 2.2). These interactions between the incoming photons and the surface electrons of Au NPs result in high absorption coefficient, exhibited through a maximum absorption peak in UV-visible (UV-Vis) spectroscopy. [15]

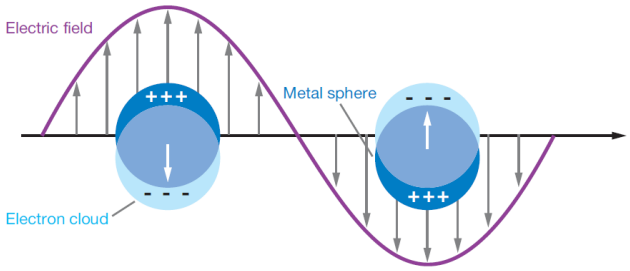

Figure 2.2 Schematic showing localized surface plasmon reference (LSPR) in a metallic NP. [16]

Mie-Drude theory helps predict the position and shift of LSPR peaks. Mie solved the Maxwell's equations using quasi- static approximation, for a spherical nanoparticle of radius a, irradiated by z-polarized light of wavelength λ. When $a/\lambda < 0.1$, the magnitude of the electric field appears static around the NP. Solving the Maxwell's equation using the quasi static approximation yields the following EM field outside the particle:

$$\overrightarrow{\mathbf{E}_{\mathbf{out}}}(x,y,z) = E_0\hat{\mathbf{z}} - \left[\frac{\varepsilon_{in}-\varepsilon_{out}}{\varepsilon_{in}+2\varepsilon_{out}}\right]a^3E_0\left[\frac{\hat{\mathbf{z}}}{r^3} - \frac{3z}{r^5}\left(x\hat{\mathbf{x}}+y\hat{\mathbf{y}}+z\hat{\mathbf{z}}\right)\right] \qquad (11)$$

ε_{in} is the dielectric constant of the metal NP, ε_{out} is the dielectric constant of the medium. Under such conditions, when the dipole oscillation contributes significantly to the extinction cross-section, a simplified expression for the extinction cross-section can be obtained as below:

$$\sigma_{ext} = \frac{18\pi\varepsilon_{out}^{\frac{3}{2}}V}{\lambda}\frac{\varepsilon_2(\lambda)}{\left[\varepsilon_1(\lambda)+2\varepsilon_{out}\right]^2+\varepsilon_2(\lambda)^2} \qquad (12)$$

where ε_1 and ε_2 are the real and imaginary parts of the complex metal dielectric function respectively:

$$\varepsilon_{in} = \varepsilon_1 + i\varepsilon_2 \qquad (13)$$

When the dielectric constant of the metal is roughly equal to $-2\varepsilon_{out}$, the EM field is enhanced relative to the incident field, a condition defined as LSPR. For spherical Au NPs, LSPR maximum is obtained around 520 nm, however, the peak position is dependent on size, shape, material and local dielectric properties.[16]

$\lambda_{\max}$, the wavelength at which LSPR happens has a functional dependence on the dielectric function of the medium. In order to establish this, Drude model, [17, 18] that describes how the free electrons experience damping due to the positive lattice and applied EM field, is used to define ε_1

$$\varepsilon_1 = 1 - \frac{\omega_p^2}{\omega^2+\gamma^2} \qquad (14)$$

Where, ω_p is the plasma frequency, γ is the damping parameter of the bulk metal. For visible and near infrared frequencies, $\gamma << \omega_p$. Further, at resonance condition, equation (14) simplifies to:

$$\omega_{\max} = \frac{\omega_p}{\sqrt{2\varepsilon_{out} + 1}} \tag{15}$$

$\omega_{\max}$ is the LSPR peak frequency, related to $\lambda_{\max}$ as follows:

$$\lambda_{\max} = \frac{2\pi c}{\omega_{\max}} \tag{16}$$

where, c is the velocity of light. Substituting $\varepsilon_{out} = n_{out}{}^2$ in equation (15) provides the following expression:

$$\lambda_{\max} = \lambda_p \sqrt{2n_{out}^2 + 1} \tag{17}$$

Where, $\lambda_{\max}$ is the LSPR peak wavelength and λ_p is the wavelength corresponding to the plasma frequency of the bulk metal and n_{out} is the refractive index of the medium.

Introduction of a thin surface layer changes the extinction cross-section given by: [19]

$$\sigma_{ext} = 4\pi R^2 \, \mathrm{k}^* \, \mathrm{Im}\left[\frac{(\varepsilon_s - \varepsilon_{out})(\varepsilon_c - 2\varepsilon_s) + (1-g)(\varepsilon_c - \varepsilon_s)(\varepsilon_{out} + 2\varepsilon_s)}{(\varepsilon_s + 2\varepsilon_{out})(\varepsilon_c + 2\varepsilon_s) + (1-g)(2\varepsilon_s - 2\varepsilon_{out})(\varepsilon_c - \varepsilon_s)} \right] \tag{18}$$

where, $\varepsilon_c, \varepsilon_s$ are the complex dielectric functions of the core and the shell respectively, g is the volume fraction of the shell layer and R is the radius of the coated particle.

The changes in the local environment, due to the presence of an adsorbed species will also cause a shift in $\lambda_{\max}$ as follows:[16]

$$\Delta\lambda_{\max} = m\Delta n \left[1 - \exp\left(\frac{-2d}{l_d} \right) \right] \tag{19}$$

Here, m is the bulk refractive index response of the NPs, Δn is the change in refractive index induced by the adsorbate, d is the effective adsorbate layer thickness, and l_d is the characteristic EM-field-decay length.

Introduction of anisotropy also changes the extinction cross-section. For elongated ellipsoids, using the dipole approximation according to the Gans treatment, the extinction is given as:[18]

$$\sigma_{ext} = \frac{2\pi\varepsilon_{out}^{\frac{3}{2}} V}{3\lambda} \sum_j \frac{\left(1/P_j^2\right)\varepsilon_2}{\left\{\varepsilon_1 + \left[\left(1-P_j\right)/P_j\right]\varepsilon_{out}\right\}^2 + \varepsilon_2^2} \tag{20}$$

Where P_j s are the depolarization factors along the three axes A, B and C respectively of the nanorod (NR) with A > B = C, defined as

$$P_A = \frac{1-e^2}{e^2}\left[\frac{1}{2e}\ln\left(\frac{1+e}{1-e}\right)-1\right] \tag{21}$$

$$P_B = P_C = \frac{1-P_A}{2} \tag{22}$$

$$e = \left[1-\left(\frac{B}{A}\right)^2\right]^{\frac{1}{2}} = \left(1-\frac{1}{(AR)^2}\right)^{\frac{1}{2}} \tag{23}$$

Where AR is the aspect ratio (A.R) of the NRs.

The extinction spectrum in equation (20) shows two peaks, one corresponding to the transverse plasmon mode (x,y contributions) while the other corresponding to the longitudinal plasmon mode (z contribution) (Figure 2.3).

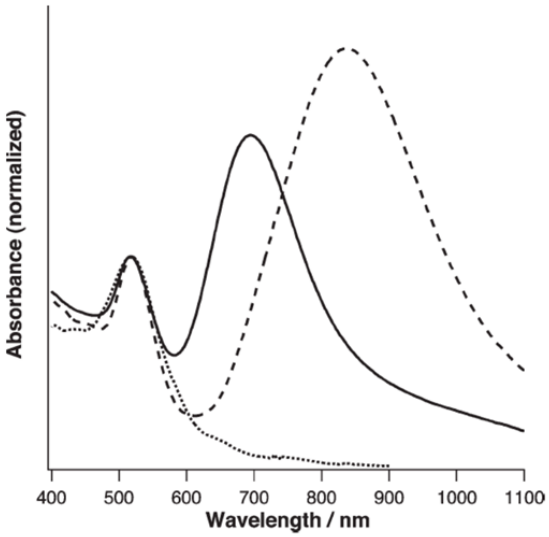

Figure 2.3 UV-Vis spectra of colloidal water suspensions of Au nanostructures. Dotted curve: nanospheres (diameter 15–25 nm). Solid curve: low A.R. NRs. Dashed curve: high A.R. NRs. Extinction is normalized at ca. 520 nm. [20]

The factor weighting ε_{out}, which is 2 for spherical particles, is $\left[\left(1-P_j\right)/P_j\right]$, a quantity that increases with A.R. and can be much greater than 2. This leads to a bathochromic shift (red

shift) of the plasmon peak with increasing A.R., as well as increased sensitivity to the dielectric constant of the surrounding medium. [17]

2.2.2 Anisotropic Au nanostructures

Fine controlling the A.R. (defined as the ratio of length to diameter) of Au nanostructures has become important, as this enables wide range of optical properties that can be explored by changing the A.R. Anisotropy splits up the single LSPR band, generally observed for spherical Au NPs, into at least two distinct peaks, representative of the transverse and longitudinal axes. The larger A.R structures have a larger extinction coefficient, whereby they scatter more light at longitudinal plasmon wavelength, thereby rendering improved applications in optical imaging. On the other hand, the smaller A.R. structures absorb more light at the longitudinal plasmon wavelength, paving way for photothermal applications (Figure 2.3).[21-23]

The most common synthetic methods for Au NRs can be broadly divided into – (a) Electrotemplated synthesis [24] (b) Photochemical reduction technique [25] (c) Three step seeded growth [26] (d) One step Ag-assisted seeded growth [27] and (e) 'Seedless' growth approach.[28]

In recent years, the seeded growth synthesis has gained immense popularity owing to the fact that a wide array of shapes and sizes can be synthesized using modifications that include small organic additives, binary surfactant mixtures and other synergistic strategies to help control growth.[29-32] The seeded growth procedure utilizes small Au NP seeds (~1.5 nm) stabilized with a cationic surfactant, CTAB (Cetyltrimethylammonium bromide). The growth solution is made of chloroauric acid ($HAuCl_4$), CTAB and a small amount of silver nitrate ($AgNO_3$) wherein, ascorbic acid that reduces Au^{3+} to Au^{+1}, is added. Thereafter, the seed solution is added to the growth solution and the nanostructures are allowed to grow at 35°C. The resulting solutions are purified using dialysis or centrifugation. This method always results in lower A.R (1.5- 5) rods as compared to the seeded growth without Ag.[33] However, modifications in this method using binary surfactant mixtures have also made it possible to synthesize high A.R. structures.[34] A schematic of the overall process is depicted in Figure 2.4.

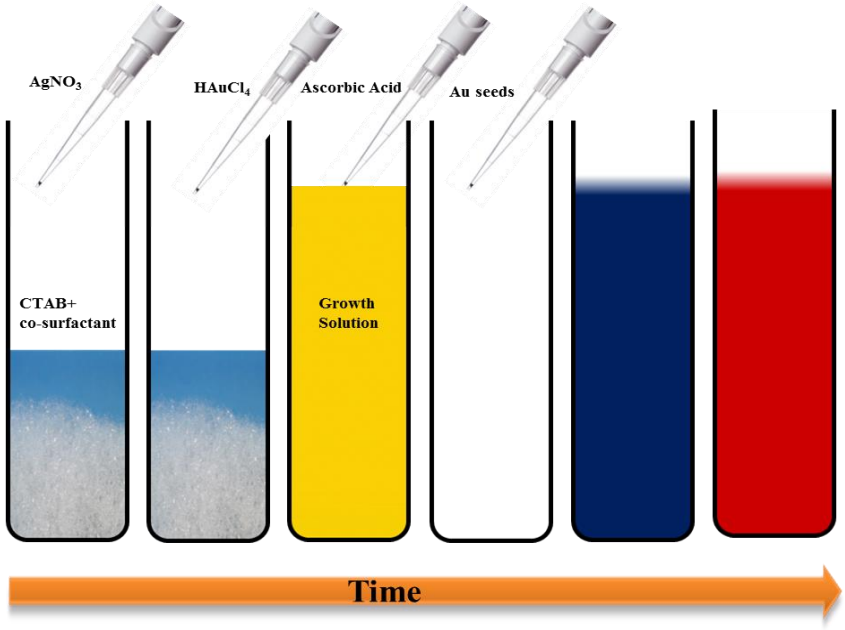

Figure 2.4 Schematic showing a Ag-assisted seeded growth process for synthesis of anisotropic gold nanostructures.

The underlying principle for seeded growth method comprises two fundamental steps – (i) generation of Au seed particles at high values of supersaturation, (ii) followed by directed growth of these seed particles in the presence of surfactants, organic additives or binary surfactant mixtures at low values of supersaturation. In the first step, high supersaturation is used to generate very small and uniform, spherical seed particles. Thereafter, the reaction conditions are altered by using a milder reducing agent than used in the first step. The growth of the nanostructures is affected at a much slower rate in this step by using a templating surfactant or molecule, that directs the seeds to grow into larger particles of defined morphologies.[35] In order to explain the differences in structures obtained using the Ag-assisted seeded growth synthesis, three different mechanisms have been proposed.

These include metallic silver serving as capping agent at certain faces of the nanostructures, the Ag-surfactant complex serving as a face-specific capping agent, and silver ions changing the shape of surfactant micelles (micellar template growth) (Figure 2.5).[36]

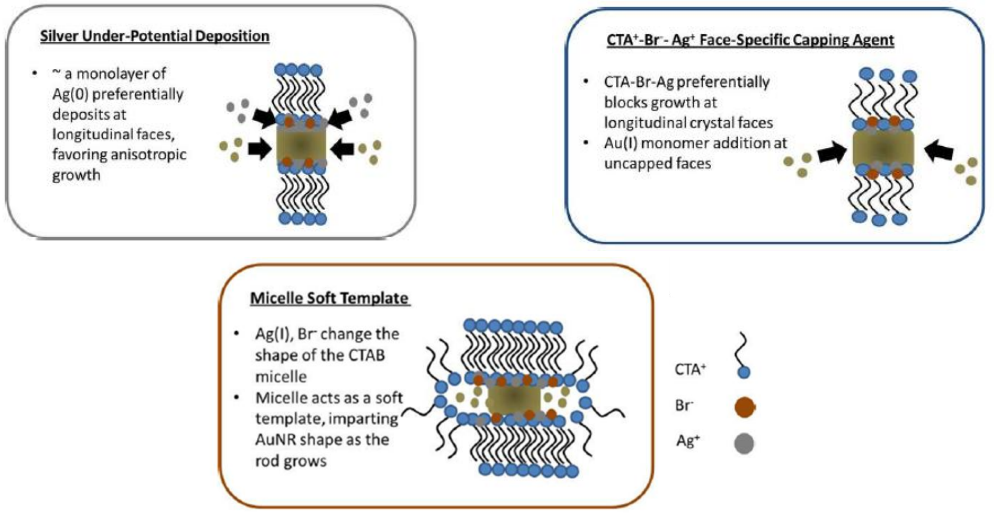

Figure 2.5 Simplistic overview of (a) Ag under potential deposition (b) face specific capping and (c) surfactant templating as mechanism for growth of Au NRs.[36]

2.2.2.1 Under-potential deposition (UPD)

UPD refers to the electrodeposition of metal monolayer(s) on a foreign metal substrate at potentials significantly less negative than that for deposition on the same metal surface as the adsorbate.[37] The underpotential shift is proportional to the work function difference of the two metals. The work function of Ag is lower than that of Au by more than 0.5 eV; therefore, the UPD of Ag over Au is expected.[38]

A compact silver monolayer can be formed preferably on the {110} facets of the gold nanocrystals. The {110} facet is not a densely packed surface, and it has higher energy than the {100} and {111} facets.[39] The silver monolayer over Au {110} acts as a strongly binding surfactant to protect the facet from further growth. The top faces of the growing NRs (i.e., Au {100} facets) are only partially covered by Ag, and therefore grow faster, leading to a one-dimensional growth along the {100} direction. The orientation of the NRs on the carbon grid, further indicate that the {110} facets are in fact dominant during the growth process. Although advanced characterization techniques should be able to locate the presence of Ag on the Au NR surfaces, it is very difficult to ascertain the state of silver (metallic or ionic), since these exist in a dynamic equilibrium under atmospheric conditions. [40]. This has led researchers to believe that instead of elemental Ag, face specific capping could be due to other Ag based structures.

2.2.2.2 Face-specific capping

This mechanism of Au NR growth relies on the fact that an Ag(I) bromide complex adsorbs to specific faces, promoting anisotropic growth. A complex between CTAB and Ag bromide has been recognized by nuclear magnetic resonance (NMR) and X-ray photoelectron spectroscopy (XPS) to be the entity at the surface of Au NRs, resulting from an *in situ* formation during the synthesis protocol.[41] The basic difference with the previously mentioned mechanism is what initially binds to the surface with minor difference in how the reaction proceeds.

The reduction of silver ions under synthesis conditions can be neglected since the reducing power of ascorbic acid is too positive at low pH.[42] On the other hand, the concentrations are above the solubility product of bulk AgBr (Ksp = 5.35 X 10^{-13}), thereby facilitating the formation of AgBr on the gold NRs.This AgBr is presumed to deposit on rod surfaces at the Au-CTAB interface. This helps in stabilizing the rods and further help direct growth by hindering growth from a specific facet. The less densely covered facets are thereby promoted to grow in this approach. Evidence that points to the presence of AgBr on the NRs includes chemical shifts in 1H NMR spectra for capped Au NRs being identical to that of a AgBr-CTAB preformed complex and XPS data that suggest that the detectable silver is present as Ag(I). [43]

2.2.2.3 Surfactant Templating

One of the most widely accepted mechanisms in connection to growth of Au NRs by the seed mediated approach is the surfactant templating. Surfactants are well known to act as soft templates or nano-reactors in determining the shape and size of the formed NPs. The micelles containing reactants collide owing to Brownian motion, occasionally coalesce and exchange their contents leading to reaction. [44] The critical packing parameter (CPP) of a surfactant that takes into account the volume of the hydrophobic chain (V_C), the cross sectional area of the hydrophobic core of the aggregate expressed per molecule in the aggregate (a), and the length of the hydrophobic chain (L_C) gives an overall behaviour of the surfactants in solution.

$$CPP = \frac{V_C}{L_C a} \qquad (24)$$

Among the major properties that can be exploited from the knowledge of CPP, the most important for the ongoing discussion is the different shapes of micelles that stem from varying CPP. The micelles can range from spherical, cylindrical, bilayers or even inverted structures when the CPP varies. [45] The mechanism employing surfactant templating emphasizes that

CTAB micelles are inherently rod-shaped under Au NR synthesis conditions. This happens due to a simultaneous action of the silver and bromide ions which alter the shape of the CTAB micelle. Thus, the micelles do act as soft templates to direct AuNR growth.[28]

Although, the above mentioned hypotheses are often used to explain the growth of Au nanostructures in case of seed-mediated method, it is very difficult to account for various shapes with absolute certainty. Therefore, several combinations are often used to interpret the growth processes. An alternative to this growth limit has been proposed as a two-step process. Initially, the Au NPs grow anisotropically up to a maximum A.R. Thereafter, the micelles burst out releasing the NRs which finish their growth isotropically until the growth reagents are exhausted.[46] With the advent of new *in-situ* characterization techniques like liquid-cell TEM, small angle X-ray scattering (SAXS) and already existing robust techniques like XPS, UV-Vis, NMR, it might be possible to address some of the key issues towards identifying which mechanistic route the synthesis is following. Although, atomistic description of the role of different compounds in the synthesis of NRs has been discussed elsewhere, [47] it might also be possible to do molecular simulations to scan through energy configurations of intermediate entities expected to be formed. It might also be possible to do a detailed energy configuration analysis of the various facets to better appreciate the growth parameters.

2.3 Fe NPs

Magnetic nano-particles (MNPs) form an important class of nanoscale materials, finding wide applications in targeted drug delivery, magnetic resonance imaging (MRI), diagnosis and treatment of illnesses such as cancer, cardiovascular diseases, and neurological diseases among other applications.[48] In addition, Fe oxide NPs upon successful guidance to the tumours, can be used to kill malignant tissues via hyperthermia.[49] Current clinical diagnostic and therapeutic techniques have already been influenced by their unique physical properties and ability to function at the cellular and molecular level of biological interactions.

2.3.1 Magnetic properties

Magnetism originates from the magnetic dipoles associated to the electron spin and orbital moment. Magnetic materials are classified based on the external energy required for the reversal of their magnetization, more precisely quantified based on magnetic susceptibility (χ), which is defined as the ratio of the induced magnetization (M) to the applied magnetic field (H). Based on these, materials can be classified into the following three categories:

i) Diamagnetic materials- In diamagnetic materials, the magnetic moment is antiparallel to H resulting in very small and negative susceptibilities (-10^{-6} to -10^{-3}). They do not retain magnetic properties when the external field is removed.

ii) Paramagnetic materials- Materials with magnetic moments aligned parallel to H and susceptibilities on the order of 10^{-6} to 10^{-1} are described as paramagnetic.

iii) Ferri- and ferromagnetic materials - In these materials, magnetic moments also align parallel to H, coupling interactions between the electrons of the material result in ordered magnetic states, i.e., magnetic domains, and large spontaneous magnetization. The susceptibilities of these materials depend on their atomic structures, temperature, and the external field H.

Typically, the saturation magnetization (M_s) values of NPs, corresponding to the complete alignment of all individual moments in a sample, are smaller than their corresponding bulk phases due to disordered crystal structure resulting from high surface curvature, which increases with particle size reduction.

For nanometric sizes, ferri- or ferromagnetic materials, such as MNPs, become a single magnetic domain and therefore maintain one large magnetic moment. However, at sufficiently high temperature, called the blocking temperature T_B, thermal energy is sufficient to induce free rotation of the particle resulting in a loss of net magnetization in the absence of an external field. This property, marked by the lack of remnant magnetization (M_R) after removal of external fields and zero coercivity (the external field required to reduce the magnetization back to zero, H_C), is known as super-paramagnetism.[50, 51] This describes the magnetic behavior of a material in which all the spins are always collinear to each other but its anisotropy energy is too low to keep them aligned along a particularly stable magnetocrystalline direction. Furthermore, the coupling interactions within these single magnetic domains result in much higher magnetic susceptibilities than paramagnetic materials, this transition happening below the Curie temperature of the material. Figure 2.6 shows the differences in magnetization behaviours for superparamagnetic and ferro/ferri magnetic materials.

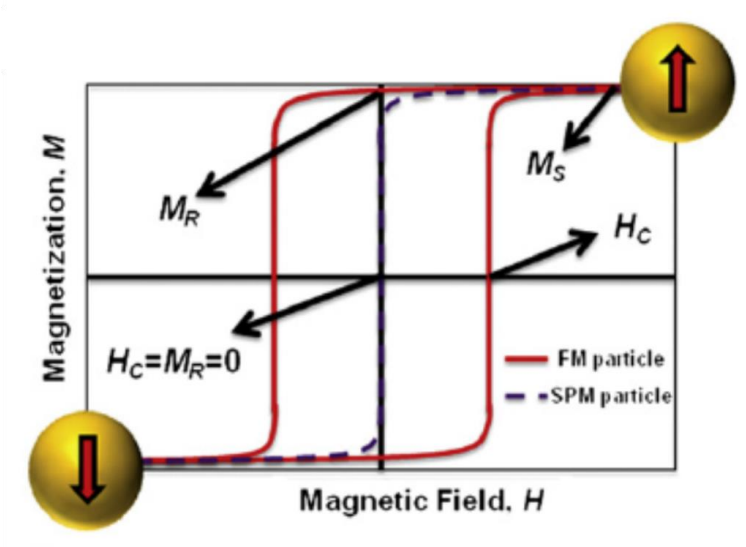

Figure 2.6 Parameters describing the strength and magnetization of superparamagnetic (SPM), ferrimagnetic and ferromagnetic(FM) materials.[50]

3 Polymer based NPs

Polymer based NPs represent a wide collection of NPs that have gained immense interest in the field of drug delivery, owing to their biodegradability, biocompatibility, ease of surface functionalization, controlled degradation, capability to carry hydrophobic drugs among other properties.[52] They occur in mostly two forms - nanospheres and nanocapsules. While in case of nanospheres, drug molecules may be adsorbed or bound at the surface or encapsulated within the particle, nanocapsules are vesicular systems in which the drug is confined to a cavity consisting of a liquid core (either oil or water) surrounded by a shell. [53] The drug is more protected in the latter case, while the position of the drug in case of nanospheres will largely dictate the release profile.

3.1 Classification

There can be different basis for classification of such NPs. Based on synthesis, they can be prepared either from preformed polymers or by direct polymerization of monomers using classical polymerization. Dispersion of preformed polymers can be carried out via solvent evaporation, nano-precipitation, salting-out, dialysis, supercritical fluid technology among others, while direct polymerization can be carried out via micro-emulsion, mini-emulsion, surfactant-free emulsion, interfacial polymerization, controlled/living radical polymerization and so on.[53]

Based on the composition, polymer based NPs can be classified into polymeric NPs, micelles, or dendrimers.

3.1.1 Polymeric NPs

Polymeric NPs include naturally occurring albumin, chitosan, and heparin or synthesized polystyrene-maleic anhydride copolymer, polyethylene glycol (PEG), and poly-L-glutamic acid (PGA) among others that feature drug conjugation to the side chain with a cleavable linker. Some examples include Albumin-Taxol (Abraxane), PGA-Camptothecin (CT-2106) PGA-Taxol (Xyotax). [54-56] Another category of NPs that falls in this sub-class are hydrogels – three dimensional structures that have high affinity for water. As this thesis has dealt with hydrogels and hydrogel based NPs, this will be dealt with in subsequent sections.

3.1.2 Polymeric micelles

Polymeric micelles consist of a hydrophobic core and hydrophilic shell made up of block copolymers. The inner core encapsulates the poorly water-soluble drug, whereas the outer shell or corona of the hydrophilic block of the copolymer protects the drug from the aqueous

environment. The outer layer further stabilizes the NPs against recognition *in vivo* by the reticuloendothelial system (RES). In addition to the already mentioned advantages of polymer based NPs, these micelles can be engineered by means of ligand coupling or addition of pH-sensitive moieties, strategies that improve active targeting to the diseased site.[57] The synthesis of such NPs involves two main steps: synthesis of the amphiphilic block copolymer and its conversion to micelles at critical micelle concentration (CMC) using various techniques. PEG-pluronic-Doxorubicin, PEG-PolyAcrylic acid- Doxorubicin (NK911) are some examples of polymeric micelles widely studied for cancer treatment.[58, 59]

3.1.3 Dendrimers

Dendrimers are hyper-branched structures, characterized by three compartments -the multivalent surface, an outer shell just beneath the surface having a well-defined microenvironment and the core, which is protected from the surroundings, creating a microenvironment surrounded by the dendritic branches. These three parts of the dendrimer can be tailored specifically for the desired purposes, that include applications as drugs for antibacterial and antiviral treatment, as glycocarriers for targeting modified tissue in malignant diseases or as scaffolds for presenting vaccine antigens among others. [60] Besides being responsive to pH, salt concentration, ionic strength, several of them are non-toxic, non-immunogenic, able to cross bio-barriers such as intestine, blood-tissue barriers, cell membranes and are able to stay in circulation long enough to target specific structures. One of the most widely studied dendrimer systems for drug delivery applications includes Polyamidoamine (PAMAM) based systems like PAMAM- Methotrexate, PAMAM-platinate and so on.[61, 62] However, toxicity related to these products have prevented most of them from making to clinical trials. On the other hand, Stratus CS Acute Care (Dade Behring), containing dendrimer-linked monoclonal antibody, and SuperFect (Qiagen), a product based on modified "Tomalia-type PAMAM" dendrimers, are already in the market as FDA (U.S. Food and Drug Administration) approved products. [63]

3.2 Hydrogels – Synthesis, properties and applications

Hydrogels are three dimensional gel networks composed of a hydrophilic organic polymer component that may absorb from 10–20% up to thousands of times their dry weight in water.[64] Hydrogels in the nano-regime are often referred to as nanogels (NGs). In this work, these would be used interchangeably. The high water content gives rise to the fluid-like transport properties. The hydrophilic polymer units are cross-linked, leading to dimensional stability. Cross-linking can either be by covalent interactions (permanent or chemical gels) or

noncovalent interactions like molecular entanglements, and/or secondary forces including ionic, H-bonding or hydrophobic forces (reversible or physical gels).[65] Besides this classification, hydrogels can be naturally occurring such as collagen, gelatine, starch, alginate, agarose or synthetic, that are prepared using chemical polymerization methods. Although, these are the most commonly used classifications, there exist in literature several other classifications, for example, based on polymeric composition, configuration, physical appearance, electrical charge among others.[66]

Hydrogels can show remarkable stimuli responsiveness wherein, they are capable of undergoing swelling-collapse in response to a wide range of stimuli that include temperature, electric or magnetic field, light, pressure, sound, pH, solvent composition, ionic strength, and molecular species.[67-69] These offer several advantages over conventional drug delivery systems such as liposomes, microspheres, cyclodextrins and so on not only by providing a finer temporal control over drug release due to their large surface area, but also by allowing longer circulation times and targeting properties upon suitable functionalization. Further, hydrogels are known to provide high encapsulation stability to the drug molecule in addition to high loading and encapsulation efficiencies, rendering longer circulation times.[70]

One of the most widely studied class of responsive polymers is temperature responsive poly-(alkylacrylamides), specifically poly(N-isopropylacrylamide) (pNIPAm). There exist hydrogen bonds between the amide side chains of the polymer molecules and water. The isopropyl group on the side chain induces hydrophobic structuring of the water leading to entropically driven polymer-polymer interactions, known as the hydrophobic effect. The conformation of the polymer chains in a solvent are guided by the interactions between solvent-solvent, solvent-polymer and polymer-polymer, often described in terms of the solubility parameter (χ). A polymer molecule stays in a random coil-structure in solvents for which $\chi < 0.5$, whereas, it transforms into a globule structure at $\chi > 0.5$.[71] In case of pNIPAM, this coil to globule transition happens at a certain temperature called the lower critical solution temperature (LCST ~ 31° C), where there is a phase separation.[72] This happens due to an entropically favoured release of bound and structured water at high temperatures, owing to breakage of hydrogen bonds. This in turn makes the polymer–polymer hydrophobic interactions dominate over the polymer–solvent interactions, leading to phase separation. In a similar way, the cross-linked hydrogels obtained from this polymer swell in water under a critical temperature and collapse above it. This temperature is called the volume phase transition temperature (VPTT) of the hydrogel.[73] While LCST or VPTT is defined as a single

temperature from a thermodynamic standpoint, real systems undergo phase transition over a range of temperatures owing to inherent polydispersity stemming from different chain lengths, branching, crystallinity.[74] In addition, system polydispersity arises due to different crystalline and amorphous domains within the particles, particle size distribution and flocculation states. A common method to estimate this transition temperature is to measure a spectroscopic parameter like optical density, turbidity, absorbance, size or specific heat as a function of temperature and assign the transition temperature at the average of the sigmoidal plot of the curve or at the mid-point of the range.[75-79]

One of the most common methods used for synthesizing thermo-sensitive hydrogels is free radical precipitation polymerization.[80] The major advantage of this method is the ease with which particles having a very narrow size distribution can be produced. Synthesis happens via homogeneous nucleation above the LCST of the homopolymer. Under these conditions, the initiator decomposes to release sulphate radicals. The NIPAm monomer is attacked by the sulphate radical, leading to radical propagation and chain growth. Upon reaching a critical length, the chain collapses upon itself forming precursor particles, and hence the name precipitation polymerization (Figure 3.1). The precursor particles further grow by aggregation with other precursor particles. This can happen via capture by existing particles, capture by growing oligoradicals, and by monomer addition. In most cases, the charge imparted by the initiator stabilizes the hydrogels once they have reached a critical size. Although, commonly used anionic surfactants like sodium dodecyl sulphate (SDS) also serves the purpose of initial colloidal stabilization of the nuclei particles. Hence, the surfactant concentration can be tuned to control the size of the hydrogels.[65] Although the surfactant plays a major role in controlling the size of the hydrogels, their presence in the final product can be a deterrent to uses in biomedical applications owing to immune responses, non-degradability and/or degradation to harmful remnants.

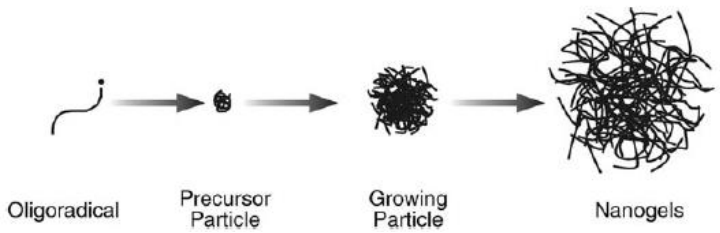

Figure 3.1 Schematic showing precipitation polymerization of hydrogels. [65]

Multi-response is introduced in these hydrogels by incorporating pH-dependent co-monomers. One of the frequently studied temperature and pH-dependent hydrogels is that of poly (N-isopropylacrylamide-co-acrylic acid) (pNIPAm-AAc). [81, 82] The addition of another stimuli responsive block allows for multiple phase transition behavior with temperature besides adding response to two external stimuli, viz. temperature and pH. pNIPAm-AAc undergo collapse with decrease in pH. This happens due to protonation of the carboxylic acid groups of the poly AAc blocks with an increasing pH. The thermodynamic model developed by Siegel can be used to explain the swelling/deswelling characteristics while changing the pH of the medium.[83] This model considers three sources contributing to the total free energy - (i) hydrogel-solvent system; (ii) hydrogel-solvent mixing, (iii) deformation of polymer networks and osmotic pressure of mobile ions. The hydrogel-solvent mixing component is dominated by the poly AAc segments that undergo dissociation with an increase in pH. A dramatic decrease in the free energy of mixing is caused when the pH changes from low to high values, since dissociated poly AAc segments are more hydrophilic than non-dissociated segments. This hydrophobic to hydrophilic transition thus explains the consequent swelling of the hydrogels upon increasing pH. However, this dissociation is affected by the deformation degree of the polymer network, mostly affected by the cross linking density and the osmotic pressure of OH^- and Na^+ ions. A sharp volume transition happens at a pH slightly below neutral conditions. This is reflective of the fact that pH is high enough to overcome the osmotic pressure leading to counter-ion-shielding effects within the poly AAc domains. [84] A synergistic effect of the favourable free energy of hydrogel-solvent mixing and de-cross-linking of bound poly AAc segments in the domains comes into play once the osmotic pressure is overcome, causing further swelling with increase in pH.

pNIPAm based hydrogels have been shown to be effective candidates in biomedical applications with examples ranging from tumour-targeting, bioresponsive microlenses, nonfouling biomedical device coatings, RNAinterference (RNAi) carriers for cancer therapy among other applications.[85] Some of the recent advancements are discussed here.

pNIPAM based hydrogels using two biodegradable crosslinkers, poly(3-caprolactone) dimethacrylate (PCLDMA) and bisacryloylcystamine (BACy) have shown a thermo-induced slow sustained and a reduction-induced fast release of Levofloxacin. In addition, these could be biodegraded slowly in the presence of glutathione (GSH), the main reducing agent inside cells, at 37°C.[86] Intravitreal injection of a Polyethylene (glycol) Diacrylate (PEG-DA) crosslinked pNIPAM hydrogel was developed for injectable drug delivery on retinal function.

These showed a VPTT approximately 32 °C, above which the swelling behaviour decreases with subsequent burst release. The gel was able to encapsulate and release various proteins including bovine serum albumin (BSA), immunoglobulin G (IgG), and, finally, bevacizumab and ranibiumab.[87] In another interesting study, peptide-labeled poly(N-isopropylmethacrylamide) (pNIPMAM) hydrogels with a high loading capacity for siRNA have been developed and have been shown to effectively target ovarian carcinomas via receptor-peptide binding.[85] In a recent study, poly (amido-amine) (PAA) cross linked pNIPAM based hydrogels have been shown to effectively load activin B (a transforming growth factor known to possess neuroprotective behaviour). Thereafter, the hydrogels showed sustained release of activin B for over 5 weeks whereby contributing to substantial cellular protection and behavioural improvement. The authors suggest their potential as a therapeutic strategy for Parkinson's Disease. [88]

4 Hybrid NPs

As the name suggests, hybrid NPs are formed by combinations of the different inorganic NPs discussed in Chapter 2 and polymer based NPs discussed in Chapter 3. The main advantage of researching on hybrid NPs is their multifunctionality, stemming from both the counterparts. However, incorporation of both the counterparts can give rise to different morphologies that include core-shell, Janus or dumbbell shaped NPs, alloy NPs, layer-by-layer coated (LBL) NPs, or self-assembled NPs. The discussion here will be limited to core-shell NPs.

The thickness of the core and shell can affect the surface properties. Besides, the physico-chemical properties are affected by the relative thickness of core and shell components, diameter, composition and synthesis employed.[89] Core-shell NPs have received much attention due to their superior optical, electronic, catalytic, magnetic, gelling, stimuli-responsive properties emanating from both the core and shell. By combing different cores with shells, a multitude of properties can be mixed and matched to suit the needs of desired applications. Further interest in these materials stems from the adaptability of their structure and versatility in environmental, biomedical and catalytic applications. [90, 91] However, proper control of shell thickness and uniform coating of the shell are problems associated with the various synthesis methods. The most commonly observed difficulties stem from agglomeration of core particles in the reaction media, formation of separate particles of shell material, incomplete coverage of the core surface, and control of the reaction rate.[92]

Core-shell hybrid NPs can be classified into the following three categories based on the material comprising the core and the shell: Inorganic core-inorganic shell, polymeric core-polymeric shell, inorganic core-polymeric shell or vice-versa. (Figure 4.1) Besides these, there could be multiple shells on a single core.[92]

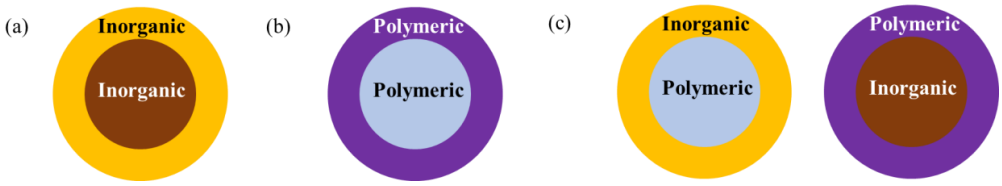

Figure 4.1 Illustration showing different kinds of Core-Shell Hybrid NPs.

The core-shell fabrication can be achieved either in-situ (during synthesis) or post-synthesis, wherein, the shell is grown atop the core NPs, after the core synthesis reaction has happened. Some of the most commonly used synthesis protocols are discussed here.

4.1 Synthesis Methods

The most common method for synthesis of inorganic core-shell NPs features solution based synthetic route using a metal precursor, reducing agent and/or passivating ligand. Post synthesis of the shell is done atop the core NPs using the second metal precursor. Core (Fe, Cu)-Shell (Au, Pt, Pd, and Ag) NPs have been synthesized in presence of ascorbic acid/Vitamin C in aqueous medium, where, Cu and or Fe served as nucleation sites for the growth of a noble metal nanoshell overlayer.[93] Core-shell structured Fe_3O_4@Au and Fe_3O_4@Au@Ag NPs have been synthesized by depositing Au and Ag on the Fe_3O_4 NP surface in aqueous solution, after transferring the oleylamine and oleic acid capped Fe_3O_4 NPs (synthesized via thermal decomposition) to the aqueous phase.[94]

Another commonly used method for core-shell NPs is the reverse micelle based synthetic route. (Figure 4.2) This method employs mixing two reverse micellar solutions, one containing the metal precursor and the other containing the reducing agent. The drops collide owing to Brownian motion, occasionally coalesce and exchange their contents leading to reaction. [95]

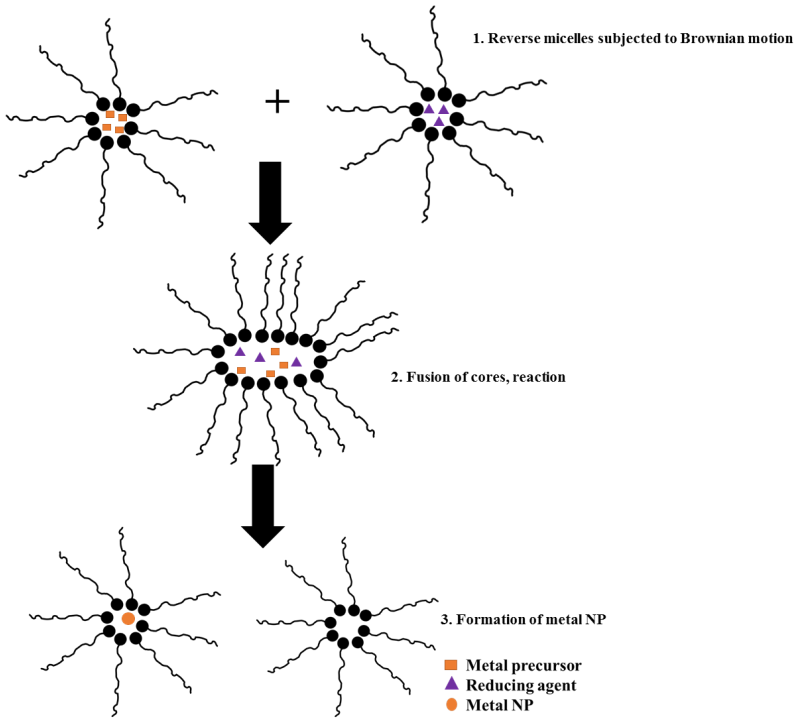

Figure 4.2 Schematic showing reverse micelle based synthetic route for metallic NPs.

These nano-sized droplets act as the nano-reactors for the synthesis of desired NPs of various shapes and sizes. As the reactants are confined within the droplets, size and shape control of the synthesized NPs are easily achieved by controlling the size of these droplets. Core–shell iron–gold (Fe@Au) NPs have been synthesized by a reverse micelle procedure, wherein the Fe core was first synthesized, followed by formation of the Au shell.[96] Ni@Au NPs have been chemically synthesized through a redox-transmetalation method in reverse microemulsion.[97]

Core-shell hydrogels are most commonly synthesized via precipitation polymerization,[98] that happens in a two-step process, formation of the core followed by the shell. Similar to the core synthesis, the reaction is performed at a temperature higher than the VPTT, whereby, the core particles are in a collapsed state and serve as nuclei for growth of the shell. pNIPAm-AAc hydrogels have been synthesized using this method, with fine control of size and polydispersity of the NPs.[69]

Although core-shell NPs find potential applications in biomedical field that include controlled release of drugs, targeted drug delivery, bioimaging, cell-labelling, biosensors among others, the current discussion will be limited to their applications in the field of drug delivery.

4.2 Drug Delivery Applications

Current research focusses on controlled release of drugs, with greater emphasis on targeting nanocarriers loaded with desired drugs to the diseased site. The drug can reach the intended site via passive or active targeting. The former consists of the transport of nanocarriers through leaky tumor capillary fenestrations into the tumor interstitium and cells by convection or passive diffusion, a phenomenon known as enhanced permeability and retention (EPR) effect. On the other hand, active targeting involves ligands attached at the surface of the nanocarriers for binding to appropriate receptors expressed at the target site.[99] Once the nanocarrier has reached the site of action, it has to be further taken up inside the cells, so that the drug can be released inside the cells. This happens via endocytosis, an active transport process.[100] The release of the drug is dependent on the interaction between the drug and the carrier as well as the release medium, method of drug loading, material properties of the carrier among other factors. Here, some of the frequently used models to understand release of drugs from nanocarriers, will be discussed.

4.2.1 Drug Release models

Controlled release of a drug is further dependent on drug release mechanisms which can be diffusion-controlled, chemically controlled, osmotically controlled or swelling and/or

dissolution-controlled.[101] Some of the widely used models describing release kinetics are highlighted here.

Diffusion- controlled systems can either have the drug separated from the environment by a thin membrane (reservoir systems) or the drug dispersed/dissolved in the polymer matrix (matrix systems).

The diffusion in one dimension can be described using Fickian diffusion theory:

$$\frac{\partial c_i}{\partial t} = \frac{\partial}{\partial z}\left(D_{ip}(\mathrm{c}_i)\frac{\partial c_i}{\partial z} \right) \qquad (25)$$

where, c_i is the concentration of species i, D_{ip} is the diffusion coefficient of species i in the polymer matrix, and z and t represent position and time, respectively.

Irrespective of the geometry, the drug release rate is of zero-order for reservoir systems. In this case D_{ip} is independent of concentration and equation (25) becomes:

$$\frac{\partial c_i}{\partial t} = D_{ip}\frac{\partial^2 c_i}{\partial z^2} \qquad (26)$$

However, in case of matrix systems, the solubility of the drug in the polymer matrix becomes a controlling factor for the drug release. D_{ip} is affected by the structural characteristics of the polymer. Solving equation (25) for different geometries yields a $t^{1/2}$ dependence of the drug release in most cases.

One of the most used models to describe release from matrix systems, based on pseudo steady state assumptions, is the Higuchi model, given by:

$$M_t = A\sqrt{Dc_s(2c_0 - c_s)t} \qquad (27)$$

Here, M_t represents the cumulative amount of drug released at time t, A is the surface area of the device, D is the drug diffusivity in the carrier, c_0 and c_s are the initial drug concentration and the drug solubility within the polymer, respectively.

Besides these, a semi-empirical power law equation has been widely used to describe drug release from polymeric systems:

$$\frac{M_t}{M_\infty} = kt^n \qquad (28)$$

Here, M_t and M_∞ are the cumulative amounts of drug released at time t and infinite time, respectively; k contains structural and geometric information about the device, and n is indicative of the drug release mechanism (Table 4-1). [102] Fickian diffusion is characterized by diffusion coefficient, while Case- II transport is described by a relaxation constant that accounts for the swelling-collapse behaviour of the drug delivery system. Anomalous release behavior is intermediate between Fickian and Case-II.[103]

Table 4-1 Drug release mechanisms from different geometries based on the values of n.

Thin film	Sphere	Cylinder	Drug Release Mechanism
0.5	0.45	0.43	Fickian diffusion
0.5 < n < 1	0.45 < n < 0.89	0.43 < n < 0.85	Anomalous transport
1	0.89	0.85	Case-II transport

Drug release from polymer systems that swell due to solvent influx may be described by Narasimhan and Peppas model for polymer dissolution based on the molecular mechanism. The model describes solute transport in a one-dimensional system, such as a film, slab, disk or tablet.

$$\frac{M_d}{M_{d,\infty}} = \frac{v_{d,eq} + v_d^*}{2L}\left(\sqrt{2At} + Bt\right) \qquad (29)$$

where, L is the half-thickness of the polymer and $v_{d,eq}$ and v_d^* are the equilibrium and characteristic concentrations of drug. A and B are parameters that depend upon the diffusion coefficients, the chain disentanglement rate, and the solvent and drug concentrations.[104]

4.2.2 Hybrid NPs in drug delivery

Ferrogels consisting of superparamagnetic iron oxide nanoparticles (SPIONs) and ABA-type triblock copolymers consisting of one poly(propylene oxide) (PPO) block and two poly(ethylene oxide) (PEO) blocks, have been shown to effectively release hydrophobic drugs like indomethacin. The release rate is enhanced under the effect of magnetic field owing to constriction of the ferrogel, which happens due to the SPIONS orienting and approaching each other in response to the magnetic field. This leads to local increase of concentration in the PPO cores, resulting in a large concentration gradient between the PPO cores and the water channels

existing in between the close packed micelles and thus leading to diffusion of indomethacin into the interconnecting aqueous moiety.[105]

Wu et al have also reported the preparation of multifunctional Ag–Au bimetallic NP core with a thermo-responsive PEG-based hydrogel shell. The targeting ligands of hyaluronic acid chains were semi-interpenetrated into the surface networks of the gel shell. These constructs were shown to be ideal candidates for simultaneous optical temperature sensing, targeted tumour and combined chemical and photothermal treatment. The fluorescence signal emanating from the Ag-Au core can be used for imaging. On the other hand, drug release can be induced by a synergestic effect due to the heat generated by external Near-Infrared (NIR) irradiation and the temperature increase of local environmental media. [106]

In another study, a hybrid NP system was formulated with chitosan, β-glycerophosphate and Fe_3O_4 magnetic NPs. In the presence of a magnetic field, the injectable hydrogels significantly prolonged intravesical Bacillus Calmette–Guérin (BCG) residence time. The magnetic properties of the NPs coupled with the thermo-responsive behaviour of the hydrogels resulted in a higher antitumor efficacy for superficial bladder, in comparison to traditional BCG therapy.[107] Hilt et al have shown collapse with increasing temperature for hybrid systems comprising Fe_3O_4 NPs incorporated in pNIPAm hydrogels. Upon exposure to an external alternating magnetic field, the heating of superparamagnetic Fe_3O_4 NPs leads to a rise in the temperature of the system. To further demonstrate the pulsatile release of drugs upon demand, the study has focussed on the loading and release of a model Pyrocatechol violet dye. Although, a suppression in the release rate was observed, primarily due to a result of the collapse of the hydrogel network with heating, the system properties can be varied by controlling the particle loading of the system.[108]

A pNIPAm-AAc hydrogel with near-infrared (NIR) absorbing silica–gold nanoshells was designed as a platform for pulsatile delivery of cancer therapeutics. The hybrid material was loaded with either doxorubicin or a DNA duplex (a model nucleic acid therapeutic). The release of both the drugs was triggered optically. This NIR light exposure witnessed two to five-fold increase in drug release. Drug delivery profiles were further influenced by both the molecular size of the drug and chemical properties.[109]

Although, extensive research is being carried out to usher in stimuli-responsive drug-delivery systems, very few nanosystems have reached the clinical stage. There are several reasons that include their sophisticated designs, leading to complex manufacturing processes; inefficient

tissue-penetration depth and focusing to avoid damage to healthy tissues; nontrivial optimizations required for the translation of each stimulus from preclinical experimental models to daily clinical practice among other reasons. [110]

5 Characterization Techniques

In this chapter, a brief overview of the relevant characterization techniques used during the course of the thesis work, is presented. Size determination techniques include dynamic light scattering (DLS), scanning transmission electron microscopy (S(T)EM), whereas surface characterization was done using zeta potential measurements, X-ray photoelectron spectroscopy (XPS) and other physico-chemical properties were mapped using UV-Visible (UV-Vis) spectroscopy, differential scanning calorimetry (DSC), vibrating sample magnetometry (VSM) and other techniques.[V]

5.1 Dynamic Light Scattering (DLS)

DLS works on the principle of measuring the radius of a hypothetical hard sphere that diffuses with the same velocity as the particle under examination. The reported size i.e. hydrodynamic size is indicative of the apparent size of the hydrated particle. Particles when suspended in a solution undergo Brownian motion and hence, the intensity of the light scattered by them undergo time-based fluctuations. These fluctuations are auto-correlated in order to estimate the average diffusion coefficients ($\overline{D}$). [111, 112]

$$G_2(\tau) = A\left[1 + B\exp(-2\Gamma\tau + \mu_2\tau^2)\right] \qquad (30)$$

G_2 is the auto-correlation function, τ is the delay time, A is the amplitude or intercept of the correlation function, B is the baseline, μ_2 is a parameter that takes into account the polysdispersity of the system. Γ is given by the following equations:

$$\Gamma = \overline{D}q^2 \qquad (31)$$

$$q = \frac{4\pi n}{\lambda_0}\sin\left(\frac{\theta}{2}\right) \qquad (32)$$

where q is the scattering vector, λ_0 is the vacuum laser wavelength, n is the medium refractive index, θ is the scattering angle and $\overline{D}$ is given by Stokes Einstein equation:

$$R_H = \frac{k_B T}{6\pi\eta\overline{D}} \qquad (33)$$

[V] VSM measurements were done at Department of Engineering Sciences, Uppsala University, Sweden by Dr. Roland Mathieu and Dr. P. Anil Kumar, High Resolution TEM imaging (HRTEM) was carried out by Dr. Gurvinder Singh at NTNU.

R_H is the hydrodynamic radius, T is the absolute temperature and η is the solvent viscosity.

Linearization of equation (30) leads to:

$$y(\tau) = \frac{1}{2}\ln\left[AB\exp(-2\Gamma\tau + \mu_2\tau^2)\right] \approx \frac{1}{2}\ln\left[AB\right] - \langle\Gamma\rangle\tau + \frac{\mu_2}{2}\tau^2 = a_0 - a_1\tau + a_2\tau^2 \qquad (34)$$

DLS sizes reported here are the Z-average particle sizes (D_z) calculated based on the technique of cumulants as mentioned above :

$$D_z = \frac{1}{a_1}\frac{k_B T}{3\pi\eta}\left[\frac{4\pi n}{\lambda_0}\sin\left(\frac{\theta}{2}\right)\right]^2 \qquad (35)$$

The polydispersity index (PDI) which gives a measure of the size distribution is calculated from the second moment (a_2) of the distribution as follows:

$$PDI = \frac{2a_2}{a_1^2} \qquad (36)$$

The hydrodynamic sizes of the NPs have been measured using a Malvern Zetasizer Nano-ZS instrument, and the manufacturer's own software. All measurements were done in aqueous solutions and results were averaged over triplicate measurements.

For anisotropic particles, owing to multiple axes of rotation, the DLS results should not be interpreted alone. In addition, ligands attached to NPs also give different diameters when compared with diameters obtained using microscopy techniques.

5.2 Scanning Transmission Electron Microscopy (S(T)EM)

S(T)EM combines the principles of transmission electron microscopy and scanning electron microscopy and can be performed on either type of instrument. STEM imaging requires very thin samples, across which, a beam of electrons is finely focussed in a raster pattern. Interactions between the electron beam and sample atoms generate a serial signal stream, which is correlated with beam position to build a virtual image. The images during the course of this work have been taken in bright field (BF) mode, in which case, the objective aperture is positioned just below the specimen, so that only the transmitted electron beam is allowed to pass down the column. These electrons, which are scattered by relatively large angles, are collected by a high angle annular dark field detector and contribute to the image. Thus, a BF image does not get contributions from the diffracted or inelastically scattered electrons. However, similar to SEM, secondary or backscattered electrons can also be used for imaging

in S(T)EM; but higher signal levels and better spatial resolution are available by detecting transmitted electrons. One of the key advantages of using S(T)EM is to have multiple detectors operating simultaneously to collect the maximum possible information from each scan. Figure 5.1 shows a schematic of the main components in a S(T)EM.[113, 114]

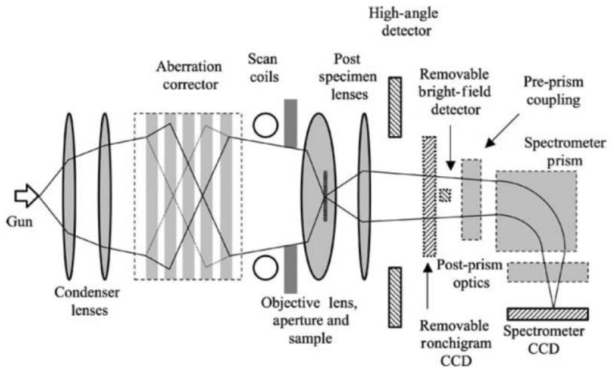

Figure 5.1 Schematic showing the main components of a high-resolution S(T)EM.[113]

S(T)EM images were acquired in BF mode, using a Hitachi S-5500 electron microscope operating at 30kV accelerating voltage. TEM grids were prepared by placing several drops of the solution on a Formvar carbon coated copper grid (Electron Microscopy Sciences) and wiping immediately with Kimberly-Clark kimwipes to prevent further aggregation owing to evaporation at room temperature. For studying the temperature effect on the NPs, the NP solutions were heated to 45°C, just prior to placing drops on the TEM grid.

5.3 Zeta potential measurements

For a charged particle in solution, the counter ions orient close to the surface, which in addition to the charges on the particle, make up the electrical double layer. The surface potential of the particle drops with distance from the surface. Zeta potential (ξ) is defined as the potential at the surface of shear, which is the actual distance from the surface at which the relative motion sets in between the immobilized layer and the mobile fluid. Although, it is difficult to ascertain this distance, the surface of shear occurs within the double layer (Figure 5.2).

The general expression for potential around a spherical particle (ψ) at low potential can be written as:[115]

$$\psi = \frac{q}{4\pi\varepsilon r}\exp(-\kappa r) \qquad (37)$$

Where, q represents the surface charge, ε is the permittivity of the medium, κ is the Debye-Huckel parameter and its reciprocal is the Debye length which is a measure of the thickness of the electrical double layer and r is the distance from the centre of the spherical particle having a radius R_s. In case of dilute solutions, in which κ^{-1} is large, the surface of shear may be regarded to coincide with the particle surface.

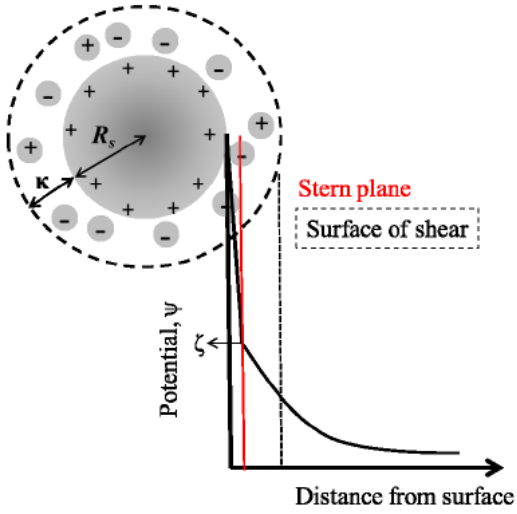

Figure 5.2 Electrical double layer for a charged spherical particle and location of the surface of shear.[115]

Further, for $\kappa R_s < 0.1$, indicating negligible distortions of the electric field around the particle, the above equation transforms to

$$\xi = \frac{q}{4\pi\varepsilon R_s} \tag{38}$$

Employing the definition of electrophoretic mobility (u) as the velocity per unit field, and using Stoke's law, Huckel's equation is obtained:

$$u = \frac{2\varepsilon\xi}{3\eta} \tag{39}$$

On the other hand, for $\kappa R_s > 100$, (indicative of field lines following the contours of the particle tangentially) Helmholtz-Smoluchowski equation is applicable for calculating u:

$$u = \frac{\varepsilon\xi}{\eta} \tag{40}$$

The above equation has been used to estimate the zeta potential values for the NPs studied in this work using Malvern Zetasizer Nano-ZS instrument, and the manufacturer's own software.

5.4 X-ray photoelectron spectroscopy (XPS)

The principle of operation of XPS involves photoelectric interaction between monochromatic X-rays and a solid or gaseous sample leading to emission of electrons with discrete kinetic energies. Electron binding energy of the i^{th} level ($E_B(i)$) is calculated using the energy balance for the photoemission process:[116]

$$h\nu = E_k + \phi + E_B(i) \qquad (41)$$

$h\nu$ is the X-ray energy, ϕ is the metal work function and E_k is the kinetic energy of the ejected electron, recorded by an electron energy analyzer.

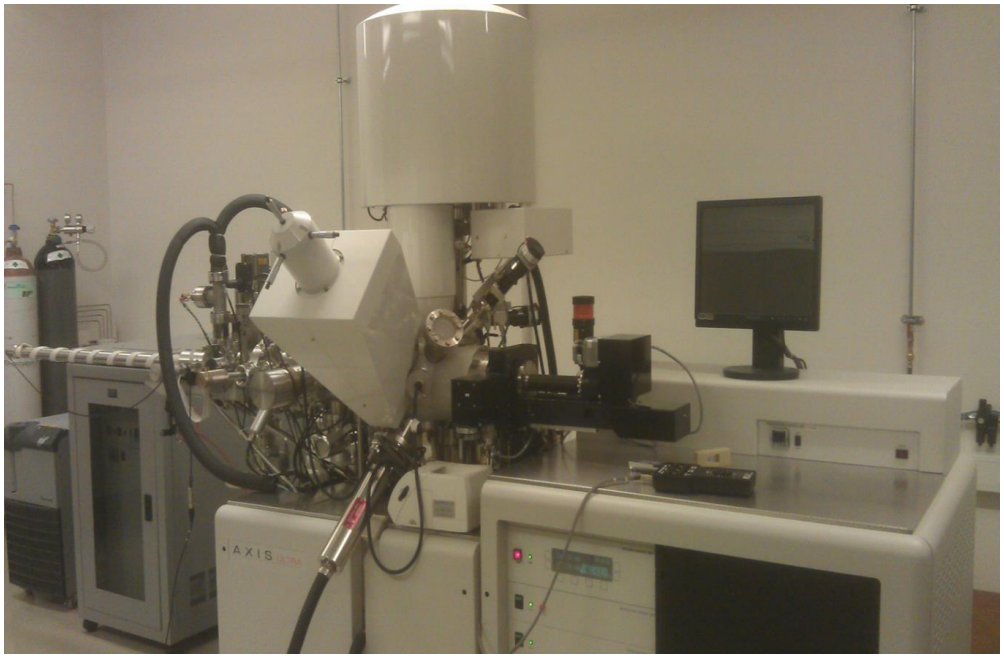

Figure 5.3 XPS instrument used for surface analysis.

XPS analyses were performed using a Kratos Axis Ultra DLD spectrometer (Kratos Analytical, UK) (Figure 5.3), equipped with a monochromatized aluminum X-ray source (Al, hυ = 1486.6 eV) operating at 10 mA and 15 kV (150 W). The instrument has three parts, namely load lock for loading the sample, sample transfer chamber and the sample analysis chamber, where the sample is impringed upon by monochromatic X-ray.

A hybrid lens (electrostatic and magnetic) mode was employed along with an analysis area of approximately 300 µm X 700 µm. Survey spectra were collected over the range of 0-1100 eV binding energy with analyzer pass energy of 160 eV. High resolution spectra of C 1s, O 1s, Fe 2p and Au 4f were obtained with an analyzer pass energy of 20 eV. XPS data were processed with Casa XPS software (Casa Software Ltd., UK).

5.5 UV-Vis spectroscopy

UV-Vis spectroscopy is based on Beer- Lambert's law that relates the absorbance (A) of a solution, a dimensionless parameter, to the path length of the sample (L) and concentration of the emitters (C).

$$A = -\log_{10}\left(\frac{I}{I_0}\right) = \alpha CL \qquad (42)$$

I_0, I refer to the intensities of incident and transmitted light respectively, while α is called the molar absorptivity. Application of this law is subjected to several assumptions that include the following. Absorbers must act independently of each other, the absorbing medium is homogenous, the medium must not be turbid and the incident light should not influence the atoms or molecules under study.[117]

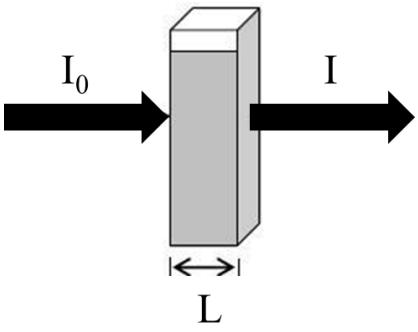

Figure 5.4 Transmission of light through a particle solution.

LSPR characteristics of Au has been studied using this technique. The maximum absorbance happens at the LSPR wavelength, which can be changed by tuning size, shape, material and local dielectric properties, highlighted in Section 2.2.1. UV-Vis spectra for Au NPs solutions were acquired with a UV-2401PC (Shimadzu) spectrophotometer. The spectra were collected over the spectral range from 200-800 nm. Calibration curves for studied drugs have been

obtained using UV-Vis spectroscopy. Loading (*L.E.*) and encapsulation efficiencies (*E.E.*) have been calculated as follows:

$$L.E. = \left(\frac{C_{drug,o} - C_{drug,t}}{C_{drug,o}} \right) * 100 \qquad (43)$$

$$E.E. = \left(\frac{C_{drug,o} * L.E.}{100 * C_{NP}} \right) \qquad (44)$$

Here $C_{drug,o}$ is the concentration (mg/ml) of the drug at the start of loading, $C_{drug,t}$ is the final concentration (mg/ml) of the drug after loading, C_{NP} is the concentration (mg/ml) of the nanocarriers (NG or coated Fe@Au NPs), concentrations of the drug being determined using the calibration curve or the absorbance method as applicable.

5.6 Differential Scanning Calorimetry (DSC)

DSC measures the energy absorbed (endotherm) or produced (exotherm) as a function of time or temperature.

In DSC analysis, the sample, whose phase change properties are to be studied, is placed in an aluminum pan. The sample pan and an empty reference pan are placed on small platforms with underlying thermocouple sensors within the DSC chamber. It either measures the electrical energy provided to heaters below the pans necessary to maintain the two pans at the same temperature (power compensation), or measures the heat flow (differential temperature) as a function of sample temperature (heat flux).[118]

The differential heat flow (heat/time) between the material and the empty reference pan is obtained as the output which gives idea of phase changes within the system. Heat capacity may be determined by taking the ratio of heat flow to heating rate:

$$C_p = \frac{Q}{\triangle T} \qquad (45)$$

where C_p is the heat capacity of the sample, Q is the heat flow through the sample over a given time, and $\triangle T$ is the temperature change over that same time. DSC measurements give information about glass transition, crystallization temperature in polymers, VPTT of hydrogels and so on.

DSC studies were performed using a TA Instruments Q2000 DSC. The scan rate was 5 °C min^{-1} for both heating and cooling curves and the samples were scanned in the temperature

range 5–45 °C. The NP solution was loaded in a Hermetic Aluminium pan while the reference pan was kept empty. The data were analysed using TA Instruments Universal Analysis 2000 © software.

6 Results and Discussion

This chapter summarizes the main findings from the papers submitted as part of this thesis. It has been divided into three sub-parts. The first deals with the research carried out in the synthesis, characterization and applications of spherical and anisotropic metallic NPs, the second deals with hydrogels and a robust method to calculate VPTT for phase changing systems and the third sub-part presents the findings from combinatorial studies of metallic and hydrogel NPs followed by functionalization tailored towards drug delivery applications.

The sequence in which the papers will be discussed is given in Figure 6.1.The two different colours indicate the main focus of each paper – synthesis (yellow) and application (blue), with a degree of colour fill representing relative composition of the paper with respect to these parameters

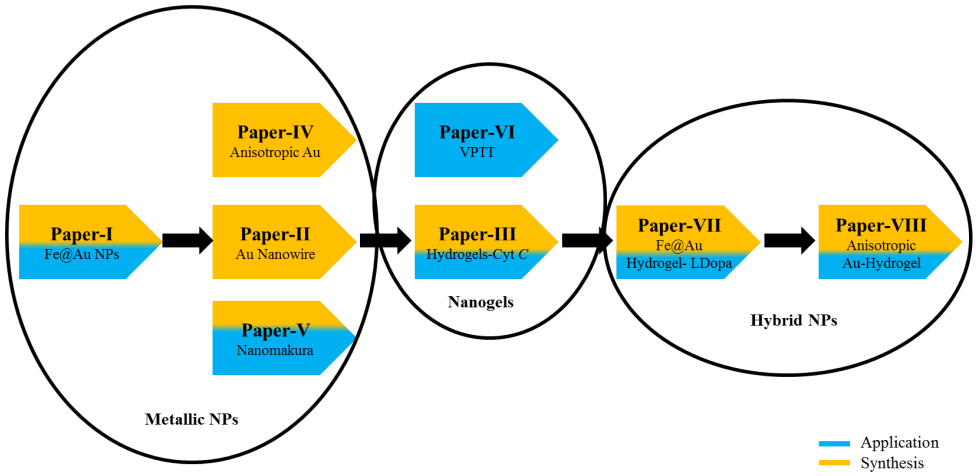

Figure 6.1 Flowline of thesis papers showing research work carried out related to metallic NPs, nanogels and hybrid NPs.

6.1 Spherical and Anisotropic metallic NPs

In this sub-section, the main results from Papers I-IV will be discussed. In essence, the main focus is on core-shell Fe@Au NPs (Paper-I), followed by growth of anisotropic Au NPs (Au nanowires (NWs)) by varying seed type (Paper-II). Further understanding of the size and shape variation of Au NPs is presented under the influence of a binary mixture of surfactants in a seed-mediated growth protocol, (Paper-III) culminating in reporting of a new Au anisotropic structure, *nanomakura* that show high cytotoxicity in cancer cell lines (Paper-IV).

6.1.1 Paper-I: Synthesis and *in vitro* cellular interactions of superparamagnetic iron nanoparticles with a crystalline gold shell.

Applied Surface Science 2014, 316(1), p.171-178.

The main aim of this paper was to synthesize core-shell Fe@Au NPs tailored towards imaging and drug delivery applications, by combining the magnetic and optical properties of the Fe core and Au shell respectively.[VI] Although, there exist a small number of successful approaches for the synthesis of MNPs@Au, many issues related to the precise control of Au shell thickness, and the detailed characterization of resultant MNPs@Au needed to be addressed. In addition, the aim was to develop a simple synthetic method involving less time-consuming purification steps, simple sequence of chemical reactions and producing monodisperse NPs with good control over magneto-plasmonic properties.

First, Fe NPs were synthesized via thermal decomposition of iron pentacarbonyl ($Fe(CO)_5$) in the presence of oleylamine (OAm). The Fe NPs were dried after removal of the surfactant by washing with hexane and acetone several times, and transferred into an aqueous phase in the presence of sodium citrate, using sonication at 80^0C for half an hour. Thereafter, a thin coating of Au was carried out in aqueous medium using water soluble Fe NPs as heterogeneous nucleation sites, leading to the formation of a continuous shell of Au around the Fe NPs. Fe@Au NPs were magnetically separated to remove freely suspended Au NPs, and re-dispersed in an aqueous phase. These were subsequently functionalized with thiolated PEG (PEG-SH). Figure 6.2 shows a schematic of the synthesis process.

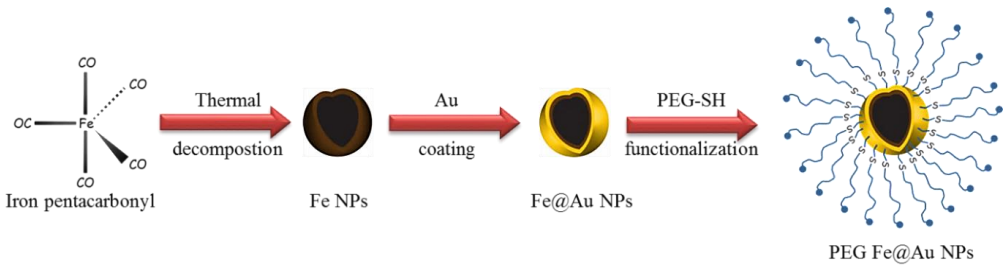

Figure 6.2 Schematic showing synthesis of Fe@Au NPs followed by functionalization with PEG-SH. Adapted from [119]

Fe NPs were observed to have an average diameter of 14 ± 1 nm, calculated from S(T)EM images (Figure 6.3 (a)). Representative BF S(T)EM image shown in Figure 6.3 (b) exhibits an increment in an average diameter ~ 24± 5 nm of Fe@Au NPs. From these data, the thickness

[VI] The cell work was done by Dr. Ioanna Sandvig and will not be discussed in full detail here.

of the Au shell was calculated to be ~ 5 nm. It is difficult to visualize a core-shell morphology of as-prepared Fe@Au NPs in electron microscopy because Au has a higher atomic number than Fe, contributing to high contrast while imaging. A shell of Au coating around Fe NPs can be confirmed by Energy Dispersive X-Ray Spectroscopy (EDX) elemental analysis, indicating the presence of Fe and Au in NPs (inset in Figure 6.3 (b)). In addition, XPS studies were also conducted in order to confirm the Au coating on Fe NPs shown by the survey spectra of Fe@Au NPs (Figure 6.3 (c)) which revealed the presence of Fe 2p and Au 4f. PEGylation was done in order to ascribe stealthy properties to the Fe@Au NPs, as PEG is known to prevent opsonisation of plasma proteins in blood onto NPs, reducing their circulation time among other properties.

DLS measurements, however, showed larger sizes of 34 ± 4 nm (Fe NPs), 71 ± 4 nm (Fe@Au NPs) and 72 ± 5 nm (PEG Fe@Au NPs), respectively, in comparison to analysis via S(T)EM. The reason for this discrepancy can be attributed either due to DLS measuring the hydrodynamic rather than the core radius of the NPs as measured by S(T)EM, a weak interparticle dipolar interaction among NPs causing weak interparticle coupling, or a combination. However, successful PEG coating was seen from UV-vis results ((Figure 6.3 (d)). It can be noted from the UV-Vis spectra that Fe NPs do not show a prominent absorption peak in the visible region, whereas Fe@Au NPs display characteristic LSPR peak at ~ 525 nm. We observed a red shift in the absorbance peak (~ 528 nm) for PEG coated Fe@Au NPs. The bathochromic shift is an indication of the increase in the size of the NPs following PEG-coating, as predicted by Mie-Drude theory. The thickness of gold shell was tuned by varying Au precursor concentration, effect on the LSPR characteristics being shown in Figure 6.3 (d). A bathochromic shift in UV-Vis spectra was observed from 528 nm to 535 nm with increasing gold precursor concentration, indicating thicker gold coating. In addition, an evolution of a second LSPR band above 600 nm with increasing gold precursor concentration was observed, which can be attributed to a change in the NP shape after gold coating.

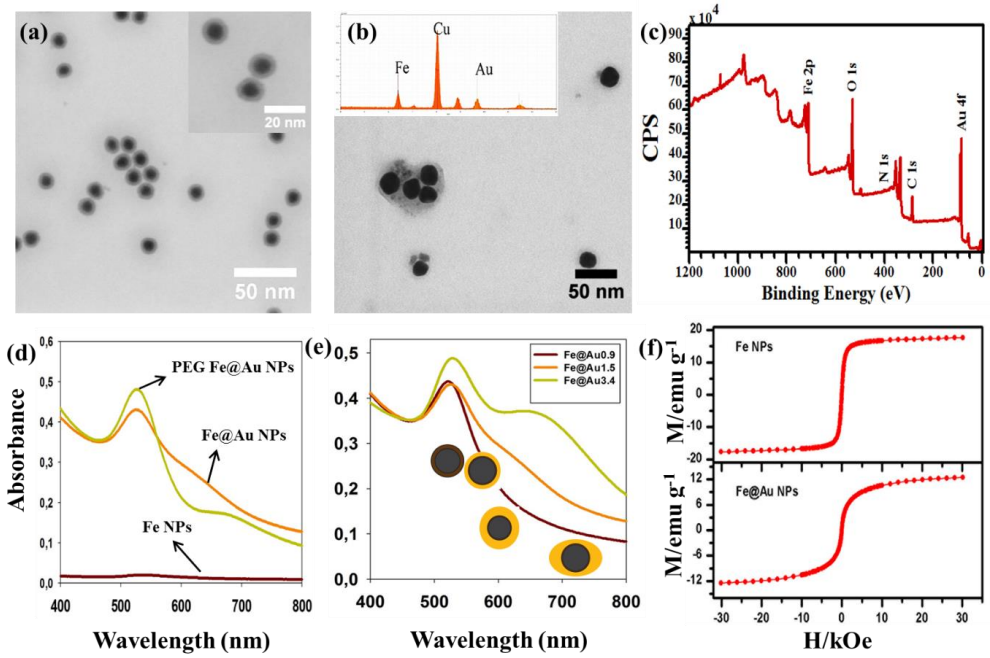

Figure 6.3 Representative BF S(T)EM images of (a) Fe@FexOy NPs (inset is a magnified image of Fe NPs), (b) Fe@Au NPs (inset is EDX spectrum for Fe@Au NPs), (c) XPS survey spectra of Fe@Au NPs. UV-Vis spectra of (d) Fe, Fe@Au and PEG coated Fe@Au NPs. (e) Fe@Au NPs synthesized using different concentrations of Chloroauric acid 0.9 mM, 1.5 mM and 3.4 mM. (f) Magnetic hysteresis curves at 300K for Fe and Fe@Au NPs. Adapted from [119]

Fe and Fe@Au NPs showed superparamagnetic properties. Figure 6.3 (e) shows the magnetization (M) versus the magnetic field (H) at 300K obtained by cycling the field between -30kOe and 30kOe. A negligible coercivity and remanence in the hysteresis loops indicates the super-paramagnetic nature of the NPs. The coating of Au shell reduces the magnetic dead layer in our samples leading to enhancement of magnetic properties of the bare Fe NPs. The M-H curves become rounder or S-shaped like as Au is coated on the NPs, again reflecting the weakening of interparticle interaction.

Having characterized the Fe@Au NPs, PEGylated NPs were used to study their interactions with two different cell types: olfactory ensheathing cells (OECs) and human neural stem cells (hNSCs), which are promising candidates for regenerative therapy of the central nervous system. These two cell types differed in terms of uptake and localization of the Fe@Au NPs post-labelling, while no cytotoxic effects were observed irrespective of label concentration or length of co-incubation with the NPs. A tendency for peri-membrane localization of the

Fe@Au NPs, rather than intracellular localization, was observed in the OECs as shown in Figure 6.4. On the other hand, the differential affinity of the OECs and hNSCs to the particles suggests that labelling and imaging protocols for *in vivo* application must be optimized for the individual cell types.

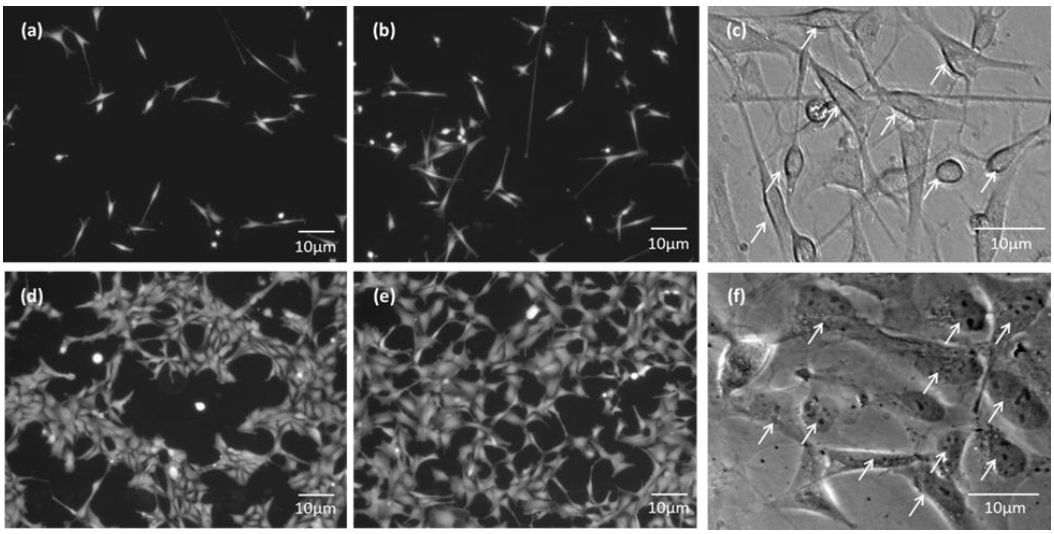

Figure 6.4 (a),(b),(d),(e) Live/Dead images of OECs and hNSCs 24h after labelling with Fe@Au NPs (a) Unlabelled OECs, (b) OECs with Fe@Au NPs, (d) Unlabelled hNSCs and (e) hNSCs with Fe@Au NPs. (c), (f) Differential interference contrast (DIC) images of labelled OECs and hNSCs, respectively, showing Fe@Au uptake (arrows). Adapted from [119]

The lack of observable toxic effects of the Fe@Au NPs on either cell type is very promising with regard to future *in vivo* applications involving the specific cells. Magneto-plasmonic properties exhibited by these hybrid NPs enable them suitable for theranostic as well as multimodal imaging uses. In the next paper, efforts were concerted to understand shape and size evolution of Au NPs with an intent to better tune the optical properties and throw light on growth.

6.1.2 Paper-II: Synthesis of Au nanowires with controlled morphological and structural characteristics.

Applied Surface Science 2014, 311, p.780-788.

With an aim to tune the optical properties of Au NPs and understand the role of different Au seeds on growth mechanisms, Paper-II was directed towards understanding growth of Au nanowires (NWs) using a CTAB templated seed-mediated growth protocol.

Although, there exist in literature several approaches for synthesis of Au NWs with tunable A.R.s, growth of Au NWs with controlled morphological/structural characteristics and their underlying growth process are areas that need further elucidation. The need to tailor the NWs arises from the need to better control their physical properties. These properties deem them interesting candidates for a variety of biomedical applications that include sensors, diagnostics and so on. In this paper, we investigated seed mediated approach for the synthesis of Au NWs using CTAB as a soft template and showed that morphological/structural characteristics of NWs can be controlled by choosing appropriate type of seed NPs such as nanospheres (Seed 1) and nanorods (NRs) (Seed 2) as depicted schematically in Figure 6.5 (a).

Figure 6.5 (b), (c) display BF S(T)EM images of obtained Au NWs (synthesized from Seed 1) having wire like morphology with A.Rs greater than 10^3. The average diameter of the Au NWs was determined to be ~17 ± 5 nm based on S(T)EM analysis, while their average lengths were observed to be 35 ± 5 µm. The morphology of as-synthesized NWs appeared wavy in nature with several kinks and small straight regions. The NWs were found to be poly-crystalline, shown by several discrete dark spots in the TEM diffraction pattern of single NWs (inset in Figure 6.5 (c)). On the other hand, the morphological/structural characteristics of the NWs could be altered by replacing the spherical NP seeds with NRs (Seed 2) as shown in Figure 6.5 (d). Under identical synthesis conditions, less wavy, straighter and thicker NWs (diameter~51 ± 5 nm, of average length ~20 ± 5 µm and A.R: ~400) with fewer number of kinks was observed (Figure 6.5 (d)). Electron diffraction patterns obtained showed that these NWs are single crystalline and grow rapidly along the {111} direction (inset in Figure 6.5 (d)).

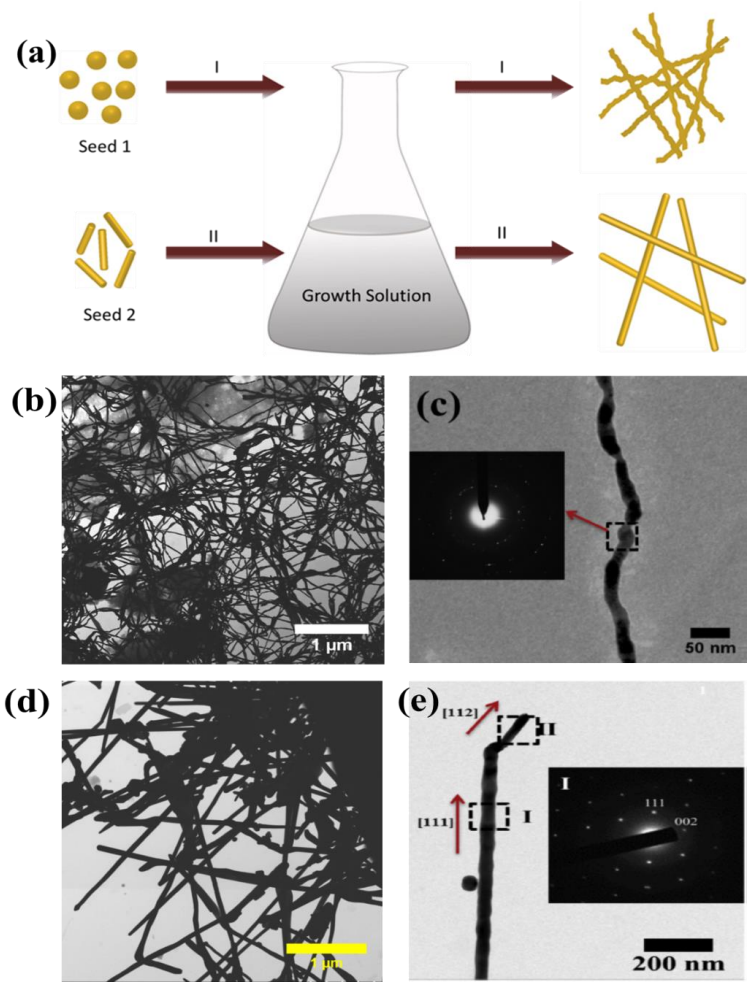

Figure 6.5 (a) Schematic illustration showing growth of Au NWs via two different types of seed NPs, (I) spherical NPs yield wavy NWs, and (II) NRs yield straight NWs. (b) BF S(T)EM image of Au NWs growth from seed 1 at pH~6.9. (c) Enlarged BF S(T)EM image of Au NWs (inset in (c) is a diffraction pattern corresponding to square region confirming the polycrystallinity in the NWs. (d) BF S(T)EM image of straight Au NWs grown from seed 2 at pH ~6.9. (e) Enlarged BF S(T)EM view of single NWs synthesized by seed 2 (inset: diffraction pattern corresponding to the region I confirming that growth direction of NWs is [1 1 1]. Adapted from [32].

In order to monitor the growth of the Au NWs, electron microscopy was used to study the samples collected at different time intervals (Figure 6.6). Figure 6.6 (a) reveals spherical NPs of average size ~10 nm except for a few elongated NPs. With further reaction progress, these NPs eventually evolved into small NRs. The lowest surface energy of {110} among the other facets resulted in the adsorption of CTAB bilayer on the {110} facets as soon as Au seed evolved into NPs containing different facets. Growth occurred more rapidly in the longitudinal

direction than that in the transverse direction in the presence of templating CTAB molecules. Variable length growing nanostructures are evident from Figure 6.6(b) suggesting the onset of NW growth between 10 and 30 min. When the reaction was carried out for 60 min, NRs further grew in size by fusing with neighbouring NPs (Figure 6.6 (c)). At the same time, several concave/convex regions, i.e., the physical contacts of two associating nanostructures could be identified (marked by arrows in inset of Figure 6.6 (c)). The physical contacts were expected to occur either by surfactant induced fusion or welding due to diffusion of atoms between growing nanostructures. Continuous and wavy high A.R. NWs were obtained after 24 h, owing to continuous growth and diffusion processes.

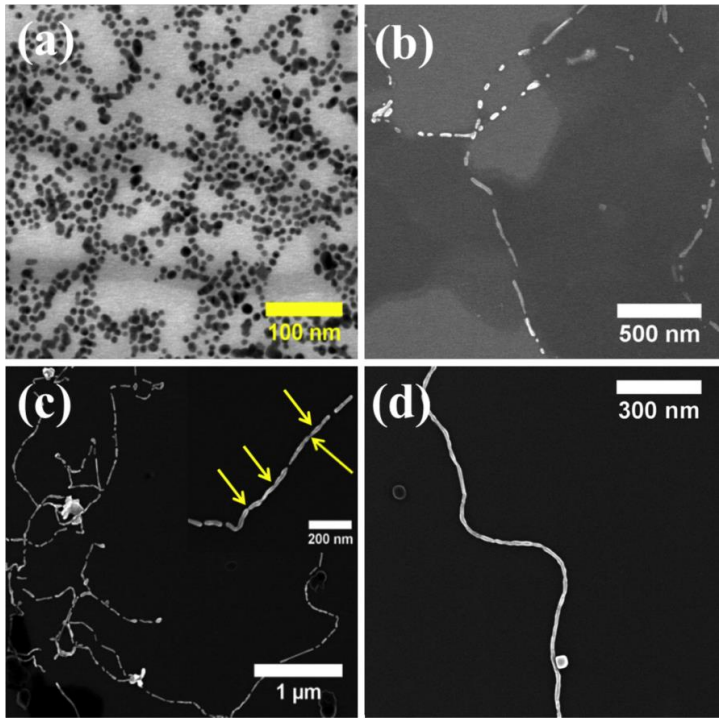

Figure 6.6 Evolution of growth of Au NWs over time, t. (a) BF S(T)EM image, t = 10 min, (b) SEM image, t = 30 min (c) SEM image, t = 60 min (the arrows in the inset show convex/concave regions or neck formation between two adjacent growing nanostructures), and (d) SEM image, t = 120 min. Adapted from [32].

Citrate capped Au spherical seeds (Seed 1) were polycrystalline (i.e., multiple crystal domains) in nature. These seeds grew in size by the addition of Au atoms in the growth solution while retaining the polycrystalline behaviour. Subsequently, wavy NWs with multiple crystal domains and twinning formed, via association of growing nanostructure that could occur in between sphere-sphere, NR–sphere–NR, and NR–NR. On the other hand, seed 2 comprised

single crystalline NRs, leading to growth in 1D in the presence of CTAB, forming single crystalline NWs via association of growing nanostructures.

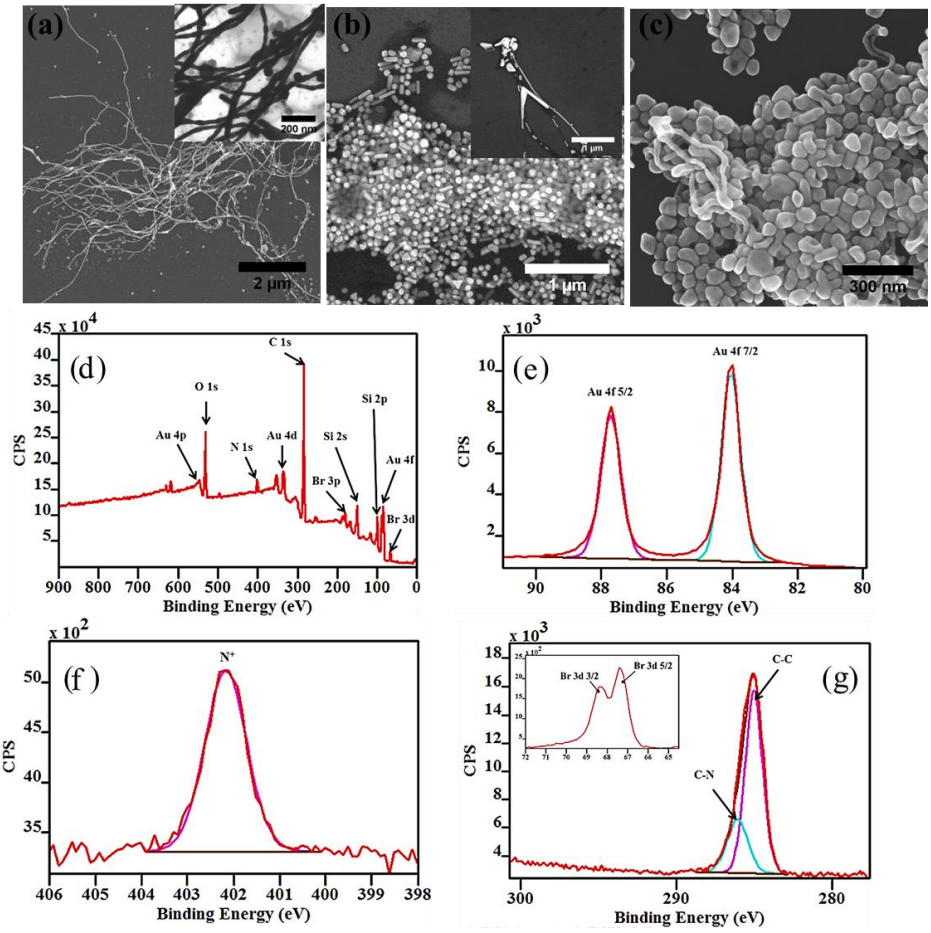

Figure 6.7 SEM images of Au NWs grown via seed 1 at different CTAB concentrations and fixed pH~6.9 (a) 25 mM, (b) 10 mM, (c) 1 mM. Inset in (a) is BF S(T)EM at higher magnification and in (b) is SEM of low A.R. NWs. (d) XPS survey spectrum of CTAB capped wavy Au NWs. XPS high resolution spectra of the (e) Au 4f, (f) N 1s, and (g) C1s (inset: Br 3d). Adapted from [32].

In order to understand the effect of different experimental conditions, concentration of CTAB, pH of the growth solution and reaction temperature were varied to see their influence on the morphology and A.R. of the NWs. As observed from Figure 6.7 (a), when the CTAB concentration was 25 mM, a mixture of long NWs and variously shaped NPs was obtained When the concentration was further reduced to 10 mM and 1 mM, shorter NWs with a very low yield and an increased amount of irregularly shaped NPs were observed (Figure 6.7 (b),

(c)). Under these conditions, a faster reduction of Au salt produced a surplus of Au atoms in the solution and caused thermodynamically stable, shorter, irregular aggregates of large NPs inhibiting growth of NWs due to an insufficient amount of Au atoms required to fill the gap at the contact point between two NPs. Alternatively, it could also be attributed to aggregation of NPs that are not fully capped by a CTAB bilayer at low surfactant concentration, which did not provide sufficient van der Waals interaction between CTAB layer, causing NPs to merge in a random fashion and form irregular shaped NPs [32]. These results suggested that an excess amount of CTAB is essential for producing long and continuous NWs. Figure 6.7 (d) - (g) show the XPS results for the Au NWs. A shift in Br $3d^{5/2}$ peak to ~67.4 eV in comparison to bulk CTAB (~68.7 eV) was observed following binding of Br to the Au surface. Further, the N 1s peak could be assigned to quaternary ammonium (N+) (from CTAB) which shifted towards a higher binding energy (~402.3 eV) and higher than pure CTAB due to the Au surface vicinity. The presence of CTAB species alone on the surface of Au NWs was thus confirmed from XPS results.

This work gave us a fundamental understanding regarding how the growth mechanism was operating at the nano-scale. However, we wanted to generalize our understanding for a large array of Au NP shapes and sizes, while using the same method of synthesis. The motivation for the next paper was thus to understand how different components added in the reaction mixture influence the shapes of anisotropic Au.

6.1.3 Paper-IV: Shape Control of gold nanostructures using binary surfactant mixtures.

Under Review in *Journal of American Chemical Society*.

In this particular work, a library of gold NPs was synthesized with controlled physico-chemical properties using Ag assisted seed mediated method, employing a binary surfactant mixture. In essence, we investigated how the shape and A.R. of Au NPs change as an increasing amount of a secondary surfactant, Didodecyldimethylammonium bromide (DDAB), is added to the growth solution containing a fixed amount of CTAB. Using a systematic approach, the effect of surfactant mole ratios, pH of the growth solution, hallide ion concentration, seed concentration, reducing agent concentration among other factors were studied in order to understand the growth mechanism of anisotropic Au NPs.

In the first set of experiments, the concentration of DDAB was varied while CTAB concentration (*i.e.,* 1.5 mmol) was kept constant. As the CTAB/DDAB increased from 2 upto 46, we noticed a change in the shape of the Au NPs from bipyramids (low CTAB/DDAB ratio)

to NRs (high CTAB/DDAB ratio) via tetrahexahedral (THH) (intermediate CTAB/DDAB ratio). CTAB is a single chain surfactant with a moderate head group area (~ 56Å^2) and a critical packing parameter (CPP) of 0.33 in water that aids the formation of spherical micelles. [120] On the other hand, DDAB is a water-insoluble, double-chained surfactant of head group area (~ 25Å^2) with a CPP of 0.62, mostly forming bilayer shaped micelles in water. [120] The addition of DDAB into CTAB solution leads to the change in the CPP of the resultant surfactant mixture depending on the ratio of CTAB/DDAB. This change is caused by the large tail volume and small head group area of DDAB decreasing the electrostatic repulsion between the quaternary ammonium groups. Therefore, the reduction in the curvature of micelle by using DDAB with CTAB promotes longer rod-like or cylindrical micelles than with CTAB alone.

At low CTAB/DDAB ratio of 2, Au bipyramid NPs of longitudinal length (l) ~ 1.2 µm and transverse width (w) ~ 382 nm (A.R. ~ 3.1) with high yield (~ 70%) were obtained as main reaction product (Figure 6.8 (a)). Au bipyramids of small size (i.e., l = 666 nm, w = 180 nm, and A.R. = 3.7) were obtained at increased CTAB/DDAB ratio of 6 (Figure 6.8 (b)). The crystalline structure of Au bipyramid was determined from HRTEM (Figure 6.8 (c)). The observed spacing between the lattice fringes was ~ 0.235 nm corresponding to the interplanar spacing of Au {111} ie., {111} facets of bipyramid. The electron diffraction pattern collected at the centre of the Au bipyramid exhibits two set of spots which can be indexed to <112> and <001> zone axes corresponding to red and white regions in Figure 6.8 (d). The indexed spots in the diffraction pattern correspond to the lattice parameters: d_{111} = 0.235 nm, d_{222} = 0.119 nm, d_{220} = 0.145 nm, d_{020} = 0.206 nm, d_{311} = d_{131} = 0.126 nm, and d_{402} = 0.092. All of these measured spacings are in agreement with reported values in the literature. The remaining spots which are not indexed are caused by multiple scattering. Such a diffraction pattern is typical of twinned or decahedral nanoparticles with five-fold symmetry. Our results suggested that Au bipyramids produced in the study are face-centred cubic penta-twinned NPs grown along the <110> and are bounded with {111} and {100} facets.

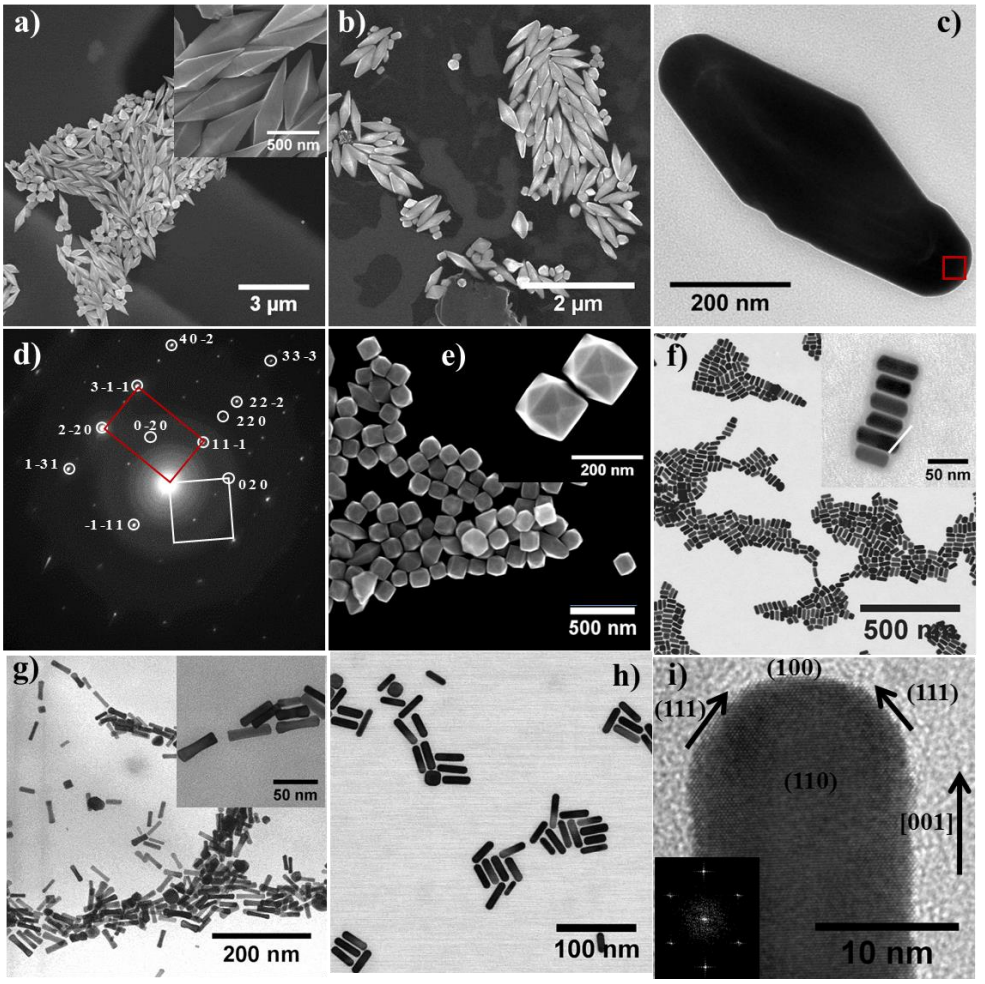

Figure 6.8 Au NPs synthesized at different CTAB/DDAB ratios (x). SEM images of Au bipyramid NPs of (a) l = 1.2 µm and w = 382 nm, x = 2 and (b) l = 666 nm and w = 180 nm, x = 6. (c) TEM image of single Au bipyramid of (b). (d) Electron diffraction pattern taken on bipyramids shown in (c). (e) SEM image of Au THH NPs, l = 198 nm and w = 168 nm, x = 8. BF-STEM images of Au NRs of f) l = 45 nm and w = 24 nm, x = 11, (g) l = 33 nm and w = 11 nm, x = 23 and (h) l = 38 nm and w = 10 nm, x = 46. (i) HRTEM image of Au NR and inset is FFT of NR. l and w are referred to as longitudinal length and transverse width respectively.

When the ratio of CTAB/DDAB was further increased to 8, the yield of Au bipyramids decreased, and elongated THH type Au NPs (l = 198 nm, and w = 168 nm, and AR~ 1.2) with high yield (~ 90%) was obtained as the main reaction product (Figure 6.8 (e)). A morphological transition from elongated THH to rod occurred in between the CTAB/DDAB ratio of 8 and 11, and NRs were obtained (Figure 6.8 (f)).On further increase in the ratio from 11 to 23 and 46, thinner NRs of smaller lengths were obtained (Figure 6.8 (g), (h)). An HRTEM image shows

the single crystalline Au NRs growing along the direction [001] (Figure 6.8 (i)). The fast fourier transform (FFT) inset of Figure 6.8 (i) revealed that sides of NRs are formed by {110} facets and the ends of NRs are bounded by {111} and {001} facets which is in agreement with previous results. NRs are thus oriented in dominant [110] direction. The {110} facet is a unique feature found in the NR synthesized in the presence of Ag because of a high surface energy of {110} facets, when compared to {111} and {100} facets. The energy of {110} facets can be minimized by specific adsorption of surfactants to these facets. Overall, these results suggested that an appropriate concentration of CTAB and DDAB (i.e., CTAB/DDAB ratio) is highly essential to achieve a shape control of the Au NPs.

In our experiments, the CTAB/DDAB molar ratio was only varied, which indicates change in the shape and size of micelle as well as the concentration of overall Br- ions while Ag+ ion concentration remains constant. At low DDAB concentration (i.e., high CTAB/DDAB ratio ~ 46), thinner and shorter AR Au NRs were formed (Fig. 1k). This can be explained by the growth of Au NPs in the thinner soft micellar template. As Au NPs develop crystal facets, the micelle forms compact packing on the Au {110} facets restricting the transverse growth of NRs by preventing the diffusion of gold atoms, while the high reduction rate of the Au species on low energy {111} facets facilitate the longitudinal growth due to lower passivation of {111} facets by micelles. The proposed mechanisms are consistent with computational studies showing the relative packing density of head groups on different facets of Au in the order; {110} > {100} > {111}. [47, 121]

As the concentration of DDAB increased in the CTAB solution (i.e., CTAB/DDAB ratio ~ 11), Au NRs were observed to grow in size and width. This suggests that mixed micelles also grow in size (both length and width) as the DDAB concentration increases in the solution. Control experiments further showed that DDAB facilitates the formation of zero-dimensional structures, while CTAB assisted in one-dimensional rod like structures. Our results are also in agreement with findings of mixed surfactants, revealing the increase in the width and length of micelles with increase in DDAB concentration in the solution.[122] An increasing concentration of DDAB in the growth solution also makes the diffiusion of Au species to the seeds sluggish. This is because of increase in the visocity of the solution as well as the migration of Au ionic species through highly dense packed micelles of DDAB and CTAB. In this case of high DDAB concentration, i.e., CTAB/DDAB ratio ~ 8, the reduction rate of Au species at the seeds is very low. Thus, the probability of Au atoms migrating from the {111} facets is very high, since Au atoms can migrate at room temperature. As a result, the rate of rapid surface

diffusion compared to the deposition leads to the formation of kinetically stabilized elongated THH Au NPs bounded with high index facets. The formation of these NPs can thus be explained in the modification of soft template to convex structure and low reduction rate of Au species.

A further addition of DDAB to the growth solution (i.e., CTAB/DDAB ~ 6 or 2) causes a change in the composition and subsequently in the structure of micelles. The reported experimental study revealed the formation of micellar structures which grow more significantly in the length than to width. As a result, Au bipyramids of micron and sub-micron sizes were obtained as main reaction products. UV-Vis results (Supporting Information of Paper-IV) suggest that during the aging for first 120 minutes, CTAB stabilized single crystalline seeds turned into polycrystalline seeds possessing five-fold symmetry because of thermodynamic ripening. As the reaction proceeds, a red shift in the peak could be noticed due to increase in the size and morphology of seed particles. When the reaction was continued for 24 hours, the micelles that act as either soft template or structure directing agent, facilitate the selective growth of bipyramids along <110> axis on the large length scale.

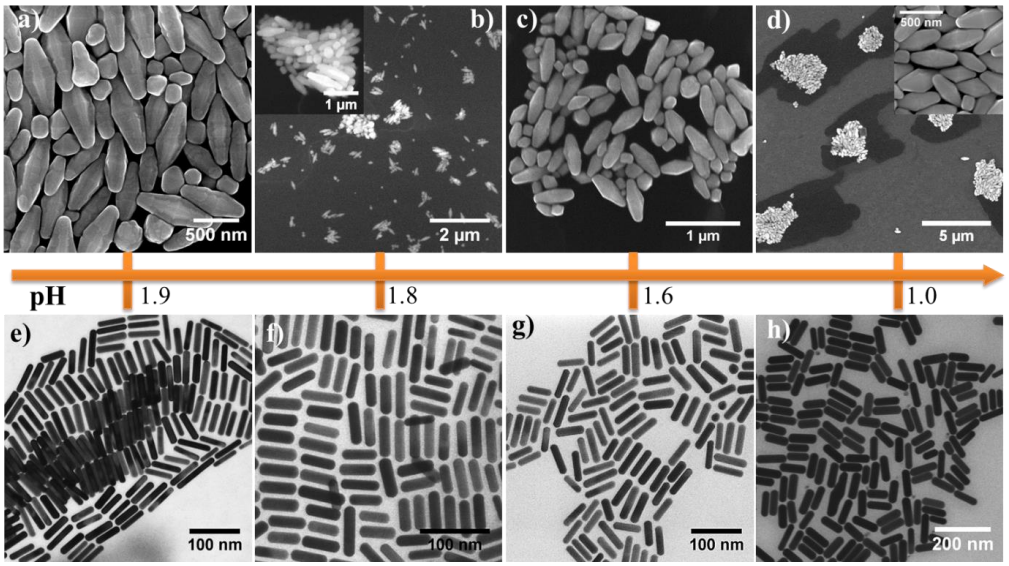

Figure 6.9 The influence of growth solution pH on the sizes of Au NPs synthesized at low and high CTAB/DDAB ratios (6 and 23) . (a-d) SEM images show decrease in the average size of Au bipyramids with decrease in pH from left (1.9) to right (1.0). (e-h) BF S(T)EM images exhibit increase in the average length of Au NRs with decrease in pH from left to right.

The pH of the growth solution has influence on the size and shape of NPs because it influences the reducing capability of ascorbic acid (AA) which is lower for acidic pH values. In the case

of Au bipyramids,(Figure 6.9 (a)-(d)), first the lengths and widths of bipyramids increased, and started decreasing with decrease in pH of the solution. In high DDAB concentration regime (CTAB/DDAB ratio 6 and below), the growth rate is very slow in acidic pH values because of low reduction potential of AA and high viscosity of the solution. Moreover, increasing amount of Cl^- also causes a change in the soft template due to modifications in the head group interactions. As a result, truncated bipyramids of different lengths were obtained in low pH solutions (Figure 6.9 (d)). While in the case of Au NRs (Figure 6.9 (e)-(h)), (low DDAB concentration regime), slow reduction of Au ion species facilitate the more selective deposition of Au atoms on specific crystal facets, i.e., on the tip of NRs under the regulation of micelle structures. As a result, Au NRs of larger sizes were achieved on decreasing the pH. Increase in the pH of the solution accelerates growth rate, that reduces the yield of Au bipyramids and NRs and favours more spherical NPs.

The growth rate of the reaction can also be controlled through the concentration of AA. When the concentration of AA was increased to 270 µL in growth solution containing low CTAB/DDAB ratio (6), a significant decrease in the yield of Au NPs was observed along with polydispersity in shape and size of Au NPs (Figure 6.10 (a)). On further increase in the AA concentration in the growth solution, ill-defined Au NPs with very low yield of Au bipyramids was noted. In the case of high CTAB/DDAB ratio (23), the dogbone morphology of NR with increase in AA concentration in the growth solution, was observed (Figure 6.10 (b)-(d)). A decrease in the yield of Au bipyramids was noticed with an increase in the AA. From the results, it is clear that the growth rate should be slow to obtain Au bipyramids with high yield. However, the morphology of Au NPs in low DDAB solution (high CTAB/DDAB ratio) changed from NRs to dogbone with increase in the amount of AA added to the growth solution. A high concentration of AA present in the solution increases the reduction rate of Au atoms. However, it also destabilizes the micellar structure to a large extent, especially on {111} facets possessing loosely packed layer of micelles (i.e., weakly bound to the surface) than to other facets {100} and {110}, where the micelles are tightly packed and bind strongly to these facets. This results in a high concentration of Au atoms deposited in the unprotected regions i.e., high deposition rate on {111} facets, and low deposition rate on other facets or low surface diffusion of Au atoms from the tip to the sides, promoting dogbone formation. When the concentration of AA increased in the growth solution of low pH, the reduction rate of Au species reduces. AA destroys the micellar structures at the tips of NRs, and slow reduction rate in acidic solution facilities the selective growth on specific crystal facets. The facets of high surface energy {110}

quickly disappear. The selective growth thus proceeds along the {111} facets, which grow in time and join to make arrow type nanodumbells.

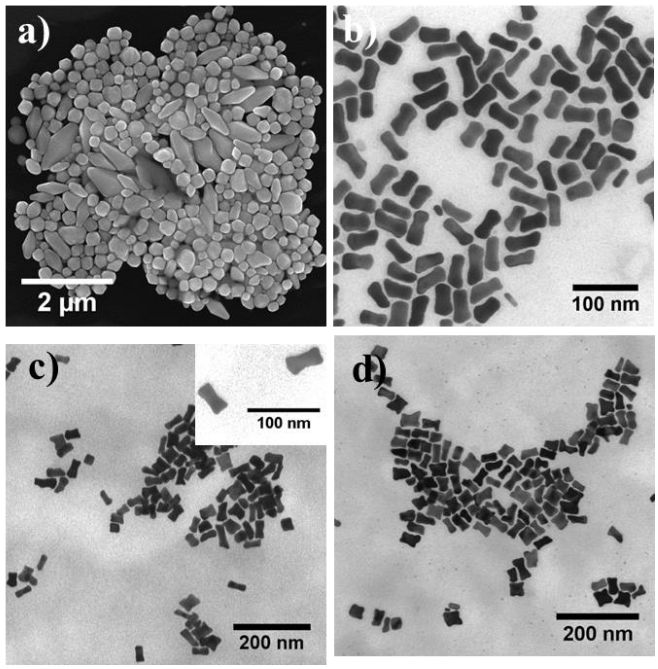

Figure 6.10 The influence of AA concentration on the morphology of Au NPs. (a) SEM image of Au NPs at low CTAB/DDAB = 6, AA = 270 µL. BFSTEM images of Au nanorods synthesized at high CTAB/DDAB = 23 at different AA concentrations, (b) AA = 270 µL, (c) AA = 500 µL, (d) AA = 1 mL.

Finally, the effect of different co-surfactants on the shape of Au NPs was shown (Figure 6.11) by replacing the DDAB with Didecyldimethylammonium chloride (DDAC) possessing Cl- ions. In this case, no change in shape of Au NPs was noticed on varying the CTAB/DDAC ratio. These experimental results suggest that increasing amount of DDAC to CTAB solution does not cause any change in the morphology of micelles as it was in the case of DDAB. This could be because of low binding affinity of Cl- ions to Au surface compared to Br- ions that causes destabilization of rod-like micelles, i.e., make micellar structures less compact or stable providing Au species in the solution easy access to growing seed particles. Therefore, Au NRs of low A.R. with less monodispersity and reaction by-products (spherical, cubic and irregular shaped NPs) were obtained. Moreover, A.R. of NRs and yield of by-product increases as the DDAC amount increases in the solution. Our findings are in agreement with computation simulation results from the mixed surfactant solutions of CTAB and CTAC (Cetyltrimethylammonium chloride).[123] When Tridodecylmethylammonium iodide (TDAI)

(bulkier co-surfactant with I^- ions) as co-surfactant was used, it also did not have any influence on the shape of Au NPs, indicating no change in the micellar structures with varying CTAB/TDAI. However, multifaceted Au NRs of large sizes with good monodispersity were synthesized at low CTAB/TDAI ratio.

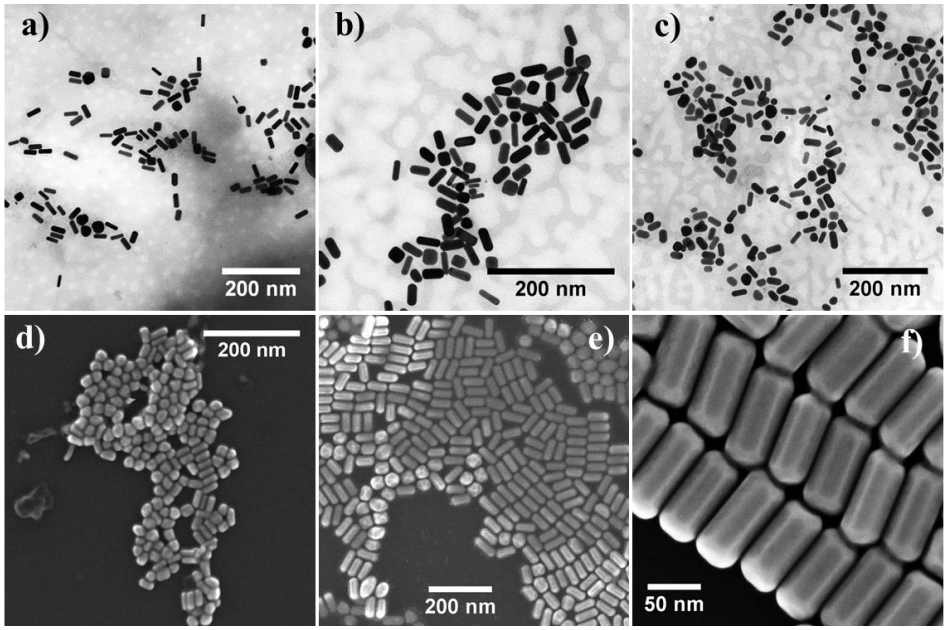

Figure 6.11 The role of counter ions present in the secondary surfactant on the morphology of Au NPs . (a-c) BF S(T)EM images of Au NRs prepared in the growth solution containing CTAB/DDAC in different ratios. The ratio increases from (a) to (c). (d) SEM images showing Au NRs grown from the solution at high CTAB/TDAI ratio (~ 23). e) Au NRs with facets synthesized in the growth solution of low CTAB/TDAI ratio (~ 11), and (f) is the magnified view of (e).

Using a systematic approach, we have thus shown that CTAB/DDAB mole ratio, pH, hallide ion concentration, seed concentration, reducing agent concentration among other factors play important roles in directing the shapes of Au NPs. As all the different shapes have been synthesized using a single protocol, the results have given us better understanding of the mechanisms that lead to anisotropy. One important conclusion from this investigation is that DDAB is the most suitable co-surfactant allowing the tunability in the micellar structure to obtain Au NPs in different shapes and sizes. This paper gave us a good control over shape, size, monodispersity of Au nanostructures prepared using Ag-assisted seeded growth method. The next paper was directed towards using some of these different shapes for understanding cellular interactions.

6.1.4 Paper-V: *Makura*-shaped gold nanostructures show high cytotoxicity in cancer cells.

Under Review in *ACS Nano*.

This paper aimed to use the seed-mediated growth process studied in Paper-IV to synthesize Au nanostructures with different sizes and shapes, functionalize them for uptake in glioblastoma-astrocytoma (GA) cells and assess their cytotoxicity in such cancer cells. In this part, the focus will be on synthesis and functionalization.[VII]

Five different shapes (Figure 6.12 (a)-(e)) of Au nanostructures were synthesized: four anisotropic structures using a single seed-mediated Ag-assisted growth approach discussed in Paper- IV (NRs, nanomakura, tetrahexahedral, bipyramidal) and spherical using a modified Turkevich method. The Au nano*makura* (*Makura* is Japanese for pillow) were reported here for the first time. HRTEM images further showed single-crystallinity for all Au nanostructures, (except for the spheres), similar to that of the CTAB coated seed particles from which they were grown.

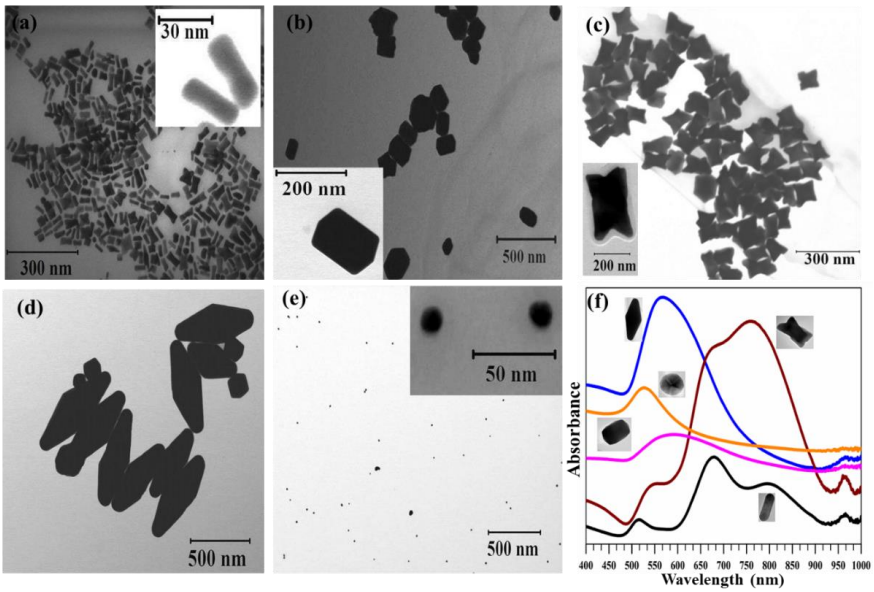

Figure 6.12 Representative BF S(T)EM images of (a) nanorods (inset is a magnified image), (b) tetrahexahedra (inset is a magnified image), (c) nano*makura* (inset is a magnified image), (d) bipyramids and (e) spheres (inset is a magnified image) (f) UV-vis spectra of the Au nanostructures.

[VII] The uptake and cytotoxicity of the different NSs will not be discussed in full detail as this part of the study was done by Dr.Birgitte Hjemeland McDonagh.

Figure 6.12 (f) shows the UV-vis spectra of all the Au nanostructures which were found to display tunable LSPR characteristics over the UV-Vis –visible- near IR range. The NRs showed at least three distinct bands- 516 nm, 679 nm and 796 nm, the strongest being the middle one. The emergence of a third band can be associated with the dispersity of the NRs caused due to the etching effect of oleic acid, which leads to the formation of NRs with rough edges. Nano*makura*, which has a more jagged surface than the NRs, showed both transverse and longitudinal resonance peaks (557 and 760 nm respectively). However, for larger structures (tetrahexahedra and bipyramids), single and broad LSPR peaks were observed at 568 nm and 593 nm, respectively. The observed range of optical properties for the Au nanostructures make them suitable candidates for bioimaging applications.

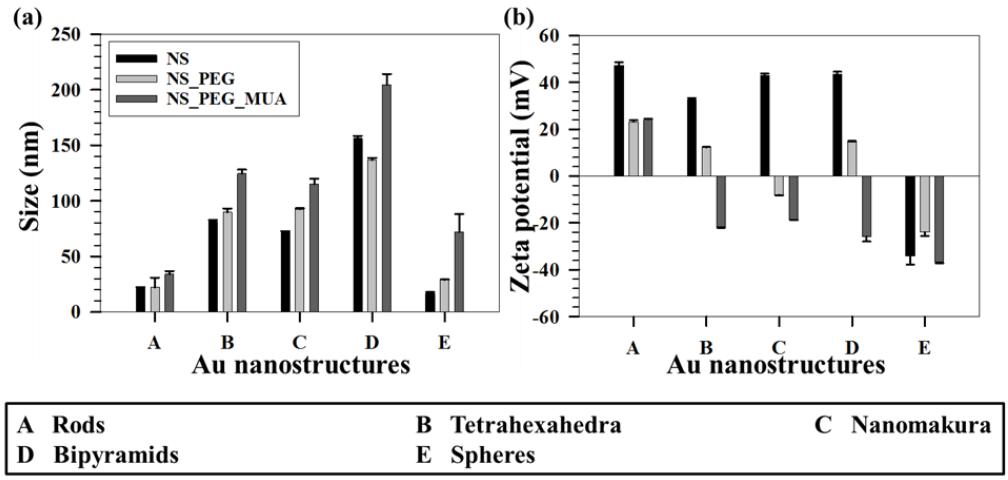

Figure 6.13 (a) Variation of DLS sizes of the Au nanostructures after each stage of functionalization. (b) Variation of zeta potentials of Au nanostructures with each stage of functionalization.

The presence of CTAB (cationic surfactant) on the surface of Au nanostructures can induce proteins to adsorb on the surface, and as such alter the process of endocytosis. Hence, CTAB was removed from the surface by a two-step functionalization procedure, primarily with PEG-SH, followed by a displacing alkanethiol, 11-mercaptoundecanoic acid (MUA). Figure 6.13 (a), (b) show the hydrodynamic sizes and zeta potentials of the Au nanostructures after each step of surface exchange. A sequential increase in the sizes was obtained when compared to the CTAB coated nanostructures, for each shape (except for bipyramids) indicating successful functionalization. However, DLS measurements are based on spherical particle assumption. Further, multiple axes of rotations of the anisotropic structures can lead to uncertainties in

measurements. On the other hand, the cationic surfactant got readily displaced with PEG - SH, which was further replaced by MUA owing to higher affinity towards Au surface. Final zeta potential values of the MUA coated nanostructures reflected negatively charged surfaces for all shapes except for the NRs. The slightly cationic charge for the NRs can be attributed to uneven coating of the small NRs or their polydispersity. It is to be noted that the initial negative surface charge of the spherical Au is due to citrate coating.

After successful coatings, the Au nanostructures were co-incubated with GA cells for 24 hours. The effect of shape and concentration on cytotoxicity were assessed with a LIVE/DEAD assay, supplemented with a nuclear stain and uptake in these cancer cells were assessed. Nanostructure uptake in cells is known to depend on the physicochemical properties, A.R. and surface characteristics of the nanostructure, as well as the cell type.

The highest cell death was noted for the nano*makura* at the highest concentration of nanostructure/cell media (Figure 6.14 (a)), in contrast to our hypothesis that the NRs would cause more damage to the cells, due to their high A.R. and apparent positive charge. This may be due to jagged surface of the nano*makura* leading to different coating densities on different facets. From preliminary light microscopy studies, all the different shapes were observed to associate with the cell membrane. However, nano*makura* and NRs appeared to be located close to the nucleus, indicating cellular uptake. Au nanostructures taken up via receptor-mediated endocytosis may eventually end up in the Golgi apparatus and this may explain the apparent trafficking of nano*makura* towards the nucleus (Figure 6.14 (g)). In order to further understand the trafficking mechanism in case of the nano*makura* (observed from light microscopy measurements), uptake was followed with TEM for 2, 6, 12 and 24 hours after co-incubation with GA cells (Figure 6.14 (b)-(m)).[VIII] TEM results confirmed that nano*makura* Au were taken up by the cells. 2 hours after co-incubation, the nanomakura appeared to be invaginated by the cellular membrane in a mechanism which resembled receptor-mediated endocytosis (Figure 6.14 (b)). At later stages, macropinocytosis was observed (Figure 6.14 (h)). Uptake of nano*makura* appeared to continue even at 24 hours, which may have been caused by the high extracellular concentration of the nanostructures (Figure 6.14 (k), (l)). At 24 hours, the cells also appeared to detach from the surface, which is an indication of cellular death (Figure 6.14 (m)).

[VIII] Ultramicrotome sectioning and TEM (80 kV) was performed by Nan E. Tostrup Skogaker at the Cellular and Molecular Imaging Core Facility (CMIC), Norwegian University of Science and Technology (NTNU).

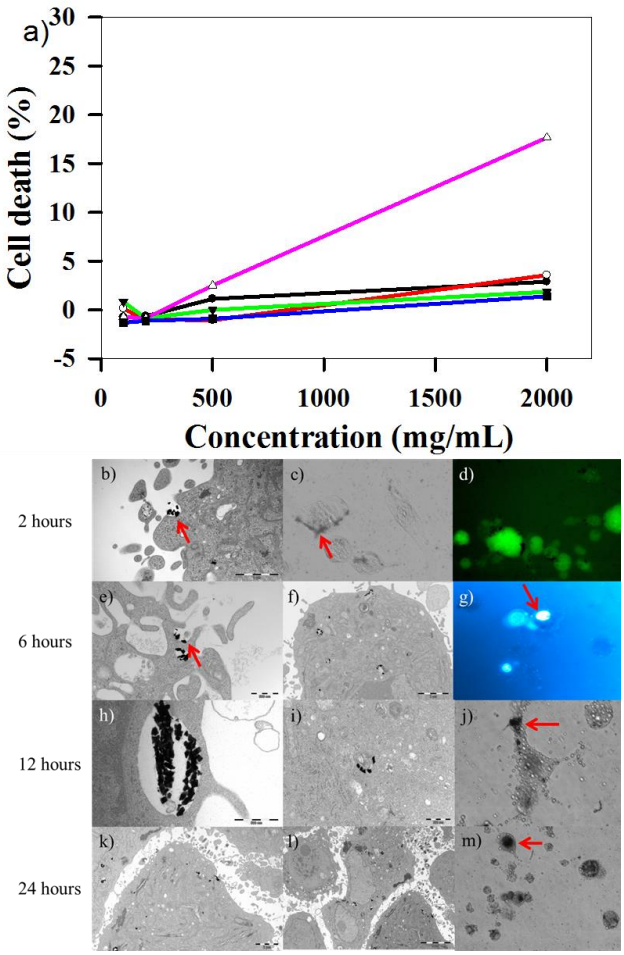

Figure 6.14 a) Percentage cell death of GA cells as a function of concentration of Au nanostructure after incubation for 24 hours. b) TEM image shows an invagination of the cellular membrane (error bar = 1 μm), and c) halogen and d) fluorescence images show association of nano*makura* at the cellular membrane. e) Uptake of nano*makura* was observed after 6 hours (error bar = 500 nm), f) with uptake in intracellular vesicles (error bar = 2 μm). g) Staining of the nucleus suggest that nano*makura* were excluded from the nucleus. h) TEM images taken after 12 hours suggest uptake via micropinocytosis (error bar = 500 nm), with i) intra-vesicular location of nano*makura* (error bar = 500 nm). j) Intracellular compartmentalization was also visible from the microscopy. Uptake of nano*makura* continued at 24 hours as seen in TEM images k) (error bar = 2 μm) and l) (error bar = 5 μm). m) Detachment of GA cells from the surface was observed, which most likely is an indication of cell death.

This successful internalization of the Au nano*makura* in cancer cells, shown by this study, coupled with their unique physico-chemical properties, render them suitable for hyperthermia and drug delivery to cancer cells, while being simultaneously imaged.

Having synthesized different shapes and sizes of metallic NPs, the next phase of the work was devoted to hydrogels and fundamental understanding of their properties.

6.2 Stimuli-sensitive Hydrogels and their Characterization

In this sub-section, the main results from Papers III and VI will be discussed. Paper III focusses on the synthesis, characterization and optimization of pNIPAm based nanogels which are further modified for drug delivery applications by incorporating Fe@Au NPs into the networks. Paper VI discusses a theoretical method to estimate the VPTT of such swelling-collapse systems, with an attempt to define quantitative parameters that describe system reversibility.

6.2.1 Paper-III: Incorporation of Fe@Au nanoparticles into multiresponsive pNIPAm-AAc colloidal gels modulates drug uptake and release.

Accepted for publication in *Colloid and Polymer Science.*

In order to exploit the temperature and pH sensitive properties of pNIPAm based NGs, efforts were concerted in this paper to optimize the synthesis of pNIPAm-AAc colloidal gels, using precipitation polymerization. With a further aim to introduce multifunctionality into these systems, Fe@Au NPs synthesized in Paper I were incorporated into the NG networks using two different methods- coating and *in-situ* growth (Fe@Au_NG_c and Fe@Au_NG_i respectively). Thereafter, a model protein drug, Cytochrome *C* (Cyt *C*) was loaded into the different systems to understand loading and release mechanisms and/or kinetics.

Figure 6.15 (a) shows the variation of sizes of the NGs upon varying different reaction parameters. As the cross-linker (Methylenebis(acrylamide)(BIS)) mole percent was increased from 5 to 8%, a substantial decrease in the size of the NGs (A-B) was observed, while a coupled increase in the SDS (sodium dodecyl sulphate) concentration (B-C) caused a larger collapse above the VPTT. This happens due to a higher cross-linking density, causing a greater collapse.

On the other hand, increasing the SDS concentration from 2mM to 5.5mM (while keeping the BIS mole percent constant) (A-D) caused a dramatic decrease (70%) in the size of the NGs. A higher initial concentration of SDS provides higher charge stabilization in addition to a denser packing around the incipient nucleation centres, whereby limiting the growth of the NGs owing to electrostatic stabilization. In essence, SDS concentration was found to be the most

dominating factor determining the size of the NGs as further shown in Figure 6.15 (b). This further suggests that the hydrophobic tails of the SDS chains interfere constructively in increasing the hydrophobicity of the NGs above VPTT, whereby causing a more efficient collapse.

The size and collapse properties of the NGs could also be modulated using different mole ratios of NIPAm, AAc and BIS, while keeping the SDS concentration constant (Figure 6.15 (a), E-F). An increase in the initial size (~ 10%) is explained through a decreased cross-linking density and reduced charge stabilization from the acidic groups of the AAc blocks. On the other hand, there is a slight decrease (~ 3%) in volumetric collapse efficiency on increasing the NIPAm content, indicating an increase in hydrophobic domains when heated above the VPTT. The effect is aided by a lower cross-linking density, yielding a loosely structured NG, thereby needing stronger force to bring together the increased hydrophobic domains during collapse.

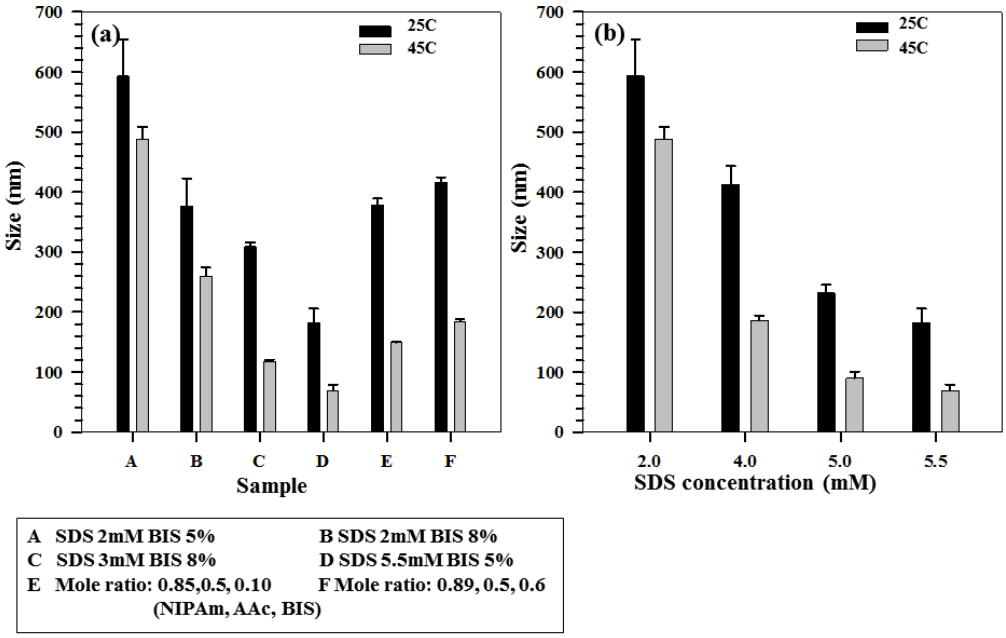

Figure 6.15 (a) Variation of sizes of the NGs synthesized using different parameters. (b) Variation of sizes of the NGs as a function of SDS concentration.

The swelling-collapse properties of the NGs were studied using DLS and are shown in Figure 6.16. The swelling ratio (α), defined as $(D/D_0)^3$, [where D (nm) represents the hydrodynamic diameter of the NG at any temperature and D_0(nm) is the diameter of the NG at room temperature] is shown as a function of temperature for a representative NG (3mM SDS, 8%

BIS). The NGs showed a reversible swelling-deswelling transition with a negligible hysteresis (Figure 6.16(a)). The driving force for aggregation is an increase in entropy from the polymer solution to a two phase system of polymer and solvent, driven by arrangement of water molecules, owing to reduction in hydrogen bonds due to temperature increase. A remarkable decrease in size (~ 27%) was also observed under acidic conditions (Figure 6.16 (b)). This is in effect due to protonation of the carboxylic acid groups of the poly AAc blocks with an increasing pH. The zeta potential, representative of the charges contributed to by the poly AAc segments, did not change appreciably as a function of temperature, (Figure 6.16 (c)) indicating that the poly AAc segments do not show temperature dependence, and their effect in the swelling/deswelling characteristics of the NGs can be widely de-coupled from the effect of the poly NIPAm chains.

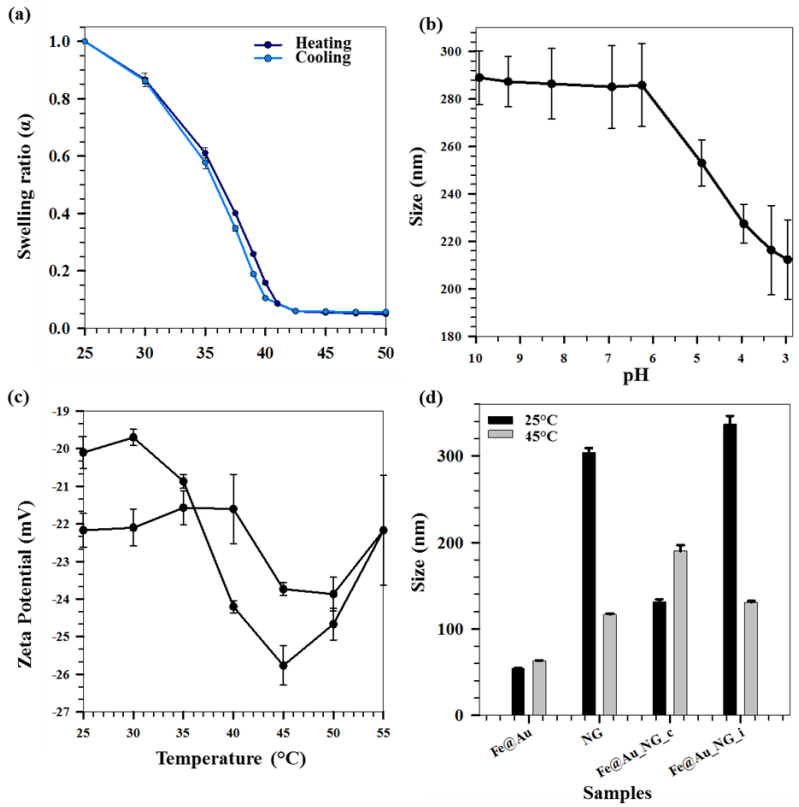

Figure 6.16 (a) Swelling ratio (α) of a representative NG as a function of temperature during heating and cooling cycles. (b) Size of a representative NG as a function of pH. (c) Zeta potential of a representative NG as a function of temperature during heating and cooling cycles. (d) Size of Fe@Au NPs, representative NG, Fe@Au_NG_c and Fe@Au_NG_i as a function of temperature.

A comparison of the DLS sizes of the Fe@Au NPs, a representative NG and Fe@Au NPs incorporated into NGs (Fe@Au_NG_c and Fe@Au_NG_i) as a function of temperature is shown in Figure 6.16 (d) . An increase in the size of the Fe@Au_NG_c NPs as a result of the increase in temperature happens as the NG units undergo entropy driven collapse above VPTT, but Fe@Au NPs act as crosslinking units pulling the gelling units together, whereby increasing their effective size. On the other hand, FeAu_NG_i resembles the collapse behaviour of the NGs, showing a volumetric collapse efficiency of 94%, analogous to that of the bare NGs. Thus, the Fe@Au_NG_i behaves similarly to the bare NGs, while the Fe@Au_NG_c resembles the characteristics of the bare Fe@Au NPs.

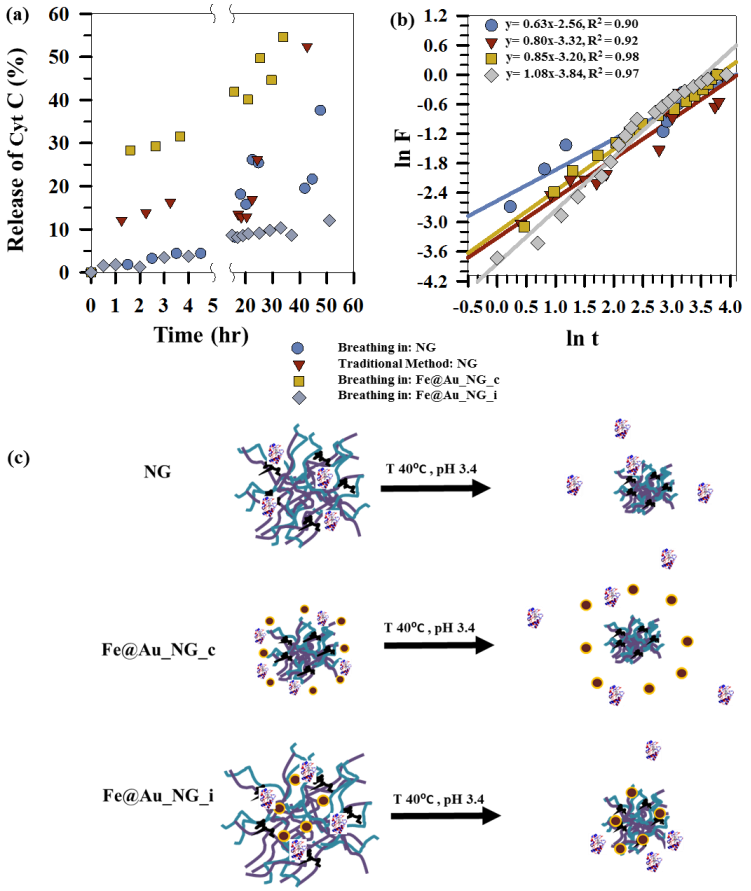

Figure 6.17 Comparison of release of Cyt *C* (loaded using breathing-in mechanism and traditional method) over time from (a) a representative NG and Fe@Au NPs incorporated into NGs at pH 3, T 40°C. (b) Plot of ln (F) as a function of ln (t) for a representative NG and Fe@Au NPs incorporated into NGs at pH 3, T 40°C. (c) Overall schematic showing release of Cyt-C at pH 3.4 and temperature 40°C from three different NG combinations- NG, Fe@Au_NG_c and Fe@Au_NG_i.

The NG systems were loaded using breathing-in mechanism, where in, the freeze-dried NGs or Fe@Au NPs incorporated into NGs were imbibed with a concentrated solution of Cyt *C*. High loading efficiencies of up to 95% were obtained for these NGs, with an encapsulation efficiency of ~ 500 µg per mg of the polymer. In case of the NG coated Fe@Au NPs, loading efficiencies of upto 32% have been obtained with encapsulation efficiencies upto ~14 µg per mg of the Fe@Au NPs. For Fe@Au_NG_i, loading efficiencies of 36.2% and encapsulation efficiencies of 109.7 µg per mg of the NG system were observed. Highest release from these systems was observed under the cumulative effect of high temperature (above VPTT) and acidic pH, specifically at 40°C and pH ~ 3. Figure 6.17 (a) shows the release profiles of Cyt *C* loaded into the NGs and Fe@Au incorporated NGs using the breathing-in mechanism and/or the traditional method, the latter refers to adding a calculated amount of the drug to the NG solutions, whereas the former relies on imbibing the freeze-dried NGs with a concentrated drug solution.

A slightly higher release was observed in case of the traditional method. This is because the drug molecule is peripherally bound to the NGs while in breathing-in case, the drug molecule traverses to the inside of the pores and hence requires more time or several stimuli factors to cause substantial release. Comparing the various NG systems, Fe@Au_NG_c showed remarkably rapid release kinetics, releasing almost 55% of the initial loaded drug over a period of ~ 40 hours in comparison to Fe@Au_NG_i. The higher release in case of Fe@Au_NG_c is due to more peripheral localization of the drug owing to incorporation of the Fe@Au NPs in the NG networks. Further, the Fe@Au NPs act as cross-linkers in case of Fe@Au_NG_c, pulling the gelled units closer together, and thereby enhancing 'squeezing' out of the drug. The release kinetics further prove that Fe@Au_NG_i behave similarly to the bare NGs.

Plotting ln F as a function of ln t, (Figure 6.17 (b)) where, F represents the cumulative fraction of the drug released at time t, gives information about the release mechanisms. It was observed here that drug release mechanisms from the Fe@Au_NG_c and Fe@Au_NG_i were that of super case transport II ($n>1$) while for the NGs alone were representative of drug release from spherical particles ($0.5<n<1$) and anomalous in nature. This relates to the conformational arrangement of the NGs which have lesser degrees of freedom in the presence of Fe@Au NPs, leading to less homogeneously defined viscous and elastic regions. The hypothesized conformational changes are depicted in the schematic in Figure 6.17 (c).

In addition to the optimization of the synthetic parameters for pNIPAm-AAc NGs, the study also shows that drug incorporation method, location of the drug and presence of Fe@Au NPs largely alter the drug release mechanism and the kinetics. Although maximum release from these systems was observed above VPTT, the swelling-collapse behaviour was not discussed quantitatively. The next paper was thus aimed at understanding reversibility of such phase changing systems using a detailed methodology.

6.2.2 Paper-VI: A robust method to calculate VPTT for hydrogels and hybrids.

Manuscript under preparation[IX].

A common method to estimate LCST or VPTT is to measure a spectroscopic parameter like optical density, turbidity, absorbance or size or specific heat as a function of temperature and assign the transition temperature at the average of the sigmoidal plot of the curve or at the mid-point of the range.[75-79] There exists no study to our knowledge where VPTT of such phase changing systems have been exhaustively calculated using a well-defined method with experimental data from both heating and cooling cycles. Our group were among the first to incorporate data from both heating and cooling experiments to understand the behaviours of NP based systems coupled with phase changing polymers. [124, 125] Understanding the phase behavior during both the cycles is the first step towards understanding system reversibility.

Thermodynamic reversibility for systems undergoing phase change has been studied taking into consideration only the initial and final state points. However, the effect of temperature or any other independent parameter on the constituting polymer chains will cause the system to go through several state points along the path, which may not be equal during heating and cooling cycles or during repeated cycles. It is therefore deemed important to consider the journey of the system through these various state points while defining system responsiveness rather than bias the system at the end state points.

In this work, three methods have been devised to obtain the VPTTs of phase changing systems under study which are named as Methods I, II and III respectively. Figure 6.18 highlights the underlying principle used in Method I and II. To start with, the variation of the normalized spectroscopic parameter (size, α_{size} and α in this case) with temperature was plotted (Figure 6.18(a)) and a 'Sigmoid, 5 Parameter' curve was fitted using SigmaPlot® version 13.0 (Figure 6.18(b)). The fit provided us with the values of the five constant parameters (a, b, c, d and e) as shown in equation (46). A fixed value of iteration (n) was selected to define the number of

[IX] The contents of this paper was evaluated by NTNU Technology Transfer AS for patenting.

desired intervals. A MATLAB® code generated a curve utilizing the interval temperature values as the abscissa coordinates and the above obtained five parameters. A mean of the lowest (T_o) and the highest (T_n) temperature values, under study, was calculated and it acted as the starting point for the code. This mean value (T_m) divided the curve into two areas (Figure 6.18(c)). Area I extended from T_m till T_n, while Area II extends from T_o to T_m. The code calculated the area of the two regions based on "Simpson's 1/3rd Rule" and later compared the two obtained area values. Relative difference of the areas was calculated as shown by equation (47). If the compared areas did not fall within the acceptable tolerance limits (defined by the user), the counter for the VPTT moved one interval towards the side of the higher area value and recalculated the areas of the newly formed regions. The final VPTT value was obtained when the relative difference of the areas fell within the tolerance limit (Figure 6.18(d)).

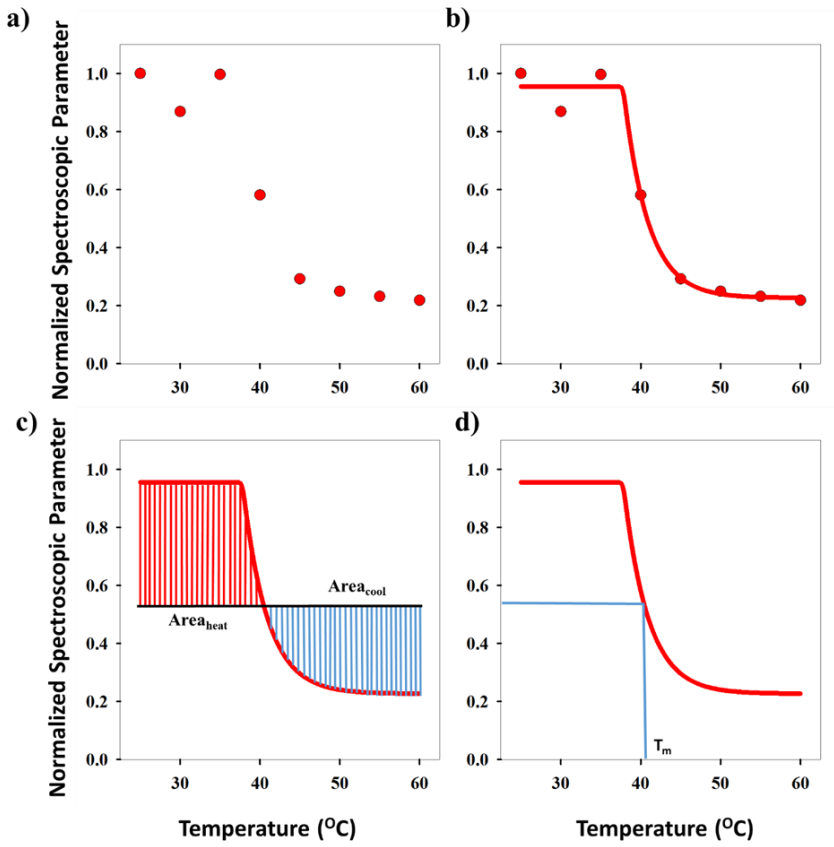

Figure 6.18 Schematic showing calculation of VPTT. (a) Normalized spectroscopic parameter as a function of independent variable (temperature, ^{0}C). (b) Fitting of Sigmoid, 5 parameter curve to the experimental dataset. (c) Area equalization algorithm. (d) Determination of VPTT using MATLAB® code.

$$y = y_0 + \frac{a}{\left[1 + e^{-\left(\frac{x - x_0}{b}\right)}\right]^c} \quad (46)$$

$$Area_{rel} = \frac{Area_{cool} - Area_{heat}}{Area_{heat}} \quad (47)$$

Method I used the above described approach. Swelling ratios, α_{hI} and α_{cI} were used for this method (equations (48) and (49)), where, D represents the diameter at a specific temperature and D_0 is the diameter at the lowest temperature of measurement. VPTT for heating and cooling cycles were calculated from the heating and cooling curves respectively. Same procedure was applied to both the heating as well as the cooling curves and two VPTTs for the heating (T_{h-I}) and the cooling (T_{c-I}) cycles were obtained respectively.

$$\alpha_{h-I} = \left(\frac{D}{D_0}\right)^3 \quad (48)$$

$$\alpha_{c-I} = \left(\frac{D}{D_0}\right)^3 \quad (49)$$

Method II was an extension of method I. The swelling ratio for heating cycle was defined as in Method I (equation (50)), but de-swelling ratio was used for the cooling cycle instead of the swelling ratio (equation (51)). These swelling ratios were used in the curve fitting and parameter generation by SigmaPlot®. The intermediate values of heating (T_{ih-II}) and cooling (T_{ic-II}) VPTTs were calculated using the area equalization approach similar to Method I. Using these two intermediate values, the corresponding α values were determined (α_{h-II} and α_{c-II}). A mean of these α values (α_{mII}) was taken to generate the final VPTTs from the curve namely, T_{h-II} and T_{c-II}.

$$\alpha_{h-II} = \left(\frac{D}{D_0}\right)^3 \quad (50)$$

$$\alpha_{c-II} = \left(\frac{D_n}{D}\right)^3 \quad (51)$$

Method III provided a compact approach in the calculation of VPTTs. The swelling ratios for the heating as well as the cooling cycles were defined as in method II and the curves were generated in a similar manner. Instead of calculating the intermediate values of the respective

swelling ratios as in Method II, an average value of the swelling and de-swelling ratios was determined from the raw data as shown by equations (52) and (53). Heating and cooling VPTTs were then calculated from α_{mh-III} and α_{mc-III}, namely as T_{h-III} and T_{c-III} respectively.

$$\alpha_{mh-III} = \left(\frac{\alpha_{h0} - \alpha_{hn}}{2} \right) \qquad (52)$$

$$\alpha_{mcIII} = \left[\frac{\alpha_{cn} - \alpha_{co}}{2} \right] \qquad (53)$$

Thus, the first two methods (Methods I and II) were based on equalizing the areas of swelled and collapsed states while the third method (Method III) estimated the VPTT values using mean heating and cooling swelling ratios (α_{mh-III}, α_{mc-III}) over the whole data range.

Determination of the VPTTs might give a rough estimate of the reversibility of the systems but it is still not an absolute criterion for commenting on the reversibility of the systems. In order to define overall system reversibility, a general approach of hysteresis was followed. Relative hysteresis (equation (54)) was calculated from the size vs temperature plots for all the samples.

$$Area_{hys} = \left| Area_{heat} - Area_{cool} \right| \qquad (54)$$

In another possible approach to determine system's reversibility, a linear correlation was fitted to the size vs temperature curves, for both the heating and the cooling cycles and the slope of the respective fits were noted (m_h and m_c). These values were used for carrying out order of magnitude analysis and determination of the reversibility parameter, defined based on m_h, m_c and m_{III}.

$$m_{III} = \left(\frac{\ln V_{m_h-III} - \ln V_{m_c-III}}{\ln T_{h-III} - \ln T_{c-III}} \right) \qquad (55)$$

The VPTTs were found to deviate the least from the respective representative mean values (at different tolerances) when α (volume normalized parameter) was used as the processing property in comparison to raw data (size) and a size normalized parameter, α_{size}. Further, a tolerance of 0.001 was set for all calculations and the reported VPTTs are for an iteration number 1000, unless otherwise stated.

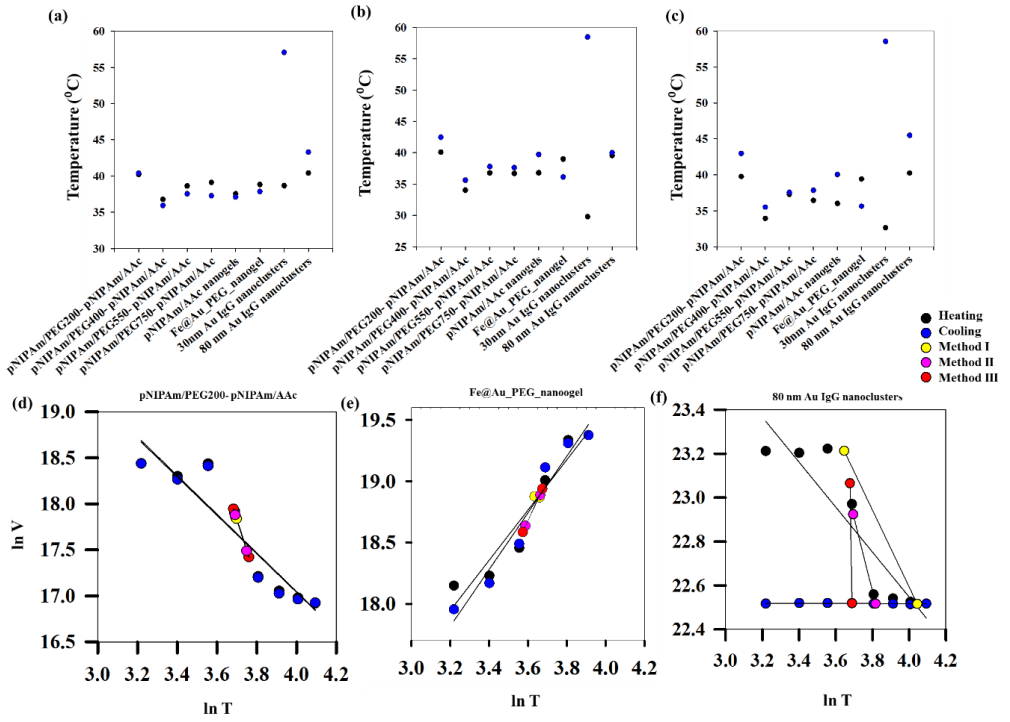

Figure 6.19 Heating and cooling VPTTs for different samples calculated using (a) Method I (b) Method II and (c) Method III respectively. Regression analysis for (d) pNIPAm /PEG200-pNIPAm/AAc, (e) Fe@Au_PEG_nanogel and (f) 80 nm Au IgG nanoclusters using experimental datasets. Yellow, pink and red points refer to volumes obtained at the calculated VPTTs for the respective systems using Methods I, II and III respectively.

Figure 6.19 (a), (b) and (c) show the heating and cooling VPTTs obtained by using methods I, II and III respectively for different phase transition systems. In addition to incorporation of both heating and cooling cycles, the VPTT obtained from each method is a representative value, as all the experimental data points have been adequately considered. The samples studied here have been synthesized during the course of the PhD work. pNIPAm/PEG**MW**-pNIPAm/AAc where, **MW** = 200, 400, 550, 750, were synthesized by Rajesh Raju.[X] pNIPAm/AAc nanogel, Fe@PEG_nanogel were synthesized as discussed in Paper-III. The third category of samples studied here involves AuNP-Immunoglobulin nanoconstructs (80nm Au IgG nanoclusters and 30nm Au IgG nanoclusters) that show a temperature dependent irreversible adsorption, owing to loss of protein structures at high temperatures, previously studied by our group. [125]

[X] Rajesh, R.; Bandyopadhyay, S.; Sharma, A.; Glomm, W.R.; **Preparation of multiresponsive p[NIPAm-co-PEGMA](core)/p[NIPAm-co-AAc (shell)] with controlled size and monodispersity**; Manuscript in preparation.

While Method I employed the use of one parameter α_h, the other two methods also used the cooling swelling ratio (α_c) with an intuitive search for a cross-over point defining an overall system behavior. pNIPAm and pNIPAm based systems show temperature responsiveness owing to a transition from a hydrophilic state to a hydrophobic state above VPTT. Incorporation of different blocks like acrylic acid (AAc), polyethylene glycol (PEG), poly(ethylene oxide) (PEO) into the polymeric architecture affect the VPTT owing to a change in the rigidity of the polymer structure.[126-128] An obvious change in the VPTT values was however observed for samples pNIPAm/PEG**MW**-pNIPAm/AAc where **MW** = 200, 400, 550, 750. On the other hand, incorporation of Fe@Au PEG NPs in pNIPAm/AAc NGs altered the VPTT- while the heating VPTT increased upon addition of the Fe@Au PEG NPs, the cooling VPTT decreased. (Samples pNIPAm/AAc nanogel, Fe@PEG_nanogel). This happens due to the presence of the Fe@Au NPs that act as cross-linkers between the gelling units, pulling them together, leading to an increase of the size as a function of temperature, an effect opposite to that for the bare NGs.

The first two methods of evaluation considered area calculations using Simpson's 1/3rd Rule, the accuracy of which is dependent on the step size and in turn on the number of iterations. During the evaluation, iteration value was kept at 1000 for all the systems. This might introduce minor errors due to approximation. However, Method III employed two parameters (α_h and α_c), but did not include the area equalization modules, meaning that, it is not as sensitive to minor variations in the curve shapes unlike the former two. Further, as explained above, the three methods provided VPTT values for both reversible and irreversible systems within the same range. Therefore, Method III is suggested to be the least computationally exhaustive method with a good estimation of both heating and cooling VPTTs. However, since VPTT is an undefined parameter for systems that do not undergo phase change or for systems undergoing irreversible changes, discrepancies were seen in the estimated values calculated using all the three methods for the cooling VPTTs for Au-IgG samples (Supporting Information for Paper-VI).

Although these methods were competent to estimate both heating and cooling VPTTs for various systems, the absolute values obtained did not give an estimate of the reversibility of these systems. The heating and cooling VPTTs obtained for pNIPAm/PEG200-pNIPAm/AAc using Method I were almost equal, while this was the same scenario for 80nm Au IgG nanoclusters, indicating that both the systems are equally reversible, if the criterion for

reversibility is assumed to be equal heating and cooling VPTTs. However, experimental data showed otherwise.

Thus, it can be assumed that this criterion is not a suitable measure of system reversibility. Figure 6.19 (d), (e) and (f) show the plots of ln V versus ln T for three representative samples, where V represents the volume of the particles and T is the temperature in K. Regression lines fitted to these datasets showed that an approximate measure of system reversibility is predicted by two factors – (i) coincidence of the regression lines for heating and cooling and (ii) coincidence of the VPTTs obtained from all the methods. For pNIPAm/PEG200-pNIPAm/AAc, both the conditions were satisfied, while for Fe@Au PEG NGs, the regression lines for heating and cooling VPTTs were not coincident and for 80nm Au IgG nanoclusters, neither of the conditions were satisfied. Qualitatively, it was possible to ascertain irreversibility in the same order rendering pNIPAm/PEG200-pNIPAm/AAc to be the most reversible and 80nm Au IgG nanoclusters to be the most irreversible among the selected samples. This is further illustrated in Figure 6.20 which demonstrates the divergence of the regression lines as we move from the most reversible sample (Figure 6.20(a)) to the irreversible sample (Figure 6.20 (c)).

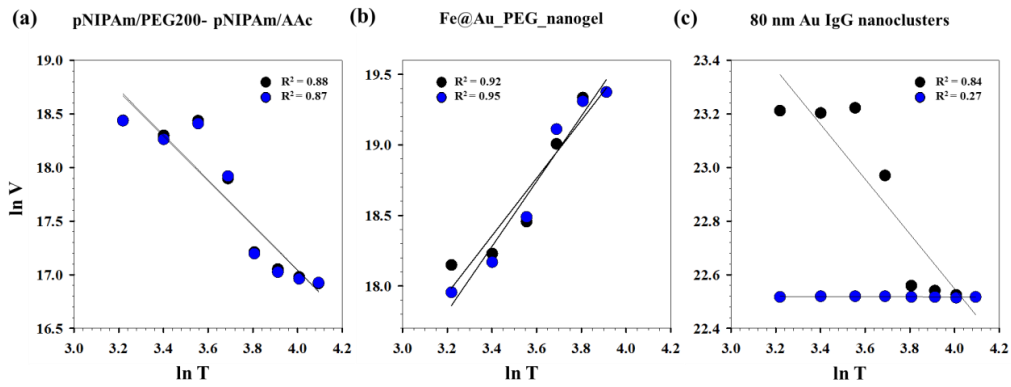

Figure 6.20 Variation of lnV vs ln T for (a) pNIPAm(PEG200-pNIPAm/Aac, (b) Fe@Au_PEG_nanogel and (c) 80nm Au IgG nanoclusters.

While the approach explained took into consideration all the experimental data points, it did not provide a quantitative description of the system reversibility. However, an order of magnitude analysis helped us to treat this semi-quantitatively as follows.

A judging criterion for reversibility can be defined in terms of the order of magnitude analysis as follows:

$$O\left(R_{m_h}\right) = O\left(R_{m_c}\right)\text{: Reversible System} \qquad (56)$$

$$O\left(R_{m_h}\right) \neq O\left(R_{m_c}\right)\text{: Irreversible System} \qquad (57)$$

Here,

$$R_{m_h} = \left|\frac{m_{III}}{m_h}\right| \qquad (58)$$

$$R_{m_c} = \left|\frac{m_{III}}{m_c}\right| \qquad (59)$$

m_h and m_c represent the slopes of the regression lines of $\ln V$ and $\ln T$ for heating and cooling cycles respectively. Table 6-1shows the differences in the order of magnitudes of the irreversible samples as compared with other reversible ones. Although, this criterion defined system reversibility, it failed to reflect the extent of reversibility of a particular system.

Table 6-1 Order of magnitude analysis data for all samples.

Samples	m_h	m_c	m_{III}	R^2		Order of magnitude	
				heat	cool	R_{mh}	R_{mc}
pNIPAm/PEG200-pNIPAm/Aac	-2.1	-2.1	-6.8	0.88	0.87	1	1
pNIPAm/PEG400-pNIPAm/Aac	-1.4	-1.3	-8.4	0.75	0.73	1	1
pNIPAm/PEG550-pNIPAm/Aac	-1.9	-1.7	-67.9	0.85	0.79	2	2
pNIPAm/PEG750-pNIPAm/Aac	-1.8	-1.7	-12.9	0.92	0.9	1	1
pNIPAm/AAc nanogels	-5	-4.8	-16.1	0.84	0.86	1	1
Fe@Au_PEG_nanogel	2	2.3	3.5	0.92	0.95	1	1
30nm Au IgG nanoclusters	-0.2	0	-0.1	0.94	0.26	0	2
80 nm Au IgG nanoclusters	-1	0	-1.2	0.84	0.27	1	3

In the search for a quantitative parameter that describes the system reversibility taking into account all the state points which the system passes through both during heating and cooling cycles, the reversibility parameter (RP) was developed:

$$RP = \left|\log_n \left\| \left(\frac{m_h - m_c}{m_h}\right) * 10n \right\|\right| \qquad (60)$$

Where, n is an integer greater than or equal to 1.

The condition of reversibility was defined as follows:

$$RP \leq 0.1n \quad \text{: Reversible} \quad (61)$$

$$0.1n < RP < 0.2n \quad \text{: Partially irreversible} \quad (62)$$

$$RP = 0.2n \quad \text{: Irreversible} \quad (63)$$

Applying the same methodology, it was possible to ascertain a system parameter to each of the samples that describes the swelling-collapse behavior. The RP and percentage irreversibility (Figure 6.21 (a), (b)) follow the same trend as the relative hysteresis area curve for the samples (Supporting Information), the latter does not ascribe a definite system parameter and only gives a relative understanding of system reversibility. On the other hand, RP is also a predictive parameter that has the capability to estimate either the temporal state of the system state or its state after several cycles of operation, depending on whether RP has been calculated from time-based or cycle-based data respectively.

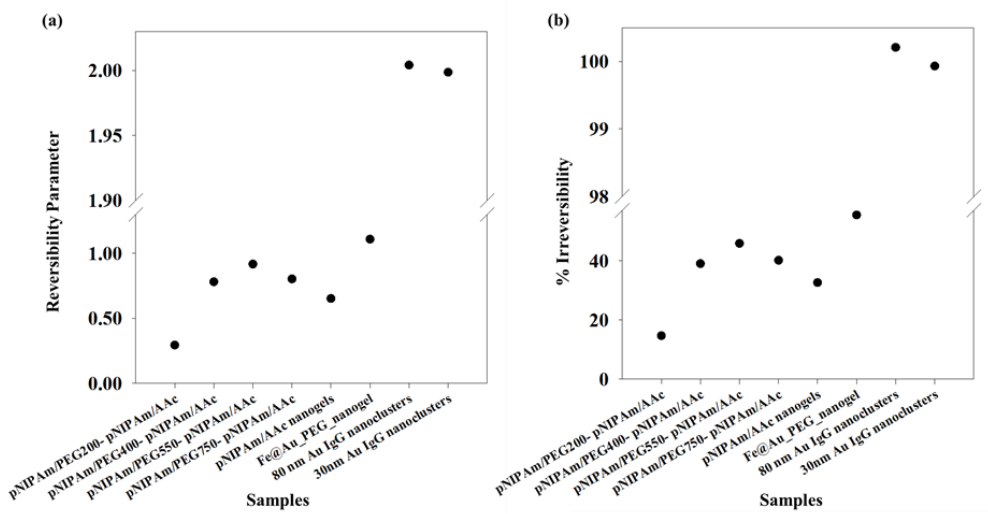

Figure 6.21 (a) Reversibility parameters and (b) Percentage irreversibilities for all samples.

We stress that the RP could be a very important parameter for systems that lose utility over time or usage owing to fouling. Further, for a system in operation, the whole setup need not be changed in instances of system malfunctioning, but the operation window can be changed based on previous system state values. This would not only reduce investment costs, but also reduce system down-time. One of the foreseeable situations is improved performance of various bio sensors based on polymer properties. Thus, with the discovery of a new parameter that is capable of defining system reversibility, it will help in understanding the behavior of systems that undergo stimuli driven swelling-collapse.

6.3 Hybrid NPs

This final sub-section culminates in two important papers, Papers-VII and VIII, that deal with combination of nanomaterials that include metallic and polymeric NPs, with an attempt to obtain superior properties in drug delivery applications. Findings from Paper-III showed that coating is the preferred method for NP incorporation over *in-situ* growth. Hence, coating strategy was used for both papers here. Paper-VII deals with different polymeric coatings on Fe@Au NPs, with an aim to understand the influence of functionalization on loading and release of L-Dopa, a drug for Parkinson's disease. Paper-VIII further analyses the effect of shape on the release of Cyt-C for different Au NPs incorporated in NIPAm based hydrogels.

6.3.1 Paper-VII: Influence of polymer coating on release of L-Dopa from Core-shell Fe@Au nanoparticle systems.

Manuscript under preparation.

This study was directed towards understanding the effect of different stimuli-responsive polymer shells on Fe@Au core-shell NPs with respect to thermoresponse as well as loading and release characteristics. Loading and release studies were carried out using L-Dopa, an orally administered drug used for treatment of Parkinson's disease. L-Dopa is the precursor for the neurotransmitter dopamine and is de-carboxylated to the latter in capillary endothelial cells, once carried across the blood brain barrier.[129]

Fe@Au NPs were synthesized according to the protocol used in Paper I. Thereafter, a solution based approach was used to functionalize these NPs with different commercial and in-house synthesized polymeric shells (Figure 6.22).

The bare Fe@Au NPs showed a size of 68 ± 1 nm and were found to be superparamagnetic (negligible remanence and coercivity, saturation magnetization ~ 12emu/g at room temperature) in accordance with the results reported in Paper I. A high zeta potential of -27± 1 mV (Figure 6.23 (b)) rendered stability to these NPs in aqueous medium. An increase in size was observed for the coated Fe@Au NPs when compared to the uncoated ones (Figure 6.23 (a)). This supports successful coating of Fe@Au NPs for all the polymers used here. Fe@Au_PEG_Microgel shows a drastic increase in size in comparison to the other samples. Microgel refers to pNIPAm_AAc gels synthesized in Paper III.[XI] This is primarily due to the arrangement of the Fe@Au NPs that act as bridge molecules between the microgel units as has

[XI] The abbreviations pNIPAM and PNIPAAM are interchangable in this sub-section owing to different abbreviations used during the development of different manuscripts.

been reported in Paper III. On the other hand, in case of the other systems, the respective polymer adsorbs to the Fe@Au NPs either via charge based interactions or non-specific interactions.

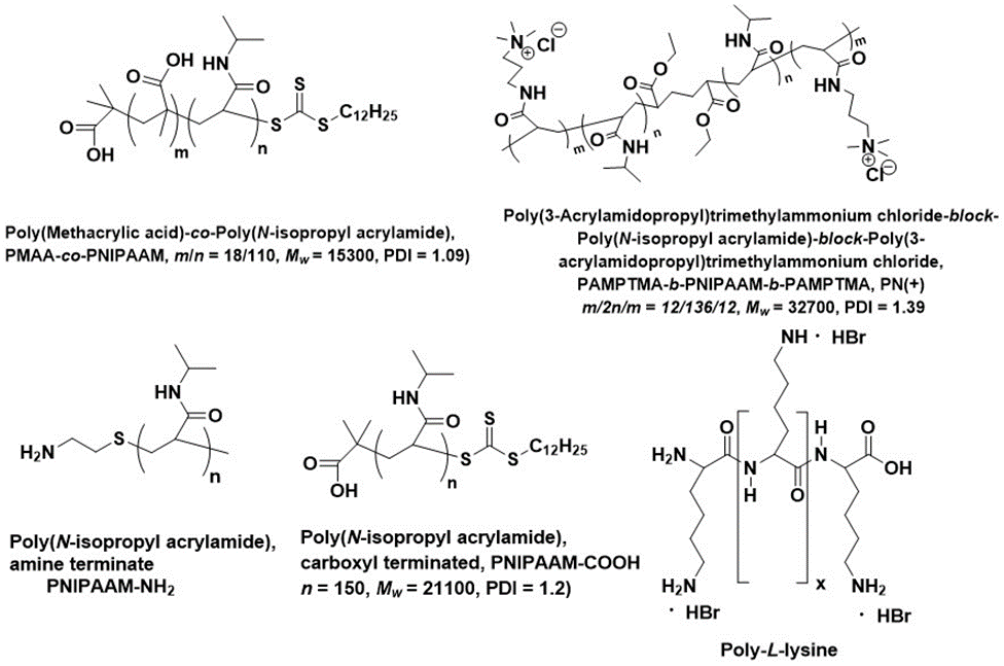

Figure 6.22 Chemical structures, molecular weights and polydispersities of synthesized and commercial polymers applied in this study.

The increase in size was accompanied by a decrease in zeta potential, for the Fe@Au NPs coated with Bovine serum albumin (BSA), PEG and microgel. This happens following redistribution of the surface charges while the total charge in the system remains conserved. On the other hand, the Fe@Au NPs coated with cationic polymers, PN(+), PNIPAAM-NH_2 and Poly-L-lysine showed an increase in the zeta potential. This stems from charge density matching between the negatively charged Au surface and the cationic polymers. Coating with PMAA-co-PNIPAAM also showed an increase in the zeta potential that can be traced back to charge density matching. Although, PNIPAAM-COOH and PMAA-co-PNIPAAM both showed negative surface charges in water phase, the change in zeta potential of the Fe@Au coated with the respective polymers followed an opposite trend. This could be either due to different contact points between the polymer and the citrate on the Au surface or a different

charge density matching owing to differences in molecular weights and thus different surface conformations of the two polymers.

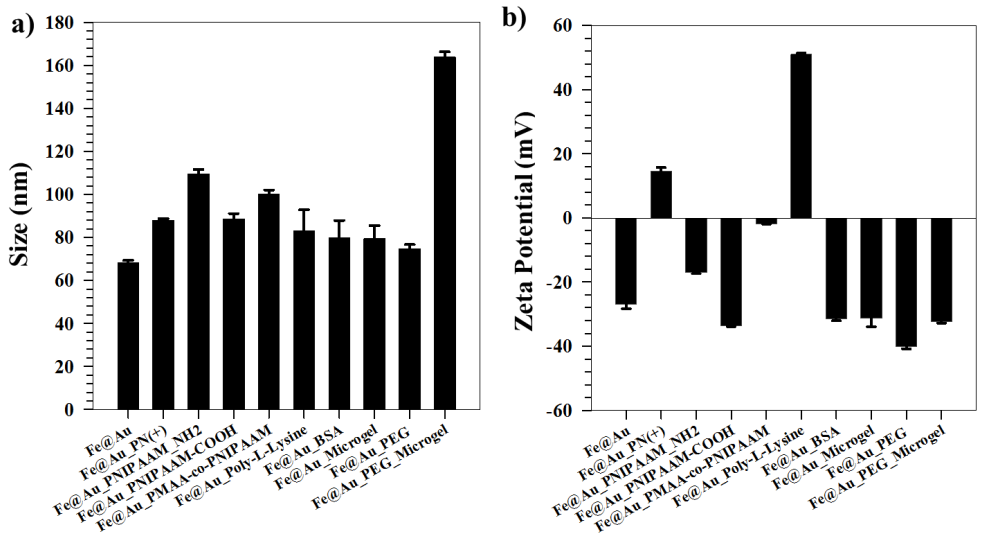

Figure 6.23 (a) Hydrodynamic sizes of both bare and coated Fe@Au NPs. (b) Zeta potentials of both bare and coated Fe@Au NPs.

Fe@Au NPs showed characteristic LSPR signature at 524 nm. Upon coating of the Fe@Au NPs with PEG, a bathochromic red shift was obtained (527 nm), proving a successful coating of the Fe@Au NPs with PEG, as has been reported in Paper I. Upon coating with microgel, a blue shift of the LSPR peak to 523 nm was observed (Figure 6.27(a)). This is primarily because of high water swelling capacity of the microgels that absorb water from the immediate vicinity of the Fe@Au NPs, leading to a more hydrophobic environment around the NPs. However, if PEG coating was followed by microgel coating, the LSPR peak shifted to 527nm, resembling a similar LSPR position as in case of Fe@Au_PEG, which is in agreement with the hypothesized surface water extraction. The Fe@Au NPs were found to be located in between the microgel particles, forming interconnecting bridges. With an increase in temperature, the microgel units collapse, causing a shrinking of the microgel volume. However, the cross-linking Fe@Au NPs pull together the gelling units as shown in Figure 6.27(b). This leads to an apparent increase in the size of Fe@Au_Microgel as a function of increasing temperature as also observed in Paper III. This is further supported by DLS results which show that the Fe@Au_Microgel system swelled when heated from 25 ^{0}C to 40 ^{0}C (Figure 6.27(e)).

The temperature dependent swelling-collapse for both the microgel systems were captured using DLS (Figure 6.27(c), (d)). Fe@Au_Microgel showed a 15% higher volumetric swelling compared to Fe@Au_PEG_Microgel, owing to incorporation of PEG molecules in the latter case. This is due to decreased net dipole moment of PEG with increasing temperature, leading to a more hydrophobic behavior. [120] The presence of PEG aids in lowering the VPTT of this system (36.7 ± 0.6^0 C) compared to Fe@Au_Microgel (38.4 ± 0.4^0 C). The lowering of VPTT is guided by the entropy driven volumetric collapse of the microgel that presses out the water entrapped within the microgel structure. The elevated temperature causes a decrease in dipole moment and a concomitant increase in hydrophobicity of PEG. This aids in increasing the entropy change between the swollen and collapsed states, leading to lowering of thermal energy required to drive this process spontaneously ($\Delta G > 0$). The swelling-collapse behavior of Fe@Au_PEG_Microgel was found to be 90% more reversible as compared to Fe@Au_Microgel, indicated by their relative hysteresis areas of swelling ratio curves. The lower hysteresis in case of Fe@Au_PEG_Microgel is aided by the PEG units that are hydrophobic at higher temperatures. The increase in hydrophobicity of PEG with increasing temperature may be attributed to increased rotation of the bonds at higher temperature, thereby reducing the number of polar ethylene oxide conformations or due to reduced hydration of oxygen atoms in PEG. [130-133] This enables a uniform collapse of the hydrogel units, further aided by the PEG chains, that in turn reduce irreversible losses, when the system passes through the same state points during the cooling cycle. In addition, temperature does not cause substantial aggregation for the constituent Fe@Au or Fe@Au_PEG NPs, shown by their relatively constant sizes.(Figure 6.24 (e)). The negatively charged NPs also electrostatically stabilize the systems, further substantiated by high zeta potential values (Figure 6.24 (f)).

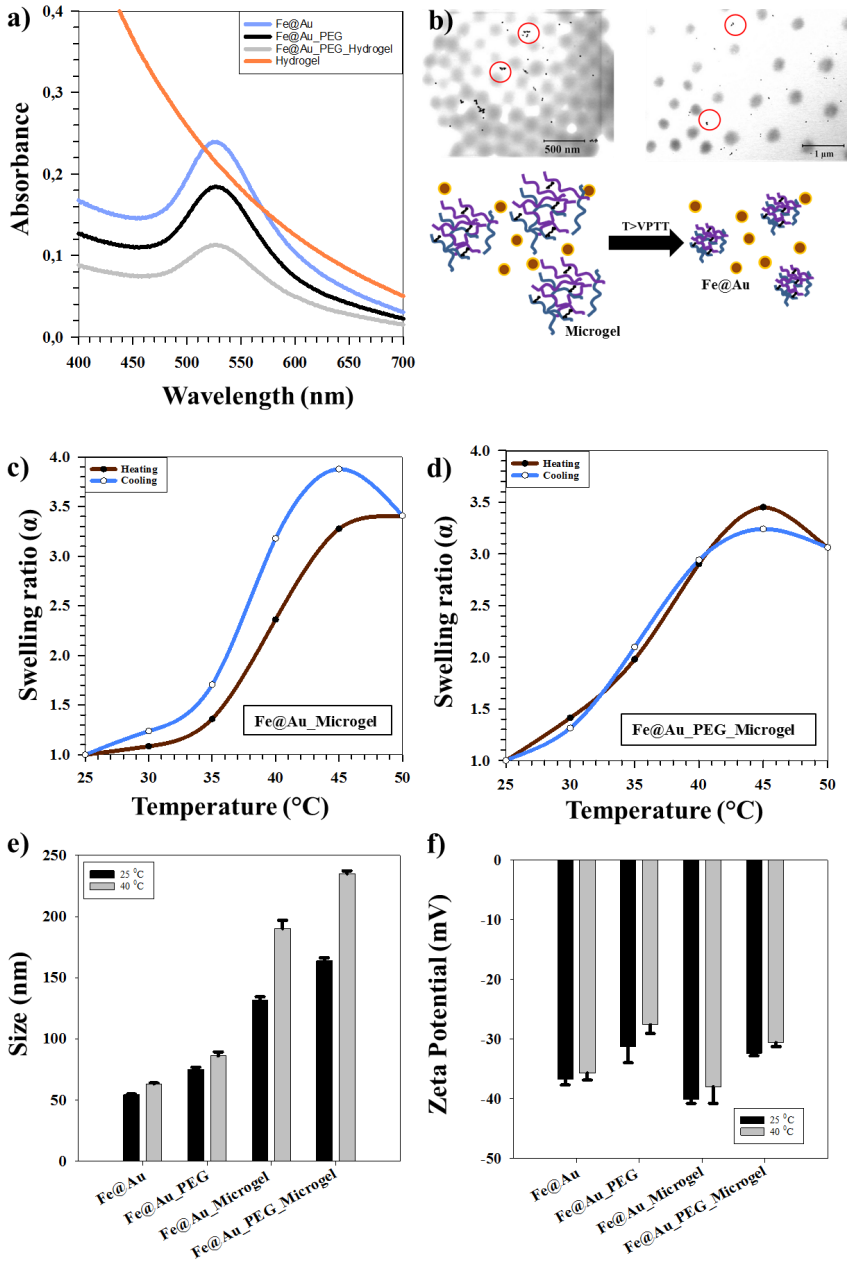

Figure 6.24 (a) Comparison of the UV-Vis spectra for the bare Fe@Au NPs with Fe@Au NPs coated with different polymers. (b) S(T)EM images of Fe@Au_Microgel at 25^0C and after heating it to 40^0C (top panel). Red circles indicate the location of Fe@Au NPs. Schematic showing the collapse of microgel units above VPTT, which are pulled together by the Fe@Au NPs. Variation of swelling ratios as a function of temperature of (c) Fe@Au_Microgel and (d) Fe@Au_PEG_Microgel. Variation of (g) Hydrodynamic sizes (nm) and (h) Zeta potentials (mV) of different Fe@Au coated systems at 25°C and 40°C.

Among all the systems studied, Fe@Au_Microgel, Fe@Au_PEG and Fe@Au_PEG_Microgel were observed to show the highest loading efficiencies for L-Dopa and hence, they were used for monitoring the release of L-Dopa at 40°C, pH 3.5 release conditions. Fe@Au_Microgel showed the highest release, delivering almost 87% of the loaded drug after 31 hours. Introduction of PEG causes hindrance in the release as seen from the release kinetics of both Fe@Au_PEG and Fe@Au_PEG_Microgel that released 56% and 29% over almost 60 and 55 hours, respectively (Figure 6.25 (a)). Although the loading efficiencies are comparable for the three systems, the hindered release from the PEG based systems can be attributed to stronger dipole-dipole interactions between the carboxy group of PEG-SH and amino group of L-Dopa. This also explains why only a very small fraction of loaded L-Dopa is released, while a major fraction of it still remains tightly bound to the carrier. While comparing the release profiles of L-Dopa from Fe@Au coated with PN(+) (cationic) and PNIPAAM-COOH respectively, (Figure 6.25 (b)) it is observed that in either case, the release is hindered with respect to that from Fe@Au_Microgel. It should also be noted that the loading efficiencies in case of PN(+) and PNIPAAM-COOH samples are much lower than for the microgel.

The nature of transport of the drug in case of all the samples is that of Super Case II transport ($n>1$) except for Fe@Au_Microgel, where the release is representative of non-Fickian diffusion from thin films (Figure 6.25 (c), (d)). Super Case II transport refers to drug release as a result of both diffusion and relaxation of polymer chains, which happens for the aforementioned samples primarily because the polymer chains respond to temperature and pH over time as well. On the other hand, in case of Fe@Au_Microgel, the microgel chains collapse almost instantaneously as a function of temperature and/or pH resulting in a thin film conformation that releases the drug via non-Fickian diffusion. This also explains why this sample showed the highest release of L-Dopa over time, releasing almost 87% of the loaded drug.

The diffusional exponent results in addition to the release kinetics showed that drug- NP interaction and response of the polymeric coating to temperature and pH largely control both the drug release mechanism and the kinetics. This indicates that the choice of coating and modulation of release parameters can greatly influence the release kinetics of L-Dopa from Fe@Au NP systems. However, in this study, the effect of shape was not investigated. This was addressed in the next paper.

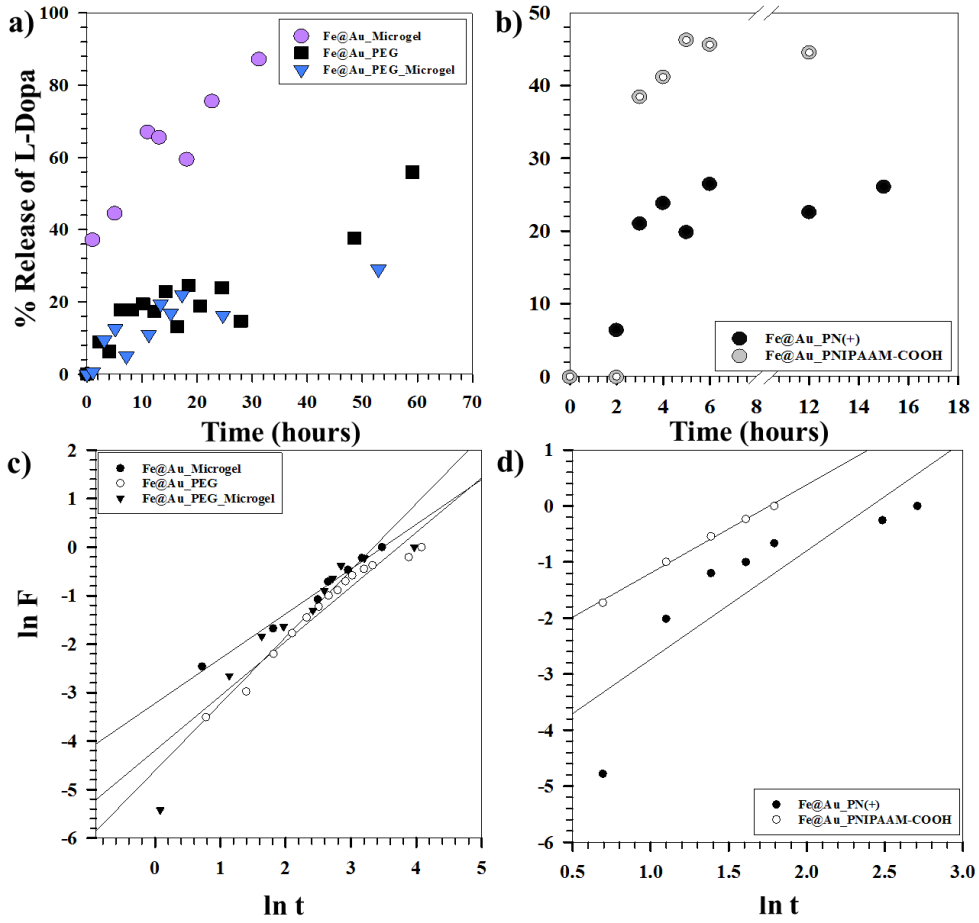

Figure 6.25 Release kinetics of L-Dopa at 40°C and pH 3.5 from (a) Fe@Au_Microgel, Fe@Au_PEG, Fe@Au_PEG_Microgel, (b) Fe@Au_PN(+) and Fe@Au_PNIPAAM-COOH respectively. Plots of ln F versus ln t for (c) Fe@Au_Microgel, Fe@Au_PEG, Fe@Au_PEG_Microgel, (d) Fe@Au_PN(+) and Fe@Au_PNIPAAM-COOH respectively.

6.3.2 Paper-VIII: Influence of different shaped Gold nanoparticles functionalized with NIPAm based hydrogels on the release of Cytochrome *C*.

Under Review in *The Journal of Physical Chemistry C.*

Having controlled the growth of Au NPs in Paper IV and optimized the synthesis of pNIPAm_AAc hydrogels in Paper III, the effect of anisotropy on the loading and release of Cyt *C* from hybrid systems was investigated in this paper. The main aim of this paper was to replace the cationic CTAB from the surfaces of the different shapes of Au NPs with PEG followed by coating with pNIPAm-AAc hydrogel, in an attempt to combine the optical properties of gold and the stimuli sensitive swelling-collapse properties of the hydrogel.

Five different shapes of AuNPs namely; spheres (AuNS), rods (AuNR), tetrahexahedral (AuHex), bipyramids (AuBP), and nano*makura* (AuNM) were synthesized following the method reported in Paper V. Among the NPs studied, the smallest NPs were the NRs, namely AuNR, having a hydrodynamic size of 14.4 ± 0.7 nm. The DLS results further showed that the sizes of other anisotropic NPs decreased in the order hexagonal, bipyramids and nanomakura respectively (AuHex > AuBP > AuNM). However, the hydrodynamic sizes when compared to the S(T)EM analysis, showed that the largest NPs were the bipyramids (length: 382 ± 107, diameter: 107 ± 45) while the smallest were the spherical NPs (AuNS) having a size of 17 ± 2 nm. The differences can be attributed to measurement principles and the diameters being reported. Table 6-2 shows the sizes of the different AuNPs measured using S(T)EM and DLS. It can be observed that the anisotropic NPs showed larger sizes compared to the DLS hydrodynamic sizes, while the size of the spherical NPs showed close agreement with their hydrodynamic radii. The slight increase in the DLS size is observed due to measurements of different diameters (DLS measures hydrodynamic radius while S(T)EM measures dry radius), due to DLS measuring the hydrodynamic radius rather than the core radius of the NPs as measured by S(T)EM, a weak interparticle dipolar interaction among NPs causing weak interparticle coupling, or a combination, as reported previously [119].

The A.R of AuNRs (3.4 ± 0.5) was comparable to that of AuBPs (3.8 ± 0.5), although their sizes differed considerably. A similar trend was noted for AuHex and AuNM having ARs 1.4 ± 0.2 and 1.5 ± 0.4 respectively. These variations in sizes were in accordance to the results obtained in Paper V.

Table 6-2 Differences in the sizes of Au NPs obtained from S(T)EM and DLS measurements.

AuNPs	A.R. (avg ± std. dev.)	S(T)EM size (nm) Length/width	DLS size (nm)
AuNR	3.4 ± 0.5	41.8 ± 4.1 /12.6 ± 1.5	14.4 ± 0.7
AuHex	1.4 ± 0.2	232.6 ± 24.6 / 170.7 ± 20.1	164.8 ± 5.6
AuBP	3.8 ± 0.5	381.7 ± 106.8 / 106.5 ± 45.3	144.9 ± 1.1
AuNM	1.5 ± 0.4	117.7 ± 14.8 / 83.2 ± 13.6	97.4 ± 2.4
AuNS	-	17.2 ± 2.2	22.5 ± 0.4

The CTAB layer was subsequently reduced by sequential coating with PEG followed by pNIPAm-AAc hydrogel, both the functionalization steps were optimized with respect to size and zeta potential measurements. Figure 6.26 shows the S(T)EM images of bare Au NPs and PEG-hydrogel coated NPs. In Paper III, it was shown that NPs reside on the periphery of the hydrogel units and act as cross-linkers, pulling the hydrogel matrix closer. The cross-linking density accounted for in such systems depends on the size, shape, particle number, surface functionalization among other factors. Herein, it was observed that all the different shaped AuNPs were located peripherally with respect to the hydrogel units for all the systems. It was also observed that higher number of particles for AuNS, AuNR and AuNM cross-linking the gelling units, while fewer and bigger AuBP and AuHex acted as bridge molecules connecting the gelling units.

Figure 6.27 (b)-(e) show the changes in UV-Vis spectra for AuNR, AuHex, AuBP, AuNM and AuNS respectively, upon coating with PEG (0.5 mg/ml) followed by hydrogel (3.3 mg/ml). while Figure 6.27 (a) shows the UV-Vis spectra for the CTAB coated Au NPs. AuNS showed a bathochromic shift from 523 nm to 529 nm upon coating with PEG, that induces a hydrophilic environment around the NPs as has been shown before [119]. However, upon coating with hydrogel, the LSPR peak blue shifted (524 nm) due to absorption of water from the NP surrounding by the hydrogel, leading to a relatively water deficient surrounding in immediate vicinity of the NPs. In case of the anisotropic NPs, blue shift in the LSPR maxima was observed after both PEG as well as hydrogel coating. A hypsochromic shift in the LSPR maximum upon PEG coating may be attributed to gradual replacement of the CTAB bilayer with PEG, leading to uneven coating of PEG due to shape anisotropy. In addition, different coating densities on

different facets of the anisotropic NPs, different conformations of the hydrogel guided by different shapes of the AuNPs or a combination of both also explain the shift. On subsequent coating with hydrogel, the observed blue shift is most likely due to water absorption properties of the hydrogel leading to decreased water content adjacent to the AuNPs as observed for the spherical NPs as well.

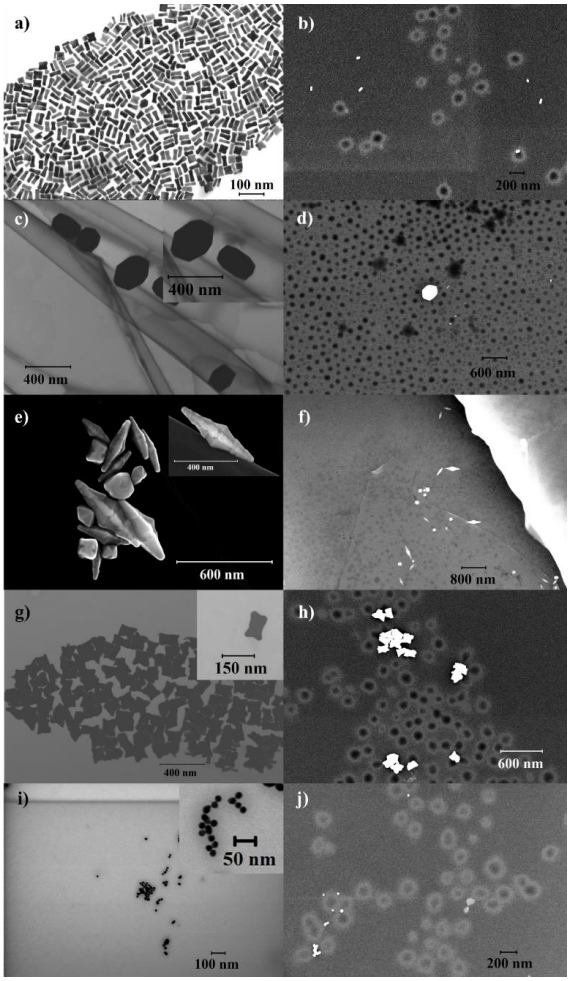

Figure 6.26 S(T)EM images of a) AuNR, b) PEG-hydrogel coated AuNR, c) AuHex, d) PEG-hydrogel coated AuHex, e) AuBP, f) PEG-hydrogel coated AuBP, g) AuNM, h) PEG-hydrogel coated AuNM, i) AuNS and j) PEG-hydrogel coated AuNS.

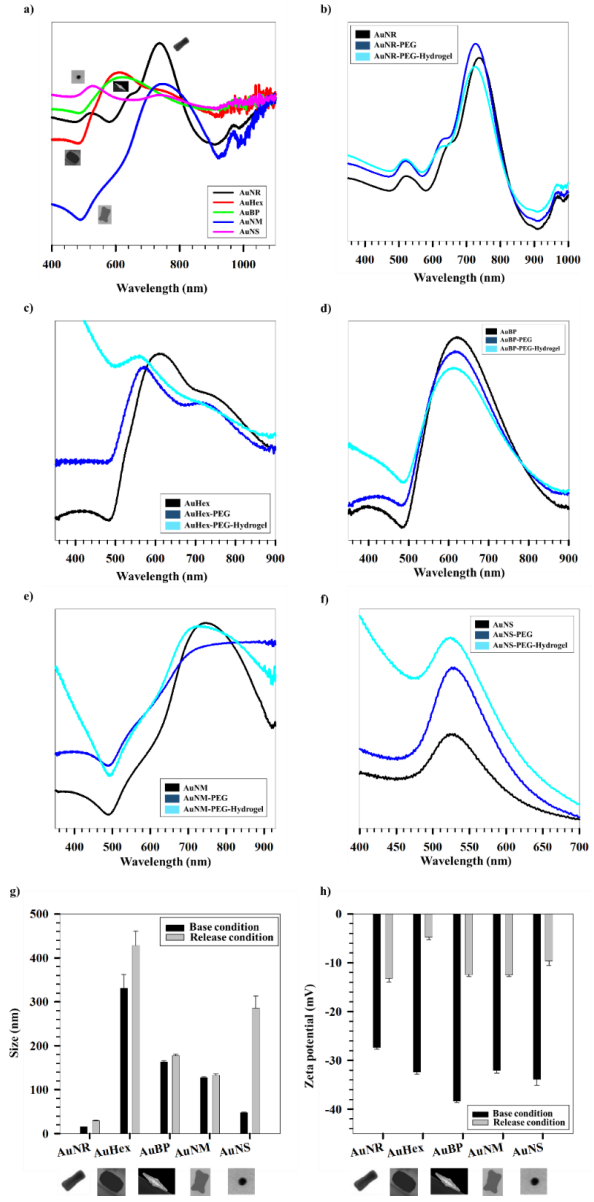

Figure 6.27 a) UV-Vis spectra for different shaped AuNPs. Variation of UV-Vis spectra after coating with PEG followed by hydrogel coating for b) AuNR, c) AuHex, d) AuBP, e) AuNM and f) AuNS. Variation of g) hydrodynamic sizes and h) zeta potentials of different shaped AuNPs measured at base and release conditions respectively.

DLS and zeta potential measurements performed for all the samples at base conditions (room temperature and pH at synthesis conditions) and at release conditions (40^{O}C, pH 3) as shown in Figure 6.27 (g) and (h) respectively show a swelling collapse behavior of the PEG-hydrogel coated AuNPs. AuNS showed the maximum swelling efficiency of ~ 99%, which is defined as the ratio of the volume change of the NPs between the base and release conditions to the volume at release condition. The VPTT of the pNIPAm-AAc hydrogels used in this study has been previously reported as 39^{O}C in Paper III. The individual hydrogel units thereby collapse under release conditions as a result of the combined effect of temperature and pH. However, these collapsed hydrogel blocks are pulled together by bridging AuNPs of different shapes. As evidenced from the S(T)EM images (Figure 6.26), several hydrogel units are bridged by few large particles (AuBP and AuHex), whereas these units are cross-linked by larger number of smaller NPs (AuNS, AuNR and AuNM), resulting in higher flexibility of the collapsing network. This is exhibited in high swelling efficiencies of the smaller NPs.

Hydrogel-PEG coated AuNPs were loaded with model protein drug, Cyt *C*, using modified breathing in method. All the systems showed high loading efficiencies (L.E. ~ 80%) for higher hydrogel concentration (Figure 6.28 (a), (b)). An immediate effect on the L.E. was observed upon decreasing the hydrogel concentration to 1.7 mg/ml. AuNR, AuHex and AuNS showed L.E. ~ 40%, whereas L.Es. of AuBP and AuNM remained unchanged. This is mostly explained as loading of Cyt *C* into hydrogel-PEG coated AuNPs takes place primarily via interaction between Cyt *C* and the hydrogel units.

Figure 6.28 (c) and (d) show the Cyt *C* release profiles from different AuNP systems with 1.7 and 3.3 mg/ml hydrogel coating respectively, release being measured via time dependent dialysis using UV-Vis spectroscopy. Upon increasing the hydrogel concentration used for coating the AuNPs, an enhanced release of Cyt *C* was observed for AuNR, AuHex and AuNS. On the other hand, no substantial change in the release percentage of Cyt *C* was evidenced for AuBP and AuNM. The release percentages followed the same order as L.E.s, indicating diffusion based released governed by Cyt *C* concentration gradient. However, when comparing the release profiles of AuNR and AuBP at higher hydrogel concentration (both having same L.Es.), a formidable increase in release percentage was seen for AuBP. This may be attributed to the larger sizes of AuBP in addition to lower particle numbers, when compared to AuNR, leading to greater porosity for drug diffusion out of the matrix. A similar trend was noted for AuNS and AuHex, the latter (highest L.E.) showing the maximum release percentage among all the systems studied. Although the L.E of AuNM was comparable to that of AuNS (particle

numbers higher than that of AuNM), the AuNS act as efficient cross-linkers owing to their smaller sizes, pulling closer the collapsing hydrogel units. This creates higher porosity in the matrix enabling more drug to escape into the release medium. Thus, the release of Cyt *C* from the AuNPs is guided by their sizes, shapes, particle concentrations and efficiencies in acting as cross linkers among the hydrogel units under release conditions among other parameters.

Figure 6.28 (e) and (f) show the variations of rate constants and release exponents respectively for all the AuNP systems, measured at different time intervals throughout the release of Cyt *C*. The release domains for AuNR, AuHex and AuNS were divided into two time regimes (Part-I and Part-II), whereas for AuBP and AuNM, they were divided into three time regimes (Part-I, Part-II and Part-III) based on distinguishably different release zones over these time regimes. On fitting the data to different rate models, the systems showed a best fit with zero order release kinetics. A decrease in the rate constant can be observed in all the five AuNP systems with an increase in time. This is interpreted in terms of a temporal decrease in concentration gradient of the drug inside the hydrogel-PEG coated AuNPs and the bulk of the release medium. This determines the driving force for the diffusion of Cyt *C* out of the hydrogel matrix.

Peppas' equation, which relates the log of cumulative fraction of drug released (F) with time to the log of time [134], was used to determine the release geometry followed by different AuNP systems. It can be observed that all the AuNPs followed a spherical/cylindrical geometry in the first phase of release which transformed into thin film over time. This is indicated by a temporal transition of the release exponent (n), obtained from regression analysis of ln F versus ln t plots (Supporting Information), from values close to 1 to values higher than 1. At the onset of release, the hydrogel-PEG coated AuNPs behave mostly as spherical units, squeezing out the drug, owing to collapse of the individual hydrogel units. The rate of collapse of the hydrogel units is retarded by the presence of inorganic NPs in the matrix, due to cross-linking effect provided by the AuNPs. This effect is dependent on the shape, size and particle numbers and determines how effectively the spherical/cylindrical to thin film transition will happen. Higher values of release exponent (>1) indicate Super Case-II transport of Cyt *C*, a mode of drug release that combines diffusion controlled and visco-elastic relaxation controlled drug release [102, 135].

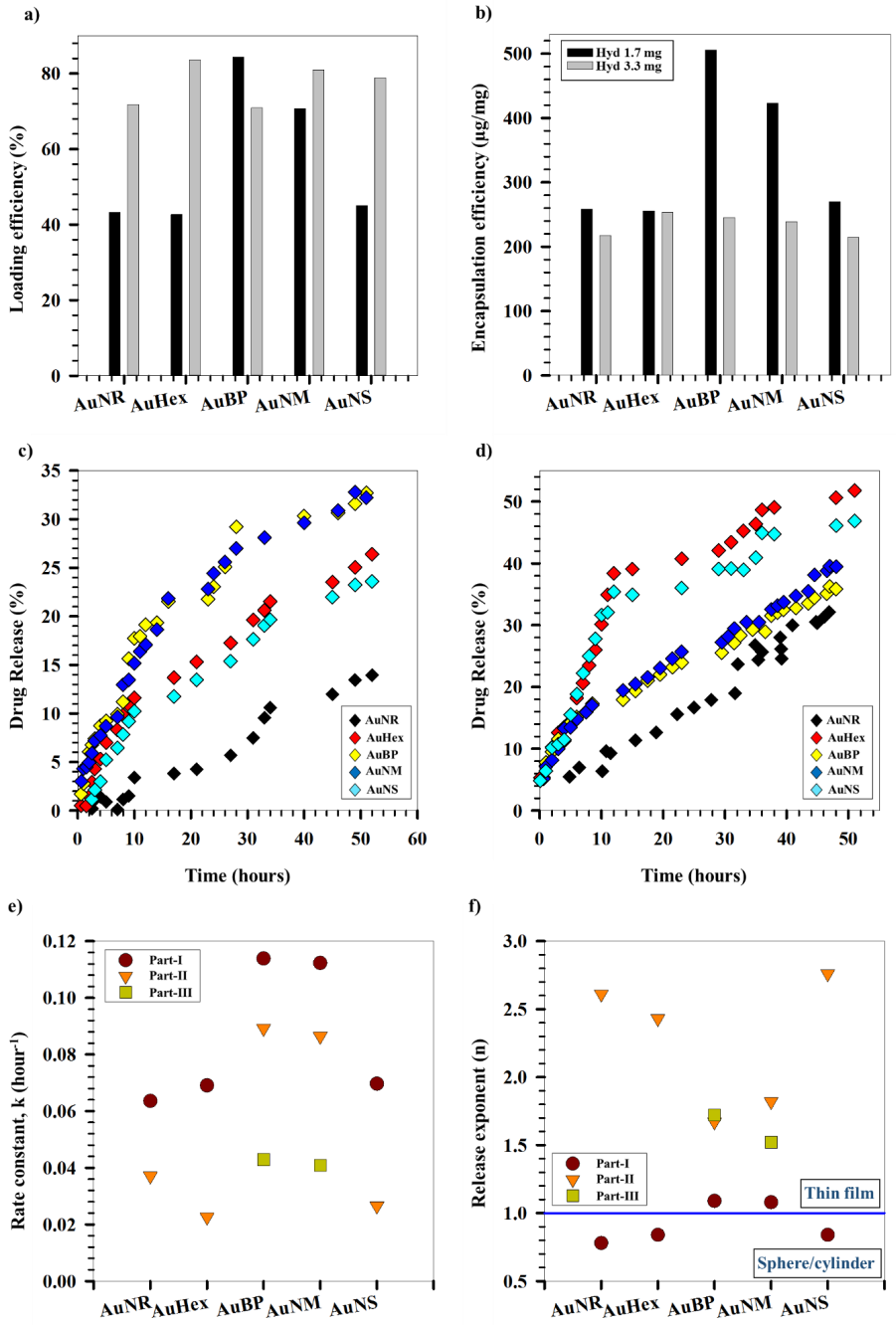

Figure 6.28 a) Loading and b) Encapsulation efficiencies for different shaped AuNPs for two different hydrogel concentrations. Release kinetics of Cyt *C* from different shaped AuNPs for c) 1.7 mg/ml and d) 3.3 mg/ml hydrogel concentrations respectively. e) Rate constants and f) release exponents for Cyt *C* release from different shaped AuNPs.

Thus, we observe that upon combining metallic Au NPs and polymeric pNIPAm-AAc hydrogels, we are able to incorporate both optical and stimuli sensitive properties into the nanoconstructs. Further, AuNP shape, size, number density and hydrogel content were found to influence the loading as well as release kinetics of Cyt *C* from these systems.

7 Conclusions and Future Work

This thesis has focused on two different kinds of nanomaterials, namely metallic NPs that possess remarkable optical and magnetic properties and stimuli sensitive pNIPAm based hydrogels which show temperature and/or pH dependent swelling-collapse behaviour. These NPs have been functionalized with different moieties in order to tune them for drug delivery applications, finally culminating in hybrid NPs formed by a combination of metallic and polymeric NPs.

Paper I has shown that it is possible to grow a crystalline Au shell on superparamagnetic Fe NPs using a solution based synthetic approach, whereby combining the optical and magnetic properties from the shell and core respectively. PEGylated Fe@Au NPs were further shown to have no appreciable cytotoxic effects on two different cell types (OECs and hNSCs), proving them as promising candidates for biomedical applications.

The next Paper was directed towards understanding growth of anisotropic Au NWs in order to control their optical properties. CTAB templated seed-mediated growth protocol was used in this work. The study gave us a fundamental understanding regarding how the nature of the seed plays an important role in the growth mechanism, and hence in the final products obtained. However, it was desired to generalize our understanding for the growth mechanisms governing the synthesis of anisotropic Au NPs of various shapes and sizes, while using the same method of synthesis. The motivation for Paper III was thus to investigate the effects of surfactant mole ratios, pH of the growth solution, hallide ion concentration, seed concentration, reducing agent concentration on the growth of anisotropic Au NPs. An important conclusion from the investigation was that DDAB is the most suitable co-surfactant allowing the tunability in the micellar structure to obtain Au NPs in different shapes and sizes. In addition, DDAB facilitates the formation of zero-dimensional structures, while CTAB assists in one-dimensional rod like structures. Using the method from Paper III, five different shapes of Au NPs, including nano*makura* (reported for the first time) were synthesized. The cationic CTAB on the surfaces of Au NPs was replaced subsequently with PEG and MUA. Thereafter, nano*makura* Au was shown to have cytotoxic effects on GA cancer cells, rendering its applicability in hyperthermia and drug delivery to cancer cells, while being simultaneously imaged.

With an attempt to exploit the temperature and pH sensitive properties of pNIPAm based NGs, the synthesis of pNIPAm-AAc colloidal gels using precipitation polymerization was optimized in Paper III. The effect of the surfactant SDS was found to be the most crucial factor in

controlling their sizes. Fe@Au NPs synthesized in Paper I were incorporated into the NG networks using two different methods- coating and *in-situ* growth (Fe@Au_NG_c and Fe@Au_NG_i respectively). Fe@Au_NG_i were found to behave similarly to the bare NGs, while the Fe@Au_NG_c resembled the characteristics of the bare Fe@Au NPs. Further, Fe@Au_NG_c showed remarkably rapid release kinetics for model protein drug Cyt *C* under the influence of acidic pH and temperature above the VPTT of the collapsing gels. Further understanding of VPTTs of such swelling-collapse systems was dealt with in Paper VI. In this work, a methodology was developed to determine the VPTTs of phase changing systems, based on measurement of a parameter (here, hydrodynamic size) that varies with temperature. The methodology was applied on different systems synthesized during the thesis work to compare the VPTTs obtained using our method and those reported previously. A novel reversibility parameter was further defined and is being reported here for the first time, that takes into account all the state points through which the system passes through, in comparison to previous studies which base it on the system end points alone.

Papers VII and VIII dwelt on hybrid NPs, formed by coating Fe@Au NPs and anisotropic Au NPs with pNIPAm-AAc microgels respectively. The physico-chemical properties of these hybrid Fe@Au NPs were optimized leading to loading of L-Dopa in these systems. Highest release of L-Dopa was obtained for the pNIPAm-AAc coated Fe@Au NPs. This is ascribed to a collapse of the microgel units above VPTT, followed by cross-linking effect of the Fe@Au NPs, pulling together the gelled units. On the other hand, the role of shape on loading and release characteristics of Cyt-C from Au NPs incorporated into pNIPAm-AAc microgels was investigated in Paper VIII. Results showed that AuNP shape, size, particle number density and microgel content are found to influence the loading as well as release kinetics.

The current work has shown that combination of nanomaterials leads to enhancement of physico-chemical properties stemming from the counterparts. Although, some of the studies have concentrated to explore the growth mechanism of anisotropic NPs, future work can use techniques like UV-Vis spectroscopy, cryo-TEM in combination with numerical simulations to map out the kinetics of growth. In addition, the robust methodology developed for VPTT determination should be expanded for systems already in use to understand the predictive capability of the reversibility parameter. Further, studies can be concerted towards loading multiple drugs in the hybrid systems discussed here, with an aim to tune their release in response to different stimuli for different drug. These can prove important candidates for

delivery of both hydrophobic and hydrophilic components from multi-stimuli responsive theranostic nanocarriers.

8 Bibliography

1. Howes, P.D., R. Chandrawati, and M.M. Stevens, *Colloidal nanoparticles as advanced biological sensors.* Science, 2014. **346**(6205): p. 53-+.
2. Alex, S. and A. Tiwari, *Functionalized Gold Nanoparticles: Synthesis, Properties and Applications-A Review.* Journal of Nanoscience and Nanotechnology, 2015. **15**(3): p. 1869-1894.
3. Ma, X.W., Y.L. Zhao, and X.J. Liang, *Theranostic Nanoparticles Engineered for Clinic and Pharmaceutics.* Accounts of Chemical Research, 2011. **44**(10): p. 1114-1122.
4. Mitragotri, S., et al., *Accelerating the Translation of Nanomaterials in Biomedicine.* Acs Nano, 2015. **9**(7): p. 6644-6654.
5. Ferrari, M., *Nanovector therapeutics.* Current Opinion in Chemical Biology, 2005. **9**(4): p. 343-346.
6. Daniel, M.C. and D. Astruc, *Gold nanoparticles: Assembly, supramolecular chemistry, quantum-size-related properties, and applications toward biology, catalysis, and nanotechnology.* Chemical Reviews, 2004. **104**(1): p. 293-346.
7. G, C., *Nanostructures and Nanomaterials: Synthesis, Properties and Applications*. 2004: Imperial College Press.
8. Wu, Z.H., S.L. Yang, and W. Wu, *Shape control of inorganic nanoparticles from solution.* Nanoscale, 2016. **8**(3): p. 1237-1259.
9. Kashchiev, D. and G.M. van Rosmalen, *Review: Nucleation in solutions revisited.* Crystal Research and Technology, 2003. **38**(7-8): p. 555-574.
10. Mullin, J.W., *Crystallization*. 2001: Elsevier Butterworth-Heinemann.
11. Cao, Z., *Nanostructures and Nanomaterials Synthesis, Properties & Applications*. 2004: Imperial College Press.
12. Chang, J. and E.R. Waclawik, *Colloidal semiconductor nanocrystals: controlled synthesis and surface chemistry in organic media.* Rsc Advances, 2014. **4**(45): p. 23505-23527.
13. Khlebtsov, N. and L. Dykman, *Biodistribution and toxicity of engineered gold nanoparticles: a review of in vitro and in vivo studies.* Chemical Society Reviews, 2011. **40**(3): p. 1647-1671.
14. Dykman, L. and N. Khlebtsov, *Gold nanoparticles in biomedical applications: recent advances and perspectives.* Chemical Society Reviews, 2012. **41**(6): p. 2256-2282.
15. Petryayeva, E. and U.J. Krull, *Localized surface plasmon resonance: Nanostructures, bioassays and biosensing-A review.* Analytica Chimica Acta, 2011. **706**(1): p. 8-24.
16. Willets, K.A. and R.P. Van Duyne, *Localized surface plasmon resonance spectroscopy and sensing.* Annual Review of Physical Chemistry, 2007. **58**: p. 267-297.
17. Mayer, K.M. and J.H. Hafner, *Localized Surface Plasmon Resonance Sensors.* Chemical Reviews, 2011. **111**(6): p. 3828-3857.
18. Link, S. and M.A. El-Sayed, *Shape and size dependence of radiative, non-radiative and photothermal properties of gold nanocrystals.* International Reviews in Physical Chemistry, 2000. **19**(3): p. 409-453.
19. Mulvaney, P., *Surface plasmon spectroscopy of nanosized metal particles.* Langmuir, 1996. **12**(3): p. 788-800.
20. Okamoto, H. and K. Imura, *Near-field imaging of optical field and plasmon wavefunctions in metal nanoparticles.* Journal of Materials Chemistry, 2006. **16**(40): p. 3920-3928.
21. Jain, P.K., et al., *Noble Metals on the Nanoscale: Optical and Photothermal Properties and Some Applications in Imaging, Sensing, Biology, and Medicine.* Accounts of Chemical Research, 2008. **41**(12): p. 1578-1586.
22. Dreaden, E.C. and M.A. El-Sayed, *Detecting and Destroying Cancer Cells in More than One Way with Noble Metals and Different Confinement Properties on the Nanoscale.* Accounts of Chemical Research, 2012. **45**(11): p. 1854-1865.
23. Eustis, S. and M.A. El-Sayed, *Why gold nanoparticles are more precious than pretty gold: Noble metal surface plasmon resonance and its enhancement of the radiative and nonradiative properties of nanocrystals of different shapes.* Chemical Society Reviews, 2006. **35**(3): p. 209-217.

24. Hulteen, J.C. and C.R. Martin, *A general template-based method for the preparation of nanomaterials.* Journal of Materials Chemistry, 1997. **7**(7): p. 1075-1087.
25. Kim, F., J.H. Song, and P.D. Yang, *Photochemical synthesis of gold nanorods.* Journal of the American Chemical Society, 2002. **124**(48): p. 14316-14317.
26. Gole, A. and C.J. Murphy, *Seed-mediated synthesis of gold nanorods: Role of the size and nature of the seed.* Chemistry of Materials, 2004. **16**(19): p. 3633-3640.
27. Sau, T.K. and C.J. Murphy, *Room temperature, high-yield synthesis of multiple shapes of gold nanoparticles in aqueous solution.* Journal of the American Chemical Society, 2004. **126**(28): p. 8648-9.
28. Jana, N.R., *Gram-scale synthesis of soluble, near-monodisperse gold nanorods and other anisotropic nanoparticles.* Small, 2005. **1**(8-9): p. 875-882.
29. Ye, X.C., et al., *Using Binary Surfactant Mixtures To Simultaneously Improve the Dimensional Tunability and Monodispersity in the Seeded Growth of Gold Nanorods.* Nano Letters, 2013. **13**(2): p. 765-771.
30. Lai, J.P., et al., *One-pot synthesis of gold nanorods using binary surfactant systems with improved monodispersity, dimensional tunability and plasmon resonance scattering properties.* Nanotechnology, 2014. **25**(12).
31. Ye, X.C., et al., *Seeded Growth of Monodisperse Gold Nanorods Using Bromide-Free Surfactant Mixtures.* Nano Letters, 2013. **13**(5): p. 2163-2171.
32. Singh, G., et al., *Synthesis of Au nanowires with controlled morphological and structural characteristics.* Applied Surface Science, 2014. **311**: p. 780-788.
33. Sau, T.K. and C.J. Murphy, *Seeded high yield synthesis of short Au nanorods in aqueous solution.* Langmuir, 2004. **20**(15): p. 6414-20.
34. Nikoobakht, B. and M.A. El-Sayed, *Preparation and growth mechanism of gold nanorods (NRs) using seed-mediated growth method.* Chemistry of Materials, 2003. **15**(10): p. 1957-1962.
35. Grzelczak, M., et al., *Shape control in gold nanoparticle synthesis.* Chemical Society Reviews, 2008. **37**(9): p. 1783-1791.
36. Lohse, S.E. and C.J. Murphy, *The Quest for Shape Control: A History of Gold Nanorod Synthesis.* Chemistry of Materials, 2013. **25**(8): p. 1250-1261.
37. Herrero, E., L.J. Buller, and H.D. Abruna, *Underpotential deposition at single crystal surfaces of Au, Pt, Ag and other materials.* Chemical Reviews, 2001. **101**(7): p. 1897-1930.
38. Liu, M.Z. and P. Guyot-Sionnest, *Mechanism of silver(I)-assisted growth of gold nanorods and bipyramids.* Journal of Physical Chemistry B, 2005. **109**(47): p. 22192-22200.
39. Wang, Z.L., et al., *Surface reconstruction of the unstable {110} surface in gold nanorods.* Journal of Physical Chemistry B, 2000. **104**(23): p. 5417-5420.
40. Glover, R.D., J.M. Miller, and J.E. Hutchison, *Generation of Metal Nanoparticles from Silver and Copper Objects: Nanoparticle Dynamics on Surfaces and Potential Sources of Nanoparticles in the Environment.* Acs Nano, 2011. **5**(11): p. 8950-8957.
41. Hubert, F., F. Testard, and O. Spalla, *Cetyltrimethylammonium bromide silver bromide complex as the capping agent of gold nanorods.* Langmuir, 2008. **24**(17): p. 9219-9222.
42. Pal, T., et al., *Organized media as redox catalysts.* Langmuir, 1998. **14**(17): p. 4724-4730.
43. Liu, X.H., et al., *A novel cetyltrimethyl ammonium silver bromide complex and silver bromide nanoparticles obtained by the surfactant counterion.* Journal of Colloid and Interface Science, 2007. **307**(1): p. 94-100.
44. Bréchignac C, H.P., Lahmani M., *Nanomaterials and Nanochemistry*. 2006.: Springer.
45. Hiemenz C.Paul, R.R., *Principles of Colloid and Surface Chemistry*.
46. Hubert, F., et al., *Growth and Overgrowth of Concentrated Gold Nanorods: Time Resolved SAXS and XANES.* Crystal Growth & Design, 2012. **12**(3): p. 1548-1555.
47. Almora-Barrios, N., et al., *Theoretical Description of the Role of Halides, Silver, and Surfactants on the Structure of Gold Nanorods.* Nano Letters, 2014. **14**(2): p. 871-875.
48. Sun C, J.S.H.L.b., Zhang M, *Magnetic nanoparticles in MR imaging and drug delivery.* Advanced Drug Delivery Reviews 2008. **60**: p. 1252–1265.
49. Xu, C.J. and S.H. Sun, *New forms of superparamagnetic nanoparticles for biomedical applications.* Advanced Drug Delivery Reviews, 2013. **65**(5): p. 732-743.

50. Krahne, R., et al., *Physical properties of elongated inorganic nanoparticles.* Physics Reports-Review Section of Physics Letters, 2011. **501**(3-5): p. 75-221.
51. Hervault, A. and N.T.K. Thanh, *Magnetic nanoparticle-based therapeutic agents for thermo-chemotherapy treatment of cancer.* Nanoscale, 2014. **6**(20): p. 11553-11573.
52. Cho, K.J., et al., *Therapeutic nanoparticles for drug delivery in cancer.* Clinical Cancer Research, 2008. **14**(5): p. 1310-1316.
53. Rao, J.P. and K.E. Geckeler, *Polymer nanoparticles: Preparation techniques and size-control parameters.* Progress in Polymer Science, 2011. **36**(7): p. 887-913.
54. Gradishar, W.J., et al., *Phase III trial of nanoparticle albumin-bound paclitaxel compared with polyethylated castor oil-based paclitaxel in women with breast cancer.* Journal of Clinical Oncology, 2005. **23**(31): p. 7794-7803.
55. Sabbatini, P., et al., *Phase II study of CT-2103 in patients with recurrent epithelial ovarian, fallopian tube, or primary peritoneal carcinoma.* Journal of Clinical Oncology, 2004. **22**(22): p. 4523-4531.
56. Bhatt, R.L., et al., *Synthesis and in vivo antitumor activity of poly(L-glutamic acid) conjugates of 20(S)-camptothecin.* Journal of Medicinal Chemistry, 2003. **46**(1): p. 190-193.
57. Kedar, U., et al., *Advances in polymeric micelles for drug delivery and tumor targeting.* Nanomedicine-Nanotechnology Biology and Medicine, 2010. **6**(6): p. 714-729.
58. Batrakova, E.V., et al., *Anthracycline antibiotics non-covalently incorporated into the block copolymer micelles: In vivo evaluation of anti-cancer activity.* British Journal of Cancer, 1996. **74**(10): p. 1545-1552.
59. Nakanishi, T., et al., *Development of the polymer micelle carrier system for doxorubicin.* Journal of Controlled Release, 2001. **74**(1–3): p. 295-302.
60. Boas, U. and P.M.H. Heegaard, *Dendrimers in drug research.* Chemical Society Reviews, 2004. **33**(1): p. 43-63.
61. Malik, N., E.G. Evagorou, and R. Duncan, *Dendrimer-platinate: a novel approach to cancer chemotherapy.* Anti-Cancer Drugs, 1999. **10**(8): p. 767-776.
62. Majoros, I.J., et al., *PAMAM Dendrimer-Based Multifunctional Conjugate for Cancer Therapy: Synthesis, Characterization, and Functionality.* Biomacromolecules, 2006. **7**(2): p. 572-579.
63. Yavuz, B., S.B. Pehlivan, and N. Unlu, *Dendrimeric Systems and Their Applications in Ocular Drug Delivery.* Scientific World Journal, 2013.
64. Hoffman, A.S., *Hydrogels for biomedical applications.* Advanced Drug Delivery Reviews, 2002. **54**(1): p. 3-12.
65. Nayak, S. and L.A. Lyon, *Soft Nanotechnology with Soft Nanoparticles.* Angewandte Chemie International Edition, 2005. **44**(47): p. 7686-7708.
66. Ahmed, E.M., *Hydrogel: Preparation, characterization, and applications: A review.* Journal of Advanced Research, 2015. **6**(2): p. 105-121.
67. Suzuki, A. and T. Tanaka, *Phase-Transition in Polymer Gels Induced by Visible-Light.* Nature, 1990. **346**(6282): p. 345-347.
68. Ghosh, S. and T. Cai, *Controlled actuation of alternating magnetic field-sensitive tunable hydrogels.* Journal of Physics D-Applied Physics, 2010. **43**(41).
69. Jones, C.D. and L.A. Lyon, *Synthesis and characterization of multiresponsive core-shell microgels.* Macromolecules, 2000. **33**(22): p. 8301-8306.
70. Chacko, R.T., et al., *Polymer nanogels: A versatile nanoscopic drug delivery platform.* Advanced Drug Delivery Reviews, 2012. **64**(9): p. 836-851.
71. Painter, P.C. and M.M. Coleman, *Essentials of polymer science and engineering*. 2008: DEStech Publications, Inc.
72. Schild, H.G., *Poly (N-Isopropylacrylamide) - Experiment, Theory and Application.* Progress in Polymer Science, 1992. **17**(2): p. 163-249.
73. Constantin, M., et al., *Lower critical solution temperature versus volume phase transition temperature in thermoresponsive drug delivery systems.* Express Polymer Letters, 2011. **5**(10): p. 839-848.

74. Bekhradnia, S., et al., *Structure, swelling, and drug release of thermoresponsive poly(amidoamine) dendrimer-poly(N-isopropylacrylamide) hydrogels.* Journal of Materials Science, 2014. **49**(17): p. 6102-6110.
75. Zhang, H. and J.C. Kim, *Hydroxyethyl Acrylate-Based Polymeric Amphiphiles Showing Lower Critical Solution Temperature.* Journal of Macromolecular Science Part a-Pure and Applied Chemistry, 2015. **52**(2): p. 138-146.
76. Fucinos, C., et al., *Temperature-and pH-Sensitive Nanohydrogels of Poly(N-Isopropylacrylamide) for Food Packaging Applications: Modelling the Swelling-Collapse Behaviour.* Plos One, 2014. **9**(2).
77. Nomura, K., et al., *Temperature-responsive copolymer brush constructed on a silica microparticle by atom transfer radical polymerization.* Colloid and Polymer Science, 2015. **293**(3): p. 851-859.
78. Spizzirri, U.G., et al., *Thermo-Responsive Albumin Hydrogels with LCST Near the Physiological Temperature.* Journal of Applied Polymer Science, 2011. **121**(1): p. 342-351.
79. Gao, X.Y., et al., *pH- and thermo-responsive poly(N-isopropylacrylamide-co-acrylic acid derivative) copolymers and hydrogels with LCST dependent on pH and alkyl side groups.* Journal of Materials Chemistry B, 2013. **1**(41): p. 5578-5587.
80. Zhang, H., *Controlled/"living" radical precipitation polymerization: A versatile polymerization technique for advanced functional polymers.* European Polymer Journal, 2013. **49**(3): p. 579-600.
81. Pelton, R., *Temperature-sensitive aqueous microgels.* Advances in Colloid and Interface Science, 2000. **85**(1): p. 1-33.
82. Wu, X., et al., *The Kinetics of Poly(N-Isopropylacrylamide) Microgel Latex Formation.* Colloid and Polymer Science, 1994. **272**(4): p. 467-477.
83. Siegel, R.A., *Pulsed and self-regulated drug delivery*

1990 CRC Press, Boca Raton, FL.
84. Ni, H., H. Kawaguchi, and T. Endo, *Preparation of pH-sensitive hydrogel microspheres of poly(acrylamide-co-methacrylic acid) with sharp pH-volume transition.* Colloid and Polymer Science, 2007. **285**(7): p. 819-826.
85. Smith, M.H. and L.A. Lyon, *Multifunctional Nanogels for siRNA Delivery.* Accounts of Chemical Research, 2012. **45**(7): p. 985-993.
86. Gan, J.Q., et al., *Biodegradable, thermoresponsive PNIPAM-based hydrogel scaffolds for the sustained release of levofloxacin.* Rsc Advances, 2016. **6**(39): p. 32967-32978.
87. Mieler, W.F., *Thermoresponsive hydrogels as a new ocular drug delivery platform to the posterior segment of the eye.* Trans Am Ophthalmol Soc, 2008. **106**: p. 206-214.
88. Li, J., et al., *A drug delivery hydrogel system based on activin B for Parkinson's disease.* Biomaterials, 2016. **102**: p. 72-86.
89. Ethayaraja M, B.R., *Model for Core-Shell nanoparticle Formation by Ion-Exchange Mechanism.* Ind. Eng. Chem. Res., 2008. **47**: p. 5982-5985.
90. Goodman, D.W., *Chemistry on monolayer metallic films.* Ultramicroscopy, 1990. **34**: p. 1-9.
91. Sahiner, N., S. Butun, and P. Ilgin, *Hydrogel particles with core shell morphology for versatile applications: Environmental, biomedical and catalysis.* Colloids and Surfaces A: Physicochemical and Engineering Aspects, 2011. **386**(1–3): p. 16-24.
92. Chaudhuri, R.G. and S. Paria, *Core/Shell Nanoparticles: Classes, Properties, Synthesis Mechanisms, Characterization, and Applications.* Chemical Reviews, 2012. **112**(4): p. 2373-2433.
93. Nadagouda, M.N. and R.S. Varma, *A Greener Synthesis of Core (Fe, Cu)-Shell (Au, Pt, Pd, and Ag) Nanocrystals Using Aqueous Vitamin C.* Crystal Growth & Design, 2007. **7**(12): p. 2582-2587.
94. Zeng, H. and S. Sun, *Syntheses, Properties, and Potential Applications of Multicomponent Magnetic Nanoparticles.* Advanced Functional Materials, 2008. **18**(3): p. 391-400.
95. Ethayaraja, M., Ravikumar, C., Muthukumaran, D., Dutta, K., Bandyopadhyaya, R., *CdS-ZnS core-shell nanoparticle formation: Experiment, mechanism, and simulation.* Journal of Physical Chemistry C 2007. **111**: p. 3246-3252

96. Jafari, T., A. Simchi, and N. Khakpash, *Synthesis and cytotoxicity assessment of superparamagnetic iron–gold core–shell nanoparticles coated with polyglycerol.* Journal of Colloid and Interface Science, 2010. **345**(1): p. 64-71.
97. Chen, D., et al., *Properties of Core−Shell Ni−Au Nanoparticles Synthesized through a Redox-Transmetalation Method in Reverse Microemulsion.* Chemistry of Materials, 2007. **19**(14): p. 3399-3405.
98. Nayak, S. and L.A. Lyon, *Soft nanotechnology with soft nanoparticles.* Angewandte Chemie-International Edition, 2005. **44**(47): p. 7686-7708.
99. Danhier, F., O. Feron, and V. Préat, *To exploit the tumor microenvironment: Passive and active tumor targeting of nanocarriers for anti-cancer drug delivery.* Journal of Controlled Release, 2010. **148**(2): p. 135-146.
100. Alberts, B., A. Johnson, and J. Lewis, *Molecular Biology of the Cell*. 2002, New York: Garland Science.
101. Langer, R. and N. Peppas, *Chemical and Physical Structure of Polymers as Carriers for Controlled Release of Bioactive Agents - a Review*. Journal of Macromolecular Science-Reviews in Macromolecular Chemistry and Physics, 1983. **C23**(1): p. 61-126.
102. Siepmann, J. and N.A. Peppas, *Higuchi equation: Derivation, applications, use and misuse.* International Journal of Pharmaceutics, 2011. **418**(1): p. 6-12.
103. Ritger, P.L. and N.A. Peppas, *A simple equation for description of solute release II. Fickian and anomalous release from swellable devices.* Journal of Controlled Release, 1987. **5**(1): p. 37-42.
104. Fu, Y. and W.J. Kao, *Drug release kinetics and transport mechanisms of non-degradable and degradable polymeric delivery systems.* Expert Opinion on Drug Delivery, 2010. **7**(4): p. 429-444.
105. Qin, J., et al., *Injectable Superparamagnetic Ferrogels for Controlled Release of Hydrophobic Drugs.* Advanced Materials, 2009. **21**(13): p. 1354-1357.
106. Wu, W.T., et al., *Core-shell hybrid nanogels for integration of optical temperature-sensing, targeted tumor cell imaging, and combined chemo-photothermal treatment.* Biomaterials, 2010. **31**(29): p. 7555-7566.
107. Zhang, D., et al., *A magnetic chitosan hydrogel for sustained and prolonged delivery of Bacillus Calmette-Guerin in the treatment of bladder cancer.* Biomaterials, 2013. **34**(38): p. 10258-10266.
108. Satarkar, N.S. and J.Z. Hilt, *Hydrogel nanocomposites as remote-controlled biomaterials.* Acta Biomaterialia, 2008. **4**(1): p. 11-16.
109. Strong, L.E., S.N. Dahotre, and J.L. West, *Hydrogel-nanoparticle composites for optically modulated cancer therapeutic delivery.* Journal of Controlled Release, 2014. **178**: p. 63-68.
110. Mura, S., J. Nicolas, and P. Couvreur, *Stimuli-responsive nanocarriers for drug delivery.* Nature Materials, 2013. **12**(11): p. 991-1003.
111. Koppel, D.E., *Analysis of Macromolecular Polydispersity in Intensity Correlation Spectroscopy - Method of Cumulants.* Journal of Chemical Physics, 1972. **57**(11): p. 4814-&.
112. Chamanzar, M., et al., *Hybrid integrated plasmonic-photonic waveguides for on-chip localized surface plasmon resonance (LSPR) sensing and spectroscopy.* Optics Express, 2013. **21**(26): p. 32086-32098.
113. Varela, M., et al., *Materials characterization in the aberration-corrected scanning transmission electron microscope.* Annual Review of Materials Research, 2005. **35**: p. 539-569.
114. Pennycook, S.J., et al., *Scanning Transmission Electron Microscopy for Nanostructure Characterization*, in *Scanning Microscopy for Nanotechnology: Techniques and Applications*, W. Zhou and Z.L. Wang, Editors. 2007, Springer New York: New York, NY. p. 152-191.
115. Rajagopalan, R. and P.C. Hiemenz, *Principles of colloid and surface chemistry.* Marcel Dekker, New-York, 3e édition, ISBN 0, 1997. **8247**(9397): p. 8.
116. Hollande.Jm and W.L. Jolly, *X-Ray Photoelectron Spectroscopy.* Accounts of Chemical Research, 1970. **3**(6): p. 193-&.
117. Hornyak, G.L., et al., *Introduction to Nanoscience & Nanotechnology*. 2008: CRC press.

118. Mraw, S.C., *Mathematical treatment of heat flow in differential scanning calorimetry and differential thermal analysis instruments.* Review of Scientific Instruments, 1982. **53**(2): p. 228-231.
119. Bandyopadhyay, S., et al., *Synthesis and in vitro cellular interactions of superparamagnetic iron nanoparticles with a crystalline gold shell.* Applied Surface Science, 2014. **316**: p. 171-178.
120. Holmberg, K., et al., *Surfactants and Polymers in Aqueous Solution*. 2002: John Wiley & Sons, Ltd.
121. Meena, S.K. and M. Sulpizi, *Understanding the Microscopic Origin of Gold Nanoparticle Anisotropic Growth from Molecular Dynamics Simulations.* Langmuir, 2013. **29**(48): p. 14954-14961.
122. Ono, Y., et al., *Effects of micelle-to-vesicle transitions on the degree of counterion binding.* Journal of Colloid and Interface Science, 2005. **287**(2): p. 685-693.
123. Meena, S.K., et al., *The role of halide ions in the anisotropic growth of gold nanoparticles: a microscopic, atomistic perspective.* Physical Chemistry Chemical Physics, 2016. **18**(19): p. 13246-13254.
124. Volden, S., et al., *Effect of Charge Density Matching on the Temperature Response of PNIPAAM Block Copolymer-Gold Nanoparticles.* Journal of Physical Chemistry C, 2012. **116**(23): p. 12844-12853.
125. Volden, S., et al., *Gold Nanoparticles Affect Thermoresponse and Aggregation Properties of Mesoscopic Immunoglobulin G Clusters.* Journal of Physical Chemistry C, 2011. **115**(23): p. 11390-11399.
126. Shibayama, M., S. Mizutani, and S. Nomura, *Thermal properties of copolymer gels containing N-isopropylacrylamide.* Macromolecules, 1996. **29**(6): p. 2019-2024.
127. Virtanen, J., C. Baron, and H. Tenhu, *Grafting of poly(N-isopropylacrylamide) with poly(ethylene oxide) under various reaction conditions.* Macromolecules, 2000. **33**(2): p. 336-341.
128. Virtanen, J. and H. Tenhu, *Thermal properties of poly(N-isopropylacrylamide)-g-poly(ethyl oxide) in aqueous solutions: Influence of the number and distribution of the grafts.* Macromolecules, 2000. **33**(16): p. 5970-5975.
129. McDonagh, B.H., et al., *L-DOPA-Coated Manganese Oxide Nanoparticles as Dual MRI Contrast Agents and Drug-Delivery Vehicles.* Small, 2016. **12**(3): p. 301-306.
130. Börjesson, J., et al., *Effect of poly(ethylene glycol) on enzymatic hydrolysis and adsorption of cellulase enzymes to pretreated lignocellulose.* Enzyme and Microbial Technology, 2007. **41**(1–2): p. 186-195.
131. Saeki, S., et al., *Upper and lower critical solution temperatures in poly (ethylene glycol) solutions.* Polymer, 1976. **17**(8): p. 685-689.
132. Karlstroem, G., *A new model for upper and lower critical solution temperatures in poly(ethylene oxide) solutions.* The Journal of Physical Chemistry, 1985. **89**(23): p. 4962-4964.
133. Kjellander, R. and E. Florin, *Water structure and changes in thermal stability of the system poly(ethylene oxide)-water.* Journal of the Chemical Society, Faraday Transactions 1: Physical Chemistry in Condensed Phases, 1981. **77**(9): p. 2053-2077.
134. Costa, P. and J.M.S. Lobo, *Modeling and comparison of dissolution profiles.* European journal of pharmaceutical sciences, 2001. **13**(2): p. 123-133.
135. Brazel, C.S. and N.A. Peppas, *Modeling of drug release from swellable polymers.* European journal of pharmaceutics and biopharmaceutics, 2000. **49**(1): p. 47-58.

Contributions

Paper - I

The experiments were planned and carried out by Sulalit, except for the cell studies which were carried out by Dr. Ioanna Sandvig. Magnetic measurements were done in Uppsala by Dr. Kumar and Dr. Mathieu. XRD measurements were done by Dr. Singh. The manuscript was written by Sulalit, although all the other authors contributed to data interpretation and revisions.

Paper - II

Majority of the experiments were carried out by Dr. Singh although Sulalit contributed to preliminary experiments and interpretation of the data. XPS analysis was done by Sulalit.

Papers - III, VI, VII, VIII

The experiments were planned and carried out by Sulalit and master students Marte, Alvi and Anuvansh. The manuscripts were written by Sulalit, although all the other authors contributed to data interpretation and revisions.

Paper - IV

Majority of the experiments were carried out by Dr. Singh and Sulalit. The manuscript was written by Dr. Singh and Sulalit, although all the other authors contributed to data interpretation and revisions.

Paper - V

The synthesis and functionalization experiments were carried out by Sulalit, while the cell studies were performed by Dr. McDonagh. The manuscript was mostly written by Sulalit, while the cell study part was written by Dr. McDonagh. All the other authors contributed in further data analysis and successive revisions.

APPENDED PAPERS

Paper- I:

Synthesis and *in vitro* cellular interactions of superparamagnetic iron nanoparticles with a crystalline gold shell.

Applied Surface Science 316 (2014) 171–178

Contents lists available at ScienceDirect

Applied Surface Science

journal homepage: www.elsevier.com/locate/apsusc

Synthesis and *in vitro* cellular interactions of superparamagnetic iron nanoparticles with a crystalline gold shell

Sulalit Bandyopadhyay[a,*], Gurvinder Singh[a], Ioanna Sandvig[b], Axel Sandvig[b,c], Roland Mathieu[d], P. Anil Kumar[d], Wilhelm Robert Glomm[a,e]

[a] Ugelstad Laboratory, Department of Chemical Engineering, Norway
[b] MI Lab and Department of Circulation and Medical Imaging, Norwegian University of Science and Technology (NTNU), N-7491 Trondheim, Norway
[c] Department of Neurosurgery, Umeå University Hospital, Umeå, Sweden
[d] Department of Engineering Sciences, Uppsala University, Box 534, SE-75121 Uppsala, Sweden
[e] Sector for Biotechnology and Nanomedicine, SINTEF Materials and Chemistry, N-7465 Trondheim, Norway

ARTICLE INFO

Article history:
Received 31 January 2014
Received in revised form 7 July 2014
Accepted 14 July 2014
Available online 12 August 2014

Keywords:
Core–shell nanoparticles
Oleylamine
Multifunctional
Cytotoxicity
Multimodal imaging
Cell labeling

ABSTRACT

Fe@Au core–shell nanoparticles (NPs) exhibit multiple functionalities enabling their effective use in applications such as medical imaging and drug delivery. In this work, a novel synthetic method was developed and optimized for the synthesis of highly stable, monodisperse Fe@Au NPs of average diameter ~24 nm exhibiting magneto-plasmonic characteristics. Fe@Au NPs were characterized by a wide range of experimental techniques, including scanning (transmission) electron microscopy (S(T)EM), X-ray diffraction (XRD), X-ray photoelectron spectroscopy (XPS), energy dispersive X-ray spectroscopy (EDX), dynamic light scattering (DLS) and UV–vis spectroscopy. The formed particles comprise an amorphous iron core with a crystalline Au shell of tunable thickness, and retain the superparamagnetic properties at room temperature after formation of a crystalline Au shell. After surface modification, PEGylated Fe@Au NPs were used for *in vitro* studies on olfactory ensheathing cells (OECs) and human neural stem cells (hNSCs). No adverse effects of the Fe@Au particles were observed post-labeling, both cell types retaining normal morphology, viability, proliferation, and motility. It can be concluded that no appreciable toxic effects on both cell types, coupled with multifunctionality and chemical stability make them ideal candidates for therapeutic as well as diagnostic applications.

1. Introduction

Synthesis of magnetic nanoparticles (MNPs) of tunable sizes has received a great scientific attention owing to their applications in targeted drug delivery, magnetic resonance imaging (MRI) and treatment of cancer by hyperthermia [1–8]. A common property exploited in life sciences and biomedicine is superparamagnetism allowing the alignment of all spins under an external magnetic field [9]. Despite their tremendous use in biomedical applications, MNPs often tend to aggregate due to strong interparticle dipolar interactions in high ionic strength environment of biological solutions [10]. This causes the enlargement of nanoparticle size, influencing their magnetic properties and limiting their practical use. While MNPs with higher magnetic moment and higher anisotropy would be ideal to improve their performance and dosage, they are often hampered by a low degree of chemical stability, increased toxicity coupled with low plasma half life [11]. Therefore, a major challenge is to increase solution stability and reduce NP toxicity without compromising their magnetic properties.

To overcome these limitations, several procedures have been reported whereby the MNPs are modified with a thin layer of polymers/organic molecules, metal oxide or a metal [12–14]. Among these, a thin protective shell of gold (Au) around the MNPs provides high stability due to its chemical inertness, low cytotoxicity, simple bioconjugation through well-understood surface chemistry such as Au–S [15], and high catalytic activity while supported on metal or metal oxide supports [16]. Upon further functionalization with molecules such as PEG (poly (ethylene glycol)), NP aggregation can also be prevented, besides exploiting cloaking properties of PEG [17]. Au NPs display tunable and environmentally sensitive localized surface plasmon resonance (LSPR) within the visible range, which makes them suitable candidates for biosensors, and

* Corresponding author at: Ugelstad Laboratory, Department of Chemical Engineering, Norway. Tel.: +47 45071041.
E-mail addresses: sulalit.bandyopadhyay@ntnu.no, ratnavo@gmail.com (S. Bandyopadhyay).

http://dx.doi.org/10.1016/j.apsusc.2014.07.081
0169-4332/

good contrast agents for computed tomography (CT) [18,19] as well as photo-acoustic imaging [20]. Thus, core@shell NPs formed by unifying a nanoscale magnetic core within a thin metallic shell can act as a dual contrast agent for MRI and CT. To date, various approaches have been developed for the synthesis of MNPs@Au, such as hydroxyl amine seeding, reverse micelle templating, attachment of Au NPs onto amino-silane modified iron oxide NPs, laser ablation, sonochemical reaction, γ-ray radiation, etc. [8,21–24].

Despite a small number of successful approaches for the synthesis of MNPs@Au and the exploration of their applications in different areas, many issues related to the precise control of Au shell thickness, and the detailed characterization of resultant MNPs@Au need to be addressed. In addition, some limitations associated with earlier methods also include time-consuming purification steps, intricate sequence of chemical reactions, broad size distribution, and poor magnetic responses due to uncontrolled or uneven coating of Au shell around MNPs [25]. The control over size of the resultant MNPs@Au is very important which not only has a pronounced effect on toxicity and retention but also on mode of administration. In some cases, successive gold coating steps are needed to ensure sufficiently stable Fe@Au NPs [26]. Remaining solvents or surfactants may also result in opsonization *in vivo* and other potential side effects, and thus biocompatibility becomes a serious concern [27].

Here, we report a new synthetic procedure for the formation of Fe@Au NPs with a crystalline Au shell on amorphous Fe NPs, their solution and magnetic properties, as well as their interaction with two cell lines. Our approach provides control over Au shell thickness *via* tuning the concentration of Au salt in the solution. First, Fe NPs were produced *via* thermal decomposition of iron pentacarbonyl ($Fe(CO)_5$) in the presence of oleylamine (OAm) [28]. Later, these NPs were transferred to an aqueous phase, and a shell of Au was grown over presynthesized Fe NPs seeds *via* reduction of Au salt in the presence of sodium citrate. Scanning (transmission) electron microscopy (S(T)EM), X-ray diffraction (XRD), X-ray photoelectron spectroscopy (XPS), energy dispersive X-ray spectroscopy (EDX), dynamic light scattering (DLS), and ultraviolet–visible spectroscopy (UV–vis) were used to characterize the Fe@Au NPs. These NPs were subsequently functionalized with O-[2-(3-Mercaptopropionylamino)ethyl]-O′-methylpolyethylene glycol (PEG-SH) molecules which have been used at various concentrations for *in vitro* labeling of two different cell types which are promising candidates for regenerative therapy of the central nervous system: [29,30] olfactory ensheathing cells (OECs) and human neural stem cells (hNSCs). These two cell types differed in terms of uptake and localization of the Fe@Au NPs post-labeling, while no cytotoxic effects were observed irrespective of label concentration or length of co-incubation with the NPs. The magnetic properties of Fe, Fe@Au, and PEGylated Fe@Au NPs were measured by Quantum Design MPMS system indicating supermagnetic behavior. Thus, Fe@Au NPs were found to be have low cytotoxicity, aptly suited for a wide array of applications including bioimaging, drug delivery and other biodiagnostic and/or biomedical applications.

2. Materials and methods

Iron pentacarbonyl ($Fe(CO)_5$, 99.99%), octadecene (ODE, 90%), oleylamine (OAm, 70%), chloroauric acid (99.999%), sodium citrate, O-[2-(3-Mercaptopropionylamino)ethyl]-O′-methylpolyethylene glycol (PEG-SH) of molecular weight 5000 Da were purchased from Sigma–Aldrich.

2.1. Synthesis of Fe NPs

Fe NPs were synthesized *via* thermal decomposition of $Fe(CO)_5$ in ODE in the presence of OAm. The reaction scheme modified from the one reported by Sun et al. [31] is detailed herein. In essence, a mixture of ODE (50 mL) and OAm (740 μL) was degassed under Ar atmosphere and vigorous stirring at 120 °C for 30 min. The temperature was raised to 180 °C and 1.8 mL of $Fe(CO)_5$ was injected into the hot reaction mixture and the reaction was continued for 20 min. After cooling down to room temperature, the supernatant was decanted and the magnetic bar coated with Fe NPs was washed with 20 mL hexane and 40 mL acetone. Fe NPs were magnetically separated, and the product was washed two times with 20 mL acetone. Subsequently, these Fe NPs were dried in a stream of nitrogen.

2.2. Synthesis of Fe@Au NPs

The schematic protocol for Fe@Au NPs synthesis is illustrated in Fig. 1. 5 mg of the as synthesized Fe NPs were dissolved in 10 mL of 10 mM sodium citrate solution using sonication at 80 °C for half an hour. Citrate stabilized Fe seed solution (brown solution) was added to a 50 mL reaction flask and the resultant solution was maintained to 70 °C under mild stirring. 10 mL of 1.5 mM chloroauric acid (the concentration of the gold precursor was optimized by performing experiments at concentrations both below and above this experimental value) was added dropwise and allowed to react for 20 min under vigorous stirring. The solution turned purplish red around 8 min after reaction. Thereafter, the solution was cooled down to room temperature, and Fe@Au NPs were magnetically separated to remove free Au NPs. A video of the synthesis protocol showing the color change during the course of the reaction and influence of the magnet on the final product can be found in the supporting information.

2.3. PEG coating of Fe@Au NPs

Two milligrams of PEG-SH was mixed with 5 mg of the as synthesized Fe@Au NPs dissolved in 5 mL of MQ water and stirred for 1 h to covalently modify the surface of the NPs [32]. The resulting PEG coated Fe@Au NPs were collected by centrifugation at 10,000 rpm for 20 min and washed twice with MQ water. These

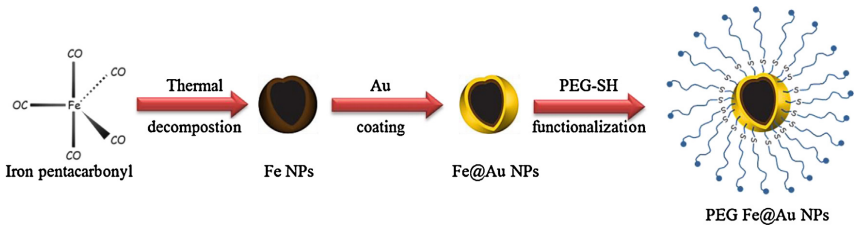

Fig. 1. Simplified schematic showing sequence of synthesis of PEG modified Fe@Au NPs.

NPs were stored at concentrations of 1 mg/mL at 4 °C to prevent further aggregation.

2.4. Cell studies

Two different cell types were used for the cell studies, namely OECs and hNSCs. OECs were purified from neonatal Fischer rats at P8 according to Barnett and Roskams [33]. Purified OECs were cultured in Dulbecco's Modified Eagle's Medium (DMEM GlutaMAX) with 1.25% gentamicin and 5% FBS (Autogen Bioclear) on poly-L-lysine (PLL) coated multi-well plates (Corning). The cultures were supplemented with 500 ng/mL fibroblast growth factor 2 (FGF2) (Peprotech, London, UK), 50 ng/mL heregulin (hrgβ1) (R&D Systems Europe Ltd, Abingdon, UK), and 10^{-6} M forskolin.

Undifferentiated H9-derived, hNSCs (Gibco, Invitrogen) were cultured on laminin-coated multi-well plates (Corning) in StemPro NSC serum-free medium (Gibco, Invitrogen) containing 20 ng/mL basic recombinant human fibroblast growth factor (bFGF) (Gibco, Invitrogen) and 20 ng/mL recombinant human epidermal growth factor (EGF) (Gibco, Invitrogen).

2.4.1. Cell labeling with Fe@Au NPs

PEG coated Fe@Au NPs were added to 50% confluent OEC and hNSC cultures at concentrations of nanoparticles/media volume of 1 μg/mL, 100 μg/mL, 1 mg/mL and incubated for 6 h, 12 h, and 24 h at 37 °C with 7% CO_2 and 5% CO_2, respectively.

2.4.2. LIVE/DEAD® cell viability assay

The viability of OECs and hNSCs was qualitatively assessed by visualization of live and dead cells, stained by calcein and ethidium homodimer-1 (EthD-1), respectively, using LIVE/DEAD® assay (Invitrogen, Life Technologies) immediately after 6 h, 12 h and 24 h incubation with Fe@Au-PEG NPs. LIVE/DEAD® solution was prepared in 4.5 mL sterile PBS with 2.7 μL calcein (Invitrogen), and 12 μL ethidium homodimer (Invitrogen), added to the labeled cell cultures at 1:1 (v/v), and incubated for 30 min at 37 °C. The cultures were subsequently imaged on an Axiovert 200 M fluorescent microscope (Zeiss, Germany) using AxioVision Rel. 4.3 software.

2.4.3. Prussian Blue staining

Prussian Blue kit was used for detection of intracellular iron. Following 12 h of incubation with PEG coated Fe@Au NPs, OECs and hNSCs were fixed with 4% paraformaldehyde and subsequently stained with Prussian Blue according to the supplier's recommended protocol.

2.5. Characterization techniques

2.5.1. Scanning (transmission) electron microscopy [S(T)EM] and energy dispersive X-ray spectroscopy [EDX]

S(T)EM images and EDX analyses were acquired using a Hitachi S-5500 electron microscope operating at 30 kV accelerating voltage. TEM images were obtained in bright field mode. TEM grids were prepared by placing several drops of the solution on a Formvar carbon coated copper grid (Electron Microscopy Sciences) and wiping immediately with Kimberly–Clark kimwipes to prevent further aggregation owing to evaporation at room temperature.

2.5.2. Dynamic light scattering [DLS] and zeta potential measurement

The size distribution and zeta potential of the NPs were measured using a Malvern Zetasizer Nano-ZS instrument, and the manufacturer's own software. The solvent used for the Fe NPs was n-hexane while for the other NPs, MQ water was used.

2.5.3. Ultraviolet–visible spectroscopy [UV–vis]

UV–vis spectra were acquired with a UV-2401PC (Shimadzu) spectrophotometer. The spectra were collected over the spectral range from 200 to 800 nm.

2.5.4. X-ray photoelectron spectroscopy (XPS)

XPS analyses were performed using a Kratos Axis Ultra DLD spectrometer (Kratos Analytical, UK), equipped with a monochromatized aluminum X-ray source (Al, $h\upsilon = 1486.6$ eV) operating at 10 mA and 15 kV (150 W). A hybrid lens (electrostatic and magnetic) mode was employed along with an analysis area of approximately 300 μm × 700 μm. Survey spectra were collected over the range of 0–1100 eV binding energy with analyzer pass energy of 160 eV, and high resolution spectra of C 1s, O 1s, Fe 2p and Au 4f were obtained with an analyzer pass energy of 20 eV. XPS data were processed with Casa XPS software (Casa Software Ltd., UK).

2.5.5. X-ray diffraction (XRD)

XRD patterns were collected from Bruker AXS D8 Focus with Cu K_α radiation ($\lambda = 1.5418$ Å). Samples for XRD measurement were prepared by depositing several drops of concentrated solution of NPs on a single crystalline silicon holder.

2.5.6. Magnetic measurements

Zero-field-cooled (ZFC) and field-cooled (FC) magnetization *versus* temperature (*M*–*T*) and room temperature magnetization *versus* field (*M*–*H*) measurements were performed using a Quantum Design MPMS system.

3. Results and discussion

The main steps involved in a typical synthesis of Fe@Au NPs and subsequent surface modification with PEG are shown in Fig. 1. Fe NPs were synthesized using a previously reported method [31]. These Fe NPs rapidly oxidize upon exposure to the air, forming a thin surface layer of natural iron oxide. The S(T)EM image displayed in Fig. 2(a) and its inset reveal a core–shell morphology of Fe MNPs, *i.e.*, Fe@Fe_xO_y. It is difficult to predict the exact nature of the shell composition as both the core and shell are amorphous in nature as confirmed by XRD measurements, which is also consistent with previous reports (Fig. 2(e)) [34,35]. The number average diameter of these NPs was measured over 200 NPs and was found to be 14 ± 1 nm. The Fe NPs were dried after removal of the surfactant by washing with hexane and acetone several times, and transferred into an aqueous phase in the presence of sodium citrate. The citrate-functionalized Fe NPs were found to be stable in an aqueous phase without any aggregation (Fig. S1 in the supporting information). Later, a thin coating of Au was carried out in aqueous medium using water soluble Fe NPs as heterogeneous nucleation sites, leading to the formation of a continuous shell of Au around the Fe NPs. The resultant product of Fe@Au NPs were magnetically separated to remove freely suspended Au NPs, and redispersed in an aqueous phase.

Representative bright field (BF) S(T)EM images shown in Fig. 2(b) exhibit an increment in an average diameter ∼24 ± 5 nm of Fe@Au NPs which are subsequently functionalized with PEG-SH (Fig. 2(c)). From these data, the thickness of the Au shell is calculated to be ∼5 nm. DLS measurements, however, show larger sizes of 34 ± 4 nm (Fe NPs), 71 ± 4 nm (Fe@Au NPs) and 72 ± 5 nm (PEG Fe@Au NPs), respectively, in comparison to analysis *via* S(T)EM. The reason for this discrepancy can be attributed either due to DLS measuring the hydrodynamic radius rather than the core radius of the NPs as measured by S(T)EM, a weak interparticle dipolar interaction among NPs causing weak interparticle coupling, or a combination. It is difficult to visualize a core–shell morphology of as-prepared Fe@Au NPs in electron microscopy because Au has a higher atomic

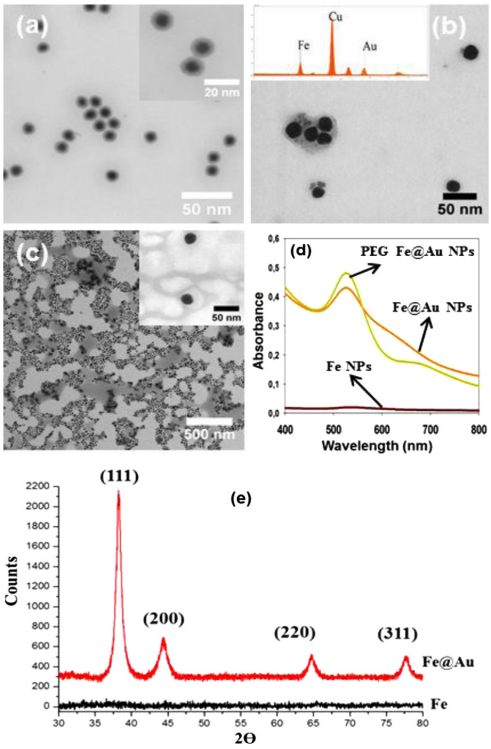

Fig. 2. Representative BF S(T)EM images of (a) Fe@Fe_xO_y NPs (inset is an magnified image of Fe NPs), (b) Fe@Au NPs (inset is EDX spectrum for Fe@Au NPs), (c) PEG functionalized Fe@Au NPs (enlarged view of PEG functionalized Fe@Au NPs). (d) UV–vis spectra of Fe, Fe@Au and PEG Fe@Au NPs. (e) XRD spectra for Fe and Fe@Au NPs.

number than Fe, contributing to high contrast while imaging. A shell of Au coating around Fe NPs can be confirmed by EDX elemental analysis, indicating the presence of Fe and Au in NPs (inset in Fig. 2(b)). Moreover, UV–vis spectroscopy was used to characterize the various steps of Fe NP surface functionalization (Fig. 2(d)). It can be noted from the UV–vis spectra that Fe NPs do not show a prominent absorption peak in the visible, whereas Fe@Au NPs display an absorption peak at ~525 nm, which is a characteristic LSPRof Au NPs. We observe a red shift in the absorbance peak (~528 nm) for PEG coated Fe@Au NPs. The bathochromic shift is an indication of the increase in the size of the NPs following PEG-coating, as predicted by Mie–Drude theory [36].

XRD pattern of the Fe@Au NPs shows diffraction peaks at 2θ values of 38.3, 44.4, 64.7, 77.7, corresponding to (1 1 1), (2 0 0), (2 2 0), (3 1 1) planes, respectively, revealing the crystalline nature of the Au shell on amorphous Fe NPs [34,37] (Fig. 2(e)). We also estimated the average crystallite size of Fe@Au NPs obtained from half width diffraction peaks using Scherrer's formula, yielding ~8.5 ± 2 nm, which is very small compared to the size (~24 ± 5 nm) measured by TEM. This can be understood by considering that all diffraction peaks in XRD pattern correspond to only crystalline phase of the materials (*i.e.*, the Au layer), and an average size measured by XRD corresponds to the actual size of the Au shell. Such a shell thickness of Au layer ~4 ± 1 nm from XRD is in good agreement with shell thickness as measured by S(T)EM. XPS studies were also conducted in order to examine the Au coating on Fe NPs, revealing the presence of Fe 2p before and both Fe 2p and Au 4f after Au coating (Fig. 3(a and c)). In addition, a high resolution XPS spectrum of Fe NPs shows three photoelectron peaks at ~711 eV and ~725 eV corresponding to binding energies of $2p_{3/2}$ and $2p_{1/2}$ of oxidized Fe (III), and ~707 eV assigned to zero-valent Fe (Fig. 3(b)) [38]. Fig. 3(d) shows a high resolution spectrum of Au4f which consists of two peaks with binding energies of ~84 eV and ~87 eV corresponding to elemental Au(0), further confirming the presence of Au coating over Fe NPs. Taken together, our results from S(T)EM, DLS, EDX XRD, and XPS provide evidence for the successful coating of the Fe NPs with a crystalline Au layer.

Zeta potential measurements of the Fe@Au and Fe@Au-PEG NPs showed zeta potential values of −49.4 mV and −36.2 mV respectively. These high values essentially account for the electrosteric stability of the particles in aqueous solution, possibly enabling prolonged circulation times for *in vivo* applications. Furthermore, the effect of Au precursor concentration on the formation of Fe@Au NPs was investigated for controlling the surface deposition of Au onto Fe NPs. At low concentration of Au^{3+} precursor (0.9 mM), we noticed a low yield of Fe@Au NPs, where the majority of Fe NPs remained unmodified following Au coating (Fig. 4(a)). When the concentration was raised to 3.4 mM, elongated Fe@Au NPs with high yield were obtained (Fig. 4(b)). The size of these NPs was found to be ~28 ± 5 nm which is larger than the reference Fe@Au NPs (~24 ± 5 nm) synthesized at Au concentration 1.5 mM, leading to increase in the shell thickness from ~5 nm to ~7 nm based on S(T)EM size distribution analysis. Similarly, a crystallite size analysis from the XRD patterns reveals an increase in shell thickness from ~4 ± 1 nm to ~6 ± 2 nm following an increment from 1.5 mM to 3.4 mM of Au^{+3} precursor, which is consistent with STEM results (Fig. S2 in the supporting information). A bathochromic shift in UV–vis spectra is observed from 528 nm to 535 nm with increasing gold precursor concentration, indicating thicker gold coating (Fig. 4(c)). In addition, an evolution of a second LSPR band above 600 nm with increasing gold precursor concentration is observed, which can be attributed to a change in the nanoparticle shape after gold coating.

Fig. 5(a) shows the zero-field-cooled (ZFC) and field cooled (FC) magnetization *versus* temperature curves recorded in a weak magnetic field (H = 20 Oe) for Fe and Fe@Au NPs. Both samples show ZFC magnetization curves reminiscent of superparamagnets. When the sample is cooled under zero field, it shows no net alignment of spins at low temperature, resulting in a very low magnetization. As the temperature increases, the spins become progressively "unblocked", aligning toward the applied field direction, and the magnetization increases until it reaches a maximum value at a temperature commonly referred as the mean blocking temperature (T_b) of the sample. At temperature above T_b (about 90 K in our samples) the thermal energy (k_BT) overcomes the magnetic anisotropy energy barrier (*i.e.*, increased dynamic rotation of the spins prevents the alignment in the field direction), and magnetization starts decreasing with further increase in temperature [9].

However, the nature of FC magnetization curves of Fe and Fe@Au NPs are significantly different. The magnetization–temperature (M–T) curves of the Fe NPs are reminiscent of a strongly interacting nanoparticle system, with the FC magnetization value decreasing below the T_b on cooling down and the ZFC magnetization starting to rise only as T_b is approached on warming up [39]. In contrast, the Fe@Au NPs display M–T curves that are reminiscent of a weakly interacting nanoparticle system; the FC magnetization does not decrease below T_b and the ZFC magnetization starts to rise right from the lowest measured temperature. This observation matches very well with the prediction that the coating of (5 nm thick) Au shell coupled with citrate stabilization helps in

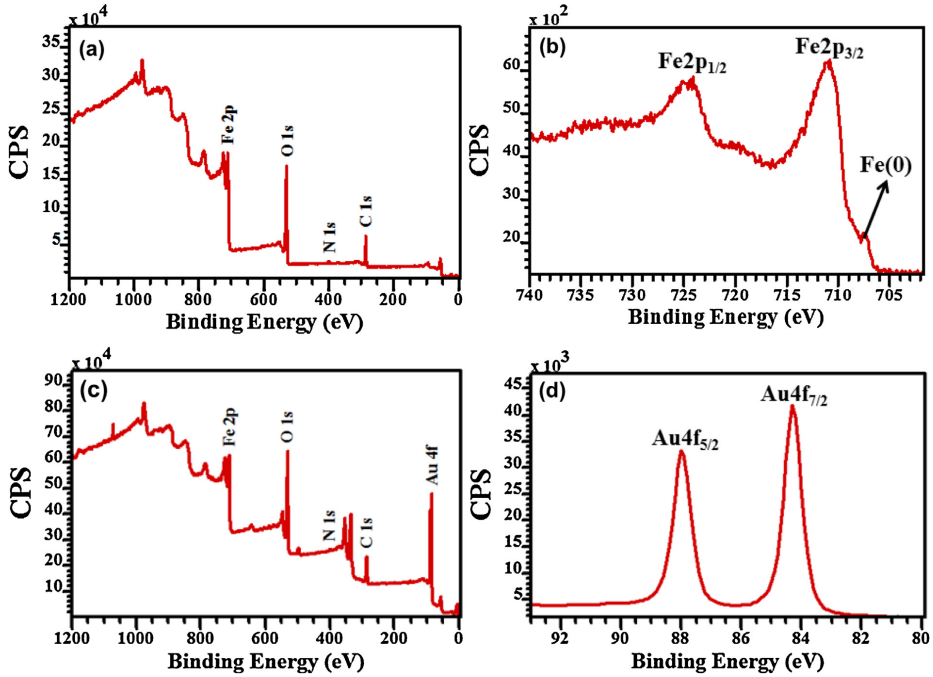

Fig. 3. (a) XPS survey spectra of Fe-NPs. (b) High resolution narrow region scan of Fe2p. (c) XPS survey spectra of Fe@Au NPs. (d) High resolution narrow region scan of Au4f.

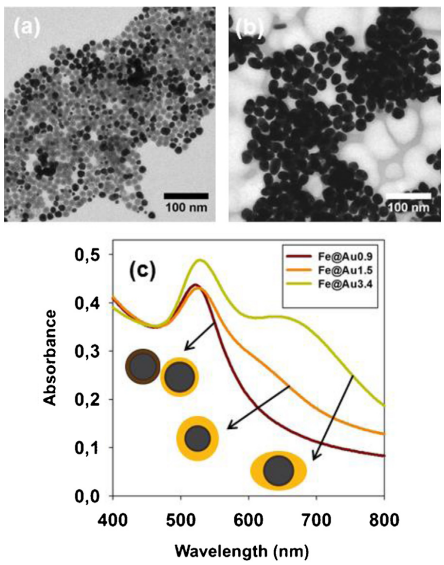

Fig. 4. BF S(T)EM images showing Fe@Au NPs formation at different Au precursor concentration, (a) 0.9 mM, (b) 3.4 mM. (c) UV–vis spectra of Fe@Au NPs synthesized using different concentrations of chloroauric acid 0.9 mM, 1.5 mM and 3.4 mM.

separating the Fe moments and hence reduces the interaction between them.

Fig. 5(b) shows the magnetization *versus* the magnetic field at 300 K obtained by cycling the field between −30 kOe and 30 kOe. A negligible coercivity and remanence in the hysteresis loops indicates the super-paramagnetic nature of the NPs. The *M*–*H* curves become rounder or S-shaped like as Au is coated on the NPs, again reflecting the weakening of interparticle interaction. It can be seen that the saturation magnetizations of the NPs are lower than that reported for bulk phase at room temperature (~218 emu/g) [40]. It is well established that that the saturation magnetization of nanomaterials decreases (in comparison to the bulk) with decreasing particle size owing to existence of surface spin disorder or the magnetic dead layer [41]. Here it is important to note that the magnetization value in emu/g for the Fe@Au NPs does not represent the actual magnetic moment of the Fe core, but it is underestimated because of the weight of Au that contributes to the total mass of the sample that is used for the magnetic measurements. In fact, if this discrepancy is corrected by roughly subtracting the weight of Au (calculated from the volume ratio of Fe and Au in a Fe@Au NP) enhanced values for the Fe magnetization are obtained. This enhancement can be explained by the fact that the coating of Au shell reduces the magnetic dead layer in our samples. Further, in the present case the possibility of increased crystallinity of Fe core on addition of Au shell cannot be ruled out, which also can lead to increased magnetic moment. This enhancement in the magnetization value of the NPs on Au addition is another advantage for biomagnetic applications. For example, higher magnetization increases the MRI contrast with the applied magnetic field due to the stronger interferences with the relaxation times of water which is the principal proton source in MRI signal [42]. Additionally,

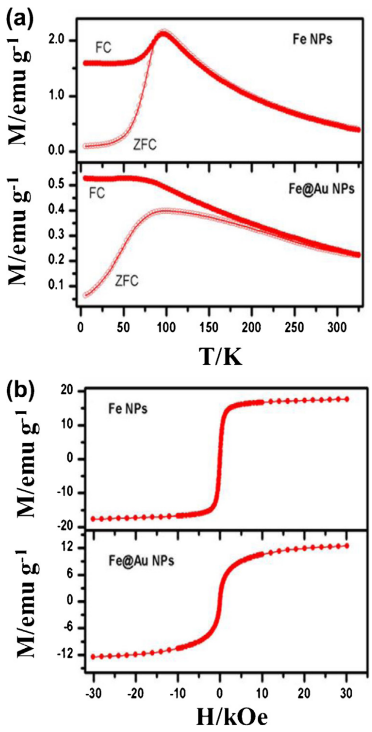

Fig. 5. (a) Temperature dependence of ZFC and FC magnetization curves measured in 20 Oe field for Fe and Fe@Au NPs. (b) Magnetic hysteresis curves at 300 K for Fe and Fe@Au NPs.

for applications that require particle manipulation by an external magnetic field at a distance, it is essential that the particle saturation magnetization is as high as possible [43]. Our magnetic measurements on the Fe@Au-PEG sample (Fig. S3 in the supporting information) prove that the addition of PEG molecules further weakens the magnetic interaction between the Fe moments. Having characterized the Fe@Au NPs, PEGylated NPs were used to study their interactions with two different cell types.

In order to assess the impact of the synthesized MNPs on cell lines, LIVE/DEAD® assays were performed at different time points after introduction of the Fe@Au-PEG NPs to cell cultures of OECs and hNSCs, respectively. Co-incubation at 37 °C did not reveal observable toxic effects of the NPs on either OECs or hNSCs. Both cell types retained viability as well as normal morphology and motility compared to controls [Fig. 6(a), (b), (d) and (e)]. Moreover, cell proliferation in terms of expected confluence at 24 h intervals did not seem to be altered by the presence of the NPs in the cultures. The above findings were consistent in all samples and were independent of NP concentration used for co-incubation.

Differential interference contrast (DIC) images and Prussian Blue assay results indicate uptake of Fe@Au-PEG NPs in >90% of both OECs and hNSCs [Fig. 6(c) and (f)]. A tendency for peri-membrane localization of the Fe@Au NPs, rather than intracellular localization, was observed in the OECs. Consistent with the above, these observations were independent of length of co-incubation or NP concentration used, while it appeared that the two cell types displayed different affinity toward the NPs. Quantification of potential peri-membrane/intracellular NP concentration was beyond the scope of the present study. Evaluation of NP-induced toxicity *in vitro* is important before proceeding to *in vivo* applications as it eliminates the risk of unwanted effects of the NPs on the cell of interest. At the same time, potential cytotoxic effects of the NPs as well as cellular uptake will be contingent on cell type and *in vitro* labeling protocol [44]. In this study, the Fe@Au NPs were applied to cells with very different antigenic, metabolic and functional profiles, *i.e.*, a glial cell (OEC) and a stem cell (hNSC), both of which are highly relevant in tissue engineering and image-guided therapy following central nervous system (CNS) injury [45,46]. The lack of observable toxic effects of the Fe@Au NPs on either cell type is very promising with regard to future *in vivo* application involving

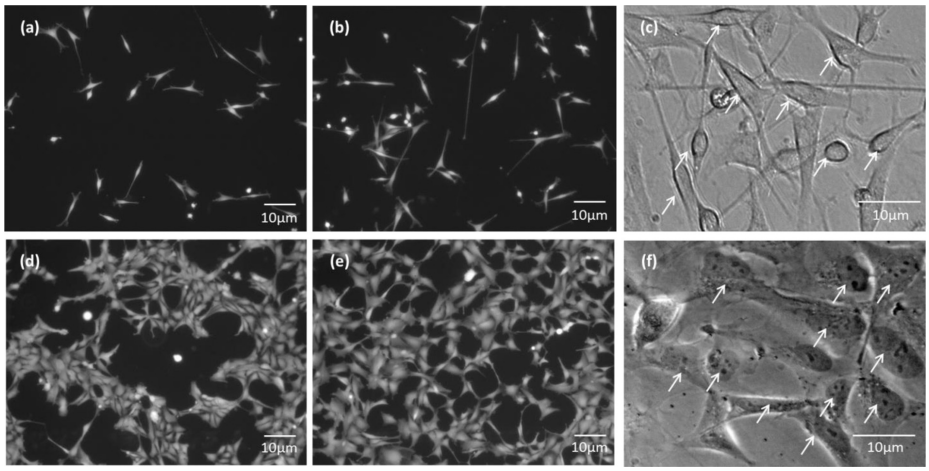

Fig. 6. (a), (b), (d) and (e) Live/Dead images of OECs and NSCs 24 h after labeling with Fe@Au NPs. (a) Unlabelled OECs. (b) OECs with Fe@Au NPs. (d) Unlabelled NSCs. (e) NSCs with Fe@Au NPs. (c) and (f) DIC images of labeled OECs and NSCs, respectively, showing Fe@Au uptake (arrows).

the specific cells. On the other hand, the differential affinity of the OECs and hNSCs to the particles suggests that labeling and imaging protocols for *in vivo* application must be optimized for the individual cell types, consistent with previous findings [44].

4. Conclusion

In summary, we have optimized and developed the synthetic conditions for designing multifunctional core–shell type NPs consisting of magnetic core surrounded by a uniform, crystalline shell of Au. The thickness of gold shell can be tuned by varying Au precursor concentration. This approach can further be extended to the coating of other noble metals with controllable thickness where metallic shell provides a surface for easy chemical functionalization and long-term stabilization of the magnetic core under physiological conditions. S(T)EM, EDX, DLS, UV–vis and XRD techniques were used to confirm the uniform coating of Au shell around an Fe core. As-synthesized Fe NPs with core–shell morphology were confirmed by XPS results which indicates that an inner core and an outer shell of MNPs are formed by Fe^0 and oxidized Fe, respectively. The presence of Au peaks in survey and high resolution XPS spectra affirm the Au coating around the magnetic core, which is also evident from XRD measurements indicating an amorphous state of Fe NPs prior to Au coating. After Au coating on Fe NPs, a crystalline phase arises which is attributed to the Au shell. The magnetic properties of NPs at various steps of surface modification were characterized, and we observe a superparamagnetic behavior at room temperature due to the absence of hysteresis loop in *M–H* curves at 300 K, and $T_b < 300$ K. From these results, it is clear that MNPs retain substantial magnetic properties even after Au coating. In addition, it has been shown that PEGylated Fe@Au NPs have no observable cytotoxic effects on either OECs or NSCs, with a tendency of peri-membrane internalization, to be further understood through *in vitro* studies. The lack of observable toxic effects of the Fe@Au NPs on either cell type is very promising with regard to future *in vivo* application involving the specific cells. Magneto-plasmonic properties exhibited by these hybrid NPs enable them suitable for theranostic as well as multimodal imaging uses.

Acknowledgements

The authors would like to thank Liaison Committee between the Central Norway Regional Health Authority (RHA) and NTNU, NorFab for financial support in connection to use of NTNU Nanolab, Swedish Research Council (VR) and the Swedish Foundation for International Cooperation in Research and Higher Education (STINT) for the financial support.

Appendix A. Supplementary data

Supplementary material related to this article can be found, in the online version, at http://dx.doi.org/10.1016/j.apsusc.2014.07.081.

References

[1] S. Laurent, D. Forge, M. Port, A. Roch, C. Robic, L.V. Elst, R.N. Muller, Magnetic iron oxide nanoparticles: synthesis, stabilization, vectorization, physicochemical characterizations, and biological applications (vol. 108, p. 2064, 2008), Chem. Rev. 110 (2010) 2574.
[2] M.A. Abakumov, S.A. Shein, H. Vishvasrao, N.V. Nukolova, M. Sokol'ski-Papkov, T.O. Sandalova, I.L. Gubskii, N.F. Grinenko, A.V. Kabanov, V.P. Chekhonin, Visualization of experimental glioma C6 by MRI with magnetic nanoparticles conjugated with monoclonal antibodies to vascular endothelial growth factor, Bull. Exp. Biol. Med. 154 (2012) 274–277.
[3] A. Antonelli, C. Sfara, E. Manuali, I.J. Bruce, M. Magnani, Encapsulation of superparamagnetic nanoparticles into red blood cells as new carriers of MRI contrast agents, Nanomedicine-UK 6 (2011) 211–223.
[4] N. Arsalani, H. Fattahi, M. Nazarpoor, Synthesis and characterization of PVP-functionalized superparamagnetic Fe_3O_4 nanoparticles as an MRI contrast agent, Express Polym. Lett. 4 (2010) 329–338.
[5] C.Y. Haw, F. Mohamed, C.H. Chia, S. Radiman, S. Zakaria, N.M. Huang, H.N. Lim, Hydrothermal synthesis of magnetite nanoparticles as MRI contrast agents, Ceram. Int. 36 (2010) 1417–1422.
[6] E.K. Lim, Y.M. Huh, J. Yang, K. Lee, J.S. Suh, S. Haam, pH-triggered drug-releasing magnetic nanoparticles for cancer therapy guided by molecular imaging by MRI, Adv. Mater. 23 (2011) 2436–2442.
[7] C.R. Thomas, D.P. Ferris, J.H. Lee, E. Choi, M.H. Cho, E.S. Kim, J.F. Stoddart, J.S. Shin, J. Cheon, J.I. Zink, Noninvasive remote-controlled release of drug molecules in vitro using magnetic actuation of mechanized nanoparticles, J. Am. Chem. Soc. 132 (2010) 10623–10625.
[8] Z. Fan, M. Shelton, A.K. Singh, D. Senapati, S.A. Khan, P.C. Ray, Multifunctional plasmonic shell-magnetic core nanoparticles for targeted diagnostics, isolation, and photothermal destruction of tumor cells, ACS Nano 6 (2012) 1065–1073.
[9] R. Krahne, G. Morello, A. Figuerola, C. George, S. Deka, L. Manna, Physical properties of elongated inorganic nanoparticles, Phys. Rep. 501 (2011) 75–221.
[10] C. Sun, J.S.H. Lee, M.Q. Zhang, Magnetic nanoparticles in MR imaging and drug delivery, Adv. Drug Deliv. Rev. 60 (2008) 1252–1265.
[11] C.C. Berry, A.S.G. Curtis, Functionalisation of magnetic nanoparticles for applications in biomedicine, J. Phys. D: Appl. Phys. 36 (2003) R198–R206.
[12] S. Seino, T. Kinoshita, Y. Otome, T. Nakagawa, K. Okitsu, Y. Mizukoshi, T. Nakayama, T. Sekino, K. Niihara, T.A. Yamamoto, Gamma-ray synthesis of magnetic nanocarrier composed of gold and magnetic iron oxide, J. Magn. Magn. Mater. 293 (2005) 144–150.
[13] L. Wang, J. Luo, M.J. Schadt, C.J. Zhong, Thin film assemblies of molecularly-linked metal nanoparticles and multifunctional properties, Langmuir 26 (2010) 618–632.
[14] S.I. Stoeva, F.W. Huo, J.S. Lee, C.A. Mirkin, Three-layer composite magnetic nanoparticle probes for DNA, J. Am. Chem. Soc. 127 (2005) 15362–15363.
[15] M. Famulok, J.S. Hartig, G. Mayer, Functional aptamers and aptazymes in biotechnology, diagnostics, and therapy, Chem. Rev. 107 (2007) 3715–3743.
[16] R.A. Sperling, W.J. Parak, Surface modification, functionalization and bioconjugation of colloidal inorganic nanoparticles, Therap. Innov. Regul. Sci. 47 (2013) 1333–1383.
[17] H. Otsuka, Y. Nagasaki, K. Kataoka, PEGylated nanoparticles for biological and pharmaceutical applications, Adv. Drug Deliv. Rev. 64 (2012) 246–255.
[18] D. Kim, S. Park, J.H. Lee, Y.Y. Jeong, S. Jon, Antibiofouling polymer-coated gold nanoparticles as a contrast agent for in vivo X-ray computed tomography imaging, Nanomedicine-Nanotechnology 3 (2007) 352.
[19] H. Liu, Y.H. Xu, S.H. Wen, Q. Chen, L.F. Zheng, M.W. Shen, J.L. Zhao, G.X. Zhang, X.Y. Shi, Targeted tumor computed tomography imaging using low-generation dendrimer-stabilized gold nanoparticles, Chem.-Eur. J. 19 (2013) 6409–6416.
[20] N. Khlebtsov, L. Dykman, Biodistribution and toxicity of engineered gold nanoparticles: a review of in vitro and in vivo studies, Chem. Soc. Rev. 40 (2011) 1647–1671.
[21] T. Zhou, B.Y. Wu, D. Xing, Bio-modified Fe_3O_4 core/Au shell nanoparticles for targeting and multimodal imaging of cancer cells, J. Mater. Chem. 22 (2012) 470–477.
[22] T. Jafari, A. Simchi, N. Khakpash, Synthesis and cytotoxicity assessment of superparamagnetic iron-gold core–shell nanoparticles coated with polyglycerol, J. Colloids Interface Sci. 345 (2010) 64–71.
[23] J. Lin, W.L. Zhou, A. Kumbhar, J. Wiemann, J.Y. Fang, E.E. Carpenter, C.J. O'Connor, Gold-coated iron (Fe@Au) nanoparticles: synthesis, characterization, and magnetic field-induced self-assembly, J. Solid State Chem. 159 (2001) 26–31.
[24] C.S. Levin, C. Hofmann, T.A. Ali, A.T. Kelly, E. Morosan, P. Nordlander, K.H. Whitmire, N.J. Halas, Magnetic-plasmonic core–shell nanoparticles, ACS Nano 3 (2009) 1379–1388.
[25] J. Schotter, O. Bethge, T. Maier, H. Brueck, Recognition of biomolecular interactions by plasmon resonance shifts in single- and multicomponent magnetic nanoparticles, Appl. Phys. Lett. 93 (2008).
[26] J.L. Lyon, D.A. Fleming, M.B. Stone, P. Schiffer, M.E. Williams, Synthesis of Fe oxide core/Au shell nanoparticles by iterative hydroxylamine seeding, Nano Lett. 4 (2004) 719–723.
[27] C.R. Sun, K. Du, C. Fang, N. Bhattarai, O. Veiseh, F. Kievit, Z. Stephen, D.H. Lee, R.G. Ellenbogen, B. Ratner, M.Q. Zhang, PEG-mediated synthesis of highly dispersive multifunctional superparamagnetic nanoparticles: their physicochemical properties and function in vivo, ACS Nano 4 (2010) 2402–2410.
[28] Z. Xu, Y. Hou, S. Sun, Magnetic core/shell Fe_3O_4/Au and Fe_3O_4/Au/Ag nanoparticles with tunable plasmonic properties, J. Am. Chem. Soc. 129 (2007) 8698–8699.
[29] S.C. Barnett, J.S. Riddell, Olfactory ensheathing cells (OECs) and the treatment of CNS injury: advantages and possible caveats, J. Anat. 204 (2004) 57–67.
[30] M. Dihne, H.P. Hartung, R.J. Seitz, Restoring neuronal function after stroke by cell replacement anatomic and functional considerations, Stroke 42 (2011) 2342–2350.
[31] Z.C. Xu, Y.L. Hou, S.H. Sun, Magnetic core/shell Fe_3O_4/Au and Fe_3O_4/Au/Ag nanoparticles with tunable plasmonic properties, J. Am. Chem. Soc. 129 (2007) 8698–8699.
[32] D. Kim, S. Park, J.H. Lee, Y.Y. Jeong, S. Jon, Antibiofouling polymer-coated gold nanoparticles as a contrast agent for in vivo X-ray computed tomography imaging (vol. 129, p. 7661, 2007), J. Am. Chem. Soc. 129 (2007) 12585.
[33] S.C. Barnett, A.J. Roskams, Olfactory ensheathing cells: isolation and culture from the neonatal olfactory bulb, Methods Mol. Biol. 438 (2008) 85–94.

[34] L.M. Lacroix, N.F. Huls, D. Ho, X.L. Sun, K. Cheng, S.H. Sun, Stable single-crystalline body centered cubic Fe nanoparticles, Nano Lett. 11 (2011) 1641–1645.
[35] S. Peng, S. Sun, Synthesis and characterization of monodisperse hollow Fe_3O_4 nanoparticles, Angew. Chem. Int. Ed. 46 (2007) 4155–4158.
[36] S. Volden, A.-L. Kjøniksen, K. Zhu, J. Genzer, B. Nyström, W.R. Glomm, Temperature-dependent optical properties of gold nanoparticles coated with a charged diblock copolymer and an uncharged triblock copolymer, ACS Nano 4 (2010) 1187–1201.
[37] G. Singh, P.A. Kumar, C. Lundgren, A.T.J. van Helvoort, R. Mathieu, E. Wahlström, W.R. Glomm, Tunability in crystallinity and magnetic properties of core–shell fe nanoparticles, Part. Part. Syst. Char. (2014), http://dx.doi.org/10.1002/ppsc.201400032.
[38] X.Q. Li, W.X. Zhang, Sequestration of metal cations with zerovalent iron nanoparticles – a study with high resolution X-ray photoelectron spectroscopy (HR-XPS), J. Phys. Chem. C 111 (2007) 6939–6946.
[39] P.E. Jonsson, Superparamagnetism and spin glass dynamics of interacting magnetic nanoparticle systems, Adv. Chem. Phys. 128 (2004) 191–248.
[40] W.D. Callister, Materials Science and Engineering: An Introduction, John Wiley & Sons, Inc., 2007.
[41] G.F. Goya, T.S. Berquo, F.C. Fonseca, M.P. Morales, Static and dynamic magnetic properties of spherical magnetite nanoparticles, J. Appl. Phys. 94 (2003) 3520–3528.
[42] H. Khurshid, C.G. Hadjipanayis, H.W. Chen, W.F. Li, H. Mao, R. Machaidze, V. Tzitzios, G.C. Hadjipanayis, Core/shell structured iron/iron-oxide nanoparticles as excellent MRI contrast enhancement agents, J. Magn. Magn. Mater. 331 (2013) 17–20.
[43] A. Figuerola, R. Di Corato, L. Manna, T. Pellegrino, From iron oxide nanoparticles towards advanced iron-based inorganic materials designed for biomedical applications, Pharmacol. Res. 62 (2010) 126–143.
[44] I. Sandvig, L. Hoang, T.C.P. Sardella, S.C. Barnett, C. Brekken, K. Tvedt, M. Berry, O. Haraldseth, A. Sandvig, M. Thuen, Labelling of olfactory ensheathing cells with micron-sized particles of iron oxide and detection by MRI, Contrast Media Mol. I 7 (2012) 403–410.
[45] I. Sandvig, M. Thuen, L. Hoang, O. Olsen, T.C.P. Sardella, C. Brekken, K.E. Tvedt, S.C. Barnett, O. Haraldseth, M. Berry, A. Sandvig, In vivo MRI of olfactory ensheathing cell grafts and regenerating axons in transplant mediated repair of the adult rat optic nerve, NMR Biomed. 25 (2012) 620–631.
[46] E. Bible, O. Qutachi, D.Y.S. Chau, M.R. Alexander, K.M. Shakesheff, M. Modo, Neovascularization of the stroke cavity by implantation of human neural stem cells on VEGF-releasing PLGA microparticles, Biomaterials 33 (2012) 7435–7446.

Supporting Information

Synthesis and *in vitro* cellular interactions of superparamagnetic iron nanoparticles with a crystalline gold shell

Sulalit Bandyopadhyay[1*], *Gurvinder Singh*[1], *Ioanna Sandvig*[2], *Axel Sandvig*[2,3], *Roland Mathieu*[4], *P. Anil Kumar*[4], *Wilhelm Robert Glomm*[1,5]

[1]Ugelstad Laboratory, Department of Chemical Engineering,

[2] MI Lab and Department of Circulation and Medical Imaging,

Norwegian University of Science and Technology (NTNU), N-7491 Trondheim, Norway.

[3] Department of Neurosurgery, Umeå University Hospital, Umeå, Sweden.

[4]Department of Engineering Sciences, Uppsala University, Box 534, SE-75121, Uppsala, Sweden.

[5]Sector of Biotechnology and Nanomedicine, SINTEF Materials and Chemistry, N-7465, Trondheim, Norway.

[*]Corresponding author's email address: sulalit.bandyopadhyay@ntnu.no

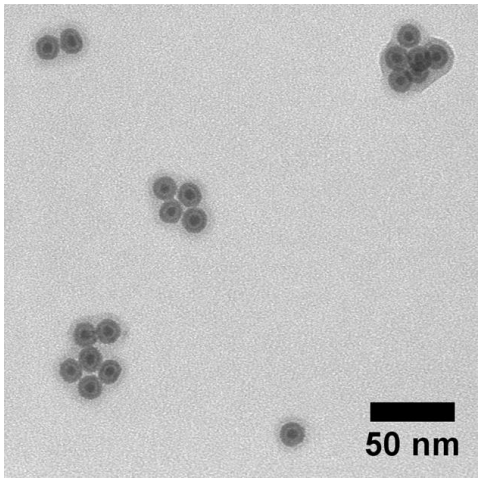

Figure S1 BF S(T)EM image of citrate stabilized Fe NPs in an aqueous phase

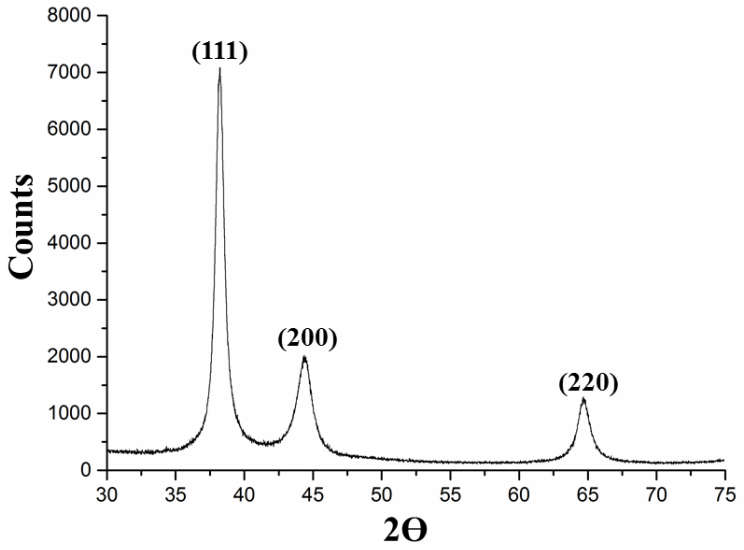

Figure S2 XRD pattern of Fe@Au NPs synthesized at high concentration of gold precursor (3.4 mM).

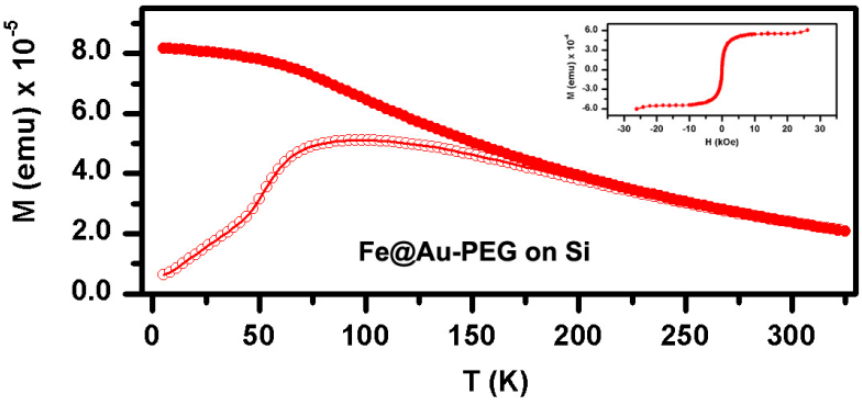

Figure S3 Magnetization hysteresis curves of Fe@Au-PEG deposited on Si. The FC magnetization curves continue to increase until the lowest temperature measured, signifying further weakening of inter particle interactions on addition of PEG molecules. The inset shows the magnetic hysteresis loop measured at 300 K for the same sample.

Paper- II:

Synthesis of Au nanowires with controlled morphological and structural characteristics.

Applied Surface Science 311 (2014) 780–788

Contents lists available at ScienceDirect

Applied Surface Science

journal homepage: www.elsevier.com/locate/apsusc

Synthesis of Au nanowires with controlled morphological and structural characteristics

Gurvinder Singh[a,*], Antonius T.J. van Helvoort[b], Sulalit Bandyopadhyay[a], Sondre Volden[a], Jens-Petter Andreassen[a], Wilhelm R. Glomm[a,c]

[a] Ugelstad Laboratory, Department of Chemical Engineering, Norwegian University of Science and Technology (NTNU), NO-7491 Trondheim, Norway
[b] Department of Physics, Norwegian University of Science and Technology, NO-7491 Trondheim, Norway
[c] SINTEF Materials and Chemistry, Biotechnology and Nanomedicine Sector, NO-7491 Trondheim, Norway

ARTICLE INFO

Article history:
Received 4 March 2014
Received in revised form 22 April 2014
Accepted 23 May 2014
Available online 2 June 2014

Keywords:
Gold
Nanowires
Template synthesis
Nanomaterials
Crystal structure
Surface characterization

ABSTRACT

A growth of one-dimensional noble metal nanostructure with controlled structural characteristic has been under intense investigation as the physical properties, for example, mechanical and electrical properties highly depend on the crystallinity of the nanostructure. Herein, we report a seed-mediated growth of gold nanowires with controlled structural and morphological characteristics, which can easily be varied by selecting appropriate seed nanoparticles, either spherical or rod type in aqueous solution at room temperature. The growth of nanowires was monitored by characterizing the samples at different time period during the reaction, and our observations suggest that growth occurs from seeds rapidly growing along one-dimension followed by surfactant induced fusion or welding and surface diffusion. The aspect ratio and morphology of these NWs can be tuned by CTAB concentration, pH and temperature of the growth solution. We show that the aspect ratio and morphology of these NWs can be tuned by the surfactant concentration, pH and temperature of the growth solution. Electron microscopy and X-ray Photoelectron spectroscopic techniques were employed for investigating structural and surface characteristics of nanowires. This approach can possibly help to synthesize nanowires of other metals with controlled crystalline behaviour which is highly essential for understanding their properties and practical applications in nanoelectronics, optical devices, catalysis, and sensors.

1. Introduction

The synthesis of anisotropic nanostructures, such as wires, belts, ribbons, tubes, and rods has been a focus of intensive investigation owing to their superior size- and shape-dependent physical properties compared to their bulk counterparts [1,2]. In particular, nanowires (NWs) made from noble metals such as gold (Au) are promising materials because they show excellent electrical, thermal and mechanical properties in addition to chemical inertness, making them ideal candidates for a range of technological applications such as catalysis, sensors, surface-enhanced spectroscopy, optical waveguides, light-emitting diodes, nanoelectronics and biomedicine/diagnostics [3–13]. Recently, it has also been shown that Au NWs incorporated into a porous scaffold can be used for repairing diseased heart tissue [14].

In the recent decade, various strategies have been proposed for the synthesis of Au NWs such as the template assisted method [15–20], oriented assembly of nanoparticles [21], physical vapor deposition [22], wet chemical synthesis based on surfactant-directed [23,24], and seed-mediated growth [5,25]. Moreover, biomineralization-inspired synthesis of Au NWs has also been reported by using *Rhodopseudomonas capsulata* under ambient conditions [26]. Among the reported synthetic strategies, seed-mediated growth has emerged as the most robust approach, capable of producing a variety of aspect ratios and morphologies from Au nanorods (NRs) and -wires to polyhedra, prisms, plates and branched nanoparticles [27–30]. Here, a surfactant such as cetyltrimethylammonium bromide (CTAB) acts as a soft template, directing the growth by diffusing Au atoms or nanoparticles into the seed particles in multiple steps forming long NWs in aqueous solution. For example, Kim et al. reported the synthesis of Au NWs of lengths up to 10 μm via a three step seed-mediated method under highly acidic conditions (pH < 3) [25]. In addition, Au NWs synthesis has also been attempted at the air–liquid interface by immersing an Au coated platinum tip into a growth solution at

* Corresponding author. Tel.: +47 73550339.
E-mail addresses: gurvinder.singh@ntnu.no (G. Singh), Wilhelm.Glomm@sintef.no (W.R. Glomm).

http://dx.doi.org/10.1016/j.apsusc.2014.05.162
0169-4332/

room temperature [31]. Later, Zhu et al. further investigated this interfacial growth mechanism and found a structural change in CTAB molecules adsorbed on Au NWs from a hydrophilic layer to a hydrophobic monolayer, enriching the air–liquid interface with NWs [32].

Although several approaches succeeded in producing Au NWs with tunable aspect ratios, growth of Au NWs with controlled morphological/structural characteristics and their underlying growth process are areas in strong need of further elucidation. Tailoring of these characteristics of NWs is essential to achieve better control over the physical properties, for example, mechanical properties can be altered by controlling lattice defects (e.g., twinning, grain size etc.) that cause hindrance to dislocation motion in the structure [12,33]. Moreover, the growth of low and high aspect ratio Au NRs has been studied over a wide range of pH upto ~7 via this seed-mediated approach [34,35], but reports on NWs synthesis with controlled structural characteristics (polycrystalline versus single crystalline) in a solution of pH from ~3 to 11 are scarce [25]. Here, we have investigated this seed mediated approach for the synthesis of Au NWs using CTAB as a soft template and show that morphological/structural characteristics of NWs can be controlled by choosing appropriate type of seed nanoparticles such as spheres and rods which is the first reporting to the best of our knowledge (Fig. 1). The growth involves reduction of Au salt by ascorbic acid (AA) in the presence of seeds, and preferential adsorption of structural directing CTAB molecules onto growing nanostructures, leading to more rapid growth along one direction. We further monitored the growth of Au NWs and observed that NWs were formed as results of fusion of growing nanostructures followed by surface diffusion. In addition, Au NWs of tunable aspect ratio can be obtained by adjusting the pH of the solution.

2. Experimental

2.1. Materials

Sodium borohydride ($NaBH_4$), and sodium hydroxide (NaOH) were received from Alfa Aesar and VWR. Gold (III) chloride trihydrate ($HAuCl_4{\cdot}3H_2O$), silver nitrate ($AgNO_3$), L-ascorbic acid (AA) and potassium bromide (KBr) were all received from Sigma Aldrich. Cetyltrimethylammonium bromide (CTAB), and sodium citrate dehydrate (NaCA) was obtained from Fisher Scientific and Merck. All chemicals were used as received without further purification.

2.2. Synthesis of gold NWs

2.2.1. Preparation of NWs from spherical nanoparticles (seed 1)

0.5 mL of 10 mM NaCA solution and 0.5 mL of 10 mM $HAuCl_4{\cdot}3H_2O$ solution were added into a glass vial containing 18.4 mL of deionized water. Ice cold solution of 100 mM $NaBH_4$ (0.6 mL) was rapidly added to NaCA + $HAuCl_4{\cdot}3H_2O$ solution under vigorous stirring, and the solution immediately turns orange-red colour. The stirring was further continued for 3 min, and the seed solution was kept undisturbed at room temperature for 3 h prior to use in growth solution. Three step seeding procedure was used to synthesize wavy NWs. For this, three different growth solutions labelled as A, B, and C contain 9 mL aqueous solution containing 100 mM CTAB and 10 mM $HAuCl_4{\cdot}3H_2O$ followed by adding 50 μL of 100 mM AA and 50 μL of 100 mM NaOH. First, 1 mL of seed solution was introduced into vial A, and shaken for 5 s. Then, 1 mL solution from vial A is transferred to vial B, and again shaken for 5 s. Finally, 1 mL solution from vial B is added into vial C, and after shaking for 10 s, the vial is left undisturbed for 24 h at room temperature. After the reaction, the solution was centrifuged for 15 min at 1500 rpm to separate NWs from irregular shaped reaction byproduct.

2.2.2. Preparation of NWs from nanorods (seed 2)

The gold nanorods seed of aspect ratio ~3 were prepared by two step process as reported by Ye et al. [38]. In a first step, gold seeds were grown by injecting 0.6 mL of freshly made 10 mM $NaBH_4$ solution into an aqueous solution containing 0.5 mM $HAuCl_4{\cdot}3H_2O$, and 200 mM CTAB under vigorous stirring. The solution colour turns into brownish-yellow and the stirring was continued for 3 min. The seed solution was aged for 30 min prior to use. Later, 96 μL of seed solution was introduced into a growth solution which was prepared in 50 mL glass vial by adding solutions in the following sequence: 15 mL of 100 mM CTAB solution and 118 mM KBr, 750 μL of 4 mM $AgNO_3$, 15 mL of 1 mM $HAuCl_4{\cdot}3H_2O$, and, 135 μL of 64 mM AA. The solution was left undisturbed at room temperature for 5 h prior to use. For the synthesis of NWs from seed 2, the growth solution was prepared in 25 mL glass vial by adding 50 μL of 100 mM AA and 50 μL of 100 mM NaOH into 9 mL aqueous solution containing 100 mM CTAB and 10 mM $HAuCl_4{\cdot}3H_2O$. After introducing 100 μL of seed solution to the growth solution, the reaction was kept without any stirring for 24 h at room temperature. Finally, the solution was centrifuged for 15 min at 1500 rpm to remove reaction byproducts, and NWs were dispersed in deionized water.

2.3. Characterization techniques

Scanning electron microscopy (SEM) and bright field scanning transmission electron microscopy (BF STEM) images were collected from Hitachi S-5500 operating at 30 kV accelerating voltage. Transmission electron microscopy (TEM) was done on a Philips CM30 and a JEOL 2010F, both operated at 200 kV. X-ray photoelectron spectroscopy (XPS) analysis were performed using a Kratos Axis Ultra DLD spectrometer (Kratos Analytical, UK), equipped with a monochromator alumina source ($Al_{k\alpha}$, $h\nu$ = 1486.6 eV). Specimens for SEM and XPS analysis were prepared by placing a few μl NWs solution on a 5 mm^2 silicon (1 0 0) wafers (Siltronix), and dried under ambient conditions. For TEM same procedure was used but on a 300 mesh Cu TEM grid with holey C-film (Ladd Research, USA).

3. Results and discussion

In a typical process for NWs growth via Fig. 1a, spherical seeds of average size ~6.2 nm (seed 1) are used as shown in Fig. 2(a). Later, these seeds were added to a growth solution prepared by injecting AA and NaOH into an aqueous solution of Au salt and CTAB. AA rapidly turns from an orange complex solution of Au salt + CTAB into a colourless solution, indicating the reduction of Au^{3+} to Au^{+} at room temperature. The addition of NaOH enhances the reducing power of AA by increasing the pH of the solution, and accelerates a further reduction of Au^{+} ions to their metallic form (Au) [32,34]. Fig. 2(b and c) displays a BF STEM image of Au nanostructures having wire like morphology with aspect ratios greater than 10^3. The average diameter of the Au NWs was determined to be ~17 ± 5 nm based on STEM analysis, while their average lengths were observed to be 35 ± 5 μm. The morphology of as-synthesized NWs appears wavy in nature with several kinks and small straight regions. The TEM diffraction pattern of single NWs reveals ring is made up of several discrete dark spots originating from multiple crystalline domains within the NWs (shown in inset of Fig. 2(c)). In this case, NWs can be considered as polycrystalline rather than to single crystalline. In the absence of NaOH, the seed nanoparticles slowly autocatalyze the reduction of Au^{+} ions to Au. As a result, Au NRs of aspect ratio ~13 were obtained over the same time period which has been previously studied by Gao et al. (see Fig. 1(d)) [36]. In addition, such Au NRs also exhibit twinning defects along the

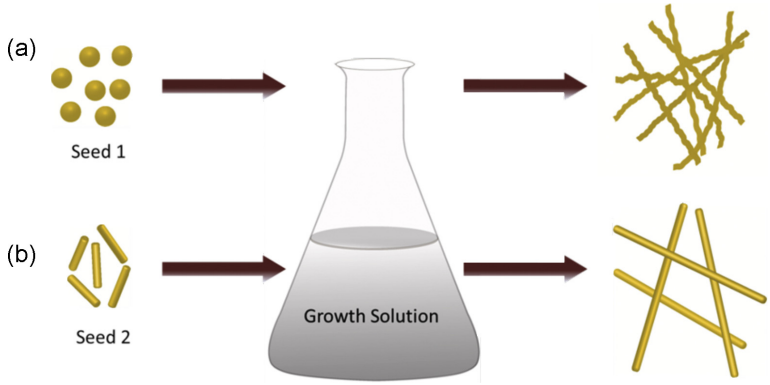

Fig. 1. Schematic illustration showing Au NWs growth via two different types of seed nanoparticles, (a) spherical nanoparticles yield wavy NWs, and (b) NRs yield straight NWs.

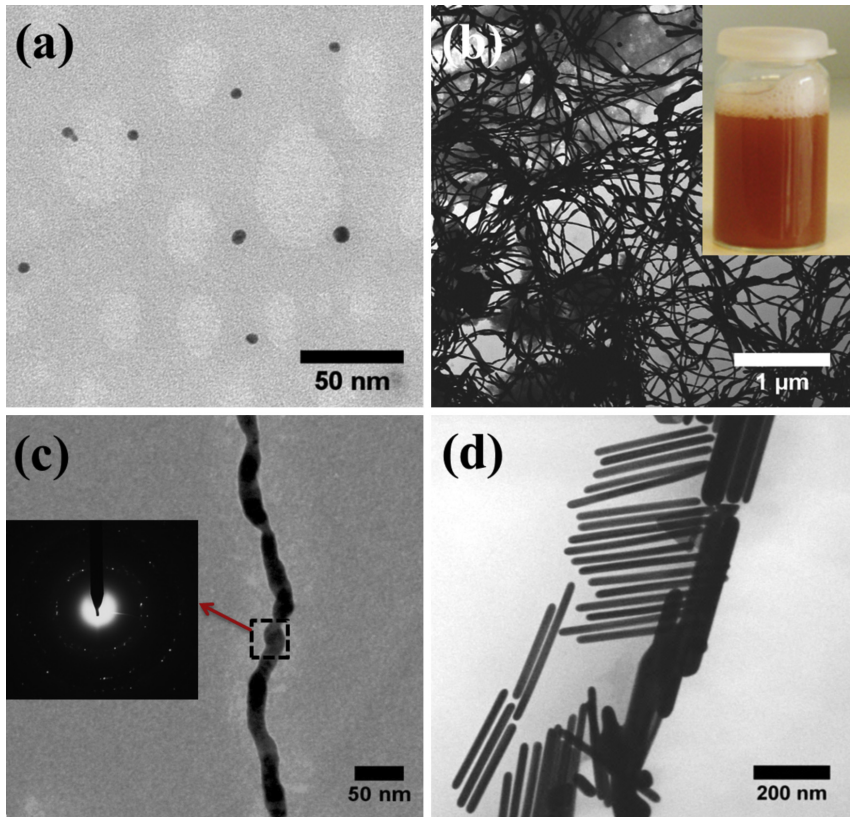

Fig. 2. BF STEM images of (a) spherical Au seed nanoparticles (seed 1) and (b) Au NWs growth from seed 1 at pH = ~6.9 and inset shows photograph of the brown colour solution of final reaction product. (c) Enlarged BF TEM image of Au NWs (insert in (c) is a diffraction pattern corresponding to square region confirming the polycrystallinity in the NWs), and (d) Au NRs synthesized from seed 1in the absence of NaOH. (For interpretation of the references to color in this figure legend, the reader is referred to the web version of the article.)

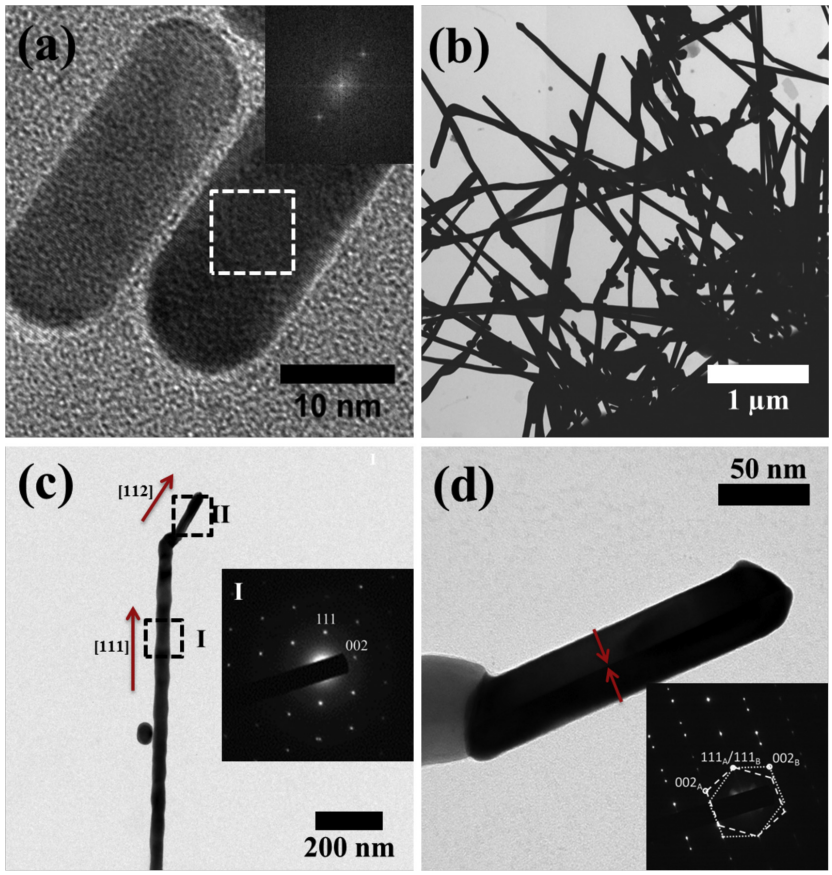

Fig. 3. (a) BF TEM images of Au NRs of seed type 2 (inset: FFT pattern of the square region indicating 1 1 1 lattice spacing along the rod axis). (b) BF STEM image of straight Au NWs grown from seed 2 at pH = ~6.9. (c) Enlarged BF TEM view of single NWs synthesized by seed 2 (inset: diffraction pattern corresponding to the region I confirming that NWs growth direction is [1 1 1]. (d) Enlarged TEM image of the region II shown in panel (c) indicating twinning perpendicular to the long axis (marked between the arrows), and its corresponding diffraction pattern confirming twinning along [1 1 2] in the long axis. Indices A and B refer to two orientations of the Au lattice.

growth direction [1 0 0] suggesting polycrystalline behaviour (see high resolution TEM image in Fig. S1 in the Supporting Information) [37]. Thus, an adequate amount of NaOH is necessary for growing long NWs.

Interestingly, the morphological/structural characteristics of the NWs can be altered by replacing the spherical nanoparticle seeds with NRs (seed 2) as shown in Fig. 1b. The single crystalline NRs of aspect ratio ~2.7 were synthesized by a protocol reported in literature (see Figs. 3(a) and S2 available in the Supporting Information) [38]. Under identical reaction conditions, less wavy, more straight and thicker NWs (diameter~51 ± 5 nm, of average length ~ 20 ± 5 μm and aspect ratio ~400) with fewer number of kinks was observed (see Fig. 3(b)). Electron diffraction patterns obtained by focusing the electron beam onto the long single NWs and small NR attached to long NWs are displayed in Fig. 3(c and d). Based on this observation, we found that long NWs are single crystalline, growing rapidly along the [1 1 1] direction (see inset in Fig. 3(c)). To the contrary, short and twinned NRs type nanostructures are formed when the growth occurs along the [1 1 2] direction, suggesting this being an unfavourable growth direction (see Fig. 3(d) and inset). These short NRs were obtained as an unwanted reaction byproduct either attached to long growing NWs or remain in the solution. These findings show that nanorod type seeds can be used to significantly foster the growth of long one-dimensional (1D) NWs and an appropriate selection of the seed type is a crucial to control morphology/structural characteristics of NWs. The key advantage associated with this approach is that by scaling up the reaction 10 times, the yield of Au NWs can be increased (see Figs. S3 and S4 available in the Supporting Information).

We have monitored the growth reaction of Au NWs in this seed-mediated method by collecting samples at different time intervals followed by quick drying onto substrates suitable for electron microscopy investigation (see Fig. 4). The growth solution slowly turns into a light pink colour after the addition of citrate capped seed 1 indicating the enlargement of seed nanoparticles by reduction of Au^{+} at an early stage. Fig. 4(a) reveals spherical nanoparticles of average size ~10 nm except for a few elongated nanoparticles. As the reaction progresses, the nanoparticles

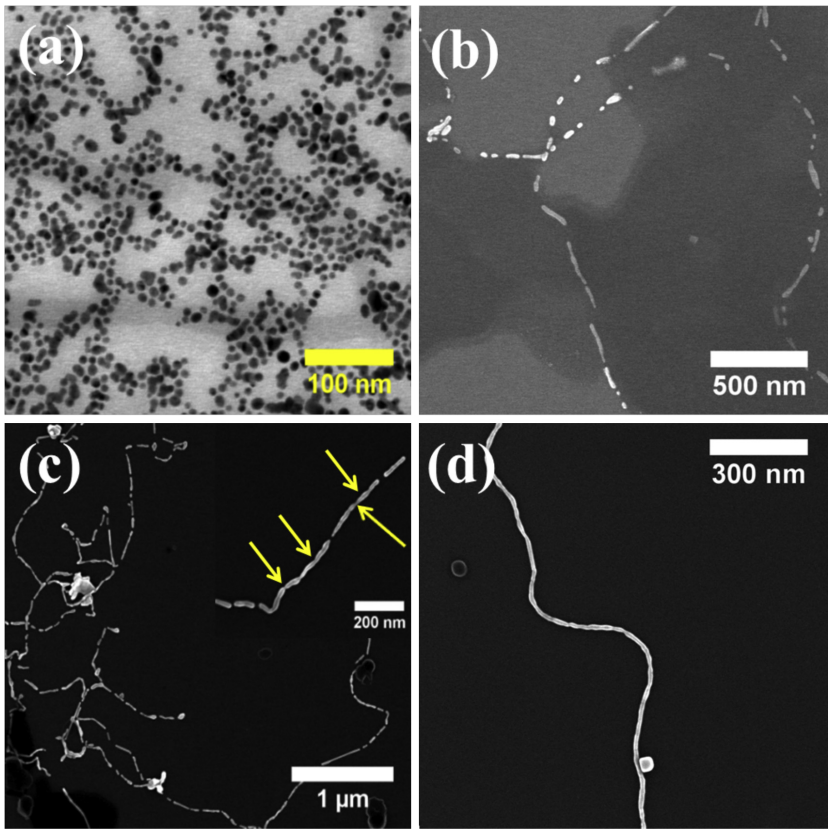

Fig. 4. Evolution of Au NWs growth over time, t (a) BF STEM image, t = 10 min, (b) SEM image, t = 30 min (c) SEM image, t = 60 min (the arrows in the inset is showing convex/concave regions or neck formation between two adjacent growing nanostructures), and (d) SEM image, t = 120 min.

eventually evolve into small NRs. It has been known that different crystalline facets possess different surface energies in the following ascending order: γ {1 1 1} < γ {1 0 0} < γ {1 1 0} [1]. The lowest surface energy of {1 1 0} among the other facets results in the adsorption of CTAB bilayer on the 110 facets as soon as gold seed evolves into nanoparticles containing different facets. Thus, the growth occurs more rapidly in the longitudinal direction than that in the transverse direction in the presence of templating CTAB molecules. The 1D alignment of variable length growing nanostructures is evident in Fig. 4(b), suggesting the onset of NWs growth between 10 and 30 min. When the reaction is carried out for 60 min, NRs further grow in size by fusing with neighbouring nanoparticles (see Fig. 4(c)). At the same time, several concave/convex regions, i.e., the physical contacts of two associating nanostructures can be identified (marked by arrows in inset of Fig. 4c). The physical contacts can occur either by surfactant induced fusion or welding due to diffusion of atoms between growing nanostructures [32,39]. These NWs can be smoothened either by permitting the surface diffusion of Au atoms along the NWs because of low energy barriers at room temperature, or from additional deposition of freshly reduced Au atoms into these regions through localized Ostwald ripening (see Fig. 4d) [40,41]. When the reaction proceeds for 24 h, continuous growth and diffusion processes result into continuous and wavy high aspect ratio NWs as shown in Fig. 2b. This proposed mechanism is in agreement with previous reports where they grow metallic NWs by different methods [32,42,43]. Similar results were also obtained by monitoring NWs growth via seed 2 nanoparticles (see Fig. S5 available in the Supporting Information).

The variation in the morphology/structural characteristics of Au NWs produced by two different types of seeds may be explained by considering the crystalline behaviour of the seeds as either single crystalline or polycrystalline and based on our observation of NWs growth. It has been noted that citrate capped Au spherical seed types particles are polycrystalline (i.e., multiple crystal domains) in nature [44]. These seeds grow in size by the addition of Au atoms in the growth solution while retaining the polycrystalline behaviour. Subsequently, wavy NWs with multiple crystal domains and twinning form when randomly oriented spherical or elongated nanoparticles unite together. This association of growing nanostructure can occur in between sphere-sphere, nanorod–sphere–nanorod, and nanorod–nanorod suggesting multiple crystalline nature of NWs. In a case of seed 2 type nanoparticles, single crystalline NRs grow in the size along

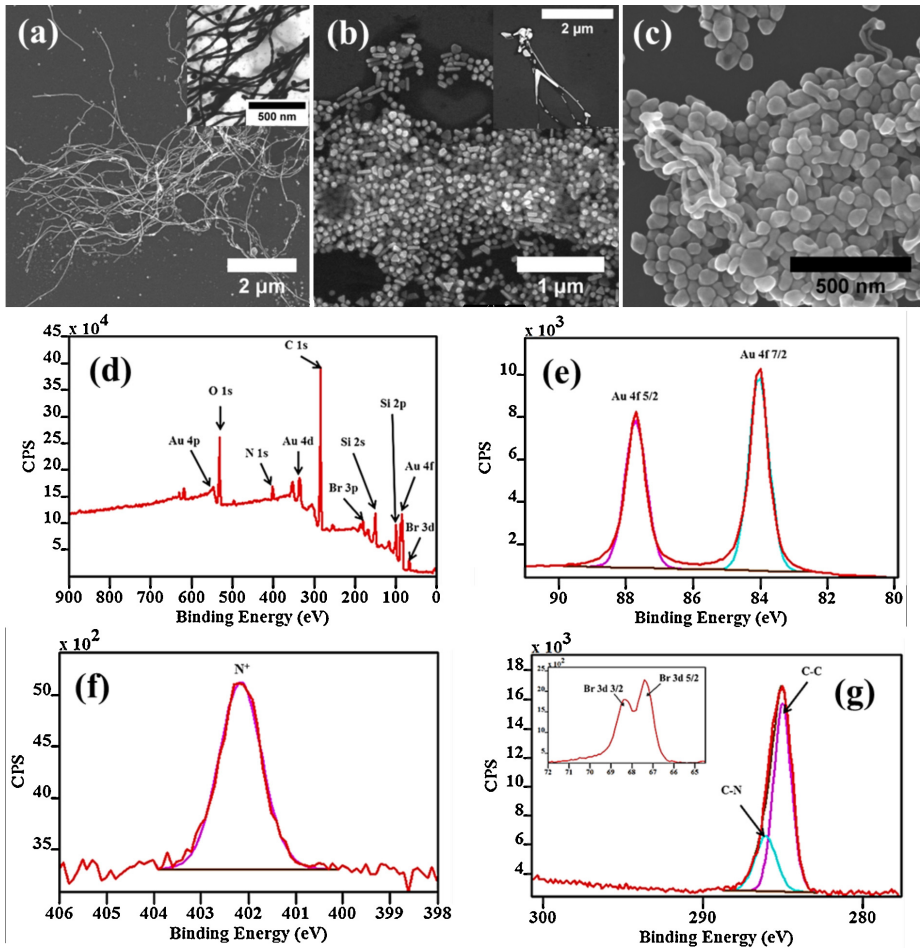

Fig. 5. SEM images of Au NWs growth via seed 1 at different CTAB concentration and fixed pH = ~6.9 (a) 25 mM, (b) 10 mM, (c) 1 mM. Inserts in (a) is BF TEM at higher magnification and in (b) SEM of low aspect ratio NWs. (d) XPS survey spectrum of CTAB capped wavy Au NWs. XPS high resolution spectra of the (e) Au 4f, (f) N 1s, and (g) C 1s (inset: Br 3d).

1D in the presence of CTAB and thus, forming a single crystalline NWs forms by association of growing nanostructures (see Fig. S5 available in the Supporting Information). Similar results were also reported by Karim et al. [45], using a polycarbonate template to grow Au NWs with controlled crystallographic characteristics by tuning the electrolyte conditions to induce polycrystallinity or single crystallinity in seeds.

To investigate how changes in the experimental conditions, for example, the concentration of CTAB, pH of the growth solution and reaction temperature, can influence the morphology and aspect ratio of the NWs, we have used spherical seeds and synthesized NWs under different experimental conditions. First, NWs were produced by varying the CTAB concentration in the growth solution, keeping all other experimental parameters constant. As a soft template, CTAB is known to have a high affinity towards Au salt, and prevents rapid reduction of Au salt by forming a CTA–CTA–$[AuBr_4]^-$ complex because Br^- ions have stronger affinity to bind Au atoms than to Cl^- ions [37]. As shown in Fig. 5(a), when the CTAB concentration was 25 mM, we noticed a mixture of long NWs and variously shaped nanoparticles. When the concentration is further reduced to 10 mM and 1 mM, shorter NWs with a very low yield and an increased amount of irregularly shaped nanoparticles were observed (see Fig. 5(b and c)). Under these conditions, a faster reduction of Au salt produces a surplus of Au atoms in the solution and causes thermodynamically stable shorter, irregular aggregates of large nanoparticles inhibiting NWs growth due to an insufficient amount of Au atoms required to fill the gap at the contact point between two nanoparticles [24,46]. Alternatively, it may also be attributed to aggregation of nanoparticles that are not fully capped by a CTAB bilayer at low surfactant concentration, which does not provide sufficient van der Waals interaction between CTAB layer, causing nanoparticles to merge

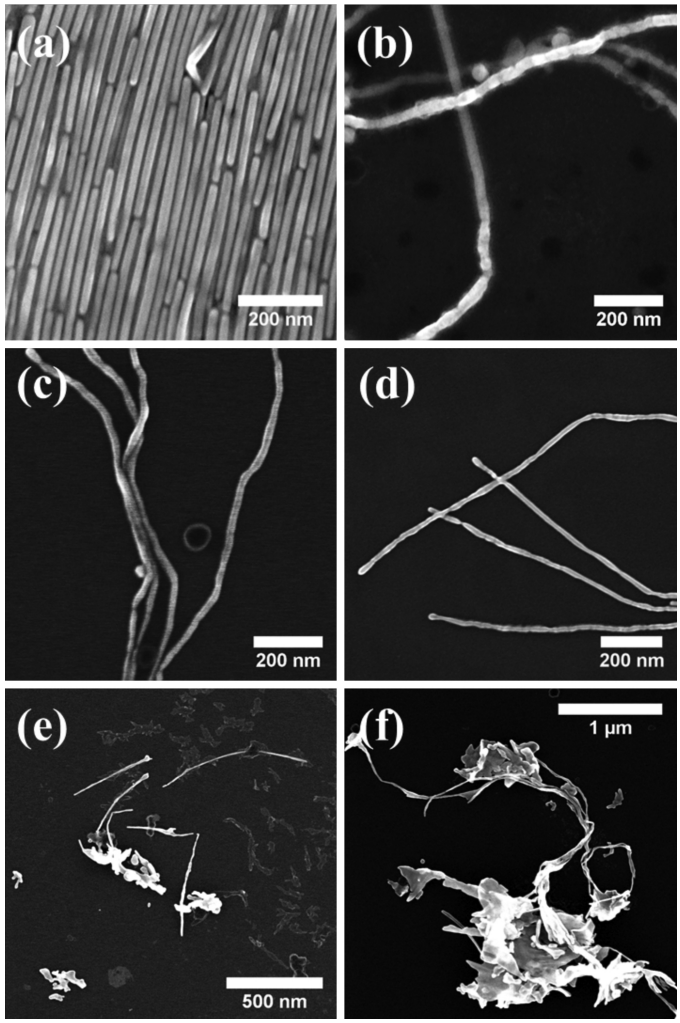

Fig. 6. SEM images showing the effect of growth solution pH on aspect ratio and morphology of as synthesized Au NWs by seed 1 in (a) pH = 3.2, (b) pH = 3.7, (c) pH = 4.1, (d) pH = 4.7, (e) pH = 8.1, and (f) pH = 11.0.

in a random fashion and form irregular shaped nanoparticles [32]. These results suggest that an excess amount of CTAB is essential for producing long and continuous NWs.

We further characterized the presence of CTAB molecules on the surface of Au NWs by X-ray photoelectron spectroscopy (XPS). The presence of Au, N, C, and Br peaks in an XPS survey spectrum are indicative of CTAB capped Au NWs (see Fig. 5(d)). Typical doublet peaks for Au (0) located at ~84.0 eV and ~87.6 eV can be seen in a high resolution XPS spectrum (see Fig. 5(e)). The N 1s peak can be assigned to quaternary ammonium (N^+) which is shifted towards a higher binding energy (~402.3 eV) and higher than pure CTAB due to the Au surface vicinity (see Fig. 5(f)) [47]. The C 1s peak splits in two components with binding energies of ~286 eV from C—N and ~285 eV from the aliphatic carbons, C—C (see Fig. 5(g)). Furthermore, a shift in Br $3d_{5/2}$ peak to ~67.4 eV in compared to bulk CTAB (~68.7 eV) is observed following binding of Br to the Au surface, which is quite consistent with previous reports [32,47]. Therefore, XPS results confirm the presence of only CTAB species on the surface of Au NWs.

Next, the effect of growth solution pH on the aspect ratio of Au NWs was examined while keeping all other experimental conditions identical. The experimental results show that the aspect ratio of the Au NWs decreases from ~415 to ~18 with the reduction in the pH of the solution from 4.7 to 3.2, which is adjusted by amount of added AA to the growth solution. (see Fig. 6(a–d)). The reduction agent, AA has pK_a value ~4.1, and can exist in two different forms,

i.e., protonated AA and deprotonated AA^- depending on the pH of the solution [34]. Deprotonated AA^- is more efficient reducing agent than to protonated AA due to the low energy barrier during electron transfer between the AA^- and CTA-$[AuBr_4]^-$ complex, which results in the increase of redox reaction rate [48]. Thus, such behaviour suggests a pH dependent redox reaction rate. At pH = 4.4 which is above pK_a value of AA, a large fraction of deprotonated AA^- present in the growth solution enhances the rate of redox reaction and results in NWs of high aspect ratio. As the pH of the growth solution decreases further below 4.1, the fraction of protonated AA increases more in comparison to deprotonated AA^- and a slow rate of redox reaction results in NWs of low aspect ratio. Other work has also found similar results suggesting a decrease in redox reaction rate or aspect ratio of nanomaterials with decreases in pH [34]. In contrast, when the pH of the solution is increased to ~8.1 and ~11.0, we observe a low yield of shorter length NWs (2–5 μm) with an increased amount of reaction byproducts of other morphologies such as flakes, and irregular shaped objects (see Figs. 6e, f and S6 available in the Supporting Information). In this case, a large fraction of deprotonated AA^- accelerates the redox reaction rapidly, producing an excess amount of Au atoms which has a high tendency to induce an irregular growth of seed nanoparticles, resulting an increase in irregularly shaped objects. Thus, the pH of the growth solution is a critical parameter for controlling the aspect ratio and morphology of NWs.

We further studied the effect of temperature on Au NWs formation. As the temperature is increased from 30 °C to 75 °C, rather irregularly shaped nanoparticles with a few nanorods were noticed compared to NWs synthesized at 30 °C (see Fig. S7 available in the Supporting Information). This behaviour can be explained by considering the stabilization of CTAB bilayer and the reaction growth rate. The "Krafft point" of CTAB is known to be ~20 °C at which micellar formation occurs, allowing shape-controlled growth of nanomaterials. At higher temperatures, the supramolecular structure of CTAB becomes unstable due to large molecular agitation or thermal fluctuations causing molecular disorderness [49]. This result further verifies the role of CTAB as a structure directing agent in the NWs formation. On the other hand, the rate of reaction increases with increment in temperature leading to faster supply of Au atoms, and formation of irregularly shaped nanoparticles occurs [48]. Similarly, effects of pH and temperature on NWs growth were also seen when NRs were used as seeds for growing NWs (see Figs. S8 and S9 available in the Supporting Information).

4. Conclusions

In summary, a general seed-mediated approach was demonstrated for the growth of variable aspect ratio NWs by employing CTAB acting as capping agent and soft template at room temperature. We show that it is possible to tune the morphological/structural characteristics of Au NWs by employing spherical or rod type seed nanoparticles. From our observations, Au NWs growth starts from seed nanoparticles followed by physical contacts between growing nanostructures and surface diffusion or/glueing of freshly reduced Au atoms, facilitating the formation of long and continuous NWs. These Au NWs are capped by CTAB molecules which is evident from XPS results. Furthermore, the effect of various experimental parameters such as CTAB concentration, pH and temperature on the Au NWs growth was studied. Here, we found that the rate of redox reaction should be moderate otherwise a too high reaction will lead to low yield of Au NWs with increment in the irregular shaped Au nanoparticles. Thus, we propose a new method for the synthesis of Au NWs which can easily be scaled up for bulk production and opens up possibilities for other research groups to study mechanical, catalytic and electrical properties of these morphological/structurally controlled Au NWs.

Acknowledgements

We thank NTNU Nanolab for providing instrumentation facilities. The Research Council of Norway is acknowledged for the support to the Norwegian Micro-and Nano-Fabrication Facility, NorFab (197411/V30).

Appendix A. Supplementary data

Supplementary data associated with this article can be found, in the online version, at http://dx.doi.org/10.1016/j.apsusc.2014.05.162.

References

[1] Y.N. Xia, P.D. Yang, Y.G. Sun, Y.Y. Wu, B. Mayers, B. Gates, Y.D. Yin, F. Kim, Y.Q. Yan, One-dimensional nanostructures: synthesis, characterization, and applications, Adv. Mater. 15 (2003) 353–389.
[2] Z.Y. Tang, N.A. Kotov, One-dimensional assemblies of nanoparticles: preparation, properties, and promise, Adv. Mater. 17 (2005) 951–962.
[3] M.T. Carlson, A.J. Green, A. Khan, H.H. Richardson, Optical measurement of thermal conductivity and absorption cross-section of gold nanowires, J. Phys. Chem. C 116 (2012) 8798–8803.
[4] M. Chirea, A. Freitas, B.S. Vasile, C. Ghitulica, C.M. Pereira, F. Silva, Gold nanowire networks: synthesis, characterization, and catalytic activity, Langmuir 27 (2011) 3906–3913.
[5] K. Critchley, B.P. Khanal, M.L. Gorzny, L. Vigderman, S.D. Evans, E.R. Zubarev, N.A. Kotov, Near-bulk conductivity of gold nanowires as nanoscale interconnects and the role of atomically smooth interface, Adv. Mater. 22 (2010) 2338–2342.
[6] K. Dawson, M. Baudequin, A. O'Riordan, Single on-chip gold nanowires for electrochemical biosensing of glucose, Analyst 136 (2011) 4507–4513.
[7] K. Dawson, J. Strutwolf, K.P. Rodgers, G. Herzog, D.W.M. Arrigan, A.J. Quinn, A. O'Riordan, Single nanoskived nanowires for electrochemical applications, Anal. Chem. 83 (2011) 5535–5540.
[8] H.J. Feng, Y.M. Yang, Y.M. You, G.P. Li, J. Guo, T. Yu, Z.X. Shen, T. Wu, B.G. Xing, Simple and rapid synthesis of ultrathin gold nanowires, their self-assembly and application in surface-enhanced Raman scattering, Chem. Commun. (2009) 1984–1986.
[9] N.I. Kovtyukhova, T.E. Mallouk, Nanowires as building blocks for self-assembling logic and memory circuits, Chem. Eur. J. 8 (2002) 4355–4363.
[10] C.W. Kuo, A.J. Lai, K.H. Wei, P. Chen, Studies of surface-modified gold nanowires inside living cells, Adv. Funct. Mater. 17 (2007) 3707–3714.
[11] Q.Q. Wang, J.B. Han, D.L. Guo, S. Xiao, Y.B. Han, H.M. Gong, X.W. Zou, Highly efficient avalanche multiphoton luminescence from coupled Au nanowires in the visible region, Nano Lett. 7 (2007) 723–728.
[12] B. Wu, A. Heidelberg, J.J. Boland, Mechanical properties of ultrahigh-strength gold nanowires, Nat. Mater. 4 (2005) 525–529.
[13] X.P. Zhang, B.Q. Sun, J.M. Hodgkiss, R.H. Friend, Tunable ultrafast optical switching via waveguided gold nanowires, Adv. Mater. 20 (2008) 4455–4459.
[14] T. Dvir, B.P. Timko, M.D. Brigham, S.R. Naik, S.S. Karajanagi, O. Levy, H. Jin, K.K. Parker, R. Langer, D.S. Kohane, Nanowired three-dimensional cardiac patches, Nat. Nanotechnol. 6 (2011) 720–725.
[15] H. Bai, K. Xu, Y. Xu, H. Matsui, Fabrication of Au nanowires of uniform length and diameter using a monodisperse and rigid biomolecular template: collagen-like triple helix, Angew. Chem. Int. Ed. 119 (2007) 3383–3386.
[16] M. Wirtz, C.R. Martin, Template-fabricated gold nanowires and nanotubes, Adv. Mater. 15 (2003) 455–458.
[17] X.M. Lu, M.S. Yavuz, H.Y. Tuan, B.A. Korgel, Y.N. Xia, Ultrathin gold nanowires can be obtained by reducing polymeric strands of oleylamine–AuCl complexes formed via aurophilic interaction, J. Am. Chem. Soc. 130 (2008) 8900–8901.
[18] C.X. Kan, W.P. Cai, G.H. Fu, C.C. Li, L.D. Zhang, Synthesis and thermal stability of gold nanowires within monolithic mesoporous silica, Appl. Phys. A 78 (2004) 1187–1191.
[19] M.S. Bakshi, F. Possmayer, N.O. Petersen, Aqueous-phase room-temperature synthesis of gold nanoribbons: soft template effect of a Gemini surfactant, J. Phys. Chem. C 112 (2008) 8259–8265.
[20] M. Ding, D.C. Sorescu, G.P. Kotchey, A. Star, Welding of gold nanoparticles on graphitic templates for chemical sensing, J. Am. Chem. Soc. 134 (2012) 3472–3479.
[21] A. Halder, N. Ravishankar, Ultrafine single crystalline gold nanowire arrays by oriented attachment, Adv. Mater. 19 (2007) 1854–1858.
[22] C.E. Cross, J.C. Hemminger, R.M. Penner, Physical vapor deposition of one-dimensional nanoparticle arrays on graphite: seeding the electrodeposition of gold nanowires, Langmuir 23 (2007) 10372–10379.
[23] M.S. Bakshi, G. Kaur, P. Thakur, T.S. Banipal, F. Possmayer, N.O. Petersen, Surfactant selective synthesis of gold nanowires by using a DPPC–surfactant mixture as a capping agent at ambient conditions, J. Phys. Chem. C 111 (2007) 5932–5940.

[24] S. Navaladian, C.M. Janet, B. Viswanathan, T.K. Varadarajan, R.P. Viswanath, A facile room-temperature synthesis of gold nanowires by oxalate reduction method, J. Phys. Chem. C 111 (2007) 14150–14156.
[25] F. Kim, K. Sohn, J.S. Wu, J.X. Huang, Chemical synthesis of gold nanowires in acidic solutions, J. Am. Chem. Soc. 130 (2008) 14442–14443.
[26] S.Y. He, Y. Zhang, Z.R. Guo, N. Go, Biological synthesis of gold nanowires using extract of *Rhodopseudomonas capsulata*, Biotechnol. Prog. 24 (2008) 476–480.
[27] J.Y. Xiao, L.M. Qi, Surfactant-assisted, shape-controlled synthesis of gold nanocrystals, Nanoscale 3 (2011) 1383–1396.
[28] T.K. Sau, C.J. Murphy, Room temperature, high-yield synthesis of multiple shapes of gold nanoparticles in aqueous solution, J. Am. Chem. Soc. 126 (2004) 8648–8649.
[29] A. Gole, C.J. Murphy, Seed-mediated synthesis of gold nanorods: role of the size and nature of the seed, Chem. Mater. 16 (2004) 3633–3640.
[30] M.R. Langille, M.L. Personick, J. Zhang, C.A. Mirkin, Defining rules for the shape evolution of gold nanoparticles, J. Am. Chem. Soc. 134 (2012) 14542–14554.
[31] Z.C. Xu, C.M. Shen, S.H. Sun, H.J. Gao, Growth of Au nanowires at the interface of air/water, J. Phys. Chem. C 113 (2009) 15196–15200.
[32] G. Zhu, H.C. Peng, J. Zeng, J.Y. Liu, Z.Z. Gu, Y.N. Xia, Facile synthesis of gold wavy nanowires and investigation of their growth mechanism, J. Am. Chem. Soc. 134 (2012) 20234–20237.
[33] M. Bernardi, S.N. Raja, S.K. Lim, Nanotwinned gold nanowires obtained by chemical synthesis, Nanotechnology 21 (2010) 285607–285612.
[34] B.D. Busbee, S.O. Obare, C.J. Murphy, An improved synthesis of high-aspect-ratio gold nanorods, Adv. Mater. 15 (2003) 414–416.
[35] Q.S. Wei, J. Ji, J.C. Shen, pH controlled synthesis of high aspect-ratio gold nanorods, J. Nanosci. Nanotechnol. 8 (2008) 5708–5714.
[36] J.X. Gao, C.M. Bender, C.J. Murphy, Dependence of the gold nanorod aspect ratio on the nature of the directing surfactant in aqueous solution, Langmuir 19 (2003) 9065–9070.
[37] J. Perez-Juste, I. Pastoriza-Santos, L.M. Liz-Marzan, P. Mulvaney, Gold nanorods: synthesis, characterization and applications, Coord. Chem. Rev. 249 (2005) 1870–1901.
[38] X.C. Ye, L.H. Jin, H. Caglayan, J. Chen, G.Z. Xing, C. Zheng, D.N. Vicky, Y.J. Kang, N. Engheta, C.R. Kagan, C.B. Murray, Improved size-tunable synthesis of monodisperse gold nanorods through the use of aromatic additives, ACS Nano 6 (2012) 2804–2817.
[39] Y. Lu, J.Y. Huang, C. Wang, S.H. Sun, J. Lou, Cold welding of ultrathin gold nanowires, Nat. Nanotechnol. 5 (2010) 218–224.
[40] N.N. Gosvami, M. Feldmann, J. Peguiron, M. Moseler, A. Schirmeisen, R. Bennewitz, Ageing of a microscopic sliding gold contact at low temperatures, Phys. Rev. Lett. 107 (2011) 144303–144307.
[41] L.H. Pei, K. Mori, M. Adachi, Formation process of two-dimensional networked gold nanowires by citrate reduction of $AuCl_4^-$ and the shape stabilization, Langmuir 20 (2004) 7837–7843.
[42] S.K. Das, A.R. Das, A.K. Guha, Microbial synthesis of multishaped gold nanostructures, Small 6 (2010) 1012–1021.
[43] B.Y. Xia, H. Bin Wu, Y. Yan, X.W. Lou, X. Wang, Ultrathin and ultralong single-crystal platinum nanowire assemblies with highly stable electrocatalytic activity, J. Am. Chem. Soc. 135 (2013) 9480–9485.
[44] M. Grzelczak, J. Perez-Juste, P. Mulvaney, L.M. Liz-Marzan, Shape control in gold nanoparticle synthesis, Chem. Soc. Rev. 37 (2008) 1783–1791.
[45] S. Karim, M.E. Toimil-Molares, F. Maurer, G. Miehe, W. Ensinger, J. Liu, T.W. Cornelius, R. Neumann, Synthesis of gold nanowires with controlled crystallographic characteristics, Appl. Phys. A 84 (2006) 403–407.
[46] J.H. Zhou, J. Zeng, J. Grant, H.K. Wu, Y.N. Xia, On-chip screening of experimental conditions for the synthesis of noble-metal nanostructures with different morphologies, Small 7 (2011) 3308–3316.
[47] F. Hubert, F. Testard, O. Spalla, Cetyltrimethylammonium bromide silver bromide complex as the capping agent of gold nanorods, Langmuir 24 (2008) 9219–9222.
[48] M. Luty-Blocho, K. Paclawski, M. Wojnicki, K. Fitzner, The kinetics of redox reaction of gold(III) chloride complex ions with L-ascorbic acid, Inorg. Chim. Acta 395 (2013) 189–196.
[49] R. Becker, B. Liedberg, P.O. Kall, CTAB promoted synthesis of Au nanorods – temperature effects and stability considerations, J. Colloid Interface Sci. 343 (2010) 25–30.

Supplementary Figures

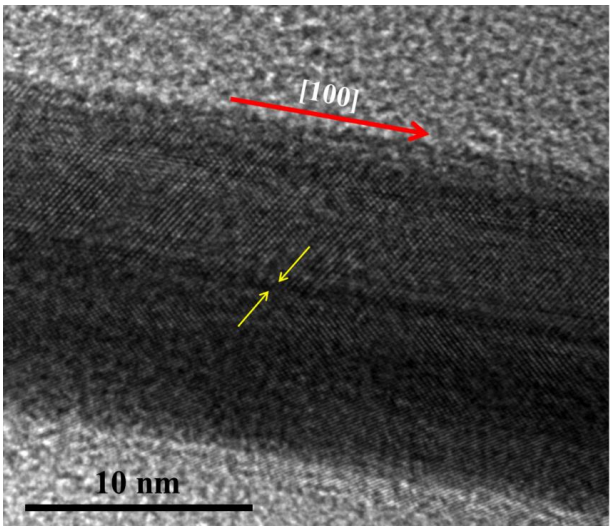

Figure S1. High resolution TEM image of Au NRs synthesized in the absence of NaOH indicating twinning defects (marked by yellow arrows) along the growth direction [100].

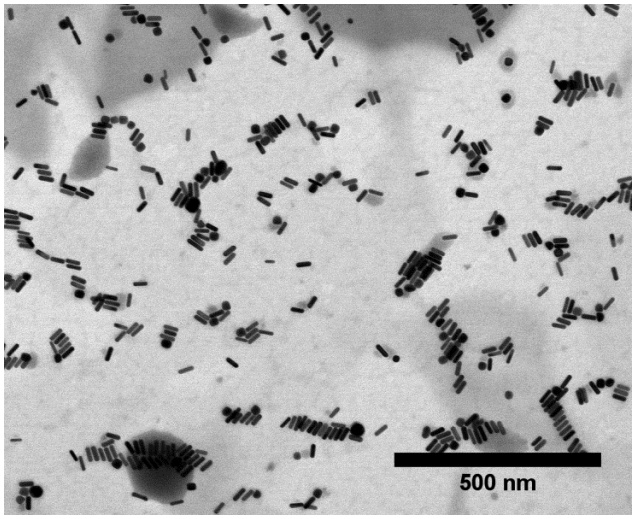

Figure S2. BF STEM image of Au NRs with an average aspect ratio ~3.

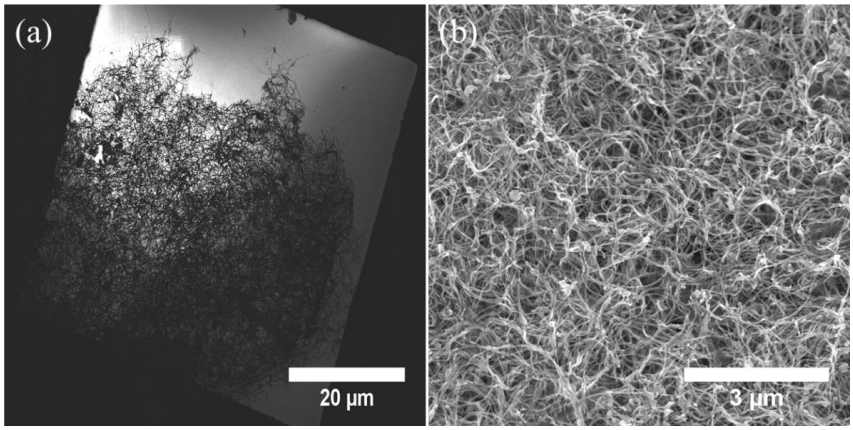

Figure S3. (a) Low magnification BF STEM image and (b) SEM image indicating high yield and homogenity of wavy Au NWs networks grown via seed type 1.

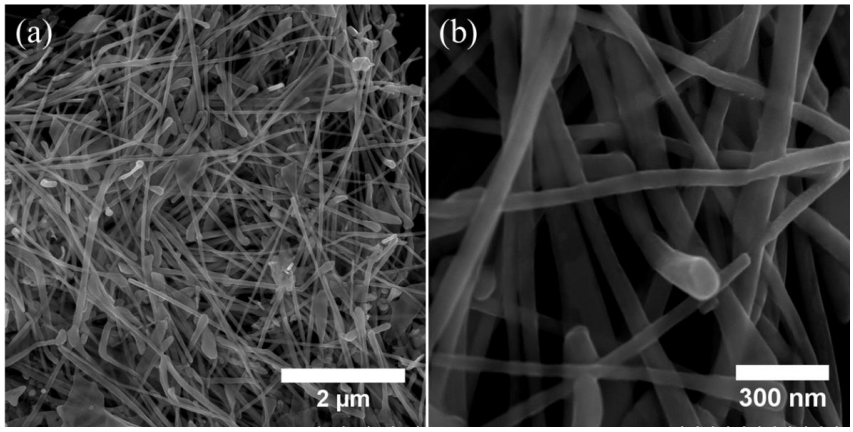

Figure S4. (a) SEM image showing straight and less wavy Au NWs with kinks synthesized by seed 2 and (b) magnified view of image (a).

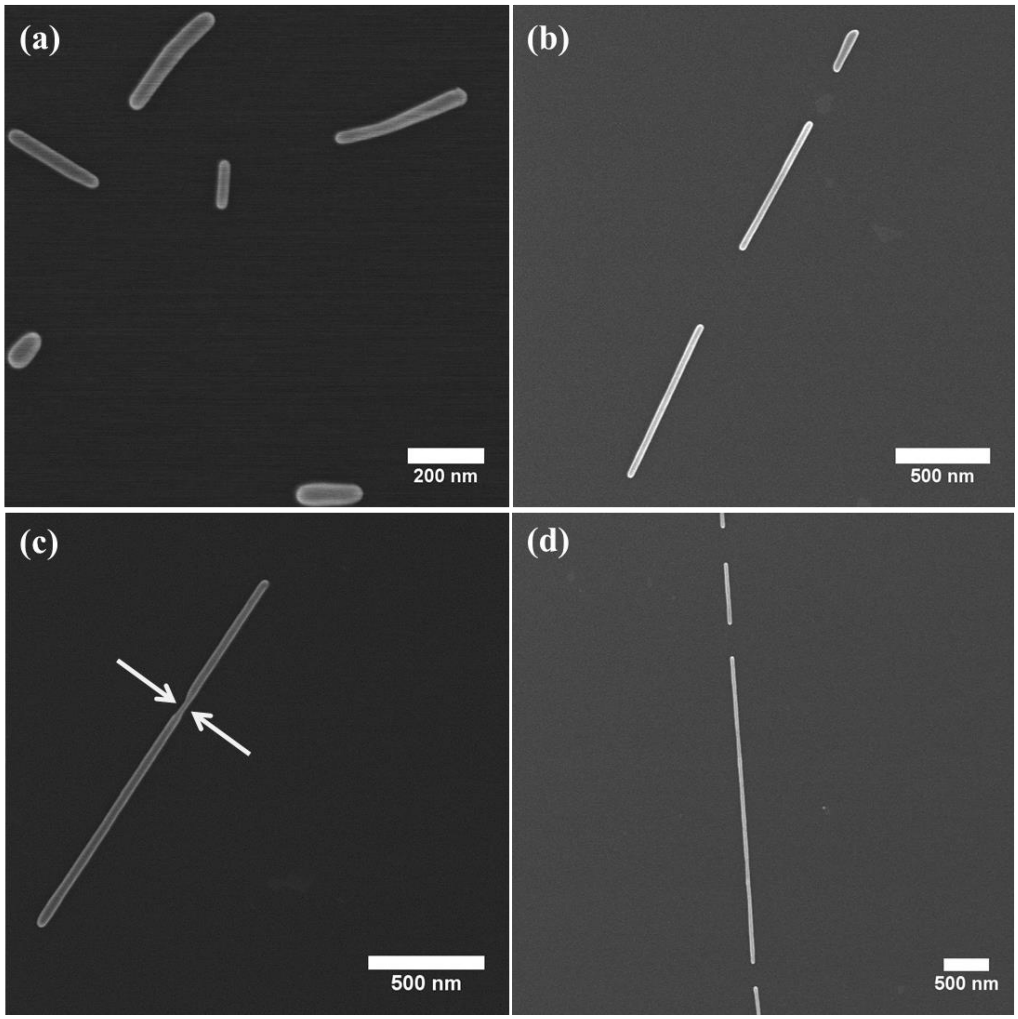

Figure S5. SEM image exhibiting the single crystalline straight NWs growth after a) 10 min, b) 25 min, c) 45 min, b) 90 min. The inward arrow in the (c) showing the neck formation between two adjacent growing nanostructures.

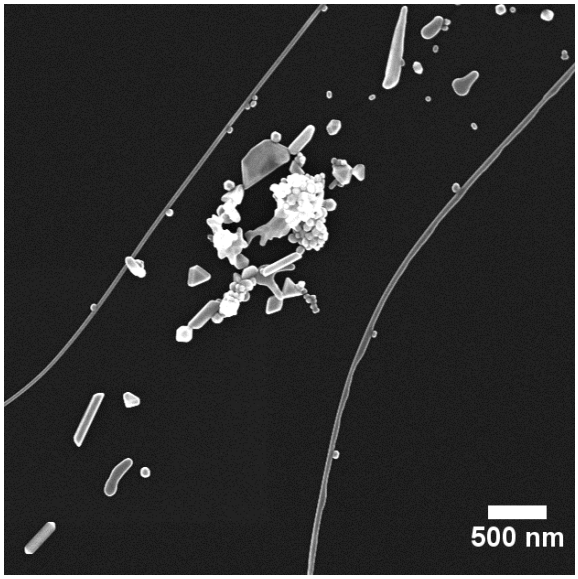

Figure S6. SEM image displaying gold NWs with reaction byproducts on carbon TEM support. Sample was grown at pH=8.1.

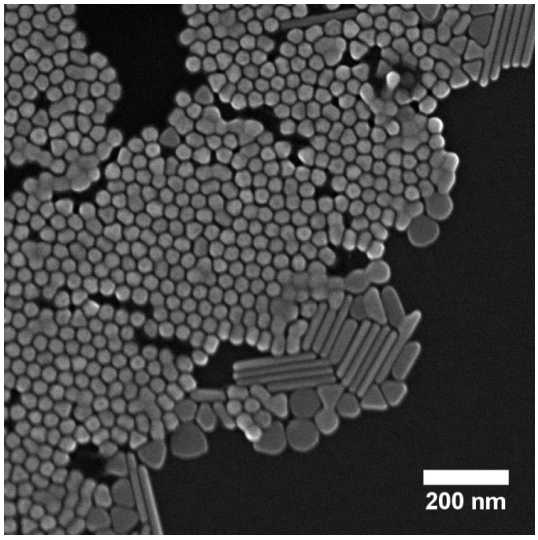

Figure S7. SEM image showing the formation of irregular shaped nanoparticles formation via seed 1 at ~75ºC.

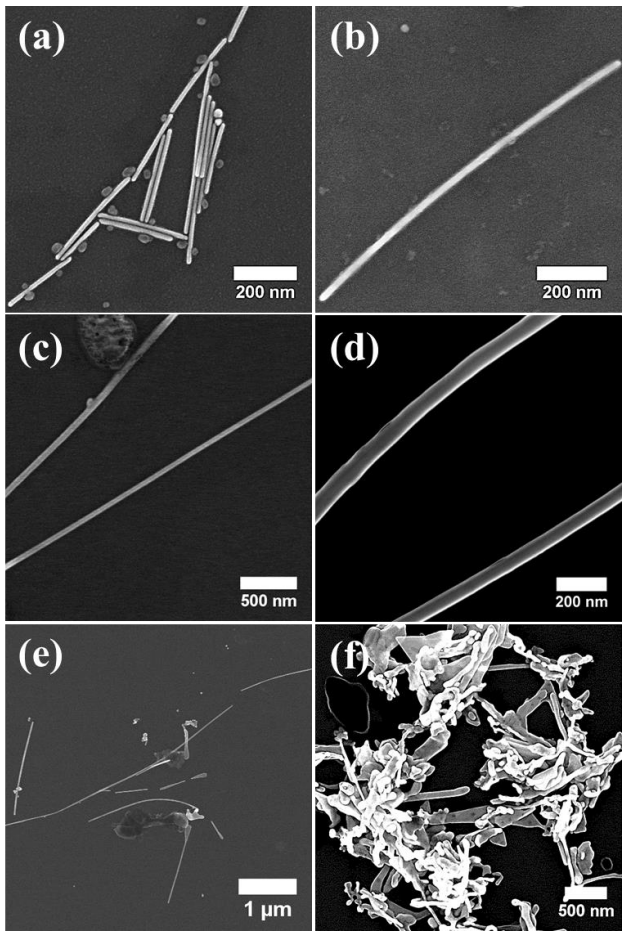

Figure S8. SEM images showing the effect of growth solution pH on aspect ratio and morphology of as synthesized Au NWs in (a) pH= 3.2, d= (b) pH= 3.7, (c) pH= 4.1, (d) pH= 4.7, (e) pH= 8.1, and (f) pH= 11.0 by using seed 2.

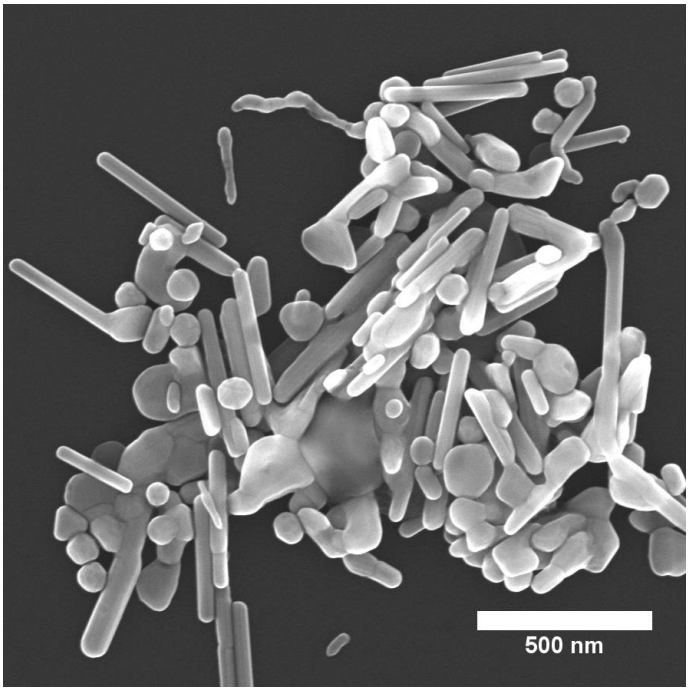

Figure S9. SEM image showing the formation of irregular shaped nanoparticles formation via seed 2 at ~75ºC.

Paper- III:

Incorporation of Fe@Au nanoparticles into multiresponsive pNIPAm-AAc colloidal gels modulates drug uptake and release.

Incorporation of Fe@Au nanoparticles into multiresponsive pNIPAm-AAc colloidal gels modulates drug uptake and release.

Sulalit Bandyopadhyay[a]†, Marte Kee Andersen[a], Muhammad Awais Ashfaq Alvi[a], Anuvansh Sharma[a], Rajesh Raju[b], Birgitte H. McDonagh[a], Wilhelm Robert Glomm[a,c]†

[a]Ugelstad Laboratory, Department of Chemical Engineering, Norwegian University of Science and Technology (NTNU), N-7491 Trondheim, Norway.

[b]Department of Chemistry, Norwegian University of Science and Technology (NTNU), N-7491 Trondheim, Norway.

[c]Polymer Particles and Surface Chemistry Research Group, SINTEF Materials and Chemistry, N-7465 Trondheim, Norway.

† *Correspondence to: Sulalit Bandyopadhyay (sulalit.bandyopadhyay@ntnu.no), Wilhelm R. Glomm (Wilhelm.Glomm@sintef.no)

ABSTRACT

Here, a synthetic method has been optimized for the synthesis of thermo and pH responsive poly(N-isopropylacrylamide-co-acrylic acid) nanogels which are subsequently loaded with Cytochrome C using a modified breathing-in mechanism. Physico-chemical properties mapped using dynamic light scattering (DLS) and differential scanning calorimetry (DSC) confirm the swelling/de-swelling kinetics as reversible with a volume phase transition temperature (VPTT) of ~ 39 °C. Fe@Au nanoparticles were incorporated inside the nanogel networks using two different methods- coating and in-situ growth. The latter bears closer resemblance to the nanogels only while the former follows the trend of bare Fe@Au nanoparticles. High loading (~96%) and encapsulation (500 µg/mg of nanogels) of Cytochrome C were obtained. Release experiments performed using a dialysis setup and monitored using UV-vis spectroscopy show the highest release at 40°C and pH 3.2 (high temperature, low pH), with maximum release from the Fe@Au coated nanogels that also show a reverse swelling-collapse trend. The location of the drug, incorporation and presence of Fe@Au nanoparticles and drug incorporation method are found to control both the drug release mechanism and kinetics.

KEYWORDS ((Nanogels, core-shell nanoparticles, Volume phase transition temperature, programmed drug release, breathing-in))

INTRODUCTION

Colloidal gels in the nano regime, more commonly referred to as nanogels (NGs), have attracted much attention in drug delivery applications especially for stimuli-responsive release; i.e.; release of cargo molecules under the influence of temperature, pH, ionic strength or other external parameters.[1, 2] NGs refer to swollen nanosized networks formed by physical or chemical cross-linking of hydrophilic or amphiphilic polymer chains.[3] These offer several advantages over conventional drug delivery systems such as liposomes, microspheres, cyclodextrins and so on,[4, 5] not only by providing a finer temporal control over drug release due to their large surface area but also by allowing longer circulation times and targeting properties upon suitable functionalization. Moreover, NGs have been shown to exhibit high loading and encapsulation efficiencies. Although loading efficiency gives an indication of the thermodynamic distribution of the drug, it is not sufficient to indicate delivery vehicle stability against leakage. [6] In this regard, cross-linked NGs are known to provide high encapsulation stability to the drug molecule, rendering them suitable for long term use.[7]

One of the most common methods that has been used for synthesizing thermo-sensitive NGs is precipitation polymerization, named after the fact that the polymer chain - upon reaching a critical length - collapses upon itself, producing pre-cursor particles.[8] This happens above the lower critical solution temperature (LCST) of the polymer.[9] In an aqueous solution, the polymer is in the hydrated state below the LCST, while it becomes hydrophobic above LCST. In a similar way, the cross-linked NGs obtained from this polymer swell in water under a critical temperature and collapse above it. This temperature is called the volume phase transition temperature (VPTT) of the NG.[10] The transition usually happens over a temperature range instead of a single temperature owing to different crystalline and amorphous domains in the polymer, branching and side-chains, molecular weight distributions among other factors. [11] However, this temperature driven transition allows for release of cargo molecule at a desired rate by fine tuning the physico-chemical properties of the NGs.

Multi-response is introduced in these NGs by incorporating pH-dependent co-monomers. One of the frequently studied temperature and pH-dependent polymeric NGs is that of poly (N-isopropylacrylamide-co-acrylic acid) (pNIPAm-AAc). [12, 13] Although monomer addition, monomer-comonomer ratios can influence the final form of the NGs, the core-shell morphology of the NGs is one of the frequently studied forms. It allows for multiple phase transition behavior with temperature besides adding response to two external stimuli, viz. temperature and pH. The cross-linked NGs also show a tendency of undergoing compression owing to a cross-link gradient in the shell.[8]

Although there exist several synthesis methods to control the size and physico-chemical properties of NGs,[7] pNIPAm-AAc NGs have rarely been investigated to understand their morphological changes under various synthetic conditions and optimize the synthesis

process. Moreover, there exists no comprehensive study highlighting the dependence of one synthetic parameter on the other with the primary aim to reduce the size of the gels in the nano regime. The size reduction among other factors is an essential requirement for effective drug delivery applications to avoid phagocytotic sequestration. Recent investigation using poly(acrylic acid) (PAA) nanogels with AuNPs has shown that gels accumulated in the liver and spleen because of their capture by phagocytic cells.[14] Further, the need to optimize the synthesis route and identify the most important synthetic parameters that influence the properties arises with a growing interest in these NGs towards hyperthermia applications when coupled with magnetic nanoparticles.[15] If the VPTT of these NGs can be maintained higher than the normal body temperature, they can be in the circulation long enough to reach the site of action, where these will collapse owing to hydrophobic change at temperatures above VPTT. A pH responsive release can be utilized in drug delivery in intracellular compartments, such as the late endosomes (pH=5) or lysosomes (pH 4.5-5), or can be tuned to respond to the slightly acidic extracellular fluid surrounding tumors (pH=6.5-7.2). [16] The dual response from both temperature and pH allow controlled release of a drug of interest in response to both the stimuli. In this respect, reversible swelling-collapse behaviour of the NGs determines the probability of repeated cycles of controlled release. However, reversibility of the NGs is a challenge to control owing to different degrees of collapse of the chains and conformational architecture of the polymers. Additionally, incorporation of multifunctionality can also be achieved via coupling NGs with magneto-plasmonic nanoparticles (NPs), whereby introducing imaging and targeting modalities along with stimuli sensitivity in one hybrid system.[17-19]

Here, we report a comprehensive study of the synthesis of pNIPAm-AAc NGs using free-radical emulsion polymerization that show reversible swelling-collapse behaviour. The influence of stabilizer and cross-linker have been investigated to understand the physico-chemical properties of the NGs. In order to incorporate imaging and targeting modalities, the NGs Fe@Au core@shell NPs were incorporated into the NGs using two methods – coating and in-situ growth, resulting in enhancement of drug release properties. The NGs and Fe@Au incorporated NGs were subsequently loaded with a heme protein- Cytochrome C (Cyt *C*), a model protein drug- to perform an array of release studies. The effects of both temperature and pH on the release of Cyt *C* have been studied to determine the dominating factor for release. The effect of drug localization and hybrid composition on the drug release kinetics and mechanisms have been studied. The NGs and their hybrids described herein are promising candidates for hyperthermia applications when coupled with magnetic NPs owing to stability and stimuli programmed release over sustained time periods.

EXPERIMENTAL

Materials and Methods

N-isopropylacrylamide (NIPAm), acrylic acid (AAc) (d= 1.051 g mL^{-1}), Cyt *C* from bovine heart, sodium dodecyl sulphate (SDS), potassium persulphate (KPS), N, N' – Methylenebis(acrylamide) (BIS), iron pentacarbonyl ($Fe(CO)_5$, 99.99%), octadecene (ODE, 90%), oleylamine (OAm, 70%), chloroauric acid (99.999%), sodium citrate and O-[2-(3-Mercaptopropionylamino)ethyl]-O′-methylpolyethylene glycol (PEG-SH) of molecular weight 5000 Da were purchased from Sigma Aldrich. n-Hexane and hydrochloric acid (HCl 37% fuming) were purchased from Merck Millipore. Sodium hydroxide (pellets AnalaR NORMAPUR® ACS) was purchased from VWR. NIPAm was recrystallized before further use (described below) while the other chemicals were used as received. All solutions were prepared using distilled de-ionized water (MQ water, resistivity ~18.2μΩ-cm) purified by Simplicity® Millipore water purification system which was further purified using 0.45μm syringe filters. Cellulose dialysis tubing (Sigma Aldrich) with a MWCO of 14kDa was used for performing dialysis, both for purification of the NGs and the release studies.

Recrystalization of NIPAm

NIPAm was recrystallized in order to remove impurities that could inhibit the polymerization reaction. The protocol has been adapted and modified from the one reported by Wu *et al*. [20] In a typical recrystallization setup, 5 g of the monomer, NIPAm, was dissolved in 50 mL of n-Hexane at 110°C in a one-necked glass flask equipped with a water condenser and the reaction was run for 2 hours. Thereafter, the flask was directly put into an ice bath for 30 minutes to allow recrystallization of the purified monomer. This solution was then filtered using φ 90 mm filter paper circles, yielding the pure monomer. After drying the purified NIPAm, it was stored at -20°C to prevent absorption of moisture.

Synthesis of pNIPAm-AAc NGs

pNIPAm-AAc NGs were synthesized using free radical emulsion polymerization.[21] A molar compostion of 85 % PNIPAm, 10 % AAc and 5 % BIS was used. [22] In essence, NIPAm (1.6mMoles) and BIS (90.8 μMoles) were put directly into the reactor under nitrogen atmosphere. Thereafter, 10mL of SDS-solution with different concentrations (2 mM, 4 mM, 5 mM, 5.5 mM) was added and the solution left to stir under nitrogen flow for 30 minutes. Prior to addition of the initiator KPS (400 μL of 103.6 mM), AAc (126 μL of 1.46 M) was added into the solution. The reaction was allowed to run for 3 hours. The NG solution was poured into a pre-washed dialysis tube (MWCO 14kDa) and dialysed overnight to remove unreacted monomers and residual reactants.

Synthesis of Fe@Au NPs

Fe@Au NPs were synthesized using a previously reported protocol developed by the authors. [17] In essence, a mixture of ODE (50 mL) and OAm (740 µL) was degassed under Ar atmosphere and vigorous stirring at 120^0C for 30 min. The temperature was raised to 180^0C, following which, 1.8 mL of $Fe(CO)_5$ was injected and the reaction was continued for 20 min. After cooling down to room temperature, the magnetic bar coated with Fe NPs was washed with a 1:2 ratio (by volume) of hexane and acetone. Fe NPs were magnetically separated, washed with acetone and dried in a stream of nitrogen. 5 mg of dried Fe NPs were dissolved in 10 mL of 10 mM sodium citrate solution using sonication at 80^0C for half an hour. Citrate stabilized Fe@Au NPs were synthesized by dropwise addition of 10 mL of 1.5 mM chloroauric acid to the Fe seed NPs under vigorous stirring. The reaction was allowed to run for 20 minutes. Thereafter, the solution was cooled down to room temperature, and Fe@Au NPs were magnetically separated to remove free Au NPs.

PEG coating of the Fe@Au NPs was done using a method reported previously by the authors.[17] Briefly, 2mg of PEG-SH was mixed with 5mg of Fe@Au NPs in a total volume of 5ml MQ water and left to stir for 1 hour. PEG coated Fe@Au NPs were collected by centrifugation.

Incorporation of Fe@Au NPs within NGs

Two different methods were used to prepare combinations of NGs with Fe@Au NPs. The first method was based on post-synthesis coating, while in case of the second method, the NGs were grown atop the Fe@Au seeds via heterogeneous nucleation.

Coating

In order to coat Fe@Au NPs with a representative NG, 3.3 mg of the lyophilized NG was added to 5 ml solution of Fe@Au NPs (concentration of 1mg/ml) and left to stir at 500 rpm for 2 hours. Thereafter, the NG coated Fe@Au NPs were separated using centrifugation at 14,500 rpm for 20 minutes. The sample would be referred to as Fe@Au_NG_c.

In-situ Method

A similar protocol was used as reported earlier for the NGs. A molar composition of 85 % PNIPAm, 10 % AAc and 5 % BIS was used. In essence, NIPAm (0.7 mMoles) and BIS (40.2 µMoles) were put directly into the reactor under nitrogen atmosphere. Thereafter, 1mg of PEG coated Fe@Au NPs and 5mL of 4mM SDS-solution were added and the solution left to stir under nitrogen flow for 30 minutes. Prior to addition of the initiator KPS (200 µL of 210.7 mM), AAc (54 µL of 1.39 M) was added into the solution. The reaction was allowed to run for 3 hours. The NG solution was poured into a pre-washed dialysis tube (MWCO 14kDa) and dialysed overnight to remove unreacted monomers and residual reactants. The sample would be referred to as Fe@Au_NG_i.

Loading of Cyt C

Loading studies of Cyt *C* were performed primarily with breathing-in mechanism using lyophilisation.[23]. For a typical loading experiment, 20 mg of the freeze dried NG was imbibed with Cyt *C* solution (10ml, 8.1 µM) and left to stir for 3 hours. Thereafter, the solution was poured into a pre-washed dialysis tube (MWCO 14kDa) and dialysed overnight to remove the unbound Cyt *C*.

For loading Fe@Au_NG_c with the protein, 5mg of NG coated Fe@Au NPs were imbibed with Cyt *C* solution (1ml, 8.1 µM) and left to stir for 2 hours. On the other hand, 1.7 mg of Fe@Au_NG_i was imbibed with Cyt *C* solution (3ml, 40.6 µM) and left to stir for 2 hours Afterwards, Cyt *C* loaded Fe@Au_NGs were separated from the unbound drug using centrifugation.

Loading efficiencies (L.E., %) and encapsulation efficiencies (E.E., mg drug per mg of NG) of Cyt *C* were calculated using the following equations.

$$L.E. = \left(\frac{C_{cyt,0} - C_{cyt,t}}{C_{cyt,0}} \right) * 100$$

$$E.E. = \frac{C_{cyt,0} * L.E}{100 * C_{NG}}$$

Where $C_{cyt,0}$ is the concentration (mg/ml) of Cyt *C* at the start of loading, $C_{cyt,t}$ is the final concentration (mg/ml) of Cyt *C* after loading, C_{NG} is the concentration (mg/ml) of the NG or NG coated Fe@Au NPs, concentrations of Cyt *C* being determined using the calibration curve (Figure S1, Supporting Information) or the absorbance method as applicable.

Release studies of Cyt C

After loading NGs with Cyt *C*, these were subjected to different release media to understand the effect of both temperature and pH on the release kinetics. Three different biologically relevant release conditions were simulated – high temperature (40°C), low pH (3.2) and high temperature along with low pH (40°C, pH 3.4) using MQ water and tuning the pH using different molar ratios of 1M NaOH and 1M HCl. In case of the Fe@Au NPs incorporated into NGs, Cyt *C* release was monitored only at high temperature along with low pH (40°C, pH 3.4). The release medium was maintained at a temperature slightly above VPTT to account for heat losses during the time study and also to ensure maximum collapse of the NGs.

Characterization techniques

Proton Nuclear Magnetic Resonance (^{1}H NMR)

^{1}H NMR spectra was recorded in a Bruker Advance DPX400 instrument. Lyophilized NG (2 mg) was suspended in D_2O (0.8 ml) and the spectra was recorded with 128 scans at 25 ^oC. The reference peak was locked in, at 4.80 for D_2O. Chemical shifts (δ) were reported in ppm**.**

Scanning (Transmission) Electron Microscopy (S(T)EM)

S(T)EM images were acquired using a Hitachi S-5500 electron microscope operating at 30kV accelerating voltage. TEM images were obtained in bright field mode. TEM grids were prepared by placing several drops of the solution on a Formvar carbon coated copper grid (Electron Microscopy Sciences) and wiping immediately with Kimberly-Clark kimwipes to prevent further aggregation owing to evaporation at room temperature. For studying the temperature effect on the NGs, NG or Fe@Au incorporated NG solutions were heated to 45°C, just prior to placing drops on the TEM grid.

Dynamic light scattering (DLS) and zeta potential measurements

The size distribution and zeta potential of the NGs were measured using a Malvern Zetasizer Nano-ZS instrument, and the manufacturer's own software. All measurements were done in aqueous solutions and results were averaged over triplicate measurements.

Ultraviolet-visible spectroscopy (UV-vis) measurements

UV–vis spectra were acquired with a UV-2401PC (Shimadzu) spectrophotometer. The spectra were collected over the spectral range from 200 to 800 nm.

Differential Scanning Calorimetry (DSC) studies

DSC studies were performed using a TA Instruments Q2000 DSC. The scan rate was 5 °C min^{-1} for both heating and cooling curves and the samples were scanned in the temperature range 5–45 °C. The NG solution was loaded in a Hermetic Aluminium pan while the reference pan was kept empty. The data were analysed using TA Instruments Universal Analysis 2000 © software.

RESULTS AND DISCUSSION

pNIPAm-AAc NGs with a wide range of sizes and physico-chemical properties were synthesized using free radical emulsion polymerization. Polymerization occurs via homogeneous nucleation, which is initiated by the sulphate radicals generated from the initiator.[24] Common steps of radical propagation and chain growth continue yielding critical polymer chain length. These collapse upon themselves, forming precursor particles. These collapsed particles grow by a combination of the following mechanisms viz

aggregation of other precursor particles, by being captured by existing particles, by capturing growing oligoradicals and by monomer addition.[8] A representative ^{1}H NMR spectrum of a representative NG showing that polymerization has proceeded onwards from its precursor (NIPAm) to afford pNIPAm can be found in the Supporting information (Figure S2). The NGs are stabilized by Coulombic repulsion from the charge imparted by the stabilizer (surfactant).

The results obtained for these NGs are sub-divided into the following three subsections that first reveal the size optimization results and their physico-chemical properties, followed by loading and encapsulation efficiencies of Cyt C and finally culminating into the release studies performed under physiological conditions.

Size optimization of the NGs and physico-chemical properties

Size and surface charge of the NGs play a major role in drug delivery applications – NPs smaller than 5.5 nm are removed through renal clearance mechanism while particles larger than 200 nm are sequestered by phagocytotic cells of the spleen.[25, 26] In the synthetic method described above, among different parameters, the influence of stabilizer (SDS) concentration, cross-linker (BIS) concentration and relative mole ratios of the monomers and cross-linker (NIPAm, AAc and BIS) have been studied. Figure 1 (a) shows the variation of size of different NGs synthesized by modifying the reaction parameters, where the error bars indicate a measure of the polydispersity of the particle distribution. Our results are in close allegiance to those observed by Lyon et al[27], although their group has controlled monodispersity as the most important parameter. Here, we report control of physico-chemical properties of the nanogels as a function of several synthetic parameters outlined in Table 1.

NIPAm (mol %)	**AAc (mol %)**	**BIS (mol %)**	**SDS (mM)**	**Size ± PDI (nm)**
85	10	5	2.0	593.10 ± 0.10
82	10	8	2.0	376.10 ± 0.10
82	10	8	3.0	309.10 ± 0.02
85	10	5	5.5	182.30 ± 0.10
85	5	10	1.6	378.20 ± 0.03
89	5	6	1.6	415.70 ± 0.02
85	10	5	4.0	412.60 ± 0.07
85	10	5	5.0	231.70 ± 0.06

An increase in the BIS mole percent (from 5 to 8%) causes a substantial decrease in the size of the NGs (A-B), while a coupled increase in the SDS concentration (B-C) causes a larger collapse above the VPTT, although the decrease in initial size is not sharply evident. This effect can be attributed to a higher cross-linking density, causing a greater collapse.
On the other hand, increasing the SDS concentration from 2mM to 5.5mM (while keeping the BIS mole percent constant) (A-D) causes a dramatic decrease (70%) in the size of the NGs. The main role of SDS is to prevent fusion of hydrophobic nuclei during polymerization.[28] This refers to initial curtailing of the size of the nucleation centres, which further grow by oligomer or monomer addition. A higher initial concentration of SDS provides higher charge stabilization in addition to a denser packing around the incipient nucleation centres, whereby limiting the growth of the NGs owing to electrostatic stabilization. The former (A) shows a volume collapse of ~45% above VPTT while the latter (D) shows a volume collapse of ~95%. This reflects the fact that the hydrophobic tails of the SDS chains interfere constructively in increasing the hydrophobicity of the NGs above VPTT, whereby causing a more efficient collapse.
The mole ratios of the monomer (NIPAm), co-monomer (AAc) and cross-linker (BIS) in the initial reaction mixture also determine the incorporation ratios in the final NGs, whereby effecting their size and collapse properties. In a typical experiment, the mole ratios were varied from 85% NIPAm : 5% AAc : 10% BIS (E) to 89% NIPAm : 5% AAc : 6% BIS (F), while keeping the SDS concentration constant. An increase in the initial size (~10%) is explained through a decreased cross-linking density and reduced charge stabilization from the acidic groups of the AAc blocks. On the other hand, there is a slight decrease (~3%) in volumetric collapse efficiency on increasing the NIPAm content. This might indicate an increase in hydrophobic domains when heated above the VPTT. The effect is aided by a lower cross-linking density yielding a loosely structured NG thereby needing stronger force to bring together the increased hydrophobic domains during collapse.
The SDS concentration was found to be the most dominating factor determining the size of the NGs. Figure 1(b) shows the variation of the size of the NGs as a function of initial SDS concentration, (error bars indicating polydispersity of particle distribution) while all other parameters were kept constant. As evident from Figure 1(b), the size of the synthesized NGs decreases with an increase in the SDS concentration. The volumetric collapse efficiency - defined as the relative change in volumes of the swollen and collapsed NGs - increases from 45% (2mM) to 95% (5.5mM) with increasing SDS concentration as indicated. As all these concentrations are well below the critical micelle concentration (CMC) of SDS (~8mM at 25°C), [29] we can ignore the tendency of formation of micelles. Moreover, any free SDS is assumed to be completely removed during dialysis. The effect of SDS is summarized as both an increase in the incipient nucleus size, onto which the chains collapse during the synthesis and an increase in the hydrophobicity of the NGs due to incorporation of the hydrophobic surfactant tails (C-12 chains). The initial increase is

seen more as an electrosteric stabilization that also explains the lowering of polydispersity while increasing SDS concentrations (Figure 1(a)). On the other hand, incorporation of SDS chains confirms a more efficient collapse above VPTT. This is due to the dominance of hydrophobic interaction forces at increased temperature, coupled with the temperature dependent collapse of the pNIPAm blocks. However, it is worthy of mention that further increase in SDS concentration did not yield smaller NGs and led to temperature driven aggregation when heated above VPTT. Thus, while it is important for the NGs to collapse, it is equally interesting to re-swell them with known efficiency.

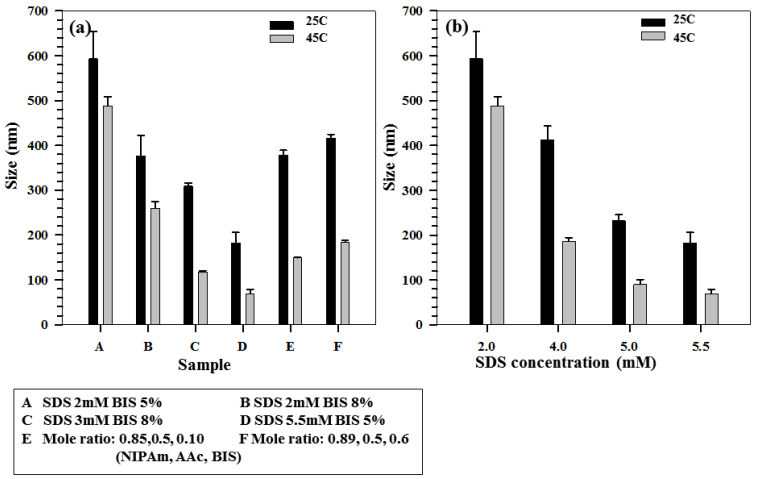

Figure 1 (a) Variation of size of the NGs synthesized using different parameters (b) Variation of size of the NGs as a function of SDS concentration (c) Representative BF S(T)EM image of NGs at 25°C (d) Representative BF S(T)EM image of NGs at 45°C.

Bright field (BF) S(T)EM images of a representative NG at 25°C and NG solution heated just prior to measurement at 45°C are shown in Figures 1(c) and 1(d) respectively. Although

the swelling-collapse behavior is difficult to capture in this case, the images show that upon heating the NGs, they tend to associate hydrophobically owing to collapse above VPTT. This effect is synergistically improved due to the presence of cross-linker. Figure 2 provides an overall schematic of the parameters that affect the size of the synthesized NGs.

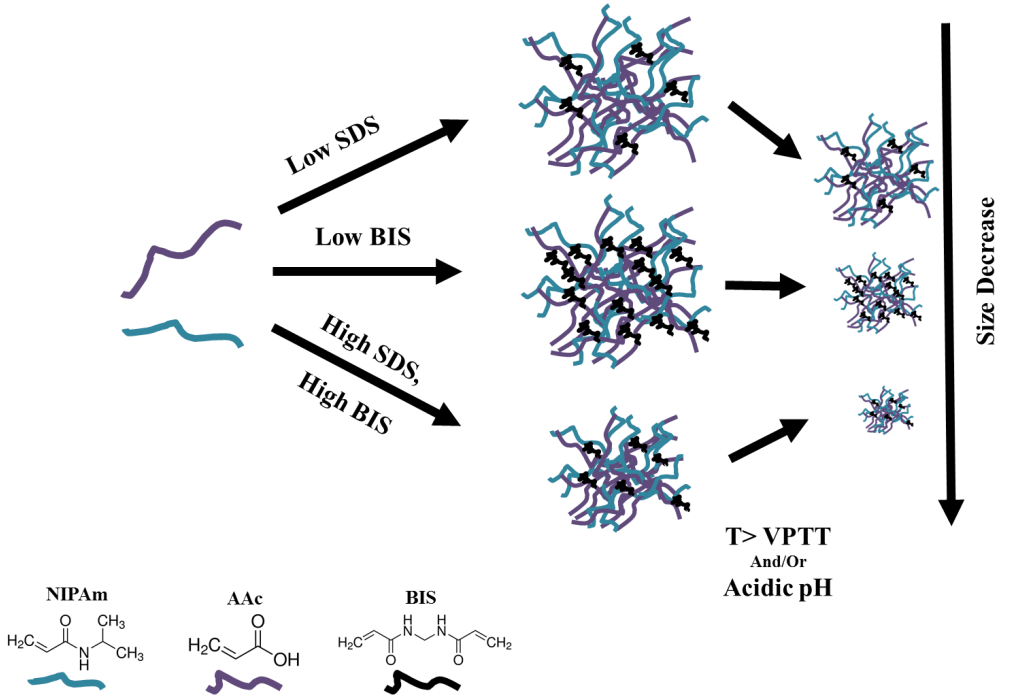

Figure 2 Schematic showing effect of various synthetic parameters on size of pNIPAm-AAc NGs.

NGs comprise polymer chains that are cross-linked to each other and their physico-chemical properties are guided by nature of the monomers, their relative composition in the NGs and the degree of cross-linking among others. The swelling-deswelling properties of the NGs are an important aspect for loading and release of biologically relevant cargo molecules like proteins, peptides and nucleic acids. In case of NGs, the cross-linking density among other factors plays an important role in determining the VPTT, collapse rate and gel properties.

Figure 3 (a) shows the variation of the swelling ratio (α) of a representative NG (3mM SDS, 8% BIS) as a function of temperature for a set of heating and cooling cycles. α is defined as $(D/D_0)^3$, where D (nm) represents the hydrodynamic diameter of the NG at any temperature and D_0(nm) represents the diameter of the NG at room temperature. The NGs show a reversible swelling-deswelling transition with a negligible hysteresis. The driving force for aggregation is an increase in entropy from the polymer solution to a two phase system of polymer and solvent. [30] The entropy of a two-phase polymer system and water

is greater than a polymer solution owing to a more ordered arrangement of water molecules adjacent to the polymer. The positive entropy change contributes towards aggregation of the polymers, thereby yielding a favourable association (free energy of association is negative since positive enthalpy change is smaller than the entropy term and does not influence association to a larger extent).[31]

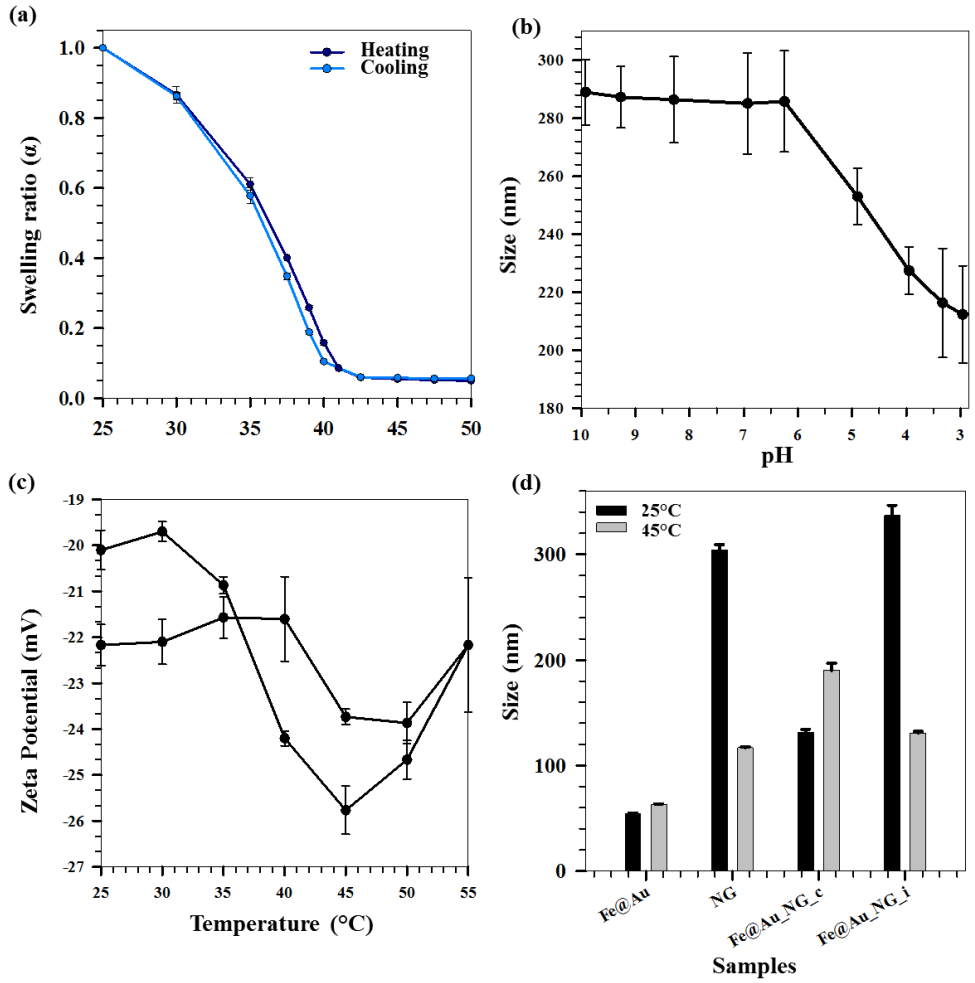

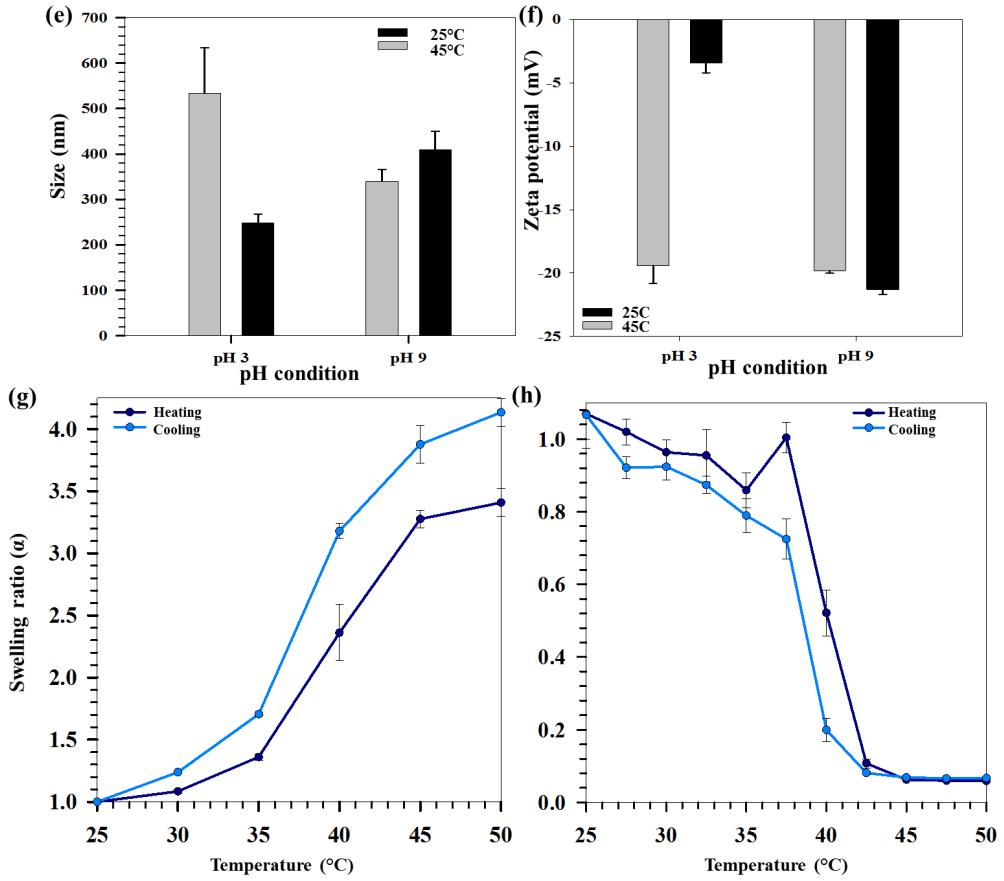

Figure 3 (a) Swelling ratio (α) of a representative NG as a function of temperature during heating and cooling cycles (b) Size of a representative NG as a function of pH (c) Zeta potential of a representative NG as a function of temperature during heating and cooling cycles (d) Size of Fe@Au NPs, representative NG, Fe@Au_NG_c and Fe@Au_NG_i as a function of temperature. (e) Size of a representative NG as a function of pH and temperature (f) Zeta potential of a representative NG as a function of pH and temperature. Swelling ratio of (g) Fe@Au_NG_c NPs and (h) Fe@Au_NG_i NPs as a function of temperature during heating and cooling cycles. The error bars represent standard deviation of a set of triplicate measurements.

Figure 3(b) shows the variation of size of a representative NG (3mM SDS, 8% BIS) as a function of pH. A remarkable decrease in size (~27%) is observed under acidic conditions. This is in effect due to protonation of the carboxylic acid groups of the poly AAc blocks with an increasing pH. The thermodynamic model developed by Siegel can be used to explain the swelling/deswelling characteristics while changing the pH of the medium.[32] This model considers three sources contributing to the total free energy - (i) NG-solvent

system; (ii) NG-solvent mixing, (iii) deformation of polymer networks and osmotic pressure of mobile ions. The NG-solvent mixing component is dominated by the poly AAc segments that undergo dissociation with an increase in pH. Dissociated poly AAc segments are more hydrophilic than non-dissociated segments, whereby a transition from lower to higher pH causes a drastic decrease in the free energy of mixing. Hydrophobic to hydrophilic transition also explains the consequent swelling of the NGs. However, this dissociation is affected by the deformation degree of the polymer network, mostly affected by the cross linking density and the osmotic pressure of OH^- and Na^+ ions. The sharp volume transition that happens at a pH slightly below neutral conditions is reflective of the fact that the pH is high enough to overcome the osmotic pressure, wherein counter-ion-shielding effects occur within the poly AAc domains. [33] Once the osmotic pressure is overcome, a synergistic effect of the favourable free energy of NG-solvent mixing and de-cross-linking of bound poly AAc segments in the domains causes further swelling with increase in pH.

Figure 3(c) depicts the variation of the zeta potential of a representative NG (4.2 mM SDS, 5% BIS) as a function of temperature. The zeta potential not only gives a measure of the surface charge of the NGs but also indicates stability of NGs in solution. A higher surface charge indicates higher stability owing to electrostatic forces. The zeta potential, representative of the charges contributed to by the poly AAc segments, does not change appreciably as a function of temperature. This is due to the fact that zeta potential is only applicable to the NGs in a semi-quantitative manner as some of the charges are buried and contribute partially to the calculated value. Additionally, there exists no well-defined slipping plane between the NG surface and the medium.[34] Herein, the relatively constant zeta potential for the NGs indicates that the poly AAc segments do not show temperature dependence, and their effect in the swelling/deswelling characteristics of the NGs can be widely de-coupled from the effect of the poly NIPAm chains. To further substantiate this, Figures 3(d) and 3(e) depict the changes in size and zeta potential as a function of both temperature and pH for a representative NG (2 mM SDS, 5% BIS). In acidic conditions (pH 3), the collapse of the NGs is substantial owing to charge based interchain repulsion, while in basic medium (pH 9), the NGs do not show much dependence on temperature. In fact, a slight increase in size could point towards aggregation driven by hydrophobic forces. On the other hand, a decrease in the zeta potential of the NGs is observed under acidic conditions, while under basic conditions, the zeta potential does not change much. The increase in cationic charge can be explained by a coupled effect of the collapse of the poly NIPAm segments due to temperature effect and protonation of functional carboxylic groups of the poly AAc segments.

Figure 3 (f) shows a comparison of the sizes of the Fe@Au NPs, a representative NG and Fe@Au NPs incorporated into NGs (Fe@Au_NG_c and Fe@Au_NG_i) as a function of temperature. An increase in the size of the Fe@Au_NG_c NPs as a result of the increase in temperature is observed in contrast with only NG. Although the NG units undergo entropy

driven collapse above VPTT, Fe@Au NPs act as crosslinking units (Figure S3, Supporting information) pulling the gelling units together, whereby increasing their effective size as evidenced from their hydrodynamic sizes. On the other hand, FeAu_NG_i resemble the NGs when it comes to temperature driven collapse, showing a volumetric collapse efficiency of 94%, analogous to that of the bare NGs. Thus, the Fe@Au_NG_i behave similarly to the bare NGs, while the Fe@Au_NG_c resemble the characteristics of the bare Fe@Au NPs. However, the increase in size for the Fe@Au NPs (volume increase 36%) may be attributed to aggregation, whereas a 67% volume increase for the Fe@Au_NG_c is mostly due to the cross-linking effect of the Fe@Au NPs that pulls together the already collapsed NG blocks.

This variation in size is further reflected in Figure 3 (g) for Fe@Au_NG_c where the heating and cooling swelling ratio curves diverge from unity with increasing temperature. These structures are much less reversible when compared to NGs alone, since, in addition to chain length, cross-linking density and presence of Fe@Au NPs further affect their size distributions as a function of temperature. For similar reasons, size dependence of NG coated Fe@Au NPs with change in pH, follows a reverse trend. These NG coated Fe@Au NPs are more stable than both the Fe@Au NPs and the NGs themselves owing to higher magnitudes of zeta potential. (Figure S3, Supporting information) Further, the effect of temperature on zeta potential follows a trend opposite to that of the NGs alone. On the other hand, Figure 3 (h) shows the variation of swelling ratio for Fe@Au_PEG_i as a function of temperature. Although, the heating cooling cycles resemble those of the bare NGs, the hysteresis area is larger. It points to these being less reversible than the bare NGs as a result of different densities of the Fe@Au cores as compared to the NGs. This density difference introduces non-homogeneity in the system properties leading to less well defined swelling-collapse behaviour.

The cross-linked NGs swell under the critical temperature and collapse above it. Thus, the VPTT is an important property of these NGs that determines their biological applications. Figure 4 shows DSC measurements of a representative NG (3mM SDS, 8% BIS) which depicts heat flow during heating and cooling cycles (Figure 4(a),(c) respectively) and specific heat capacity during heating and cooling cycles (C_P) (Figure 4 (b), (d) respectively) as a function of temperature. A gradual transition is seen in all the cases over a defined temperature range and the VPTT is calculated to be at the optimum peak position (heating curves) as ~39° C which is in good agreement with the value calculated using the average of the sigmoidal region of the size-temperature plot (Figure 3(a)). However, VPTT calculated using the cooling curves gives a slightly lower value that can be attributed to a slower re-organization of the polymeric chains in response to an otherwise faster temperature drop rate. This is not the case for the DLS study as there is sufficient time between measurements for the system to reach equilibrium. In case of the NGs coated with NPs, the transitions are not smooth owing to density gradient as a result of inorganic NP incorporation within the matrix. To consider this effect, the VPTT is defined as the

temperature where the fraction of the swelled and collapsed states is equal.[35] Using this method, the VPTTs of the NG, Fe@Au_PEG_c and Fe@Au_PEG_i are found to be 37.3 ± 0.2°C, 38.3 ± 0.5°C and 38.9 ± 0.8 °C respectively. Incorporation of the NPs causes an increase in the VPTT as compared to the bare NGs. This is because of an inherent increase of hydrophilicity of the matrix. Among the coated samples, Fe@Au_PEG_i has a higher VPTT. This may be due to different total amounts of NPs incorporated within the matrix or different arrangements of the Fe@Au NPs within the matrix (Figure S3, Supporting Information).

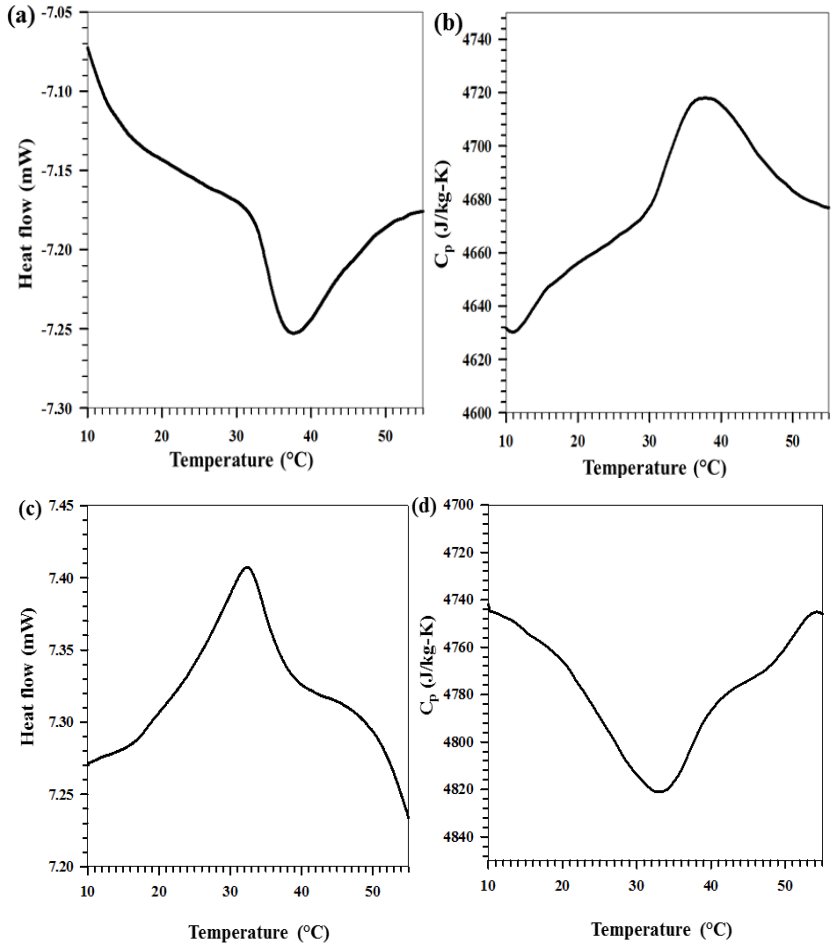

Figure 4 (a) Heat flow (during heating cycle) as a function of temperature for a representative NG (b) Specific heat capacity variation (during heating cycle) as a function of temperature for a representative NG (c) Heat flow (during cooling cycle) as a function of temperature for a

representative NG (d) Specific heat capacity variation (during cooling cycle) as a function of temperature for a representative NG.

Loading and Encapsulation

The NGs were loaded using breathing-in mechanism where in the freeze-dried NGs or NG coated Fe@Au NPs were imbibed with a concentrated solution of Cyt C. The freeze-dried NGs did not show any change in physico-chemical properties when compared to the as synthesized NGs (Figure S4, See Supporting Information). After the loading step, the free Cyt C was removed using a dialysis tubing (MWCO 14kDa). In case of the NG coated Fe@Au NPs, the free Cyt C was removed using centrifugation.

Cyt C is a highly water soluble heme protein with properties similar to model drug proteins. The heme ligand is located in the lysine rich region of the protein, that imparts a positive charge to the protein at neutral conditions (pI = 10.1, M_w = 12327 Da). [36] It is this front that can interact with negatively charged molecules resulting in complex formation. Coulombic forces between the negatively charged NGs and Cyt C result in the formation of a polymer-protein complex. This results in a release of the counterions associated with the polymer and the protein, causing an entropy gain and thus a net increase in the free energy.[37] Gel swelling yields a lower polymer segment density in the network and greater gel porosity,[34] yielding a higher loading capacity and thus the loading is carried out under swelling conditions. High loading efficiencies of up to 95% have been obtained for these NGs, with an encapsulation efficiency of ~500 µg per mg of the polymer.

The high loading efficiency can be attributed to the strong interaction between the NGs and the Cyt C under loading conditions. While it is difficult to predict the exact location of the protein inside the NG network, we hypothesize that since the initial binding events of the protein are localized at the surface, a condensation of the particle periphery happens, which limits deeper diffusion of the protein molecule.[34] While the location of the protein influences its interaction with external factors during biological applications, it is ideal when the molecule is closer to the surface and moderately bound to favour release under the influence of external stimuli and/or charge exchange with electrolytes.

In case of the NG coated Fe@Au NPs, loading efficiencies of upto 32% have been obtained with encapsulation efficiencies upto ~14 µg per mg of the Fe@Au NPs. For Fe@Au_NG_i, loading efficiencies of 36.2% and encapsulation efficiencies of 109.7 µg per mg of the nanogel system were observed. The encapsulation efficiency is based on Fe@Au NPs in the former case, while it is based on both the Fe@Au and NGs in the latter case. This means that the efficiencies are not directly comparable as it is difficult to base the calculations on one standard. However, while comparing the loading efficiencies of the systems containing Fe@Au NPs with the bare NGs, there is a drastic reduction in the loading capacity. This is primarily because of lower availability of drug binding sites within the NG, owing to presence of Fe@Au NPs in the nanogel network. (Figure S3, Supporting information)

Release Studies

Cyt C loaded NGs were subjected to different release conditions to monitor their release kinetics. A dialysis setup (Figure S5, Supporting Information) was employed to monitor the release over time. Three different conditions were chosen to understand their behaviour in response to pH, temperature and a combination of the two. These biologically relevant release conditions were simulated – high temperature (40°C), low pH (3.2) and high temperature along with low pH (40°C, pH 3.4) using MQ water and tuning the pH using different molar ratios of 1M NaOH and 1M HCl. Further, the choice of low pH can be utilized in simulating conditions where drug delivery in intracellular compartments is a matter of concern like in late endosomes (pH=5) or lysosomes (pH 4.5-5). In case of the NG coated Fe@Au NPs, high temperature along with low pH (40°C, pH 3.4) was the only condition used to monitor the release of Cyt C.

Figures 5(a), (b), (c) show the release profiles of Cyt C loaded into the NGs and Fe@Au incorporated NGs using the breathing-in mechanism and/or the traditional method. The traditional method refers to adding a calculated amount of the drug to the NG solutions, whereas the breathing-in mechanism relies on imbibing the freeze-dried NGs with a concentrated drug solution. For the sake of comparison, the concentrations of both the polymers and Cyt C were kept the same for both the methods.

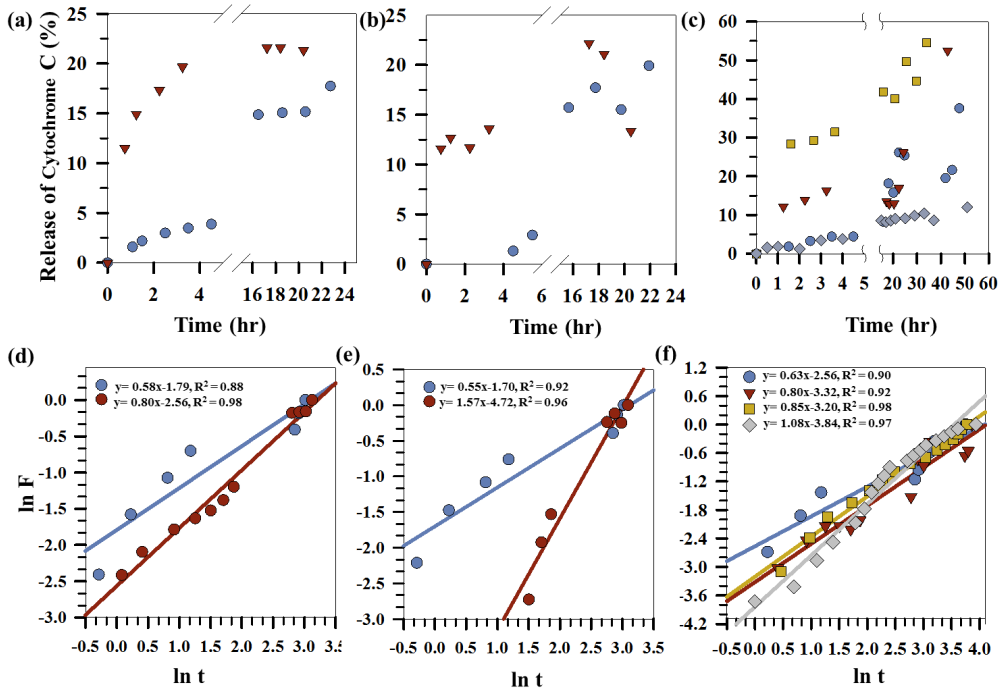

Figure 5 Comparison of release of Cyt C (loaded using breathing-in mechanism and traditional method) over time from (a) a representative NG at pH 3, T 25°C (b) a representative NG at pH 6, T 40°C and (c) a representative NG and NG coated Fe@Au NPs at pH 3, T 40°C. Plots of ln (F) as a function of ln (t) for (d) Case a (e) Case b and (f) Case c above respectively. F represents cumulative fraction of Cyt C.

In case of the NGs loaded using the breathing-in protocol, temperature or pH alone is able to cause a release of upto 20% of the loaded Cyt C over a day and no further increase is observed beyond that. A combination of the two effects- low pH and high temperature however yields a cumulative release of upto ~ 40% ranging over two days. Although, a slow release kinetics is observed, this could in effect direct towards long term encapsulation of the carrier molecule inside these NGs, leading to controlled release by variation of the external parameters. Further, the release is assumed to occur by a "squeezing out" mechanism following Fickian diffusion in the initial time period while a combination of diffusion and degradation of the NGs happens at larger time points. High temperature (above VPTT) and low pH (acidic) conditions enable maximum collapse of the NGs, squeezing out the drug loaded in the porous network.

Comparing the NGs loaded using the breathing in mechanism and the traditional method, a slightly higher release was observed in case of all the release scenarios for the latter method. This can be explained by the fact that the drug molecule is peripherally bound to

the NGs while in the case of the breathing-in case, the drug molecule traverses to the inside of the pores and hence requires more time or several stimuli factors to cause substantial release of the cargo. However, it must be noted here that higher loading and encapsulation efficiencies are obtained for the NGs loaded using the breathing-in method. An optimization between the loading capacity and external stimuli affected release of the drug molecule can be used to choose the potentiality of the NGs in the field of drug delivery.

Fe@Au_NG_c shows remarkably rapid release kinetics, releasing almost 55% of the initial loaded drug over a period of ~40 hours in comparison to Fe@Au_NG_i, which exhibits slower release kinetics, bearing closer resemblance to that from bare NGs. It is capable of releasing around 12% over a period of ~50 hours. The higher release in case of Fe@Au_NG_c is due to more peripheral localization of the drug owing to incorporation of the Fe@Au NPs in the NG networks. However, this is not the case for Fe@Au_NG_i, where the drug penetrates deeper into the more open nanogels networks, as also evidenced from S(T)EM images (Supporting Information). A more tortuous path is thus required for the loaded drug to be released, resulting in a slow kinetics. Further, the Fe@Au NPs act as cross-linkers in case of Fe@Au_NG_c, pulling the gelled units closer together, and thereby enhancing 'squeezing' out of the drug.

Figures 5(d), (e) and (f) show the plots of ln F as a function of ln t, where F represents the cumulative fraction of the drug released at time t. Majority of the drug release processes from swellable polymer systems are defined by two limiting cases, that is combination of Fickian and Case II transport mechanism. The latter is based on two assumptions- a boundary is formed between the glassy and rubbery phase of the polymer and boundary moves at constant velocity.[38, 39] The overall behavior is defined by combining diffusion-controlled and visco-elastic relaxation-controlled drug release and is given by

$$\mathbf{F = k}t^{n}$$

where, k is the rate constant and n is the diffusional exponent that determines the drug release mechanism. It is observed here that drug release mechanism from the Fe@Au_NG_c and Fe@Au_NG_i is that of super case transport II (n>1) while for the NGs alone are representative of drug release from spherical particles (0.5<n <1) and anomalous in nature. This relates to the conformational arrangement of the NGs which have lesser degrees of freedom in the presence of Fe@Au NPs, leading to less homogeneously defined viscous and elastic regions. On the other hand, different models[40] fitted to the release data yielded a linear dependence of F with t in case of traditionally loaded NGs Fe@Au_NG_c and Fe@Au_NG_i NPs, while they show square root time dependence for NGs loaded with breathing-in mechanism. (Figure S9, Supporting Information) These in conjunction with the diffusional exponent results show that drug incorporation method, location of the drug and presence of Fe@Au NPs largely alter the drug release mechanism and the kinetics. Further, the modulation of release parameters can greatly influence the release kinetics as observed from the release conditions used in the study.

CONCLUSIONS

Synthesis of external stimuli sensitive pNIPAm-AAc NGs has been optimized by varying reaction parameters. Among various parameters that included stabilizer (SDS) concentration, cross-linker (BIS) concentration and mole ratios of reactants, SDS concentration was observed to be the most important parameter to control the size of the NGs – higher concentration of SDS led to smaller NGs. The optimized NGs were used to incorporate Fe@Au NPs in order to incorporate magneto-plasmonic properties to the construct using two methods- coating and in-situ growth.

Under the influence of temperature, the NGs show a reversible swelling/deswelling kinetics, which happens due to an entropically driven expulsion of arranged water molecules. The pH response occurs due to protonation/de-protonation of the AAc blocks. This hydrophilic-hydrophobic transition has been confirmed to be reversible and the VPTT has been determined to be ~ 39°C. The size of the NGs as a function of temperature and/or pH is accounted for by a balance between Coulombic and hydrophobic forces. Fe@Au_NG_i shows a similar temperature based transition. However, an opposite effect is observed for Fe@Au_NG_c which happens as the Fe@Au NPs act as bridge molecules pulling together the gelling units.

Thereafter, Cyt *C* was loaded into the NGs and Fe@Au incorporated NGs using a modified breathing-in mechanism. This gave high loading and encapsulation efficiencies (~96% and 500µg/mg of NGs, respectively), showing a great capacity to retain drug solution. Using a dialysis setup and three different release conditions, the release kinetics of Cyt *C* was monitored. The release kinetics has been observed to be rather slow (over several hours), which hints towards their applications in sustained retainment of the encapsulated molecule. However, high release has been observed under a combination of high temperature (above VPTT) and low pH (acidic) conditions, in which case maximum de-swelling of the NGs is expected, leading to a squeezing release of the drug molecule. The release from Fe@Au_NG_i follows similar kinetics to that of the bare NGs. However, the release of Cyt *C* from Fe@Au_NG_c is the fastest, accounting for release of almost 55% of the initially loaded drug in ~40 hours. An overall schematic is shown in Figure 6 that describes the release of Cyt *C* from different configurations of the NG with the Fe@Au NPs. The drug incorporation method, location of the drug, presence of Fe@Au NPs and NP incorporation method largely alter the drug release mechanism. Thus, these temperature/pH programmed NGs can be fine-tuned for both sustained entrapment of cargo molecule and external stimuli directed release of the same by controlling the synthetic parameters and the mode of loading the cargo molecule.

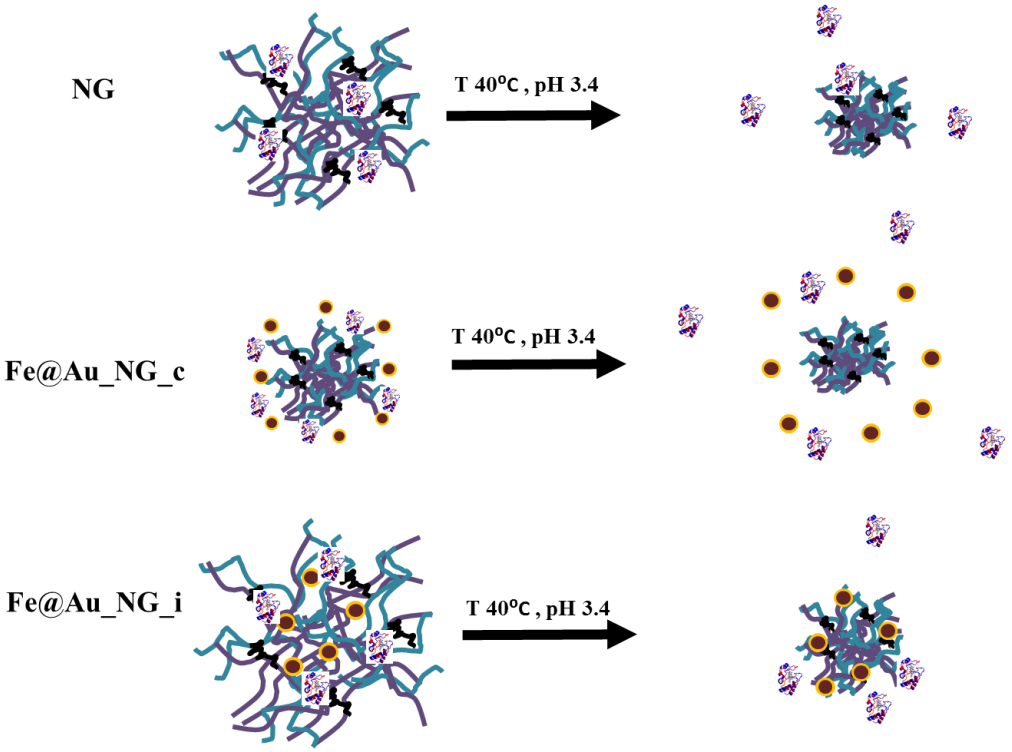

Figure 6 Overall schematic showing release of Cyt-C at pH 3.4 and temperature 40°C from three different NG combinations- NG, Fe@Au_NG_c and Fe@Au_NG_i

ACKNOWLEDGEMENTS

The authors would like to thank NorFab for financial support in connection to use of NTNU Nanolab and the Faculty of Natural Sciences and Technology, NTNU for financial support.

DISCLOSURE

The authors declare that there is no conflict of interest.

GRAPHICAL ABSTRACT

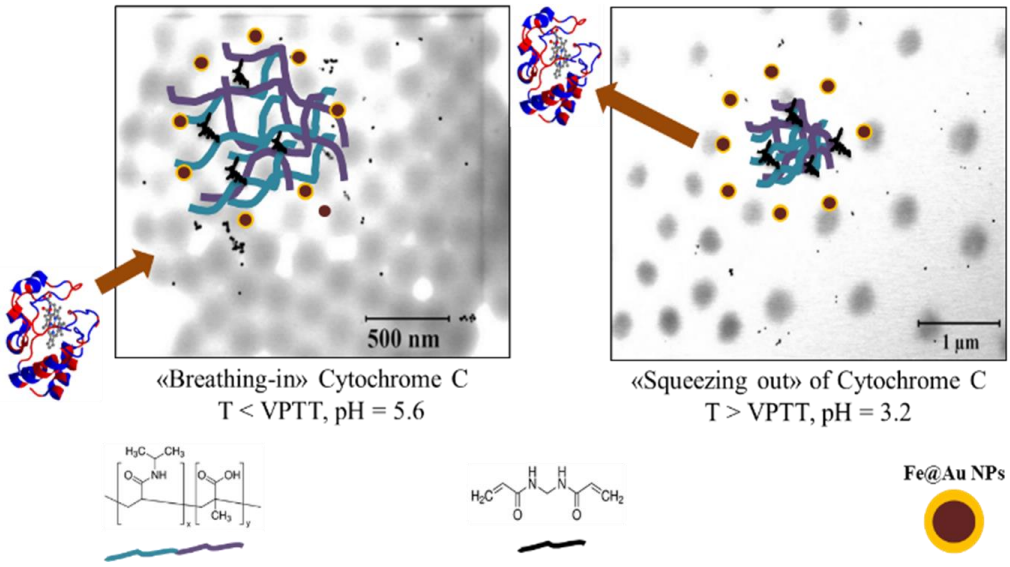

REFERENCES

1. Du, J.Z., et al., *A Tumor-Acidity-Activated Charge-Conversional Nanogel as an Intelligent Vehicle for Promoted Tumoral-Cell Uptake and Drug Delivery.* Angewandte Chemie-International Edition, 2010. **49**(21): p. 3621-3626.
2. Tamura, A., M. Oishi, and Y. Nagasaki, *Enhanced Cytoplasmic Delivery of siRNA Using a Stabilized Polyion Complex Based on PEGylated Nanogels with a Cross-Linked Polyamine Structure.* Biomacromolecules, 2009. **10**(7): p. 1818-1827.
3. Kabanov, A.V. and S.V. Vinogradov, *Nanogels as Pharmaceutical Carriers: Finite Networks of Infinite Capabilities.* Angewandte Chemie-International Edition, 2009. **48**(30): p. 5418-5429.
4. Otero-Espinar, F.J., et al., *Cyclodextrins in drug delivery systems.* Journal of Drug Delivery Science and Technology, 2010. **20**(4): p. 289-301.
5. Matteucci, M.L. and D.E. Thrall, *The role of liposomes in drug delivery and diagnostic imaging: A review.* Veterinary Radiology & Ultrasound, 2000. **41**(2): p. 100-107.
6. Torchilin, V.P., *Structure and design of polymeric surfactant-based drug delivery systems.* Journal of Controlled Release, 2001. **73**(2-3): p. 137-172.
7. Chacko, R.T., et al., *Polymer nanogels: A versatile nanoscopic drug delivery platform.* Advanced Drug Delivery Reviews, 2012. **64**(9): p. 836-851.
8. Nayak, S. and L.A. Lyon, *Soft nanotechnology with soft nanoparticles.* Angewandte Chemie-International Edition, 2005. **44**(47): p. 7686-7708.
9. Wang, X.H., X.P. Qiu, and C. Wu, *Comparison of the coil-to-globule and the globule-to-coil transitions of a single poly(N-isopropylacrylamide) homopolymer chain in water.* Macromolecules, 1998. **31**(9): p. 2972-2976.
10. Constantin, M., et al., *Lower critical solution temperature versus volume phase transition temperature in thermoresponsive drug delivery systems.* Express Polymer Letters, 2011. **5**(10): p. 839-848.
11. Bekhradnia, S., et al., *Structure, swelling, and drug release of thermoresponsive poly(amidoamine) dendrimer-poly(N-isopropylacrylamide) hydrogels.* Journal of Materials Science, 2014. **49**(17): p. 6102-6110.
12. Pelton, R., *Temperature-sensitive aqueous microgels.* Advances in Colloid and Interface Science, 2000. **85**(1): p. 1-33.
13. Wu, X., et al., *The Kinetics of Poly(N-Isopropylacrylamide) Microgel Latex Formation.* Colloid and Polymer Science, 1994. **272**(4): p. 467-477.
14. Chen, Y., et al., *Near-Infrared Emitting Gold Cluster-Poly(acrylic acid) Hybrid Nanogels.* Acs Macro Letters, 2014. **3**(1): p. 74-76.
15. Xiong, W., et al., *Dual temperature/pH-sensitive drug delivery of poly(N-isopropylacrylamide-co-acrylic acid) nanogels conjugated with doxorubicin for potential application in tumor hyperthermia therapy.* Colloids and Surfaces B-Biointerfaces, 2011. **84**(2): p. 447-453.
16. Tannock, I.F. and D. Rotin, *Acid Ph in Tumors and Its Potential for Therapeutic Exploitation.* Cancer Research, 1989. **49**(16): p. 4373-4384.
17. Bandyopadhyay, S., et al., *Synthesis and in vitro cellular interactions of superparamagnetic iron nanoparticles with a crystalline gold shell.* Applied Surface Science, 2014. **316**: p. 171-178.
18. Jafari, T., A. Simchi, and N. Khakpash, *Synthesis and cytotoxicity assessment of superparamagnetic iron-gold core-shell nanoparticles coated with polyglycerol.* Journal of Colloid and Interface Science, 2010. **345**(1): p. 64-71.
19. Zhou, T., B.Y. Wu, and D. Xing, *Bio-modified Fe3O4 core/Au shell nanoparticles for targeting and multimodal imaging of cancer cells.* Journal of Materials Chemistry, 2012. **22**(2): p. 470-477.
20. Zhou, S.Q., et al., *Light-Scattering-Studies of Poly(N-Isopropylacrylamide) in Tetrahydrofuran and Aqueous-Solution.* Polymer, 1995. **36**(7): p. 1341-1346.

21. Slomkowski, S., et al., *Terminology of polymers and polymerization processes in dispersed systems (IUPAC Recommendations 2011).* Pure and Applied Chemistry, 2011. **83**(12): p. 2229-2259.
22. Singh, N. and L.A. Lyon, *Au nanoparticle templated synthesis of pNIPAm nanogels.* Chemistry of Materials, 2007. **19**(4): p. 719-726.
23. Blackburn, W.H., et al., *Peptide-Functionalized Nanogels for Targeted siRNA Delivery.* Bioconjugate Chemistry, 2009. **20**(5): p. 960-968.
24. Ni, H.M., H. Kawaguchi, and T. Endo, *Characteristics of pH-sensitive hydrogel microsphere of poly(acrylamide-co-meth acrylic acid) with sharp pH-volume transition.* Colloid and Polymer Science, 2007. **285**(8): p. 873-879.
25. Chen, L.T. and L. Weiss, *Role of Sinus Wall in Passage of Erythrocytes through Spleen.* Blood, 1973. **41**(4): p. 529-537.
26. Choi, H.S., et al., *Renal clearance of quantum dots.* Nature Biotechnology, 2007. **25**(10): p. 1165-1170.
27. Blackburn, W.H. and L.A. Lyon, *Size-controlled synthesis of monodisperse core/shell nanogels.* Colloid and Polymer Science, 2008. **286**(5): p. 563-569.
28. Smith, M.H. and L.A. Lyon, *Multifunctional Nanogels for siRNA Delivery.* Accounts of Chemical Research, 2012. **45**(7): p. 985-993.
29. Rahman, A. and C.W. Brown, *Effect of Ph on the Critical Micelle Concentration of Sodium Dodecyl-Sulfate.* Journal of Applied Polymer Science, 1983. **28**(4): p. 1331-1334.
30. Schild, H.G., *Poly (N-Isopropylacrylamide) - Experiment, Theory and Application.* Progress in Polymer Science, 1992. **17**(2): p. 163-249.
31. Bromberg, L.E. and E.S. Ron, *Temperature-responsive gels and thermogelling polymer matrices for protein and peptide delivery.* Advanced Drug Delivery Reviews, 1998. **31**(3): p. 197-221.
32. Siegel, R.A., *Pulsed and self-regulated drug delivery* 1990 CRC Press, Boca Raton, FL.
33. Ni, H., H. Kawaguchi, and T. Endo, *Preparation of pH-sensitive hydrogel microspheres of poly(acrylamide-co-methacrylic acid) with sharp pH-volume transition.* Colloid and Polymer Science, 2007. **285**(7): p. 819-826.
34. Smith, M.H. and L.A. Lyon, *Tunable Encapsulation of Proteins within Charged Microgels.* Macromolecules, 2011. **44**(20): p. 8154-8160.
35. Fucinos, C., et al., *Temperature-and pH-Sensitive Nanohydrogels of Poly(N-Isopropylacrylamide) for Food Packaging Applications: Modelling the Swelling-Collapse Behaviour.* Plos One, 2014. **9**(2).
36. Dumetz, A.C., et al., *Patterns of protein - protein interactions in salt solutions and implications for protein crystallization.* Protein Science, 2007. **16**(9): p. 1867-1877.
37. Skobeleva, V.B., et al., *Interaction of hydrogels of acrylic acid-acrylamide copolymers with cytochrome c.* Polymer Science Series A, 2001. **43**(3): p. 315-322.
38. Siepmann, J. and N.A. Peppas, *Higuchi equation: Derivation, applications, use and misuse.* International Journal of Pharmaceutics, 2011. **418**(1): p. 6-12.
39. Brazel, C.S. and N.A. Peppas, *Modeling of drug release from swellable polymers.* European Journal of Pharmaceutics and Biopharmaceutics, 2000. **49**(1): p. 47-58.
40. Barzegar-Jalali, M., et al., *Kinetic analysis of drug release from nanoparticles.* Journal of Pharmacy and Pharmaceutical Sciences, 2008. **11**(1): p. 167-177.

Incorporation of Fe@Au nanoparticles into multiresponsive pNIPAM-AAc colloidal gels modulates drug uptake and release.

Supporting Information.

Sulalit Bandyopadhyay[a]†, Marte Kee Andersen[a], Muhammad Awais Ashfaq Alvi[a], Anuvansh Sharma[a], Rajesh Raju[b], Birgitte H. McDonagh[a], Wilhelm Robert Glomm[a,c]†

[a]Ugelstad Laboratory, Department of Chemical Engineering, Norwegian University of Science and Technology (NTNU), N-7491 Trondheim, Norway.

[b]Department of Chemistry, Norwegian University of Science and Technology (NTNU), N-7491 Trondheim, Norway.

[c]Polymer Particles and Surface Chemistry Research Group, SINTEF Materials and Chemistry, N-7465 Trondheim, Norway.

† *Correspondence to: Sulalit Bandyopadhyay (sulalit.bandyopadhyay@ntnu.no), Wilhelm R. Glomm (Wilhelm.Glomm@sintef.no)

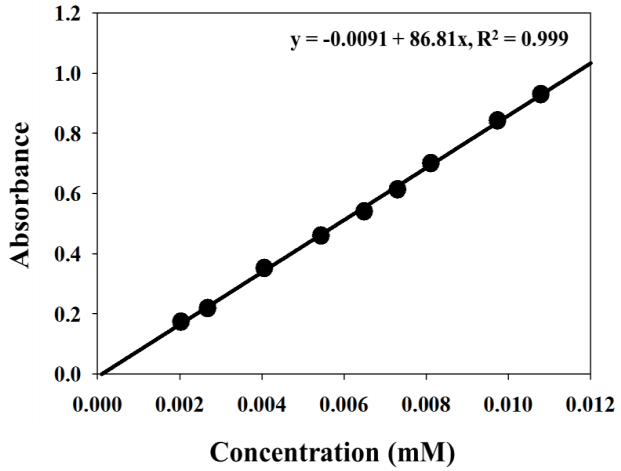

Figure S1 Calibration curve of Cytochrome C

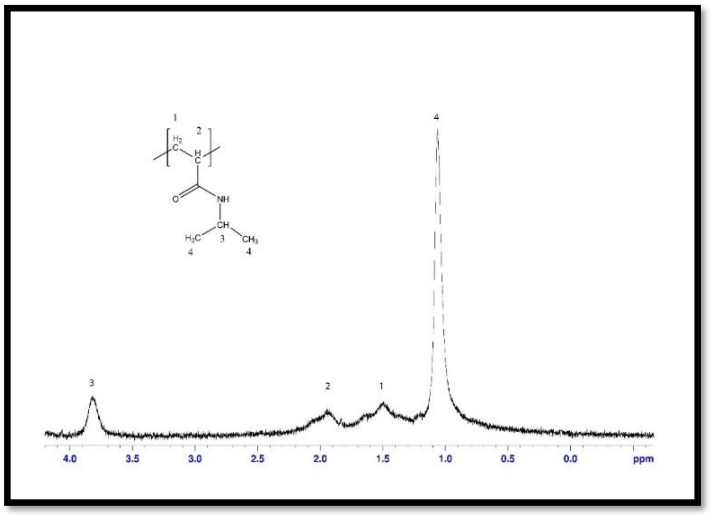

Figure S2 ^{1}H NMR spectrum of a representative nanogel in D20 (400 MHz)

The presence of broad characteristic multiplets at δ =1.95 ppm (-CH2-CH-) and δ =1.51 ppm (-CH2-CH-) along with broad singlets at δ =1.05 ppm (CH3-CH-CH3) and δ =3.85 ppm (CH3-CH-CH3) indicates that polymerization has proceeded onwards from its precursor (NIPAm) to afford nanogels.

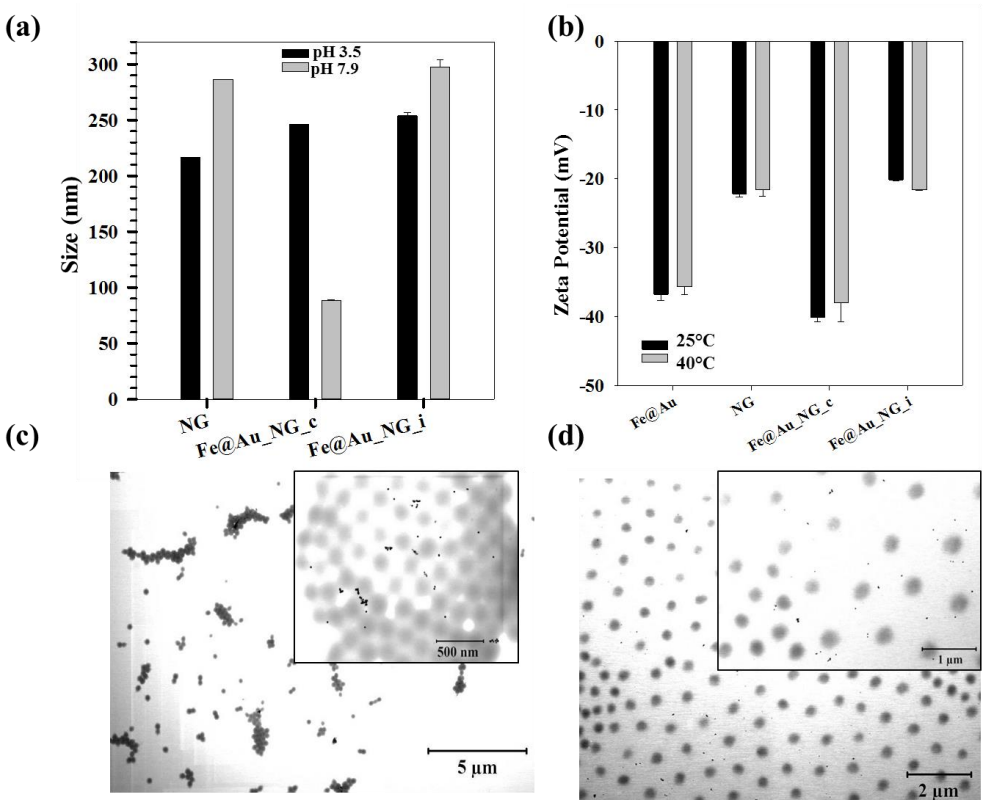

Figure S3 (a) Variation of size of NG, Fe@Au_NG_c, Fe@Au_NG_i with pH (b) Comparison of zeta potentials as a function of temperature for Fe@Au NPs, a representative nanogel and Fe@Au_NG_c and Fe@Au_NG_i Representative BF S(T)EM image of Fe@Au_NG_c (c) at 25°C and (d) at 45°C respectively. Red circles show Fe@Au NPs

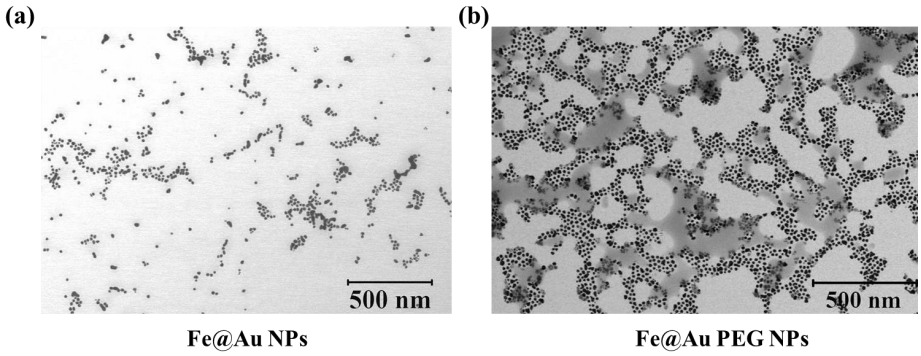

Figure S4 Representative S(T)EM image of (a) Fe@Au NPs and (b) PEG coated Fe@Au NPs.

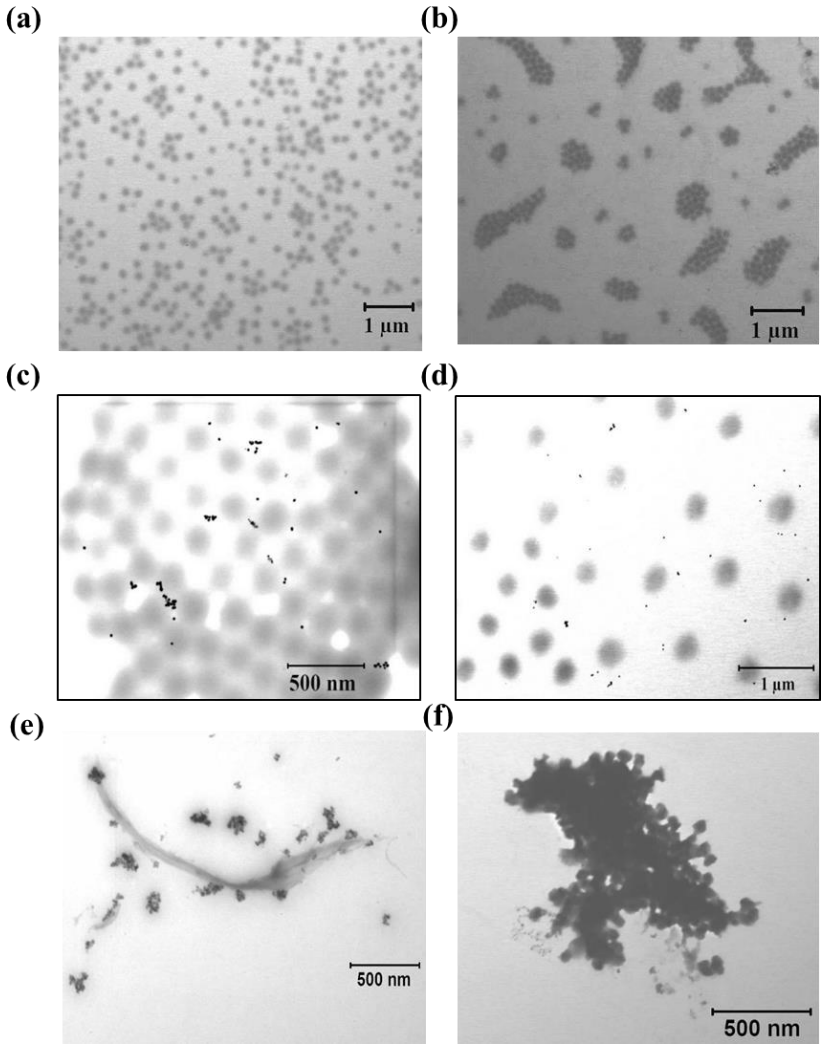

Figure S5 Representative S(T)EM images of (a) a representative nanogel at 25°C (b) at 45°C (c) Fe@AU_NG_c at 25°C (d) at 45°C (e) Fe@Au_NG_i at 25°C and (f) at 45°C respectively.

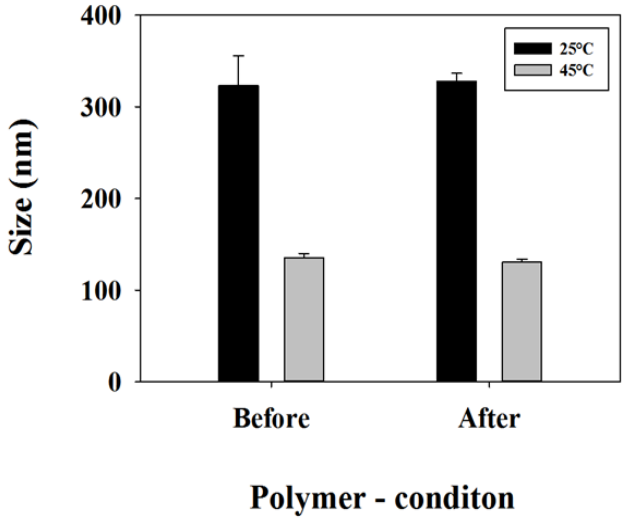

Figure S6 Variation of size of a representative nanogel before and after freeze drying

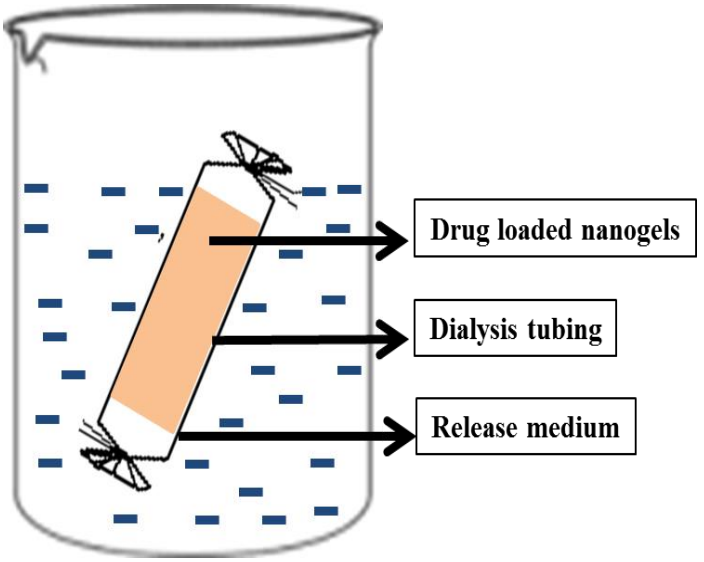

Figure S7 Schematic of the dialysis setup used for studying release from the nanogels.

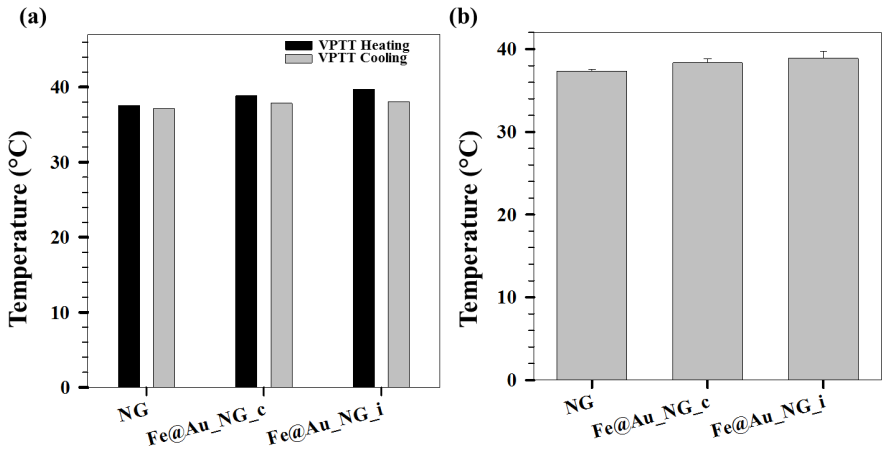

Figure S8 (a) Heating and Cooling VPTTs and (b) Average VPTTs for representative nanogel, Fe@Au_NG_c and Fe@Au_NG_i respectively.

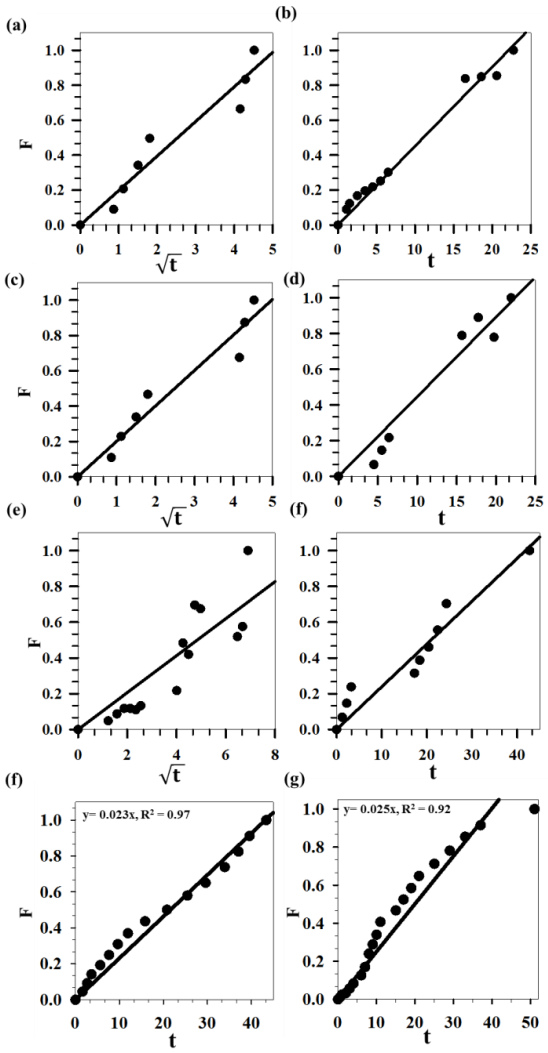

Figure S9 Fitted model for nanogel loaded with Cytochrome C (a) using traditional method and release monitored at 25C and pH 3 (b) using breathing in method and release monitored at 25C and pH 3 (c) using traditional method and release monitored at 40C and pH 6 (d) using traditional method and release monitored at 40C and pH 3 (e) using breathing in method and release monitored at 40C and pH 6 (f) using breathing in method and release monitored at 40C and pH 3 (g) Fitted model for Fe@Au_NG_i loaded with Cytochrome C using breathing in method and release monitored at 40C and pH 3

Paper- IV:

Shape Control of gold nanostructures using binary surfactant mixtures.

Shape Control of gold nanostructures using binary surfactant mixtures

Sulalit Bandyopadhyay[1], Gurvinder Singh[2*], Wilhelm Robert Glomm[1,3]

[1]Ugelstad Laboratory, Department of Chemical Engineering, Norwegian University of Science and Technology (NTNU), N-7491, Trondheim, Norway.

[2]Department of Materials Science and Engineering, Norwegian University of Science and Technology (NTNU), N-7491, Trondheim, Norway.

[3]Polymer Particle and Surface Chemistry Research Group, SINTEF Materials and Chemistry, N-7465 Trondheim, Norway.

KEYWORDS : anisotropic Au nanoparticles, nanorods, bipyramids, binary surfactant, soft template, halides, seeded growth

ABSTRACT: In recent years, efforts have been made to produce Au nanorods of different sizes through the use of binary surfactant mixture in the seed-mediated growth approach. However, our understanding as to how the ratio of two different surfactants influence the shape of the Au nanoparticles are not established yet. Here, we report on shape controlled synthesis of Au nanoparticles, using a binary surfactant mixture of CTAB (Cetyltrimethylammonium bromide) and DDAB (Didecyldimethylammonium bromide) in a silver assisted seed-mediated growth approach. A decrease in the CTAB/DDAB ratio caused a shape transition from Au nanorods to elongated tetrahexahedral and finally to Au bipyramids. The influence of various reactions parameters like pH, concentration of ascorbic acid and silver ions, and role of counter ions on the shape and size of Au NPs have been investigated at fixed CTAB/DDAB ratios. The changes in the size and morphology were caused by modifications in the soft template due to a combined role of DDAB and silver ions and slow facet-specific growth of Au NPs. These results are an advancement in understanding of synthesis of anisotropic Au NPs that is mostly controlled by interaction of the binary surfactant micelles with growing Au NPs.

1. Introduction

The seed-mediated growth approach[1-4] has been widely used to synthesize anisotropic gold (Au) nanoparticles (NPs) because of their unique shape- and size- dependent chemical and physical properties[5-7] and numerous potential applications in e.g., energy,[8] biomedical,[9-10] sensing,[11-12] catalysis,[13-15] and spectroscopic,[16-17] areas. The underlying principle for this approach comprises two main steps: (i) generation of Au seed particles using a strong reducing agent at high values of supersaturation, and (ii) directed growth of these seed particles using a mild reducing agent in the presence of surfactants,[1, 3-4] organic additives or binary surfactant mixtures[2, 18-20] at low values of supersaturation.[21] By this approach, the growth of Au NPs in different shapes have been investigated in the presence of single surfactant cetyltrimethylammonium bromide (CTAB) with or without growth directing species like Ag.[1-3, 22] However, while these reports provide mechanistic understanding of anisotropic Au NPs, the wide distribution of shapes of Au NPs along with poor size tunability effectively limits the robustness of any conclusions drawn. To overcome these limitations, a modified seed-mediated growth approach was proposed based on the use of binary surfactants or organic additives to the growth solution.

For example, the synthesis of Au nanorods (Au NRs) of tunable aspect ratio was shown by adding of benzyldimethylhexadecylammonium chloride (BDAC) in the CTAB growth solution.[2, 18] BDAC and CTAB have identical hydrophobic head groups, but, the mixed micelle structure of binary surfactants changes with increasing amount of BDAC due to the modification in the head group by benzyl ring. The micellar behaviour of CTAB can also be changed by the addition of organic additives such as sodium salicylate and sodium oleate to the CTAB growth solution.[19-20] Au NRs of tunable aspect ratio with good monodispersity can thus be obtained by this approach. The synthesis of Au bipyramid and tetrehexahedra type NPs have also been demonstrated by using binary surfactants, CTAB/CTAC (cetyltrimethylammonium chloride),[23] CTAC/sodium salicylate,[24] and CTAB/DDAB (didecyldimethylammonium bromide).[25] Despite the significant progress made in the recent years, these investigations were limited to obtain one type of anisotropic Au NPs when the different types of binary surfactant mixtures were used. However, no systematic study fully elucidating the evolution of various shapes by systematically varying the ratio between two different surfactants to design the mixed micelle template exists in the published literature.[26-28] Moreover, the concentration of co-surfactant or ratio of CTAB to co-surfactant at which the shape of Au NPs changes (*i.e.,* the transformation of NRs to other shapes) under otherwise identical reaction conditions is currently not known. Therefore, the need for such investigation is very essential not only for synthesizing Au NPs in various shapes but also for developing better mechanistic understanding of differently shaped Au NPs.

Here, we report the first study of its kind, in which Au NPs of different shapes have been synthesized by seed mediated method employing binary surfactant mixtures. Two different surfactants were selected, single chain CTAB and double chain DDAB which differ in their head group areas, tail volumes and critical packing parameters (Figure 1). CTAB modifies its micelle structure from spherical to elongated and DDAB has closed bilayer micelle structures at and above the critical micelle concentration.[27, 29] The addition of DDAB to CTAB solution modifies the micelle structures of CTAB depending on the DDAB content present in the solution. Bergström et al extensively investigated the change in the mixed micelle structures in the solution at different concentrations of DDAB by using small angle neutron scattering.[26] However, how the modified micelle structures of binary surfactant mixtures influence the shape and size of metallic NPs has not been examined. To demonstrate, we have thus selected the value of lowest and highest CTAB/DDAB ratios based on this reported literature,[27] and varied the CTAB/DDAB ratio between these two limits in the present study. We investigated how the shape and aspect ratio of Au NPs change as an increasing amount of DDAB is added to the growth solution containing fixed amount of CTAB. Using a systematic approach, we studied the influence of pH of the growth solution on the aspect ratio of Au NPs. In seed mediated process, the ascorbic acid which acts as a mild reducing agent is used for the reduction of Au^{+3} to Au^{+} in the growth solution and the silver ions facilitate the growth of anisotropic Au NPs. Therefore, the concentration of both the ascorbic acid and silver ions play important role in the preparation of shaped-controlled synthesis of Au NPs. In this work, the influence of ascorbic acid and silver ions concentration on the shape and aspect ratio of Au NPs is studied at two different CTAB/DDAB ratios. We also examine the role of counter ions (Br^-, Cl^-, I^-), *i.e.,* replacing DDAB by didecyldimethylammonium chloride (DDAC) and tridodecylmethylammonium iodide (DDAI) on the shape and aspect ratio of Au NPs (Figure 1). The results from CTAB/DDAC and CTAB/DDAI were compared with CTAB/DDAB, suggesting that the selection of appropriate co-surfactant is essential to achieve the tunability in the shape at different ratios of binary surfactants. Therefore, the work reported here is a step forward to establish the understanding how Au NPs of different shapes grow from the spherical seed particles.

2. Experimental section

2.1 Materials and methods

Silver nitrate ($AgNO_3$), didodecyldimethylammonium bromide (DDAB, 98%), didecyldimethylammonium chloride (DDAC), tridodecylmethylammonium iodide (DDAI, 97%), chloroauric acid ($HAuCl_4.3H_2O$, 99.999%), D-(–)-isoascorbic acid (AA, 98%), sodium borohydride ($NaBH_4$,>= 96%) were purchased from Sigma Aldrich. Cetyltrimethylammonium bromide (CTAB, 99%+) was received from Acros Organics. Sodium citrate dihydrate (Na-citrate, ACS grade from Merck) and hydrochloric acid (HCl 37% fuming

from Merck Millipore) and sodium hydroxide (pellets AnalaR NORMAPUR® ACS) were purchased from VWR. All chemicals were used as received without further purification. Distilled de-ionized water (resistivity ~18.2μΩ-cm, pH~6.5) purified by Millipore water purification system was used for the synthesis of Au NPs.

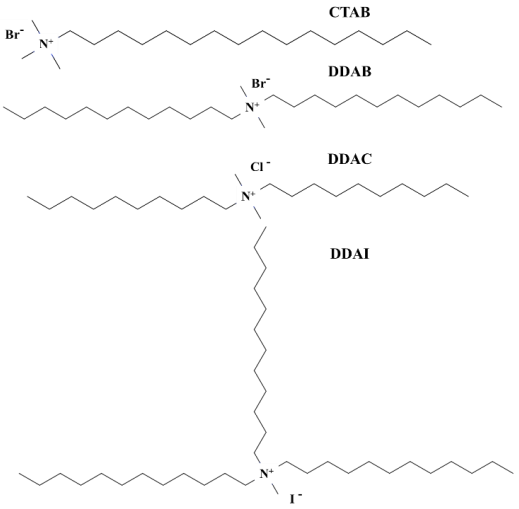

Figure 1. Molecular structures of the surfactants used in the study.

2.2 Synthesis of anistropic Au NPs

A seed mediated approach for synthesizing anistropic Au NPs was modified from the previously reported approach.[19] To prepare Au seed solution (size~3±1 nm based on TEM, Figure S1), 5ml of 0.5mM $HAuCl_4.3H_2O$ was first mixed with 5ml of 0.2M CTAB solution and allowed to stir. Thereafter, 1.6 ml of freshly prepared 3.75mM $NaBH_4$ was added to the mixture and allowed to react for 2 min under vigorous stirring (1200 rpm). Prior to use, the seed solution was aged for 30 min at room temperature in order to allow escape of the gas formed during the reaction.

For the growth solution, 0.540 g of CTAB and varying amounts of DDAB were dissolved in 15 ml of warm deionized water (80°C). The detailed information of experimental conditions corresponding to results presented in this work are reported in table S1 (Supporting Information). The solution of binary surfactant mixtures was vigorously stirred (1200 rpm) at 80°C for 30 min until the solution became transparent. This step is needed to fully dissolve DDAB which is more hydrophobic than CTAB. After cooling down the temperature of the solution to 32°C, 750 μL of freshly prepared 4 mM $AgNO_3$ was added to mixed surfactant solution. The solution was stirred (600 rpm) for 15 min at 30°C before adding 15 mL of 1 mM $HAuCl_4.3H_2O$. The resultant solution was further stirred at (600 rpm) for 15 min at 30°C temperature. After adding 135 μL of 64 mM AA to the reaction mixture, the solution was again stirred (1200 rpm) to obtain a colorless solution indicating the reduction of Au^{3+} to Au^{+}. In the final step, 96 μL of Au seed solution was added to the growth solution under vigorous stirring (1200 rpm). After 30 s, the stirring was stopped, and the resultant reaction mixture was left for 12 h at 30°C. The reaction mixture was centrifuged at 10,000 rpm for 5 min. After discarding the supernatant, the collected reaction products were washed two times with deionized water to remove the excess surfactants. Finally, the reaction products were redispersed in 5 mL deionized water. The results are presented here without any further purification step of size or shape selection. Similar protocol was adapted for CTAB/DDAC and CTAB/DDAI surfactant mixtures to synthesize anisotropic Au NPs.

2.3 Characterization techniques

Hitachi S-5500 Scanning (Transmission) Electron Microscopy (STEM) operating at accelerating voltage of 30 kV was used to acquire SEM and bright field STEM (BF-STEM) images. For BF-STEM imaging, the samples were prepared by placing several 10 μL drops of anisotropic Au NPs solution on a formvar carbon coated 300 mesh copper TEM grid (purchased from Electron Microscopy Sciences) and dried at room temperature. For SEM imaging, 25 μL solution of anisotropic Au NPs were dropped to 5 mm^2 silicon wafer (purchased from siltronix), and dried at room temperature. High resolution (HR) TEM images and electron diffraction patterns were collected from the JEOL 2100 operating at 200 kV. UV–vis spectra were acquired with a UV-2401PC (Shimadzu) spectrophotometer. The spectra were collected over the spectral range from 200 to 1000 nm.

3. Results

3.1 Effect of DDAB concentration on both morphology and aspect ratio

In the first set of experiments, the concentration of co-surfactant (*i.e.,* DDAB) was varied while CTAB concentration (*i.e.,* 1.5 mmol) was kept constant. As the CTAB/DDAB increased from 2 up to 46, we noticed a change in the shape of the Au NPs from bipyramids (low CTAB/DDAB ratio) to NRs (high CTAB/DDAB ratio) via tetrahexahedral (intermediate CTAB/DDAB ratio). At the lowest CTAB/DDAB ratio (1.9), *i.e.,* high concentration of DDAB, biypramidal NPs of longitudinal length (l) ~1.2 μm and transverse width (w) ~382 nm (aspect ratio~3.1) with high yield (~70%) were synthesized as the main reaction product, while pentatwinned and tetrahexahedral type Au NPs were obtained as minor byproducts (Figure 2a, and Figure S2). Au bipyramids of small size (l~664 nm, w~186 nm, and aspect ratio =3.5) were obtained upon slightly increasing the CTAB/DDAB ratio to 6 (Figure 2b). The crystalline structure of the Au bipyramids was determined by HRTEM and electron diffraction patterns (Figure 2c-d). Figure 2d shows a representative HRTEM image taken

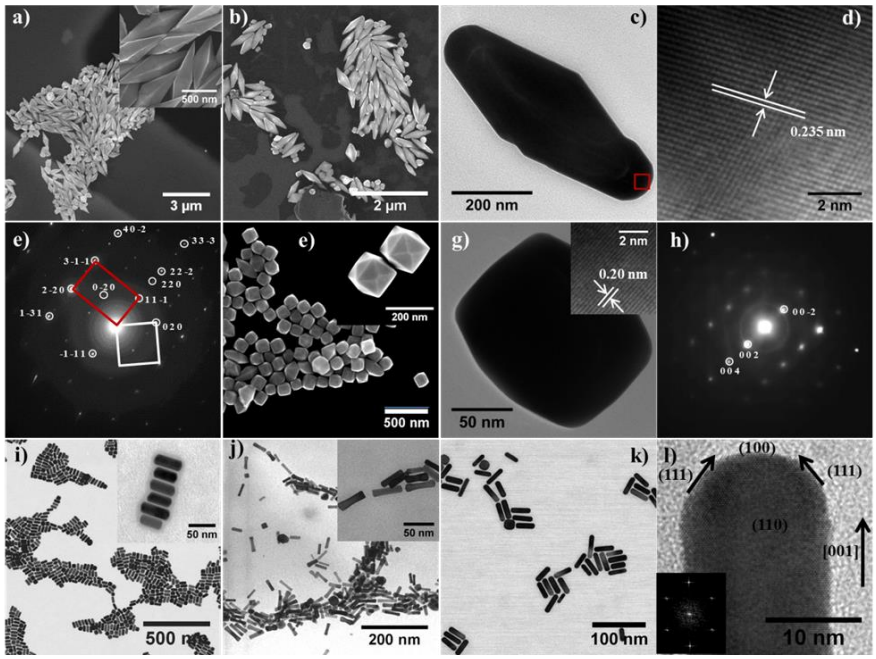

Figure 2. Au NPs synthesized at different CTAB/DDAB ratios (x). SEM images of Au bipyramid NPs of a) l=1.2±0.9 μm and w=382±30 nm, x=2 and b) l=664±78 nm and w=186±20 nm, x=6. c) TEM image of single Au bipyramid of (c). d) HRTEM image of Au NPs taken from red rectangular shown in image (c). e) Electron diffraction pattern taken on bipyramids shown in (c). e) SEM image of Au tetrahexahedral NPs, l=198 nm and w=168 nm, x=8. g) TEM image of single Au tetrahexahedral NP (inset is HRTEM image), and h) electron diffraction pattern taken on NP shown in (g). BF-STEM images of Au NRs of i) l=45±8 nm and w=24±5 nm, x=11, j) l=33±5 nm and w=10±2 nm, x=23 and k) l=38±7 nm and w=10±2 nm, x=46. h) HRTEM image of Au NR and inset is FFT of NR. l and w are referred to longitudinal length and transverse width.

from the highlighted region of single Au bipyramid in Figure 1c, and the observed spacing between the lattice fringes was ~0.235 nm, corresponding to the interplanar spacing of Au (111), *i.e.,* (111) facets of bipyramid. The electron diffraction pattern collected at the center of the Au bipyramid exhibits two set of spots which can indexed to <112> and <001> zone axes, respectively, corresponding to red and white regions respectively in Figure 2e. The indexed spots in the diffraction pattern correspond to the lattice parameters: d_{111}=0.235 nm, d_{222}=0.119 nm, d_{220}=0.145 nm, d_{020}=0.206 nm, d_{311}=d_{131}=0.126 nm, and d_{402}=0.092. All of these spacings were measured within the range of ±2% error compared to bulk values, and are in agreement with reported values in the literature.[30-31] The remaining spots which are not indexed are caused by multiple scattering. Such a diffraction pattern is typical of twinned or decahedral nanoparticles with five-fold symmetry and similar pattern was also observed for Au, Ag, and Cu multiple twinned nanoparticles in the literature.[32-33] The result suggests that Au bipyramids produced in the study are face-centered cubic pentatwinned NPs grown along the <110> while the sides are bound by {111} and {100} facets.

When the CTAB/DDAB ratio was increased to 8, the yield of bipyramids significantly decreased (~5%), and elongated tetrahexahedral (THH) type Au NPs (l=~198 nm, and w~168 nm, and aspect ratio ~1.2) with high yield (~90%) were obtained as the main reaction product (Figure 2e, and Figure S3). THH NP can be seen as a cube with six square-based pyramid, and its 24 sides belong to high index facets of {*hko*}, where $h \neq k \neq 0$. Elongated THH NPs are formed by stretching the facets along one direction. Figure 1g shows the TEM image of THH Au NP and HRTEM image acquired from the corner of the THH Au NPs, is displayed in the inset. The lattice spacing between the fringes (0.2 nm) corresponds to the interplanar spacing of Au (100). Electron diffraction pattern taken at the center of THH Au NP projected along the <310> zone axis is shown in Figure 2h and the diffraction spots reveal the single crystalline nature of Au NPs. A morphological transition from elongated THH to rod occurred in between the CTAB/DDAB ratio from 8 to 11 (*i.e.,* when the concentration of DDAB is low), and NRs were obtained (Figure 2i). On further increase in the ratio from 11 to 23 and 46, thinner NRs of smaller length were obtained (Figure 2j, and k). An HRTEM image shows the

single crystalline Au NRs growing along the direction [001] (Figure 2l). The

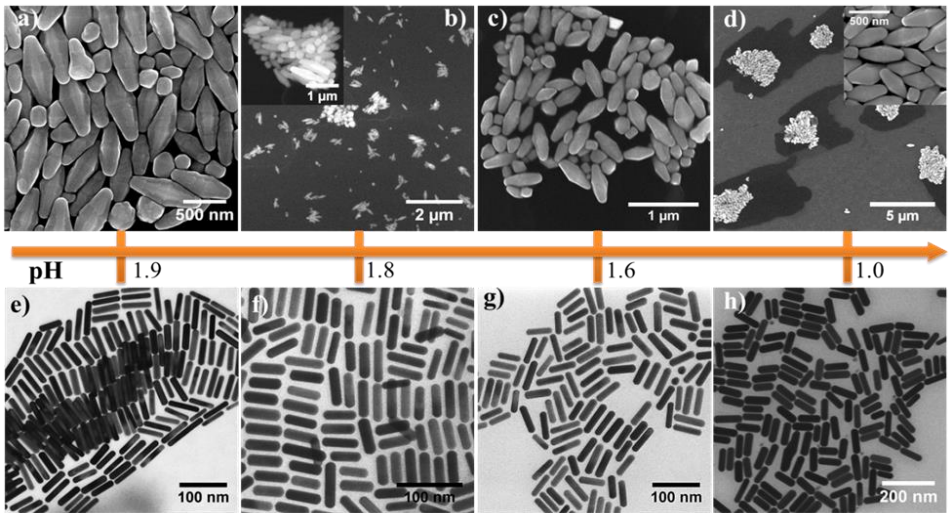

Figure 3. The influence of growth solution pH on the Au NPs size synthesized at low and high CTAB/DDAB ratios (6 and 23). (a-d) SEM images show the decrease in the average size of Au bipyramids with decrease in the pH from left (1.9) to right (1.0). (e-h) BESTEM images exhibit the increases in the average length of Au NRs with decrease in the pH from left to right.

fast fourier transform (FFT) inset of Figure 2l reveals that the sides of the NRs are formed by {110} facets and the ends of NRs are bound by {111} and {001} facets. NRs are oriented in dominant [110] direction.

We also examined the role of the co-surfactant DDAB on the evolution of different shapes. The synthesis of Au NPs was performed in the growth solution of DDAB. At low (0.06 mmol) concentration DDAB, a mixture of shapes (spherical, NRs, elongated THH) was observed (Figure S4). On increasing the concentration of DDAB to 0.26 mmol, the polydisperse NRs as main reaction product along with byproducts (elongated THH and bipyramids) were obtained (Figure S5). These results show that DDAB alone can also induce the growth of anisotropic Au NPs which is more pronounced at higher DDAB concentration (0.26 mmol). At very high DDAB concentration (0.8 mmol or above), no reaction product was obtained and the solution remains transparent even after 12 h of the reaction. This may be because of the formation of very small spherical Au NPs which were difficult to purify by centrifugation from the highly viscous reaction solution. From the control experimental results of DDAB study, no change in the shape of Au NPs was noticed with an increase in the concentration of DDAB. When 0.1 and 0.3 mmol of DDAB is present in the CTAB growth solution, Au NRs and bipyramids grew under similar condition. In another control experiment, the concentration of CTAB was varied at a fixed DDAB concentration of 0.3 mmol. At low CTAB concentration (0.27 mmol), spherical and elongated Au NPs were the main reaction products (Figure S6a and b). Elongated THH with regular shaped Au NPs were formed at 0.7 mmol of CTAB (Figure S6c). When the concentration of CTAB was increased above 1.5 mmol, *i.e.,* 3.0 mmol, monodisperse NRs were obtained (Figure S6d). We did not notice bipyramids formation at these concentrations. Overall, these results suggest that an appropriate concentration of binary surfactants (CTAB/DDAB ratio) in the growth solution is highly essential to achieve shape control of the Au NPs (*i.e.,* NRs to bypyramids via elongated THH).

3.2 Effect of pH of the growth solution on both morphology and aspect ratio

By carefully modifying the reaction conditions at fixed CTAB/DDAB ratios, it is possible to change the size and morphology of Au NPs. Among various reaction parameters, the pH of the growth solution is an important parameter because it can increase or decrease the reduction rate of Au^{3+} by increasing or decreasing the pH of the solution. Here, we also examined the role of pH on the size and morphology of Au NPs at two different CTAB/DDAB ratios, *i.e.*, 6 and 23. The pH of the growth solution was adjusted by adding different volumes of 12.1 M HCl or 0.1M NaOH. When the pH of the growth solution containing low CTAB/DDAB ratio (6) was decreased to 1.9, an increase in the length (~702 nm) and width (~260 nm) of bipyramids was observed compared to the Au bipyramids synthesized

without HCl (figure 3a). On further decrease in the pH from 1.9 to 1.7, 1.5 and 1, both the length and width of Au bipyramids decrease (Figure 3b-d, Table S2). From SEM images, it can be seen that the morphology of Au bipyramids also changes with decrease in the pH, as these appeared to be more truncated compared to those prepared without HCl. An increase in the pH of the growth solution (low CTAB/DDAB ratio) by

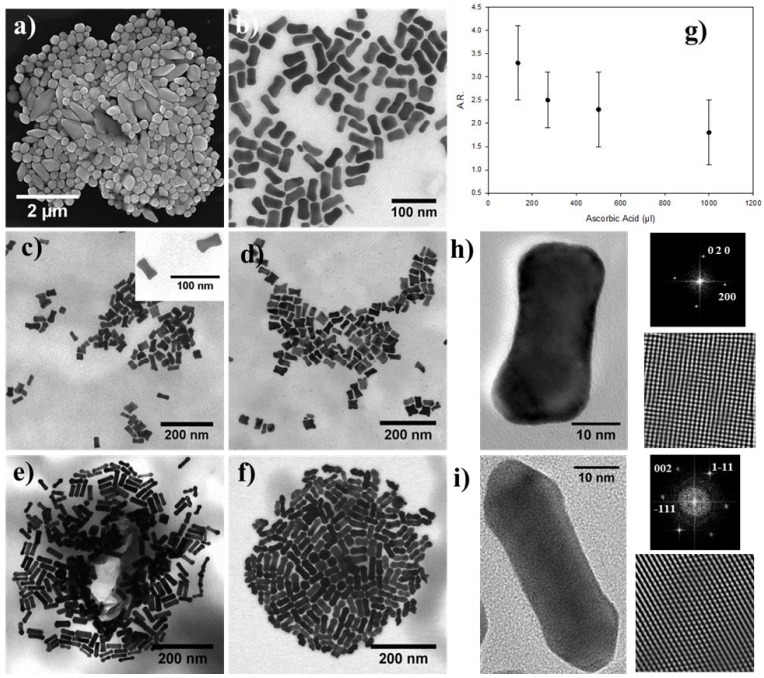

Figure 4. The influence of ascorbic acid (AA) concentration on the morphology of Au NPs. a) SEM image of Au NPs at low CTAB/DDAB=6, AA=270 µL. BFSTEM images of Au NRs synthesized at high CTAB/DDAB= 23 at different AA concentrations, b) AA=270 µL, c) AA=500 µL, d) AA=1 mL. BFSTEM image of Au NRs prepared in acidic medium with varying concentrations of AA, e) AA=150 µL, HCl=50 µL, f) AA=175 µL, HCl=50 µL. g) The variation of aspect ratio of dogbone Au NPs with AA concentration. h) HRTEM image of Au NRs shown in panel (d), FFT (top right) and inverse FFT image (bottom right). i) HRTEM image of Au NR displayed in panel (f), FFT (top right) and inverse FFT image (bottom right).

the addition of NaOH decreased the yield of Au bipyramids (Figure S7). At high CTAB/DDAB ratio, an increase in the length and width of Au NRs was noticed on decreasing the pH of the growth solution (Figure 3e-h, Table S2). In this case, we did not observe any morphological change in the Au NRs. When the pH of the solution was increased by the addition of NaOH, NRs of shorter aspect ratios were obtained. No significant change in the size and width of NRs was seen, and remained nearly constant regardless of pH (Figure S8). In the case of high pH, the reduction rate of Au^{3+} is significantly increased, compared to acidic condition. The enhanced reduction rate thus causes faster deposition of Au atoms in all direction on the existing crystallographic faces, leading to the growth of shorter length Au NRs. While under acidic conditions, high aspect ratio NRs are achieved, because the reduced reduction rate causes slow deposition of Au atoms along the [001] growth directions than to other facets.

3.3 Effect of ascorbic acid concentration on morphology and aspect ratio

Changing the concentration of ascorbic acid (AA), which acts as a mild reducing agent, provides a way to modify the morphology of Au NPs. When its concentration is increased in the growth solution, it enhances the reduction of Au ions facilitating the formation of more kinetically controlled (or less thermodynamically favorable) morphologies of Au NPs. Here, we also investigated the influence of AA concentration on the morphology and aspect ratio of Au NPs produced at low and high CTAB/DDAB ratios. When the amount of 64 mM AA was increased to 270 µL in growth solution of low CTAB/DDAB ratio (6), the yield of bypyramids decreased (~25%) and the polydispersity in shape and size of Au NPs can be seen in Figure 4a. On further increase in the AA concentration in the growth solu-

tion, it led to ill-defined Au NPs with very low yield of bipyramids (~5%). In the case of high CTAB/DDAB ratio (23), we observed the dogbone morphology of NR with increase in the AA amount from 135 µL to 270 µL in the growth solution (Figure 4b-d). No change in dogbone morphology of NR was seen on further increase in AA concentration upto 1 mL in the growth solution. However, a change in the length and width of dogbone was noticed, *i.e.,* aspect ratio of dogbone decreases with increase in the AA concentration in

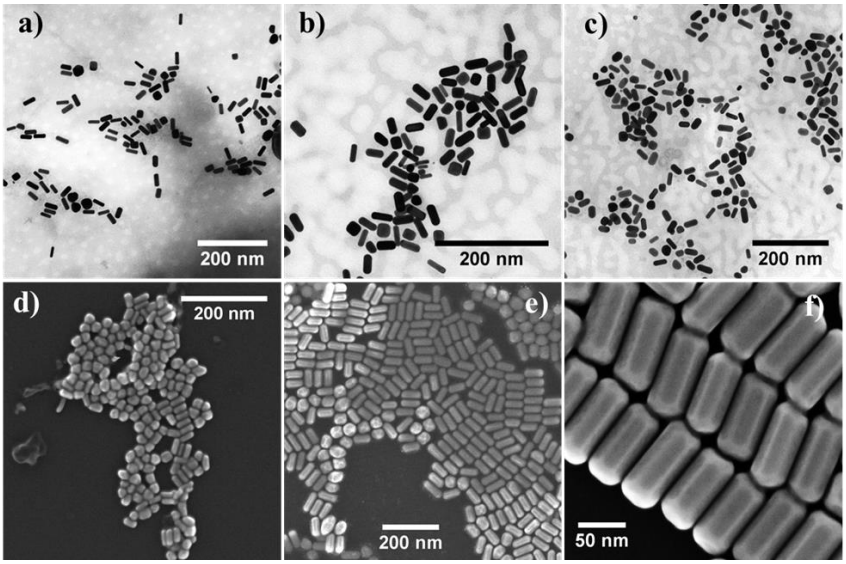

Figure 5. The role of counter ions present in the secondary surfactant on the morphology of Au NPs. (a-b) BESTEM images of Au NRs prepared in the growth solution containing CTAB/DDAC in different ratios. The ratio increases from (a) to (c). (d) SEM images showing the Au NRs grown from the solution at high CTAB/DDAI ratio (~33). e) Au NRs with faceted synthesized in the growth solution of low CTAB/DDAI ratio (~16), and (f) is the magnified view of (e). The experimental conditions for Au NPs synthesis for CTAB/DDAC and CTAB/DDAI are provided in the table S4 and S5

the growth solution (Figure 4g and Table S3). A single crystalline nature of dogbone can be seen from HRTEM, FFT and inverse FFT images (Figure 4h). These results also reveal that dogbone NR is projected along [001] and formed by {110} facets (sides), {111} and {100} facets at the ends. The dogbone morphology of NRs evolves by the rapid overgrowth of {111} facets relative to {110} and {100} facets because the surfactants are strongly attached to the high surface energy or less tightly packed {110} facets. To illustrate the role of AA concentration in the acidic condition, *i.e.,* pH=1.9, different volumes of AA solution was added to the growth solution containing CTAB/DDAB=23. Interestingly, we notice a gradual transition in the morphology from NR to dumbbell. The results show a mixture of Au NR and dumbbell shape rod morphology at AA= 150 µL and dumbbell like NPs with high yield at increased AA amount (175 µL) (Figure 4e-f). HRTEM image shows a single crystalline dumbbell NR oriented along the [110] direction. FFT and inverse FFT images reveal that dumbbell NR is bound by {110} in the sides and {111} and {100} facets in the end.

3.4 Effect of halide counterions on morphology and aspect ratio

To demonstrate the role of secondary surfactant on the morphologies of Au NPs, DDAB was replaced with DDAC. When the synthesis was performed under identical reaction conditions, Au NRs with low yield products (spherical and cubic NPs) were seen from low to high CTAB/DDAC ratios (6, 11, 23) displayed in Figures 5a-c. A slight increase in the aspect ratio of Au NRs can be noticed based on TEM size analysis with an increase in the CTAB/DDAC ratio (Table S4). The size/aspect ratio of the Au NRs can further be increased by performing Au NPs growth in the acidic medium at low and high CTAB/DDAC ratios. The size/aspect ratio of Au NRs can be decreased by growing Au NPs in basic medium at various ratios of CTAB/DDAC. By replacing DDAC with DDAI, a mixture of NRs and spherical NPs was obtained at high CTAB/DDAI ratio (~33) as shown in Figure 5d. However, a decrease in the CTAB/DDAI ratio to 16 (increasing the amount of DDAI in the solution) led to the formation of faceted Au NRs along with other reaction byproducts (Figure 5e, f and Figure S9). We did not observe any reaction product with increase in the concentration of DDAI in the growth solution (decreasing the CTAB/DDAI ratio). The high concentration of DDAI in the solution

makes the solution very viscous and cloudy which remained even after completion of the reaction. From the investigation of different types of co-surfactants, it can be concluded that the bipyramids and tetrahexahedral type shapes of Au NPs strongly depend on nature of the co-surfactant, and can be achieved via employing DDAB.

4. Discussion

The results presented here show that the judicious use of binary surfactant mixtures allows for tunability of the shape and the aspect ratio via changing the CTAB/DDAB ratio (Figure 2). CTAB is a single chain surfactant with a moderate head group area (~56Å^2) and a critical packing parameter (CPP) of 0.33 in water that aids the formation of spherical micelles.[34] On the other hand, DDAB is a water-insoluble, double-chained surfactant of head group area (~25Å^2) with a CPP of 0.62, mostly forming bilayer shaped micelles in water. [35] The addition of DDAB into CTAB solution leads to the change in the CPP of the resultant surfactant mixture depending on the ratio of CTAB/DDAB.[26-27] This change is caused by the large tail volume and small head group area of DDAB decreasing the electrostatic repulsion between the quaternary ammonium groups. Therefore, the reduction in the curvature of micelle by using DDAB with CTAB promotes longer rod-like or cylindrical micelles than with CTAB alone. In our experiment, the CTAB/DDAB molar ratio was only varied, this indicates change in the shape and size of micelle as well as the concentration of overall Br- ions while Ag+ ion concentration remains constant. At low DDAB concentration (*i.e.,* high CTAB/DDAB ratio ~ 46), thinner and shorter aspect ratio Au NRs were formed (Figure 2k). This can be explained by the growth of Au NPs in the thinner soft micellar template. As Au NPs develop crystal facets, the micelles form compact packing on the Au {110} facets restricting the transverse growth of NRs by preventing the diffusion of gold atoms, while the high reduction rate of the Au species on low energy {111} facets facilitate the longitudinal growth due to lower passivation of {111} facets by micelles. This is consistent with computational studies showing the relative packing density of head groups on different facets of Au in the order; {110}>{100}>{111}.[36]

As the concentration of DDAB increases in the CTAB solution (CTAB/DDAB ratio~11), Au NRs grow in the size and width. This suggests that mixed micelles also grow in size (both the length and width) as the DDAB concentration increases in the solution. This is likely due to the change in micellar composition caused by the replacement of CTAB by DDAB, because more hydrophobic DDAB molecules have stronger solid/liquid interfacial adsorption than to CTAB. Moreover, our control experiment study using DDAB only shows that anisotropic Au NPs grow both in the width and length, resulting in low aspect ratios (in the range of ~1 to 2) (Figure S4 and S5). Our experimental results also demonstrate that increasing the CTAB concentration relative to (a fixed concentration) DDAB increases the yield of Au NPs of higher aspect ratio (above 2) (Figure S6). From these experiments, it can be concluded that DDAB tends to facilitate spherical or elongated micelle structures, while CTAB assists in one-dimensional rod like structures. Similar observations were noticed in the reported literature suggesting an increase in the width and length of mixed micelle structure with an increase in the DDAB concentration in the CTAB solution by neutron scattering.[26-27] An increasing concentration of DDAB in the growth solution also makes the diffusion of Au species to the seeds sluggish because of increase in the viscosity of the solution. In this case of high DDAB concentration, (CTAB/DDAB ratio ~8), the reduction rate of Au species at the seeds is very low, and the probability of Au atoms migrating from the {111} facets is very high due to migration of Au atoms at room temperature. As a result, the rate of rapid surface diffusion compared to the deposition rate leads to the formation of kinetically stabilized elongated tetrahexahedral Au NPs bounded with high index facets (Figure 2e). The formation of these NPs can thus be explained in the modification of the soft template to convex structures and low reduction rate of Au species.

A further addition of DDAB to the growth solution (*i.e.,* CTAB/DDAB~ 6 or 2) causes a change in the composition and structure of micelles. The micelle structures grow more significantly in the length than to the width with an increased amount of DDAB in the solution.[26] As a result, Au bipyramidbipyramids of micron and sub-micron sizes were obtained as main reaction products. In this case, Au seed particles grow very slowly compared to growth kinetics at other high CTAB/DDAB ratios because of slow reduction of Au species in the highly viscous/thick solution. To better understand growth mechanism of Au bipyramidbipyramids, the growth of NPs over the time was monitored by UV-vis spectrum (Figure S10). After 120 mins of the reaction, an absorption peak centered at ~590 nm was noticed which is typical of decahedral Au NPs. This result suggests that during the aging of first 120 mins, CTAB stabilized single crystalline seeds turned into polycrystalline seeds possessing five-fold symmetry because of thermodynamic ripening. As the reaction proceeds, a red shift in the peak can be noticed due to increase in the size and morphology of seeds particles. When the reaction was continued for 24 hours, the micelles that act as either soft template or structure directing agent facilitate the selective growth of bypyramids along the <110> axis on the large length scale. It should be noticed that a noisy UV-vis spectra was seen at higher wavelengths, likely due to the rapid sedimentation of large sized Au bipyramids. Overall, these results demonstrate that the shape and size of Au NPs can be tuned by varying the CTAB to DDAB ratio which has not been explored in the case of binary surfactant system. However, the role of Ag^+ concentration cannot be neglected. To illustrate this, we performed control experiments at high and low CTAB/DDAB ratios (6 and 23) in the absence of Ag^+. As a result, Au NPs in various shapes were obtained which is the typical case for the growth reaction

without Ag^+ (Figure S11a and c). When 0.3 mL of Ag^+ solution was added to the growth solution, spherical Au NPs (CTAB/DDAB=23) and bipyramids (CTAB/DDAB=6) of smaller size were obtained (Figure S11b and d). These results indicate the facet specific binding of Ag^+ promoting the growth of anisotropic NPs.

pH of the growth solution has influence on the size and shape of NPs because it influences the reducing capability of AA which is lower for acidic pH values. In the case of Au bipyramid, first the length and width of bipyramids increase, and start decreasing with decrease in the pH of the solution. In high DDAB concentration regime (high CTAB/DDAB ratio 6 and below), the growth rate is very slow at acidic pH because of low reduction potential of AA and high solution viscosity. Moreover, the increasing amount of Cl^- also causes a change in the soft template due to modification in the head group interactions. As a result, truncated bipyramids of different lengths were obtained in low pH solutions. While in the case of Au NRs (low DDAB concentration regime), slow reduction of Au ions species facilitates the more selective deposition of Au atoms on specific crystal facets, i.e., on the tip of NRs under the regulation of micelle structures. As a result, Au NRs of larger sizes were achieved on decreasing the pH. The increase in the pH of solution accelerates growth rate that reduces the yield of Au bipyramids and NRs and favors the more spherical NPs.

The growth rate of the reaction can be controlled through the concentration of AA. We noticed a decrease in the yield of Au bipyramids with an increased in the AA. From the results, it is clear that the growth rate should be slow to obtain Au bipyramids with high yield. However, the morphology of Au NPs in low DDAB solution (high CTAB/DDAB ratio) changes from NRs to dogbone with increase in the amount of AA added to the growth solution. A high concentration of AA present in the solution increases the reduction rate of Au atoms. In this case, Au atoms rapidly deposit on {111} facets possessing loosely packed layer of micelles than to other facets {100} and {110}, where the micelles are tightly packed because of strong steric hindrance. This results in a high deposition rate on {111} facets, and low deposition rate on other facets or low surface diffusion rate of Au atoms migrating from the tip to the sides, promoting dogbone formation. The reduction of Au atoms can be controlled through lowering the pH of the growth solution. When the amount of AA is increased in the growth solution of low pH (~2), then moderate reduction rate of Au atoms in acidic solution facilities the selective growth on specific crystal facets. The facets of high surface energy {100} quickly disappear. The selective growth thus proceeds along the {111} facets, which grow in time and join to make arrow type nanodumbells.

Finally, we showed the effect of different co-surfactants on the shape of Au NPs (Figure 5). Replacing the DDAB with DDAC possessing Cl^- ions, no change in shape of Au NPs was noticed along with variation in the CTAB/DDAC ratio. These experimental results suggest that increasing amount of DDAC to CTAB solution does not cause any change in the morphology of micelles as it was in the case of DDAB. This can be because of low binding affinity of Cl^- ions to Au surface compared to Br^- ions that causes the destabilization of rod-like micelles, *i.e.,* make micellar structures less compact or stable providing Au species in the solution easy access to growing seed particles. Therefore, Au NRs of low aspect ratio with less monodispersity and reaction byproducts (spherical, cubic and irregular shaped NPs) were obtained. Our finding is consistent with atomistic simulation study investigating the role of binary surfactant mixture of CTAB/CTAC at different ratios.[36] Moreover, aspect ratio of NRs and yield of byproduct increases as the DDAC amount increases in the solution. When DDAI (bulkier co-surfactant with I^- ions) as co-surfactant is used, it also does not have any influence on the shape of Au NPs, indicating no change in the micellar structures with varying CTAB/DDAI. However, multifaceted Au NRs of large sizes with spherical NPs were synthesized at low CTAB/DDAI ratio. The main conclusion from this investigation is that DDAB is the most suitable co-surfactant allowing the tunability in the micellar structure to facilitate the formation of Au NPs in different shapes and sizes.

5. Conclusion

In summary, we have demonstrated the influence of DDAB concentration on the shape/morphology and aspect ratio of Au NPs. Au NRs were obtained at low DDAB concentration (high CTAB/DDAB ratio) and the shape changes to elongated THH and Au bipyramids with increase in the DDAB amount (decrease in the CTAB/DDAB ratio). These results suggest that the change in the CTAB micelle structures by DDAB, and the interfacial or interaction of the binary surfactant micelles with growing Au NPs provide a way to tailor the shape of Au NPs as well as their aspect ratio by using a simple seed-mediated growth approach. The concentration of Ag^+ ions is critical to obtain shape tunability in the fixed CTAB/DDAB ratio, and play important role in the facet-specific growth of Au NPs. The results in the absence or low Ag^+ content showed polydispersity in the shapes and sizes at different CTAB/DDAB concentrations.

The effect of growth solution pH on the morphology and aspect ratio have been investigated. The tunability in the size of bipyramids and NRs can be achieved by varying the pH of the solution which controls the reduction rate of Au ion species in the growth solution. A morphology of bipyramids changes to truncated bipyramids with decrease in the pH of the solution, but high pH of the growth solution leads to significant reduction in the yield of bipyramids.

The effect of ascorbic acid amount present in the growth solution on the morphology and aspect ratio have also been studied. The results show that the yield of bipyramids

decreases with an increase in ascorbic acid amount, however, the morphology and aspect ratio of NRs changes to dogbone and nanodumbbell. The changes in the morphology were caused by the modification in the soft template and slow facet-specific growth of Au NPs.

The role of counter ions, *i.e.,* replacing the DDAB with DDAC and DDAI on the morphology and aspect ratio of Au NPs were also investigated. We did not notice any change in the shape of Au NPs at different CTAB/DDAC(DDAI) ratios. This investigation reveals that the addition of DDAC and DDAI does not cause any change in the miceller structures and destabilize the CTAB micelle structures. As a result, Au NRs of low quality and mixtures of various shapes were obtained.

Overall, the present investigation advances our understanding to synthesize anisotropic Au NPs by engineering the design of micelle structures and interfacial/interaction between the micelles and growing seed particles through controlling the amount of co-surfactant.

ASSOCIATED CONTENT

Supporting Information. Detailed synthetic conditions for Au NPs of different shapes and sizes in the tabular form, additional TEM images and UV-vis spectra.

AUTHOR INFORMATION

Corresponding Author

* E-mail: gurvinder.singh@ntnu.no

.

Notes

The authors declare no competing financial interest.

ACKNOWLEDGMENT

The Research Council of Norway is acknowledged for the support to the Norwegian Micro- and Nano-Fabrication Facility, NorFab. The HRTEM work was carried out on the NORTEM (JEOL2100), TEM Gemini Centre, Norwegian University of Science and Technology (NTNU), Norway. This work is supported by the project NORTEM (Grant 197405) within the programme INFRASTRUCTURE of the Research Council of Norway (RCN). NORTEM was co-funded by the RCN and project partners NTNU, UiO and SINTEF.

REFERENCES

1. Jana, N. R.; Gearheart, L.; Murphy, C. J., Seed-mediated growth approach for shape-controlled synthesis of spheroidal and rod-like gold nanoparticles using a surfactant template. Adv Mater 2001, 13, 1389-1393.
2. Nikoobakht, B.; El-Sayed, M. A., Preparation and growth mechanism of gold nanorods (NRs) using seed-mediated growth method. Chem Mater 2003, 15, 1957-1962.
3. Langille, M. R.; Personick, M. L.; Zhang, J.; Mirkin, C. A., Defining rules for the shape evolution of gold nanoparticles. J. Am. Chem. Soc. 2012, 134, 14542-54.
4. Singh, G.; van Helvoort, A. T. J.; Bandyopadhyay, S.; Volden, S.; Andreassen, J. P.; Glomm, W. R., Synthesis of Au nanowires with controlled morphological and structural characteristics. Appl Surf Sci 2014, 311, 780-788.
5. Hua, Y.; Chandra, K.; Dam, D. H. M.; Wiederrecht, G. P.; Odom, T. W., Shape-Dependent Nonlinear Optical Properties of Anisotropic Gold Nanoparticles. J Phys Chem Lett 2015, 6, 4904-4908.
6. Kelly, K. L.; Coronado, E.; Zhao, L. L.; Schatz, G. C., The optical properties of metal nanoparticles: The influence of size, shape, and dielectric environment. J Phys Chem B 2003, 107, 668-677.
7. Jiang, W.; Kim, B. Y. S.; Rutka, J. T.; Chan, W. C. W., Nanoparticle-mediated cellular response is size-dependent. Nat Nanotechnol 2008, 3, 145-150.
8. Atwater, H. A.; Polman, A., Plasmonics for improved photovoltaic devices. Nat Mater 2010, 9, 205-213.
9. Huang, X. H.; El-Sayed, I. H.; Qian, W.; El-Sayed, M. A., Cancer cell imaging and photothermal therapy in the near-infrared region by using gold nanorods. J. Am. Chem. Soc. 2006, 128, 2115-2120.
10. Jain, P. K.; El-Sayed, I. H.; El-Sayed, M. A., Au nanoparticles target cancer. Nano Today 2007, 2, 18-29.
11. Kabashin, A. V.; Evans, P.; Pastkovsky, S.; Hendren, W.; Wurtz, G. A.; Atkinson, R.; Pollard, R.; Podolskiy, V. A.; Zayats, A. V., Plasmonic nanorod metamaterials for biosensing. Nat Mater 2009, 8, 867-871.
12. Wang, L. B.; Zhu, Y. Y.; Xu, L. G.; Chen, W.; Kuang, H.; Liu, L. Q.; Agarwal, A.; Xu, C. L.; Kotov, N. A., Side-by-Side and End-to-End Gold Nanorod Assemblies for Environmental Toxin Sensing. Angew Chem Int Edit 2010, 49, 5472-5475.
13. Jana, D.; Dandapat, A.; De, G., Anisotropic Gold Nanoparticle Doped Mesoporous Boehmite Films and Their Use as Reusable Catalysts in Electron Transfer Reactions. Langmuir 2010, 26, 12177-12184.
14. Zhu, W. L.; Michalsky, R.; Metin, O.; Lv, H. F.; Guo, S. J.; Wright, C. J.; Sun, X. L.; Peterson, A. A.; Sun, S. H., Monodisperse Au Nanoparticles for Selective Electrocatalytic Reduction of CO2 to CO. J. Am. Chem. Soc. 2013, 135, 16833-16836.
15. Li, L. D.; Peng, Y.; Yue, Y. H.; Hu, Y.; Liang, X.; Yin, P. G.; Guo, L., Synthesis of concave gold nanocuboids with high-index facets and their enhanced catalytic activity. Chem Commun 2015, 51, 11591-11594.
16. Lal, S.; Grady, N. K.; Kundu, J.; Levin, C. S.; Lassiter, J. B.; Halas, N. J., Tailoring plasmonic substrates for surface enhanced spectroscopies. Chem Soc Rev 2008, 37, 898-911.
17. Lee, A.; Andrade, G. F. S.; Ahmed, A.; Souza, M. L.; Coombs, N.; Tumarkin, E.; Liu, K.; Gordon, R.; Brolo, A. G.; Kumacheva, E., Probing Dynamic Generation of Hot-Spots in Self-Assembled Chains of Gold Nanorods by Surface-Enhanced Raman Scattering. J. Am. Chem. Soc. 2011, 133, 7563-7570.
18. Wadams, R. C.; Fabris, L.; Vaia, R. A.; Park, K., Time-Dependent Susceptibility of the Growth of Gold Nanorods to the Addition of a Cosurfactant. Chem Mater 2013, 25, 4772-4780.
19. Ye, X. C.; Jin, L. H.; Caglayan, H.; Chen, J.; Xing, G. Z.; Zheng, C.; Doan-Nguyen, V.; Kang, Y. J.; Engheta, N.; Kagan, C. R.; Murray, C. B., Improved Size-Tunable Synthesis of Monodisperse Gold Nanorods through the Use of Aromatic Additives. Acs Nano 2012, 6, 2804-2817.
20. Ye, X. C.; Zheng, C.; Chen, J.; Gao, Y. Z.; Murray, C. B., Using Binary Surfactant Mixtures To Simultaneously Improve the Dimensional Tunability and Monodispersity in the Seeded Growth of Gold Nanorods. Nano Lett 2013, 13, 765-771.

21. Bakshi, M. S., How Surfactants Control Crystal Growth of Nanomaterials. Cryst Growth Des 2016, 16, 1104-1133.
22. Walsh, M. J.; Barrow, S. J.; Tong, W. M.; Funston, A. M.; Etheridge, J., Symmetry Breaking and Silver in Gold Nanorod Growth. Acs Nano 2015, 9, 715-724.
23. Chateau, D.; Liotta, A.; Vadcard, F.; Navarro, J. R. G.; Chaput, F.; Lerme, J.; Lerouge, F.; Parola, S., From gold nanobipyramids to nanojavelins for a precise tuning of the plasmon resonance to the infrared wavelengths: experimental and theoretical aspects. Nanoscale 2015, 7, 1934-1943.
24. Yoo, H.; Jang, M. H., Size-controlled synthesis of gold bipyramids using an aqueous mixture of CTAC and salicylate anions as the soft template. Nanoscale 2013, 5, 6708-6712.
25. Li, J.; Wang, L. H.; Liu, L.; Guo, L.; Han, X. D.; Zhang, Z., Synthesis of tetrahexahedral Au nanocrystals with exposed high-index surfaces. Chem Commun 2010, 46, 5109-5111.
26. Bergstrom, L. M.; Skoglund, S.; Danerlov, K.; Garamus, V. M.; Pedersen, J. S., The growth of micelles, and the transition to bilayers, in mixtures of a single-chain and a double-chain cationic surfactant investigated with small-angle neutron scattering. Soft Matter 2011, 7, 10935-10944.
27. Wasbrough, M. J.; Edler, K. J.; Hawley, A. M.; Holdaway, J. A.; Price, G. J., Control of mesostructure in self-assembled polymer/surfactant films by rational micelle design. Soft Matter 2012, 8, 3357-3362.
28. Ono, Y.; Kawasaki, H.; Annaka, M.; Maeda, H., Effects of micelle-to-vesicle transitions on the degree of counterion binding. J. Colloid Interface Sci. 2005, 287, 685-693.
29. Kuperkar, K.; Abezgauz, L.; Danino, D.; Verma, G.; Hassan, P. A.; Aswal, V. K.; Varade, D.; Bahadur, P., Viscoelastic micellar water/CTAB/$NaNO_3$ solutions: Rheology, SANS and cryo-TEM analysis. J. Colloid Interface Sci. 2008, 323, 403-409.
30. Lisiecki, I., Size, shape, and structural control of metallic nanocrystals. J Phys Chem B 2005, 109, 12231-12244.
31. Zhou, G. J.; Yang, Y.; Han, S. H.; Chen, W.; Fu, Y. Z.; Zou, C.; Zhang, L. J.; Huang, S. M., Growth of Nanobipyramid by Using Large Sized Au Decahedra as Seeds. Acs Appl Mater Inter 2013, 5, 13340-13352.
32. Lisiecki, I.; Filankembo, A.; Sack-Kongehl, H.; Weiss, K.; Pileni, M. P.; Urban, J., Structural investigations of copper nanorods by high-resolution TEM. Physical Review B 2000, 61, 4968-4974.
33. Elechiguerra, J. L.; Reyes-Gasga, J.; Yacaman, M. J., The role of twinning in shape evolution of anisotropic noble metal nanostructures. J. Mater. Chem. 2006, 16, 3906-3919.
34. Warr, G. G.; Sen, R.; Evans, D. F.; Trend, J. E., Microemulsion formation and phase behavior of dialkydimethylammonium bromide surfactants. The Journal of Physical Chemistry 1988, 92, 774-783.
35. Ninham, B. W.; Nostro, P. L., Molecular forces and self assembly; in colloid, nano sciences and biology. Cambridge University Press 2011.
36. Meena, S. K.; Celiksoy, S.; Schafer, P.; Henkel, A.; Sonnichsen, C.; Sulpizi, M., The role of halide ions in the anisotropic growth of gold nanoparticles: a microscopic, atomistic perspective. Phys. Chem. Chem. Phys. 2016, 18, 13246-13254.

Table of Contents (TOC)

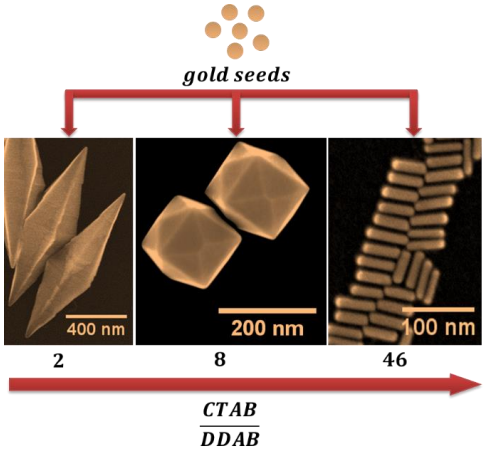

Supporting Information

Shape Control of gold nanostructures using binary surfactant mixtures

Sulalit Bandyopadhyay[1], Gurvinder Singh[2*], Wilhelm Robert Glomm[1,3]

[1]Ugelstad Laboratory, Department of Chemical Engineering, Norwegian University of Science and Technology (NTNU), N-7491, Trondheim, Norway.

[2]Department of Materials Science and Engineering, Norwegian University of Science and Technology (NTNU), N-7491, Trondheim, Norway.

[3]Polymer Particle and Surface Chemistry Research Group, SINTEF Materials and Chemistry, N-7465 Trondheim, Norway.

Corresponding Author: Dr. Gurvinder Singh (gurvinder.singh@ntnu.no)

15 mL Deionized Water		CTAB/ DDAB (molar ratio)	4 mM $AgNO_3$ (mL)	64 mM AA (mL)	Seed Solution (mL)	Results
CTAB (g, mM, mmol)	DDAB (g, mM, mmol)					
0.54, 98.77, 1.48	0.36, 51.77, 0.78	2	0.750	0.135	0.096	Figure 2a Bipyramids l=1.2±0.9 µm, w=382±35 nm
0.54, 98.77, 1.48	0.12, 17.26, 0.26	6	0.750	0.135	0.096	Figure 2b Bipyramids l=664±78 nm, w=186±20 nm
0.54, 98.77, 1.48	0.09, 12.94, 0.19	8	0.750	0.135	0.096	Figure 2e ETHH l=198±20 nm, w=168±15 nm
0.54, 98.77, 1.48	0.06, 8.63, 0.13	11	0.750	0.135	0.096	Figure 2i NRs l=45±8 nm, w=24±5 nm
0.54, 98.77, 1.48	0.03, 4.31, 0.06	23	0.750	0.135	0.096	Figure 2j NRs l=33±5 nm, w=10±2 nm
0.54, 98.77, 1.48	0.015, 2.16, 0.03	46	0.750	0.135	0.096	Figure 2k NRs l=38±7 nm, w=10±2 nm

Table S1. Summary of synthetic conditions used for growing Au NPs of different shapes. 15 mL of 1 mM $HAuCl_4.3H_2O$ was added to the solution of (CTAB+DDAB+$AgNO_3$) before adding ascorbic acid (AA) and seed solution. The length (l) and width (w) are the transverse and longitudinal dimension of the Au NPs. The dimensions were measured from SEM and TEM images by counting 200 particles. ETHH: elongated tretrahexahedral, NRs: nanorods.

CTAB/ DDAB (molar ratio)	**4 mM $AgNO_3$ (mL)**	**64 mM AA (mL)**	**12.1 M HCl (mL)**	**pH**	**Seed Solution (mL)**	**Results**
6	0.750	0.135	0.050	1.9	0.096	Figure 3a Bipyramids l=702±90 nm, w=260±38 nm
6	0.750	0.135	0.100	1.8	0.096	Figure 3b Bipyramids l=665±95 nm, w=218±25 nm
6	0.750	0.135	0.200	1.6	0.096	Figure 3c Bipyramids l=518±64 nm, w=201±25 nm
6	0.750	0.135	0.600	1.0	0.096	Figure 3d Bipyramids l=492±80 nm, w=201±20 nm
23	0.750	0.135	0.050	1.9	0.096	Figure 3e NRs l=55±8 nm, w=12±2 nm
23	0.750	0.135	0.100	1.8	0.096	Figure 3f NRs l=57±6 nm, w=14±2 nm
23	0.750	0.135	0.200	1.6	0.096	Figure 3g NRs l=62±8 nm, w=15±2 nm
23	0.750	0.135	0.600	1.0	0.096	Figure 3h NRs l=88±2 nm, w=28±2 nm

Table S2. Summary of synthetic conditions and results by the extra addition of 12.1M HCl to the growth solution. The dimensions were measured from TEM images by counting 200 particles

CTAB/ DDAB (molar ratio)	**4 mM $AgNO_3$ (mL)**	**64 mM AA (mL)**	**12.1 M HCl (mL)**	**Seed Solution (mL)**	**Results**
23	0.750	0.270		0.096	Figure 4b Dogbone NRs l=46±6 nm, w=19±4 nm
23	0.750	0.500		0.096	Figure 4c Dogbone NRs l=42±6 nm, w=19±5 nm
23	0.750	1		0.096	Figure 4d Dogbone NRs l=36±5 nm, w=22±6 nm
23	0.750	0.150	0.50	0.096	Figure 4e Dumbbell NRs l=45±5 nm, w=13±4 nm
23	0.750	0.175	0.50	0.096	Figure 4f Dumbbell NRs l=49±8 nm, w=17±4 nm

Table S3. Summary of synthetic conditions and results by the extra addition of ascorbic acid (AA) and HCl to the growth solution. The dimensions were measured from TEM images by counting 200 particles.

15 mL Deionized Water		CTAB/ DDAC (molar ratio)	4 mM $AgNO_3$ (mL)	64 mM AA (mL)	Seed Solution (mL)	Results
CTAB (g, mM, mmol)	DDAC (g, mM, mmol)					
0.54, 98.77, 1.48	0.095, 17.49, 0.26	6	0.750	0.135	0.096	Figure 5a NRs l=32±4 nm, w=13±5 nm
0.54, 98.77, 1.48	0.055, 10.12, 0.12	11	0.750	0.135	0.096	Figure 5b NRs l=30±5 nm, w=15±5 nm
0.54, 98.77, 1.48	0.024, 4.42, 0.06	23	0.750	0.135	0.096	Figure 5c NRs l=33±4 nm, w=16±3 nm

Table S4. Summary of synthetic conditions used for growing Au NPs in the presence of CTAB/DDAC.

15 mL Deionized Water		CTAB/ DDAI (molar ratio)	4 mM $AgNO_3$ (mL)	64 mM AA (mL)	Seed Solution (mL)	Results
CTAB (g, mM, mmol)	DDAI (g, mM, mmol)					
0.54, 98.77, 1.48	0.060, 6.02, 0.09	16	0.750	0.135	0.096	Figure 5e, f NRs and spherical NPs
0.54, 98.77, 1.48	0.030, 3.01, 0.05	33	0.750	0.135	0.096	Figure 5d Faceted NRs and spherical NPs

Table S5. Summary of synthetic conditions used for growing Au NPs in the presence of CTAB/DDAI.

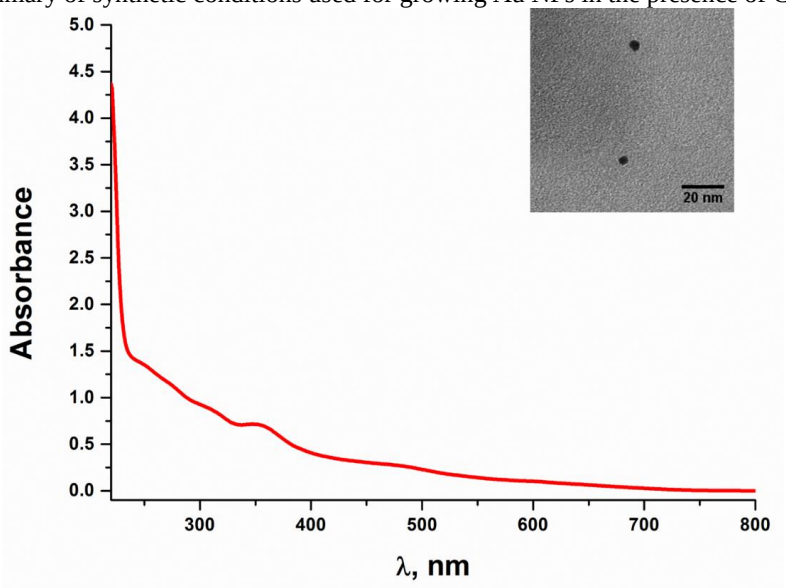

Figure S1. UV-vis spectrum and BFSTEM image show the formation of smaller size Au seed particle (3±1 nm).

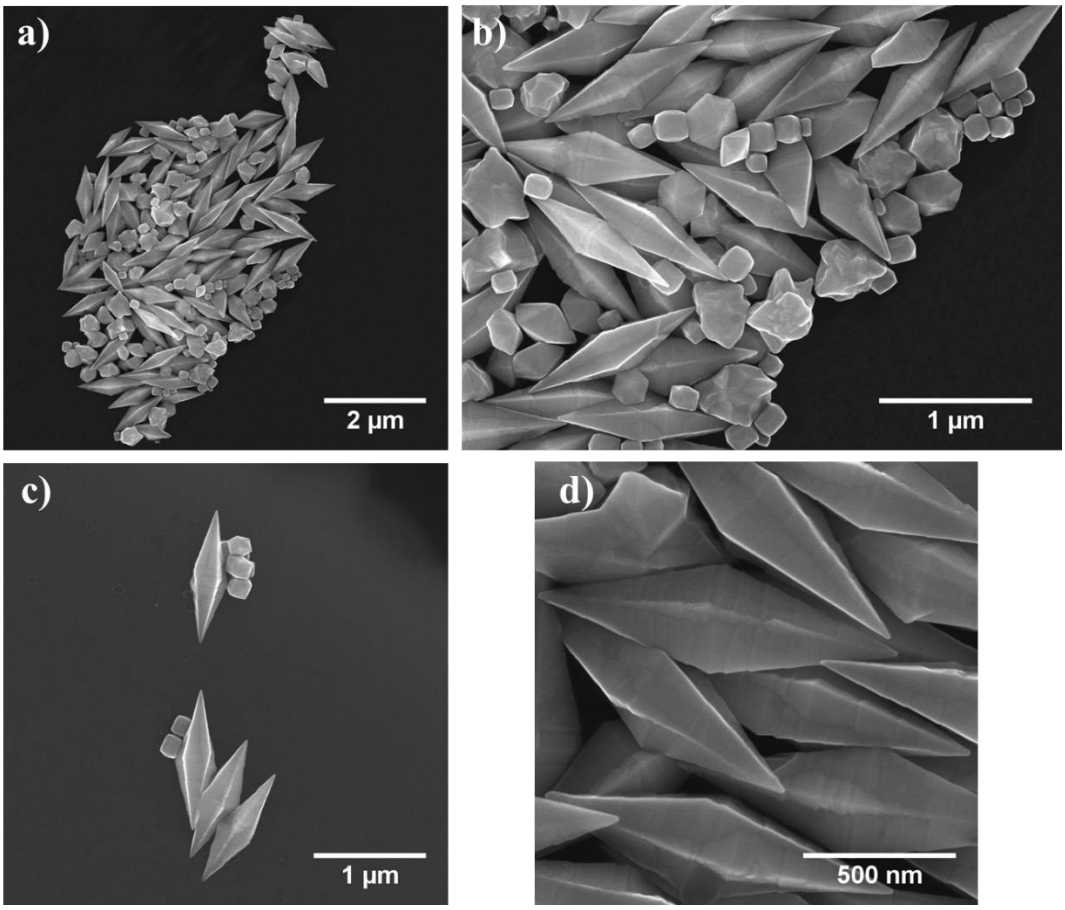

Figure S2. SEM images (a-d) show Au bipyramids and reaction byproducts taken different places on the silicon substrate. Au bipyramids were synthesized by the binary surfactant mixtures (CTAB/DDAB=2).

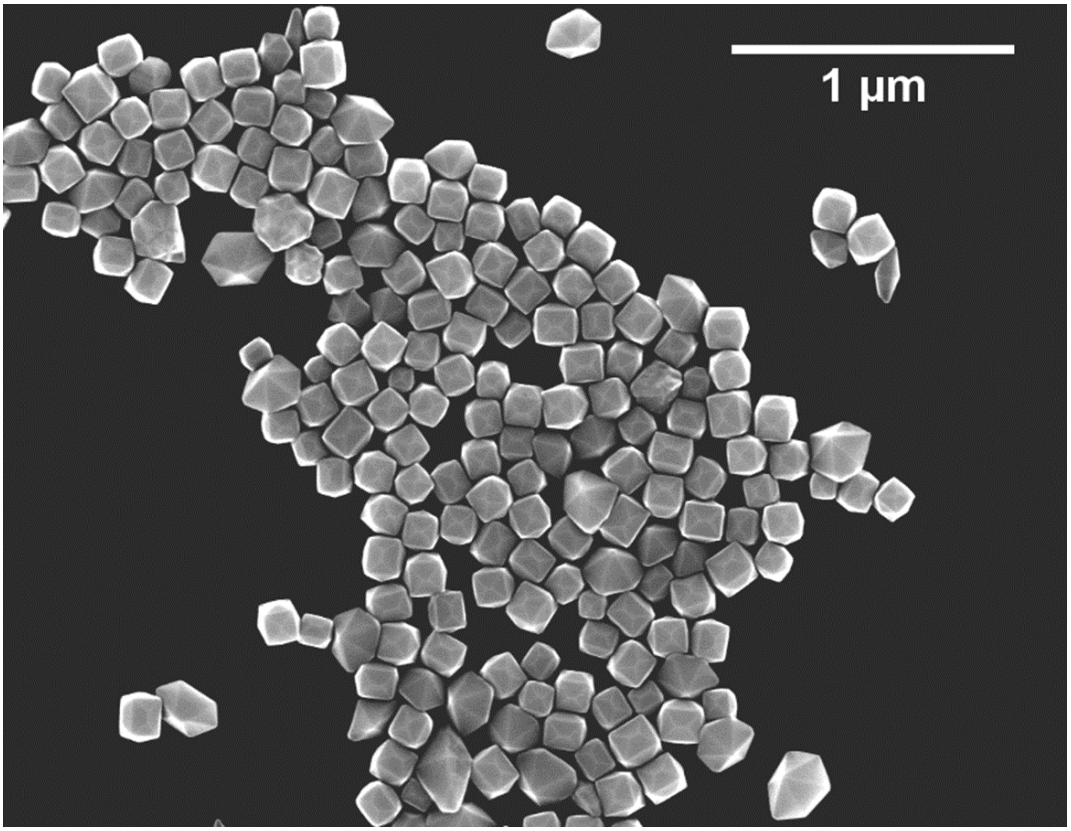

Figure S3. SEM image show high yield of elongated THH Au NPs with less reaction byproducts synthesized at CTAB/DDAB=8.

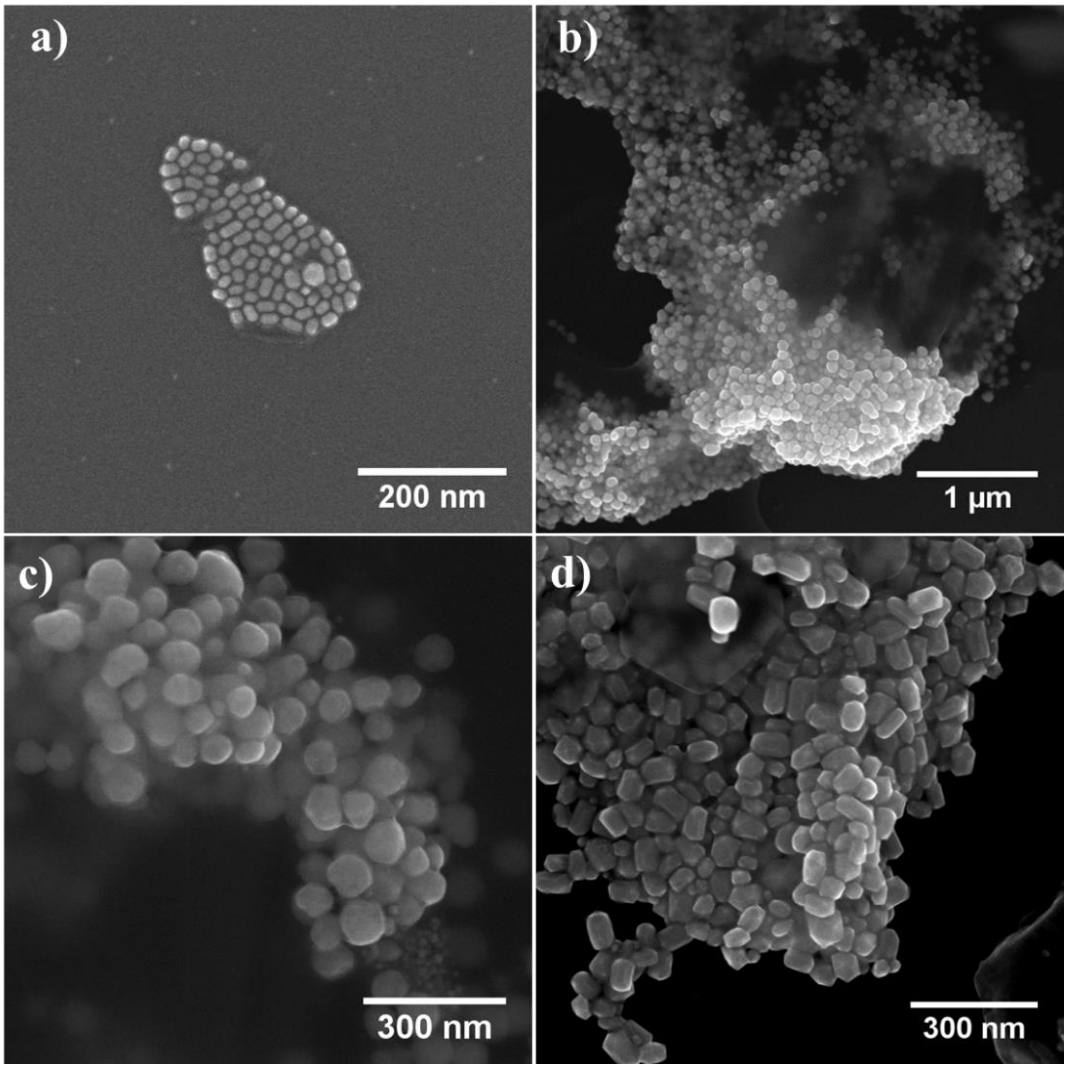

Figure S4. SEM images displaying the mixture of shapes including NRs (a), spherical and irregular shaped (b, c) and elongated THH type Au NPs synthesized in the presence of single surfactant, DDAB (0.06 mmol/8.63 mM).

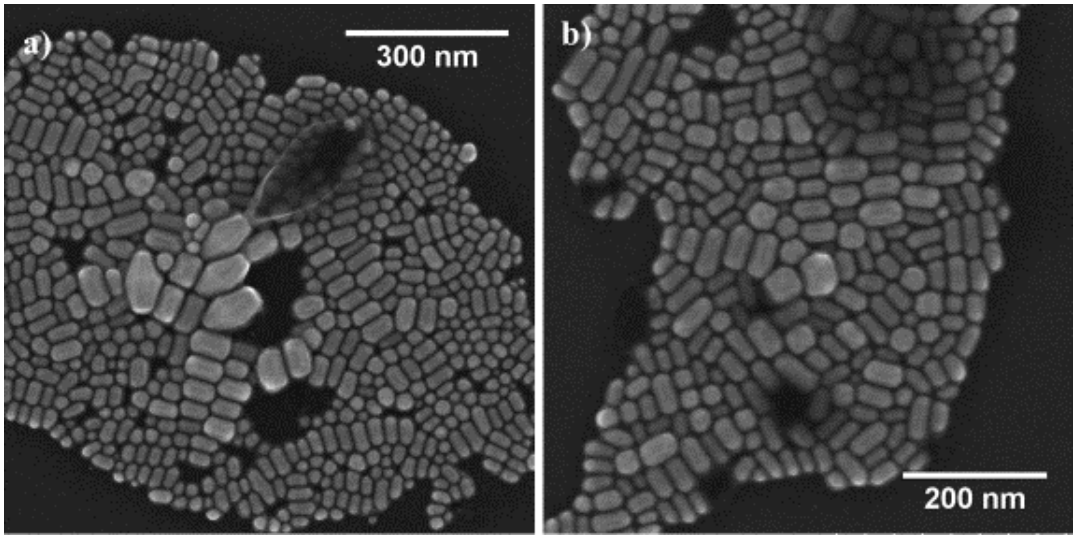

Figure S5. SEM images of polydisperse population of Au NRs and reaction byproducts (elongated THH and bipyramids) synthesized in the presence of single surfactant, DDAB (0.26 mmol/17.26mM).

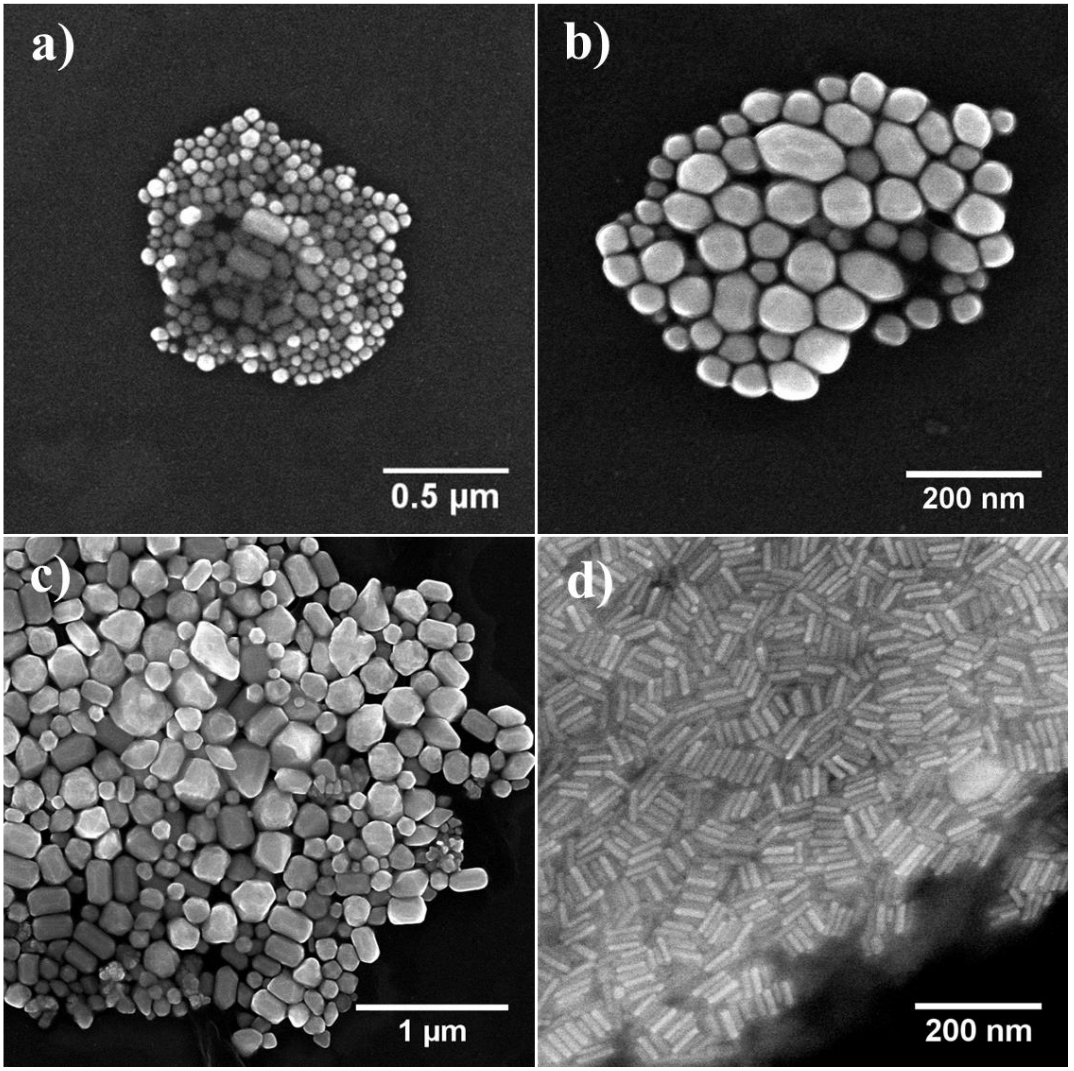

Figure S6. SEM images of Au NPs synthesized at fixed concentration of DDAB (0.26 mmol) and varying CTAB concentration. (a, b) CTAB=0.27 mmol, spherical and elongated NPs with low yield of elongated THH, c) CTAB=0.7 mmol, polydisperse elongated THH as main reaction with irregular shaped NPs as byproducts. d) CTAB=3.0 mmol, monodisperse Au NRs (aspect ratio~ 4.6).

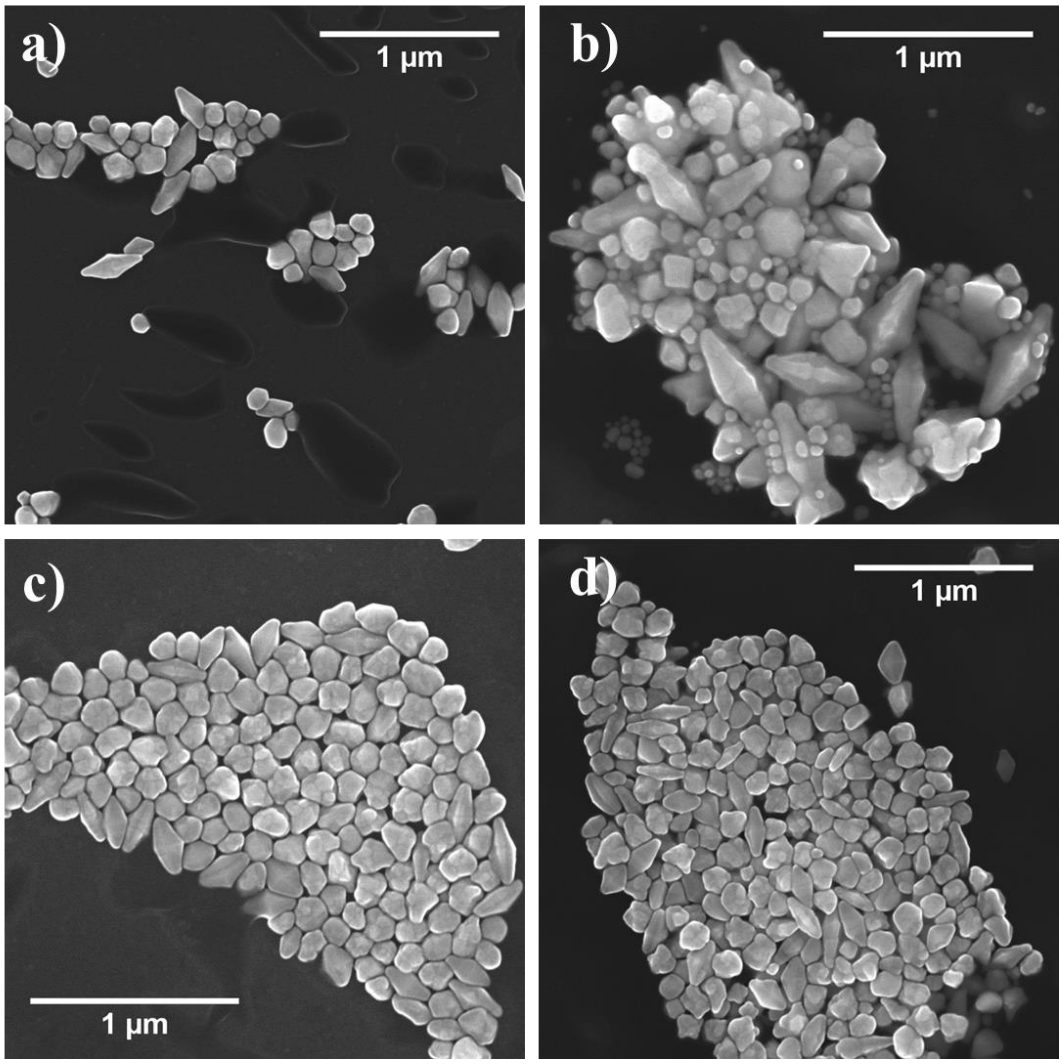

Figure S7. SEM images of Au bipyramids synthesized at low CTAB/DDAB ratio=6. The yield of Au bipyramids decreases as the pH of the solution increases by adding different volume of 0.1 M NaOH to the growth solution. (a) pH=2.9, (b) pH=3.0, (c) pH=3.1 and (d) pH=3.2.

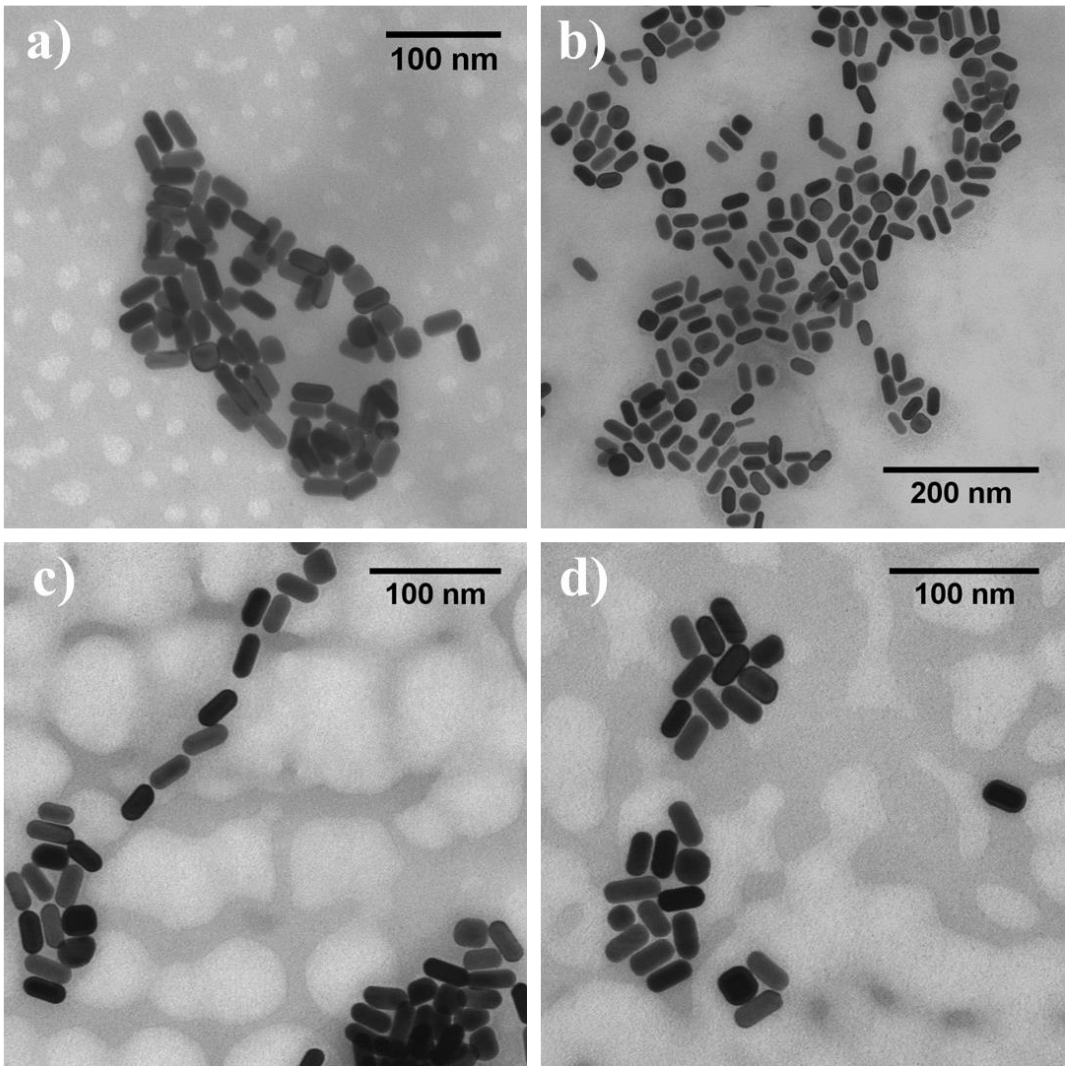

Figure S8. SEM images of Au NRs synthesized at high CTAB/DDAB ratio=23. The pH of the growth solution increases from (a) to (d) and does not have any significant influence on the aspect ratio of Au NRs. (a) pH=2.9, aspect ratio~2, (b) pH=3.0, aspect ratio~1.9, (c) pH=3.1, aspect ratio~2.3 and (d) pH=3.2, aspect ratio~1.8.

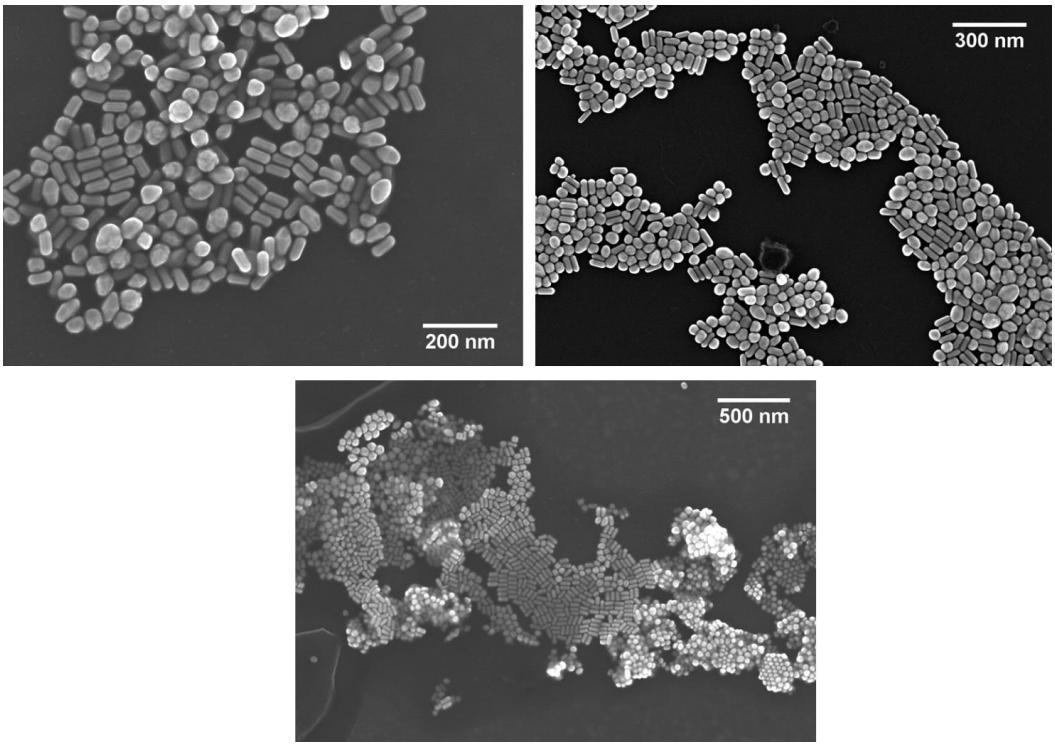

Figure S9. SEM images taken at different places on the substrate deposited with anisotropic Au NPs (mixture of faceted Au NRs and other shapes) synthesized low CTAB/DDAI ratio (~11).

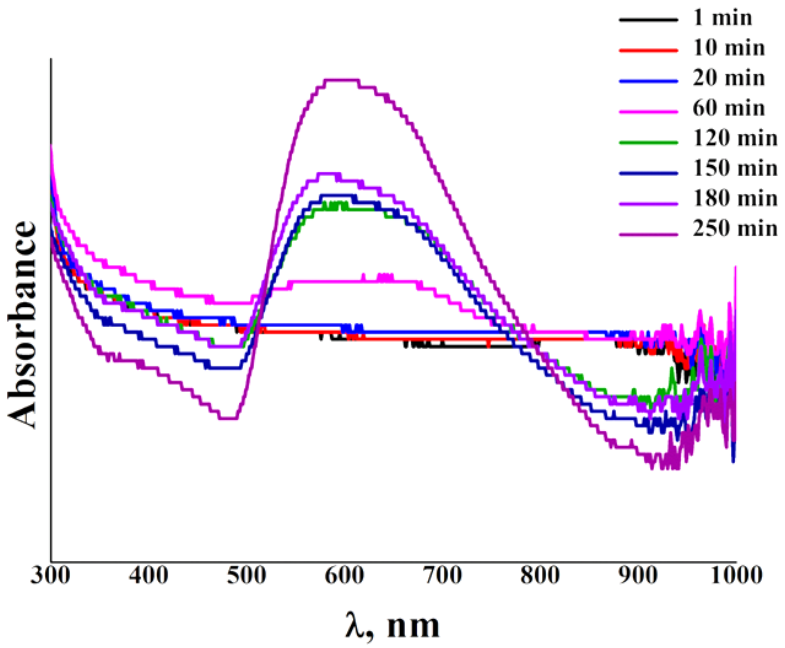

Figure S10. Temporal evolution of UV-vis spectra for the representative evolution of Au bipyramids.

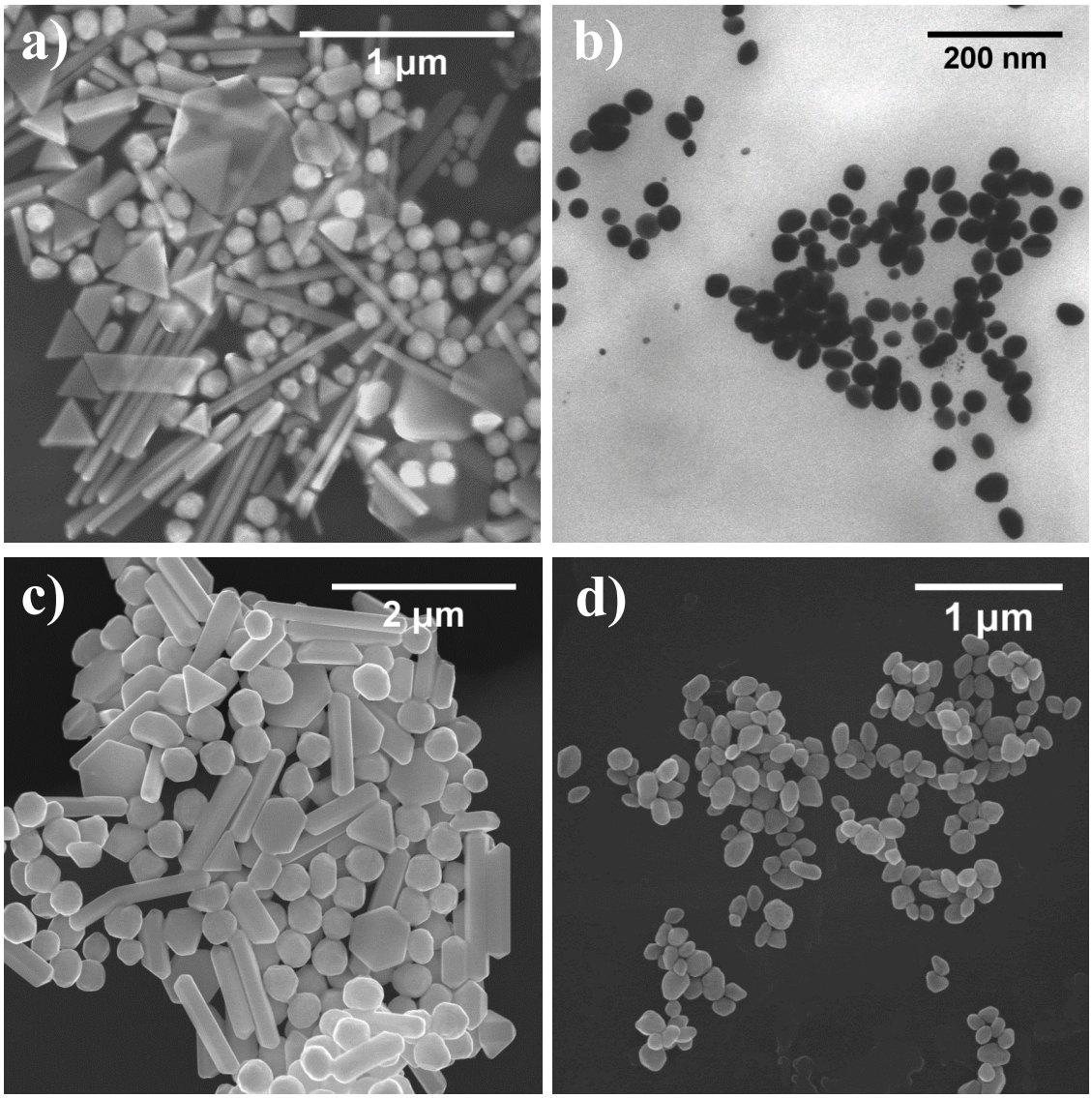
a)
1 µm
b)
200 nm
c)
2 µm
d)
1 µm

Figure S11. SEM images display the influence of Ag^+ ions the shape of Au NPs at different CTAB/DDAB ratios under identical experimental conditions. CTAB/DDAB=23 a) Ag^+ = 0 mL, Au NPs in different shapes, and b) Ag^+ = 0.3 mL, spherical/elongated Au NPs. CTAB/DDAB=6, a) Ag+ = 0 mL, mixture of various shapes of Au NPs and b) Ag+ = 0.3 mL, Au bipyramids of smaller size.

Paper- V:
Makura-shaped gold nanostructures show high cytotoxicity in cancer cells.

Is not included due to copyright

Paper- VI:

A robust method to calculate VPTT for hydrogels and hybrids.

Is not included due to copyright

Paper- VII:

Influence of polymer coating on release of L-Dopa from Core-shell Fe@Au nanoparticle systems.

Is not included due to copyright

Paper- VIII:

Influence of different shaped Gold nanoparticles functionalized with NIPAM based hydrogels on the release of Cytochrome C.

Is not included due to copyright